MOLECULAR SIMULATION OF CO_2 CAPTURE USING HYDROTALCITE

By:

Phebe Linette Bonilla Prado

Supervisor: Prof Meihong Wang

A thesis submitted in partial fulfilment of the requirement for the degree of
Doctor of Philosophy

Department of Chemical and Biological Engineering
Faculty of Engineering
The University of Sheffield

Acknowledgements

I want to thank my supervisor, Professor Meihong Wang, for the opportunity to carry out this project. I also thank Dr Mathew Aneke and Dr Toluleke Akinola for their time and discussions. Special thanks to the SCM team: Tomáš Trnka, Pier Philipsen, Thomas Soini, Alexei Yakovlev and Ole Carstensen. I would not have been able to carry out the molecular simulations without their guidance and suggestions.

I am also grateful for the help of various external researchers that kindly answered my questions, Professor John H. Harding and Professor Michail Stamatakis. Their insights helped to redirect the course of the project. Special thanks to Professor Adrianus van Duin, Professor Julian Gale, Dr Natalia Martsinovich, and Dr Colin Feeman.

A big thanks to all my friends and colleagues that contributed to my development during my stay in Sheffield. Especially those at the CBE Department, the Grantham Centre for Sustainable Futures, and the Belly dance, LatAm and Lishi Tai Chi societies. The talks we had helped me get through difficult times, and the fun kept me going.

Doing a PhD was very challenging. I would not have completed it without the support, cheering and understanding from my family. They have always encouraged me to follow my dreams and are the driver of my growth. Especial thanks to my dearest husband, Dr Jonathan J. Huerta y Munive for all the encouraging words and hours spent helping me on both academic and personal levels.

Finally, this project was possible thanks to the financial support from the National Council for Science and Technology of Mexico (CONACYT), the Grantham Centre for Sustainable Futures and the EPSRC Grant No. EP/N024540/1 Novel Adsorbent to Integrated Energy-efficient Industrial Capture.

Abstract

The excessive CO_2 emissions generated by human activities are the main factor resulting in climate change. A likely increase of 2ºC in the global average temperature is predicted to induce sea level rise and extreme weather events. Carbon Capture, Utilisation and Storage technologies will play a pivotal role in reducing these emissions and lessening the negative impacts. Currently, the most mature technology for carbon capture is chemical absorption using solvents such as mono-ethanolamine (MEA). However, this technology has the disadvantages of high energy requirements, the use of corrosive substances and elevated cost. The search for alternative cheaper and reliable capture methods is ongoing. Adsorption-based post-combustion carbon capture (PCC) has shown promising results, requiring less energy and using innocuous materials. Nevertheless, the development of adequate adsorbent materials and efficient process design for large scale implementation is still in the early stages.

In this work, we focus on adsorption-based PCC. After carrying out an extensive literature review in the advancements on adsorption carbon capture from the experimental and molecular simulation perspectives, and a survey of the bench and pilot-scale projects around the world using this technology, we selected hydrotalcites (HTs) as a potential adsorbent for capturing CO_2 from gas-fired power plant flue gases. HTs are better suited to work at the desired temperature (200ºC) in contrast with other adsorbent materials such as zeolites and activated carbon. In addition, they exhibit high CO_2 selectivity and are widely available. The main challenge for their large-scale implementation is their relatively low adsorption capacity in contrast with chemical solvents. Since their performance is influenced by their composition, synthesis, and operational conditions, an experimental approach is impractical, thus molecular simulations were employed. Molecular simulations enable systematic studies without the need for columns settings and with the appropriate tools, in less time.

To the best knowledge of the author, this is the first work employing the ReaxFF method for studying CO_2 capture using HT as adsorbents. This molecular simulation method allows the simulation of the formation of chemical bonds, even for large and complex systems as the HT. This study is the first step towards gaining a better understanding of CO_2 capture on HT at molecular level considering HT calcination, chemisorption and physisorption.

First, we developed a $Mg-Al-CO_3$ HT structure geometry with Density Functional Theory calculations. The results showed that the developed structure lattice parameters agreed with experimental measurements.

Next, we developed a specialized reactive force field (FF) and employed it for simulating the calcination process HT undergo for activation with molecular dynamics (MD) simulations. To the knowledge of the authors, this is the first FF capable of working with this HT structure. The FF generated with the Covariance Matrix Adaptation Evolutionary Strategy (CMA-ES) which had the lowest error function value was employed to carry out the calcination MD simulations. Finally, we carried out CO_2 adsorption studies with Grand Canonical Monte Carlo (GCMC) simulations at 200ºC and 1 bar to reflect PCC settings.

The MD simulations for analysing HT during calcination showed a similar decomposition trend as the one reported in the literature, starting with dehydration, a subsequent dihydroxylation, and finally a decarbonation, resulting in a mixed metallic oxides structure. For validation, we compared the surface area of the calcined simulated HT against experimental data. The simulated calcined HT exhibited a surface area of 247.63 m^2/g, which is in the expected range for calcined $Mg - Al - CO_3$ HT surface area reported by experiments. The GCMC simulations of the adsorption studies showed the HT structure has an adsorption capacity of 34.78 $molCO_2/kgHT$, which is much higher than reported in experimental studies. We attribute the disparity between the experimental and literature values to many factors related to the incipient nature of the generated FF and structure.

List of Publications and Presentations

Publications

- *Submitted*: Bonilla P., Akinola T., Wang M. (2021) “Experimental studies, molecular simulation and process modelling/simulation of adsorption-based post-combustion carbon capture for power plants: A state-of-the-art review” *Applied Energy in Oct. 2021*
- “Molecular Simulation of Post-combustion Carbon Capture using Hydrotalcites” Proceedings of the 15th Greenhouse Gas Control Technologies Conference (GHGT-15) 15-18 Mar. 2021. Available at: https://papers.ssrn.com/sol3/papers.cfm?abstract_id=3811404

Oral presentations

- “Molecular Simulation of Post-combustion Carbon Capture using Hydrotalcites” - 15th International Virtual Conference on Greenhouse Gas Control Technologies GHGT-15 15 - 18 Mar. 2021. Hosted by Khalifa University, Abu Dhabi, U.A.E.
- “Molecular simulation of CO_2 capture using Hydrotalcites” UKCCSRC Spring Web Series 2020, 5 May 2020. Hosted by the University of Sheffield, UK.
- “Development of a Reactive Force Field for ReaxFF to simulate CO_2 capture on Hydrotalcites” – 18th International Conference on Density-Functional Theory (DFT) and its Applications 22 - 26 Jul. 2019. University of Alicante, Spain.
- “Capturing CO_2 with the computer” – Engineering Research Symposium. 25 Jun. 2019. University of Sheffield. Prize “Research communicator of the Year”.
- “Molecular simulation of CO_2 capture on hydrotalcites as solid adsorbents” - CO_2 Capture and Storage Researchers Forum (CCSRF) of the United Kingdom Carbon Capture and Storage Research Centre (UKCCSRC). 4 Sep. 2018, Herriot-Watt University, Edinburgh, Scotland.

Poster presentations

- "CO_2 Capture with adsorbents: current pilot projects" UKCCSRC Autumn Web Series 2020, 12 Nov. 2020. Hosted by the University of Sheffield, UK.
- "Molecular simulation of CO_2 capture using Hydrotalcites" Symposium: Milestones on Molecular Simulation. 21 Jun. 2019. Imperial College of London, UK.
- "Molecular simulation of CO_2 capture using Hydrotalcites" Engineering Research Symposium. 25 Jun. 2019. University of Sheffield. Prize for the best poster of the department.
- "Molecular simulation of CO_2 capture on Hydrotalcites as Solid Adsorbents"- UKCCSRC Programme Conference. 12 Sep. 2018. University of Sheffield, UK.

Other activities

- "How can we capture CO_2?" - Outreach virtual talk for Y12 and Y13 students representing the Grantham Centre for Sustainable Futures. 17 Mar. 2021. Tapton School, Sheffield.
- "Delivering the new CCS agenda: CCS and the political process" – Blog for the UKCCSRC Biannual meeting: Clusters. 16 - 17 Apr. 2019. Cardiff University.
- "What are you breathing?" – Exhibition for the Blue Dot Festival- Outreach and public engagement representing the Grantham Centre for Sustainable Futures. Exhibitors: Phebe Linette Bonilla Prado (team coordinator), Rohit Chakraborty, Hamza Askari, Jonathan Sykes, Maria del Carmen Redondo Bermudez, Stephen A Jubb, Jonathan Julian Huerta y Munive. 18 - 21 Jul. 2019. Jodrell Bank Observatory, Manchester.
- "Capturing CO_2" – Outreach talk for Y11 pupils representing the Grantham Centre for Sustainable Futures. 8 Mar. 2018. Forge Valley School, Sheffield.

Content

List of Tables

List of Figures

Nomenclature

Å	Ångström, metric unit of length (1×10^{-10} m)
$\boldsymbol{E_{old}^{AMS}}$	Energy of the system produced by the optimised geometry after a move in GCMC simulations.
$\boldsymbol{E_{bond}}$	Bond energy in ReaxFF.
$\boldsymbol{E_{C2}}$	Correcting term of the behaviour of the bond formed between the C in a $-C_2-$ molecule (i.e. as a double bond, instead of triple) in ReaxFF.
$\boldsymbol{E_{coa}}$	3-body conjugation term (e.g. NO_2^-) in ReaxFF.
$\boldsymbol{E_{conj}}$	Energy of the conjugation effects (e.g. in benzene and other aromatics) in ReaxFF.
$\boldsymbol{E_{Coulomb}}$	Coulomb energy in ReaxFF.
$\boldsymbol{E_C[\rho(r)]}$	Coulomb electron repulsion of a system in DFT.
$\boldsymbol{E_{H-bond}}$	H-bond interactions in ReaxFF.
$\boldsymbol{E_{lp}}$	Energy derived from the presence of a lone electron pair in ReaxFF.
$\boldsymbol{E_{old}^{MC}}$	Energy of the original system before carrying out a move in a GCMC simulation.
$\boldsymbol{E_{Ne}[\rho(r)]}$	Potential energy or the electrostatic attraction between the nuclei and the electron density of a system in DFT.
$\boldsymbol{E_{over}}$	Energies that arise from the over-coordination of the atoms with respect to their valence in ReaxFF.
$\boldsymbol{E_{pen}}$	Penalty energy imposed for systems with two double bonds sharing an atom in a valency angle in ReaxFF.
$\boldsymbol{E_{system}}$	Total energy of the system in ReaxFF.
$\boldsymbol{E_{tors}}$	Energy of torsion angle in ReaxFF.
$\boldsymbol{E_{under}}$	Under-coordination energy of the atoms with respect to their valence in ReaxFF.

$\boldsymbol{E_{val}}$	Valence angle energy contribution in ReaxFF.
$\boldsymbol{E_{vdWaals}}$	Energy of the van der Waals interactions in ReaxFF.
$\boldsymbol{E[\rho(r)]}$	Electronic density of a system in DFT.
$\boldsymbol{E_{XC}[\rho(r)]}$	Exchange-correlation energy term that amends the deficiencies of the kinetic energy and Coulomb terms of a system in DFT.
fs	Femtoseconds ($1 \times 10^{-15}\ s$).
$\boldsymbol{Ha}$	Hartree, unit of energy in the Hartree atomic system of units ($4.3597447222071(85) \times 10^{-18}$ J).
$\boldsymbol{k}$	Boltzmann constant used in the GCMC algorithm.
$\boldsymbol{kcal/mol}$	Kilocalorie per mole, unit to measure the amount of energy per number of molecules or atoms.
kg	Kilogram, base unit of mass in the International System of Units.
$\boldsymbol{Mg_6Al_2(OH)_{16}(CO_3)\cdot 4(H_2O)}$	Magnesium aluminium hydroxide carbonate (HT).
mol	Mol, base unit of amount of substance in the International System of Units, equivalent to 6.02214076×10^{23} elementary entities.
$\boldsymbol{molCO_2/kg}$	Unit typically employed to measure the CO_2 adsorption capacity of a material per kilogram of adsorbent
ns	Nanoseconds ($1 \times 10^{-9}\ s$).
$\boldsymbol{N}$	Number of particles in ReaxFF ensembles.
$\boldsymbol{N_{inserted}}$	Number of inserted particles in GCMC simulations.
$\boldsymbol{NVT}$	Canonical ensemble with a fixed number of particles, volume and temperature.
$\boldsymbol{P}$	Pressure.
$\boldsymbol{V}$	Volume.
$\boldsymbol{V_{new}^{avail}}$	Available volume of the new system in GCMC simulations.
$\boldsymbol{V_{old}^{avail}}$	Available volume of the previous system in GCMC simulations.
$\boldsymbol{V_{new}}$	Total volume of the new system in GCMC simulations.
$\boldsymbol{V_{old}}$	Total volume of the previous system in GCMC simulations.

$\boldsymbol{s}$	Second, base unit of time in the International System of Units
$\boldsymbol{T}$	Temperature.
$\boldsymbol{T_s}[\boldsymbol{\rho}(\boldsymbol{r})]$	Kinetic energy of the electrons, assuming a non-interacting reference system in DFT.
$\boldsymbol{x_{i,TS}}$	Training set entry for calculating the error function in CMA-ES.
$\boldsymbol{x_{i,ReaxFF}}$	Modified FF entry for calculating the error function in CMA-ES.
$\boldsymbol{\mu_{MC}}$	Monte Carlo chemical potential for GCMC simulations.
$\boldsymbol{\sigma_i}$	Weight assigned to the difference between each of the entries of the training set and the modified FF for calculating the error function in CMA-ES.

Abbreviations

AC:	Activated Carbon
AMS:	Amsterdam Modelling Suite
BET:	Brunauer-Emmett-Teller
BSU:	Basic Structural Unit
CBMC:	Configurational-Bias Monte Carlo
CCUS:	Carbon Capture, Utilisation and Storage
CCC-ECL:	Cryogenic carbon capture - External Cool Looping
CDCL:	Coal Direct Chemical Looping
CFB:	Circulating Fluidized Bed
CHA:	Chabazite
CLAYFF:	Clay Force Field
CLC:	Chemical Looping Combustion
CLG:	Chemical Looping Gasification
CLOU:	Chemical Looping with Oxygen Uncoupling
CLP:	Chemical Looping Process
CLR:	Chemical Looping Reduction
CM:	Carbonaceous Material
CMA-ES:	Covariance Matrix Adaptation Evolutionary Strategy
CNF:	Carbon nanofiber
CNT:	Carbon Nanotube
CVFF:	Consistent-Valence Force Field
DFT:	Density Functional Theory
DFT/CC:	Density Functional Theory - Coupled Cluster
FAU:	Faujasites
FF:	Force Field
FF1:	Force Field generated previously by Dr Mathew Aneke

FF2: Force Field obtained in the CMA-ES-9 Run 5

FPMD: First-Principle Molecular Dynamics

FTIR: Fourier-Transform Infra-Red

GCMC: Grand Canonical Monte Carlo

GGA: Generalised Gradient Approximation

GHGT-15: 15th International Conference on Greenhouse Gas Control Technologies

GO: Geometry Optimisation

GOx: Graphene Oxide

GTI: Gas Technology Institute

HF: Hartree-Fock

HPFS: Homogeneous precipitation from solution

HT: Hydrotalcite

ICSD: Inorganic Crystal Structure Database

IPCC: Intergovernmental Panel on Climate Change

LDA: Local Density Approximation

LDH: Layered Double Hydroxide

LDHFF: Layered Double Hydroxides Force Field

LDO: Layered Double Oxides

LTA: Linde Type A zeolite

MBTSA: Moving Bed Temperature Swing Adsorption

MC: Monte Carlo

MCFF: Monte Carlo Force Field

MD: Molecular Dynamics

MEA: Monoethanolamine

MIL: Materials Institute Lavoisier

MLD: Molecular Layer Deposition

MMO:	Mixed Metallic Oxides
MOF:	Metal Organic Framework
NH:	Noosé-Hover
NETL:	National Energy Technology Laboratory
NOAA:	National Oceanic and Atmospheric Administration
PBE:	Perdew–Burke–Ernzerhof
PCC:	Post-combustion Carbon Capture
PCI:	Precision Combustion Inc
PES:	Potential Energy Surface
PSA:	Pressure Swing Adsorption
ReaxFF:	Reactive Force Field
RMC:	Reverse Monte Carlo
RMSD:	Root Mean Square Deviation
RPI:	Rensselaer Polytechnic Institute
SAS:	Solvent-Accessible Surface
SC:	Super Cell
SCC:	Self-Consistent Charge
SCM:	Software for Chemistry and Materials
SEM:	Scanning Electron Microscopy
ST:	Statistical Thermodynamics
TGA:	Thermogravimetric Analysis
TraPPE:	Transferable Potentials for Phase Equilibrium
TS:	Training Set
TSA:	Temperature Swing Adsorption
TVSA:	Temperature Vacuum Swing Adsorption
USC:	University of South Carolina
UFF:	Universal Force Field

UNFCCC:	United Nations Framework Convention on Climate Change
VFF:	Valence Force Field
VS:	Validation Set
VSA:	Vacuum Swing Adsorption
XRPD:	X-Ray Powder Diffraction

1. Introduction

1.1 Background

1.1.1 Energy demand, Climate change and CCUS

Global energy consumption has increased exponentially driven by emerging markets and population growth. In 2019, over 173,340 TWh were consumed in contrast with the estimated 5,653 TWh used in 1800 (Ritchie and Roser, 2020). Despite the historic increase in renewable energy generation of 238 GWh in 2020 (a 50% increase in wind and solar capacity than at any time in history), fossil fuels are still the main source of energy in the world (BP, 2021). Oil, gas and coal accounted for 84% of the energy mix in 2019, whereas renewable energy sources covered only 10% (BP, 2020), with coal being the largest single source accounting for 36% of the mix, its lowest level in 16 years (BP, 2020).

The main concern about the growing energy demand is the unavoidable product of the combustion of fossil fuels: CO_2. Its emissions, estimated at 32,284 million tonnes in 2020 (BP, 2021) have reached record figures. In February 2021, 416.75 ppm CO_2 were detected in the atmosphere, in contrast with the pre-industrial estimated level of 278 ppm (NOAA, 2021). Since CO_2 is a greenhouse gas, the most important contributor to radiative forcing (IPCC, 2014), its high concentration in the atmosphere results in unintended consequences. A likely increase of 2ºC in the global temperature in comparison with pre-industrial levels is predicted to rise sea level and produce extreme weather events (IPCC, 2018). Recent examples of the impact of climate change are the fires during the "Black summer" in Australia during 2019 - 2020 (Kemter *et al.*, 2021), and the heavy snowstorm in Texas, United States in February of 2021 (Bogel-Burroughs *et al.*, 2021).

A reduction in CO_2 emissions is imperative to prevent or lessen these impacts. The Paris Agreement by the United Nations aims at holding the increase of the global average temperature below 2°C above pre-industrial levels (UNFCCC, 2015) and its results are being currently discussed in the COP26 (*COP26*, 2021). Carbon Capture, Utilization and Storage technologies (CCUS) will play a pivotal role to achieve these goals.

CCUS can enable the transition to a low-carbon economy by decarbonising "hard-to-abate" sectors, such as the iron, cement, and steel industries. These technologies can also enable the production of net-zero energy and allow the re-use of infrastructure and postpone decommissioning costs (Townsend *et al.*, 2020).

However, achieving a significant reduction in CO_2 emissions through CCUS requires a global large-scale implementation. It is estimated that for achieving the Paris Agreement targets, we need to deploy a CCUS capacity of about 5,635 $MtCO_2$ per year by 2050, in contrast with the existing 40 $MtCO_2$ per year in 2020 (Page *et al.*, 2020). Unfortunately, the high cost of CCUS still hampers its commercial implementation, although encouraging progress has been made. For example, by 2012, capturing CO_2 costed about \$15 - \$75/tonCO_2, transportation ranged from \$2 - \$8/tonCO_2 and the geological storage cost ranges from \$0.5 to \$8/tonCO_2 (Fan *et al.*, 2012). Current projects, such as the FEED project in Australia, have estimated an total abatement cost of \$22/tonCO_2, well below the estimated \$40-80/tonCO_2 required by 2020 for achieving the Paris Agreement targets (Page, Turan and Zapantis, 2020).

To understand why CCUS technologies are costly we must take a closer look at the current capture technology, which is still the most expensive part of CCUS. Currently, there are three main approaches for capturing CO_2: pre-combustion, oxy-fuel, and post-combustion. Each approach has its own advantages and disadvantages depending on its application settings and the technology used.

For this work, we focus on post-combustion capture (PCC) since it allows a flexible operation (Norahim *et al.*, 2018) and easy retrofitting in existing power plants (Tuinier *et al.*, 2010; Younas *et al.*, 2016). As suggested by the name, in PCC, the CO_2 is separated from the flue gases after the fuel combustion takes place usually at 1 bar and 40 – 400 ºC. The CO_2 concentration in the flue gases varies depending on the fuel used (Zhao *et al.*, 2017). For example, for natural gas typical values range from 8 %vol to 10 vol%, whereas for coal, CO_2 concentration can be higher, between 12 %vol and 14 %vol, (Di Biase and Sarkisov, 2013; Garcés *et al.*, 2013; Hallenbeck and Kitchin, 2013; Salaudeen *et al.*, 2018). The variation in the settings and flue gases concentrations makes different PCC technologies better fit for certain applications than others.

There are four main PCC developed technologies: absorption, membrane separation, cryogenic fractionation and solid sorbents (Li *et al.*, 2013). Other technologies under development are chemical looping (Bui *et al.*, 2018), electrochemical separation (Shaw and Hatton, 2020), enzyme-enabled carbon capture (Fradette *et al.*, 2017) and micro-algae bio-fixation (Ben-Mansour *et al.*, 2016; Moreira and Pires, 2016), still on early stages. Among these technologies, the most mature is chemical absorption. It relies on chemical solvents, such as mono-ethanolamine (MEA) to separate the CO_2 from a stream of gases.

However, the use of solvents can increase the price of electricity produced in power plants due to an efficiency loss of about 10% (Wang *et al*, 2017), This is because of the large amount of energy required to regenerate the absorbent, which is reflected in the operational costs. To put this in context, amine solutions can represent a parasitic load of 25 to 40% to the energy produced by a power plant (Di Biase and Sarkisov, 2013). CO_2 PCC with amine solvents presents other disadvantages. Their volatility restricts the temperature of their application to a range between 40 and 150°C, requiring the cool down of flue gases. Also, the corrosive nature of the amines entails health and environmental risks (Areeprasert *et al.*, 2014; Rashidi and Yusup, 2016; Salaudeen *et al.*, 2018).

The search for novel processes and materials to carry out CO_2 capture with less energy in a safer manner is ongoing. Adsorption-based PCC is a promising alternative which has shown a lower energy requirement while using innocuous materials. Nevertheless, this PCC technology is still under development and requires further research to be commercialised.

1.1.2 Adsorption-based PCC

Comprehending the challenges that adsorption must overcome if it is going to compete with chemical absorption, requires first to understand how it works. Unlike chemical absorption, which relies on liquid solvents, adsorption involves porous solid materials, called adsorbents, to capture the CO_2, or adsorbate (Lawal *et al.*, 2010; IPCC, 2018). When flue gases are in contact with the adsorbent, the CO_2 attaches to its surface more readily than other components of the gaseous stream in an exothermic and spontaneous process, denominated adsorption (Dantas *et al.*, 2011; Younas *et al.*, 2016). There are two types of adsorption: physical adsorption (physisorption) and chemical adsorption (chemisorption).

Physisorption is mainly caused by van der Walls and electrostatic forces; although hydrophobic associations, non-polar and dipole-dipole interactions can also be present. Since there are no chemical reactions, the capture capacity of physisorption processes relies mainly in the mass transfer of CO_2 into the sorption sites. The mass transfer is promoted by the gas phase diffusion through the pores of the adsorbent or by pressure increase (Bhatta *et al.*, 2015a). The heat of adsorption of physisorption is in the region of 25 kJ/mol and increases when the electrostatic forces are significant. Such as the case in the charged structure of common adsorbents such as zeolites and hydrotalcites (Oliveira *et al.*, 2008; Choi *et al.*, 2009). The bond energy is around 8 – 41 $kcal\ mol^{-1}$, relatively low (Oliveira *et al.*, 2008).

This allows adsorbent regeneration by degassing, using less energy. However, due to the weakness of the van der Waals forces, physisorption is very sensitive to temperature. Over 50 °C, physical adsorption decreases substantially and is superseded by chemisorption (Dantas *et al.*, 2011; Younas *et al.*, 2016).

During ***chemisorption***, the adsorbate molecules form covalent, ionic or metallic bonds, with bond energy between 60 and 418 $kcal\ mol^{-1}$ (Younas *et al.*, 2016). This results in a considerably higher heat of adsorption, in the region of 200 kJ/mol, which requires a better heat control of the exothermic reactions during adsorption (Younas *et al.*, 2016). Utilising fluidized beds to improve heating management has been proposed. These increase the superficial velocity helps avoid the creation of hot spots (Li *et al.*, 2013). Another consequence of the creation of bonds is that the regeneration of the sorbent requires more energy, increasing operational costs. Furthermore, chemisorption can reduce the capture capacity of the material in the long term. Therefore, chemisorption is preferred for permanent binding rather than cyclic adsorption processes. Figure 1.1 summarises the main characteristics of physical and chemical adsorption.

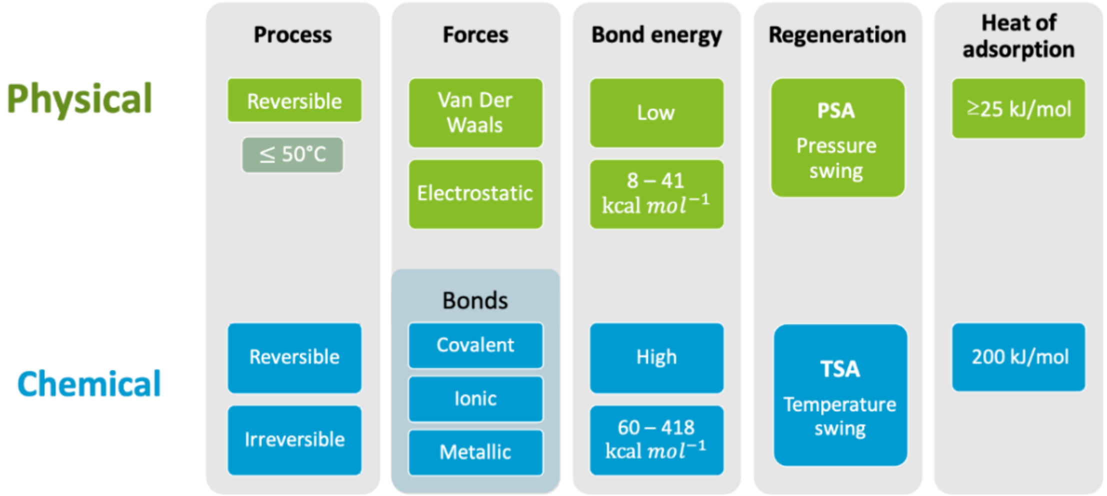

Figure 1.1 Types of adsorption.

Both physisorption and chemisorption, are often present in PCC applications. The two main factors influencing which one is prevalent are the selection of the adsorbent material and the operational parameters of the regeneration process. These aspects are critical when designing and operating an efficient adsorption system (Siegelman *et al.*, 2019).

Adsorption processes have been implemented mainly in low-temperature processes (<100°C) (Younas *et al.*, 2016), although their performance at higher temperatures remains to be studied. Adsorbents are well fitted for natural gas power plants emissions (3-5% CO_2 content) since they are more selective than other capture methods whose efficiency depends on the CO_2 concentration (Lillia *et al.*, 2018).

In contrast with the aqueous absorbents, solid adsorbents generate less waste during operation and the spent material can be disposed of without excessive environmental precautions (Younas *et al.*, 2016). Laboratory scale studies have shown that the regeneration of adsorbents is more energy efficient since fewer chemical bonds are formed (Di Biase and Sarkisov, 2013; Zhao *et al.*, 2015). As a result, adsorption has lower operational costs (Cheung and Hedin, 2014). Furthermore, adsorption systems involve lower capital investment (Zhao *et al.*, 2017) and can operate at a wider range of temperatures and pressures (León *et al.*, 2010). Nevertheless, adsorption capture still must overcome certain challenges. The adsorption capacity of the adsorbent materials and their compatibility with operational conditions are the main ones. On the other hand, there is a lack of information regarding the scalability of the adsorption since most of the studies carried out have only considered laboratory conditions.

All these advantages make a strong case for large-scale adsorption CO_2 capture in the future (Cheung and Hedin, 2014). However, adsorption on solid materials is still under development. Just as any other technology, it needs improvement before it can be widely implemented. Most of the identified challenges are related to the regeneration process and the adsorbent material, i.e., its adsorption capacity, production, and handling.

1.1.3 Regeneration processes

In order to create a cost-efficient PCC adoption process, the adsorbent material must be reused as many times as its cyclic stability allows it (Bhatta *et al.*, 2015a). At the targeted commercial scale, the lifetime of the adsorbent material determines how often it must be replaced, having a significant impact on cost. Thus, the selection of the regeneration process is as important as the adsorbent material choice. There are different methods to regenerate the adsorbent material. In general, they work by creating a difference in:

1) **Pressure**, e.g. pressure swing adsorption (PSA), vacuum swing adsorption (VSA), pressure-vacuum swing adsorption (PVSA)
2) **Temperature**, i.e. temperature swing adsorption (TSA) and electric swing adsorption (ESA) if the heat is provided by electricity (Grande and Rodrigues, 2008); or

3) **A combination of both**, e.g. vacuum-temperature swing adsorption (VTSA) and pressure-thermal swing adsorption (PTSA) (Bhatta *et al.*, 2015b; Ben-Mansour *et al.*, 2016). The most adopted methods are PSA and TSA.

PSA

The PSA process comprises CO_2 adsorption at a pressure higher than atmospheric and regeneration of the adsorbent at atmospheric pressure (Grande, 2012; Webley, 2014; Ben-Mansour *et al.*, 2016; Zhao *et al.*, 2017). Depending on the selected adsorbent, a pre-treatment to remove humidity and other impurities might be required, especially if the adsorbent is hydrophilic as in the case of zeolites (Riboldi and Bolland, 2017). The adsorption-regeneration process is designed to occur in steps, whose repetition create a cycle (Grande, 2012). Depending on the configuration of the PSA unit, the number of steps in the PCC adsorption cycle can vary from 4 to 12 steps (Riboldi and Bolland, 2017). The time each cycle requires depends on the adsorbent and configuration, ranging from a few seconds to several minutes (Abanades *et al.*, 2015).

An advantage of PSA is that it can operate at high temperatures, so the cooling step for flue gases can be skipped and energy saved (Dantas *et al.*, 2011). Additionally, since the feed stream is already at high pressure, it is possible to ensure a rapid cycling time in fixed beds (Grande, 2012). However, it is this pressurised condition that can make PSA unfavourable for PCC processes. The need to increase the pressure of flue gases can raise the energy consumption and thus operational cost (Webley, 2014; Abanades *et al.*, 2015; Riboldi and Bolland, 2017). On the other hand, un-intensified PSA processes have an unpractical footprint for treating large amounts of flue gases due to the maximum pressure drop and minimum fluidization velocity (Riboldi and Bolland, 2017). Despite these drawbacks, PSA has been used as an effective gas separation technique in industry for air separation to produce O_2 (Grande, 2012). In the case of CO_2 capture, it is seen as better fitted for pre-combustion settings, i.e. high temperature and relatively high inlet pressure, which makes the use of vacuum pressure levels unnecessary, and reduces dramatically the energy consumption (Riboldi and Bolland, 2017; Zhu *et al.*, 2018).

VSA

VSA is a modified PSA process in which adsorption takes place at atmospheric pressure and desorption under vacuum conditions (Zhu *et al.*, 2018). The vacuum level is a crucial factor that balances the CO_2 separation and the energy consumption (Riboldi and Bolland, 2017).

Since the pressure conditions are closer to the ones of flue gases coming out of combustion, VSA processes have shown promising results for PCC applications (Liu *et al.*, 2011; Shen *et al.*, 2012; Wang *et al.*, 2013; Riboldi and Bolland, 2017).Combinations of the conditions (PSA/VSA), configuration and number of steps have been studied to improve the separation performance and achieve the National Energy Technology Laboratory (NETL) of the USA Department of Energy (DOE) for CCUS: 95% CO_2 purity and 90% CO_2 recovery (Jiang *et al.*, 2020). The basic single-stage systems can be competitive in terms of energy consumption, however, if VSA is used it can be difficult to implement on large systems (Riboldi and Bolland, 2017). Using a two-stage VSA process can improve the performance; the first stage is focused on CO_2 recovery whereas the second stage objective is to achieve the desired purity. These systems can achieve 90% CO_2 recovery and purity (Riboldi and Bolland, 2017). Two-stage VPSA can go further and increase it to >95% CO_2 purity (Shen *et al.*, 2012). Further research regarding the intensification of VSA and PSA units is key for implementing adsorption at a large scale, especially since their footprint can be much larger compared to CO_2 absorption units (Riboldi and Bolland, 2015). In general, VSA and PSA processes are more suitable for small scale (~50 MW) in post-combustion settings unless multiple trains are installed, which makes them more expensive in contrast with chemical absorption (Bui *et al.*, 2018).

TSA

In TSA systems, adsorption takes place at a lower temperature than desorption (Zhao *et al.*, 2017). An interesting feature of TSA units is that they can make use of low-grade thermal energy (Jiang *et al.*, 2020), making it easy to retrofit in existing power plants (Ben-Mansour *et al.*, 2016) and reducing the energy cost. The ideal temperature range for PCC TSA goes from 30ºC to 150ºC, which is the range of temperature at which heat is available in a power plant and can be channelled from the low-pressure turbine, the flue gases waste heat or CO_2 compression (Webley, 2014). Both physisorbents and chemisorbents are compatible with TSA, although it is considered that the latter are the best fit for this application since they tend to be less sensitive to the presence of humidity (Abanades *et al.*, 2015). Chemisorbents with heat of adsorption between 40 and 70 kJ/mol are adequate for TSA applications (Webley, 2014). TSA processes can be a good option in cases where the concentration of CO_2 in the flue gases is lower, i.e. in gas-fired power plants (Abanades *et al.*, 2015).

The main disadvantage of TSA systems is the long duration of the cycle, mainly due to the cooling step, which can last hours (Webley, 2014; Abanades *et al.*, 2015). Changing the column configuration has been studied for overcoming this challenge. Circulating fluidized-bed (CFB) columns or moving beds have the advantage of increasing the heat transfer performance (Webley, 2014; Abanades *et al.*, 2015). However, CFBs are difficult to operate from the mechanical perspective since they require low gas velocity implies large column diameters (Bui *et al.*, 2018), and adsorbent attrition and poisoning is significant (Webley, 2014). Alternatively, as in the case of PSA, different configurations of the process and combinations of the conditions can improve the capture unit performance. Faster heating can be achieved if electric power is used in ESA. Yet, due to the energy cost, this configuration is best fitted for small scale applications (Bui *et al.*, 2018).

TVSA

An effective combination of temperature and vacuum conditions is the temperature vacuum swing adsorption (TVSA) process. During this process, regeneration occurs with counter-current evacuation and mild heating, reducing the vacuum required to achieve the performance parameters (Plaza and Rubiera, 2019). Recent studies showed that TVSA can duplicate the productivity of a TSA process with less than half of the energy requirement using the same adsorbent (Jiang *et al.*, 2020).

Other considerations

From a process perspective, the design of the PCC unit should consider other factors when selecting the regeneration type, such as the CO_2 loading, specific heat capacity and lower heat of adsorption, as they affect the stability, lifetime, performance and regeneration rate of the adsorbent (Bhatta *et al.*, 2015b). Additionally, the operation conditions of temperature and pressure, the efficiency of the air compressor and the fraction of heat recovery can be optimised (Zhao *et al.*, 2017). The compressor and the vacuum pump efficiencies are especially important when calculating the power consumption, and are usually assumed as 70% (Zhao *et al.*, 2017) although this assumption can underrepresent the final consumption (Bui *et al.*, 2018).

1.1.4 Adsorbent materials characteristics

The performance of an adsorbent-based PCC unit is largely influenced by the adsorbent material. There is a wide range of adsorbents that have been studied for CO_2 capture, each one with different physical and chemical characteristics that fit better some operation conditions than others. In the literature, high capture capacity and high CO_2-selectivity at low partial pressures (<0.2 bar) are highlighted (Bhatta *et al.*, 2015a,b; Lu *et al.*, 2015). These traits are interlinked with others that also affect the performance of the material, such as high porosity and high surface area (Pramod *et al.*, 2015).

However, these characteristics alone are not responsible for the final performance of the adsorption unit. The operation conditions and the regeneration process play a crucial role in extending the life of the adsorbent and in increasing efficiency. PCC applications tend to work at low pressure, around 1 bar, and usually contain about 3-15 vol% of CO_2 (Zhao *et al.*, 2015), with the rest being comprised of N_2, O_2, NO_x, water vapour and even SO_x, depending on the combusted fuel (Di Biase and Sarkisov, 2013; Hallenbeck and Kitchin, 2013; Salaudeen *et al.*, 2018). Thus, impurities tolerance is desired to extend the life of the adsorbent.

Another important trait of the adsorbent when designing the PCC unit is thermal stability, especially if temperature swing is used for regeneration. In addition, flue gases can exhibit a wide range of temperature, usually between 40 and 200°C in power plants, although some industrial streams can reach higher temperatures, from 150 to 400°C (Di Biase and Sarkisov, 2013; Hallenbeck and Kitchin, 2013; Salaudeen *et al.*, 2018). The selected adsorbent must be able to work at the expected temperature in the PCC unit. For example, carbonaceous materials work best around 50 ºC and 1 bar, metal-organic frameworks exhibit optimal adsorption at room temperature or lower and 35, whereas zeolites can work in a wide range of pressures with a temperature between 0ºC and 100ºC (Choi *et al.*, 2009; Garcés-Polo *et al.*, 2017).

In addition to the adsorption capacity and operation conditions, other characteristics must be considered from the economic perspective. For example, a competitive production cost, attrition resistance to reduce replacement frequency, recycling ability to avoid expensive disposal and a low-temperature gap between the adsorption and regeneration temperatures to reduce energy consumption (Wang *et al.*, 2011; Fakhroleslam and Fatemi, 2016; Salaudeen *et al.*, 2018). Table 1.1 presents a summary of the ideal characteristics of adsorbent materials for PCC and how they influence the cyclic process.

Table 1.1 Adsorbent characteristics influencing adsorption capacity

Category	**Adsorbent characteristics**	**Relation to the cyclic process**
Structure	• High porosity • High surface area	An increase in porosity can increase the surface area. Higher surface areas usually lead to higher adsorbent capacities.
Stability	• Thermal (minimal degradation of the material) • Mechanical (resistance to attrition) • Chemical (tolerance towards impurities)	The stability of the material to sustain the adsorption capacity and characteristics throughout several cycles extends the life of the material and reduces cost.

Category	Adsorbent characteristics	Relation to the cyclic process
Behaviour	- Selectivity for CO2 over other gases - Affinity to CO2 - Fast kinetics	Fast kinetics and CO2 diffusion rate are preferred, they also affect will affect regenerability
Production	- Low cost - Availability - Recyclability	Synthesis of the adsorbent and residues handling must be cost-effective to scale up adsorption-based PCC systems

(Bhatta,*et al.*, 2015; Pramod *et al.*, 2015; Fakhroleslam and Fatemi, 2016; Bahamon *et al.*, 2018; Salaudeen *et al.*, 2018).

Different adsorbent materials exhibit these ideal characteristics to a lesser or greater extent. Popular adsorbents in the literature are zeolites, carbonaceous materials, metal-organic frameworks and hydrotalcites, among others. Other examples are alkalized alumina Al_2O_3 (Elliot and Yi, 2020), K_2CO_3 on a support material (Park *et al.*, 2014), poly-amine (PEI) on support silica (Nelson *et al.*, 2017) and metallic oxides on zeolites (Gollakota and Yu, 2020).

1.1.5 Common adsorbent materials for CO$_2$ capture

Zeolites

Zeolites are microporous minerals with a highly ordered crystalline structure. Since they are composed of Al (III) and Si (IV), they are classified as aluminosilicates (Bhatta, Subramanyam, Chengala, Olivera, *et al.*, 2015). In zeolites, the Al (III) and Si (IV) form a negatively charged structure commonly found as a honeycomb (Younas *et al.*, 2016); although zeolites can exhibit diverse topologies, pore sizes and openings (Cheung and Hedin, 2014). The negative charge of the framework is balanced with interleaved exchangeable cations (M^{+k}), such as K, Ba, Li, Na, Mg, Ca, (Cheung and Hedin, 2014). The general chemical formula of zeolites is:

$$M^{+k}{}_{x/k}\left[Al_xSi_yO_{2(x+y)}\right]ZH_2O \tag{1.1}$$

Where Z is the number of water molecules present in the structure. Zeolites can be naturally found, although for adsorption purposes it is preferred to synthesize them to control their porosity and crystallinity (Cheung and Hedin, 2014; Pardakhti *et al.*, 2019). Their structure confers them advantageous characteristics as adsorbents. Zeolites exhibit high adsorption capacity (Dantas *et al.*, 2011; Ben-Mansour *et al.*, 2016) which can be sustained even after several cycles and fast kinetics (Choi *et al.*, 2009).

The main drawbacks of using them as PCC adsorbents are their poor thermal stability (Pramod *et al.*, 2015) and their sensibility towards impurities, especially polar gases as SO_2 (León *et al.*, 2010) and water (Bhatta *et al.*, 2015b; Ben-Mansour *et al.*, 2016; Younas *et al.*, 2016). This is challenging since both can be present in flue gases, and thus, pre-treatment is usually required, increasing the capture cost. Another factor influencing operating cost is the adsorption pressure. If zeolites are used at 2 bar or higher, a high regeneration temperature is required (Ben-Mansour *et al.*, 2016). Despite this, zeolites have shown promising results for CO_2 capture, with zeolite 13X being the most typical example already commercially available (Garcés *et al.*, 2013).

Carbonaceous materials

Carbonaceous materials (CMs) are highly porous materials mainly comprised of carbon, hence the name. The most common example is activated carbon (AC), although there are many other materials in this category, namely graphene, mesoporous carbon, carbon nanotubes (CNT) (Bhatta *et al.*, 2015b; Younas *et al.*, 2016), charcoal, coal (Ben-Mansour *et al.*, 2016), graphite, graphene oxide (GOx); carbon aerogels, polymer-based carbon (Kamran and Park, 2021). In contrast with zeolites and other adsorbents, CMs structure does not have a strong interaction with the CO_2, and thus, tend to have a lower adsorption capacity and selectivity (Zhao, Liu and Han, 2015). On the other hand, this weak interaction makes them more tolerant towards humidity and allows regeneration to be carried out through degasification (Bhatta,*et al.*, 2015b; Younas *et al.*, 2016) which requires less energy, reducing cost (Lian *et al.*, 2019).

The popularity of ACs can be explained by their wide availability and low cost. They can be obtained from naturally existing sources or synthesised from spent materials, e.g. from the pyrolysis of carbon-containing resins, fly ash or biomass (Ben-Mansour *et al.*, 2016). Depending on the precursor, ACs can exhibit different pore sizes and surface area (Bhatta *et al.*, 2015b; Younas *et al.*, 2016). These characteristics are important since a high surface area and large pore volume make ACs an excellent adsorbent at high pressure (León *et al.*, 2010), especially at high CO_2 concentration (Ben-Mansour *et al.*, 2016). The main disadvantages of ACs are the low thermal stability of their micropore structure (León *et al.*, 2010) and high attrition rates in cyclic processes (Bhatta *et al.*, 2015b). However, their consistent and reproducible behaviour (Di Biase and Sarkisov, 2013) has shown promising results for CO_2 capture, as discussed in (Rashidi and Yusup, 2016).

Metal-Organic Frameworks

Metal-organic frameworks (MOFs) are synthetic highly porous materials. Despite being introduced only in 1995 (Yaghi *et al.*, 1995), their promising results have made them a widespread adsorbent (Bahamon *et al.*, 2018). MOFs have a cubical structure, in which the edges are made of organic linkers united in the vertices by inorganic clusters (Younas *et al.*, 2016). By selecting the metal cluster, the organic linker and additional functional groups, their size and geometry can be tailored for the target application, which can range from gas storage, ion exchange and catalysts to CO_2 capture (Bahamon *et al.*, 2018).

Given the large number of possible combinations, there are over 81,000 different MOF structures in the Cambridge Structural Database (Pardakhti *et al.*, 2019). The variants used as adsorbents exhibit useful traits such as a low density (0.2 – 1 g/cm^3), good thermal and mechanical stability, well-defined porous volume, specialised chemical functionalities and extremely large surface areas, from 500 to 10,000 m^2/g (Younas *et al.*, 2016). Two examples that stand out for CO_2 capture are M-MOF-74 (M being a metal as Mg or Co) and HKUST-1 (Pardakhti *et al.*, 2019). The former has shown an impressive adsorption capacity of 8.1 molCO_2/kg at 25° and 1 bar, whereas the latter has an even higher capacity, from 8.0 to 10.2 molCO_2/kg at the same temperature, but much higher pressure, 15 bar (Bahamon *et al.*, 2018). Despite their promising results, MOFs tend to have low thermal stability (Garcés *et al.*, 2013). Moreover, their production is expensive and its scalability is still challenging (Bhatta, Subramanyam, Chengala, Olivera, *et al.*, 2015), although progress in this aspect has been achieved as will be discussed later.

Hydrotalcites

These anionic clays, hydrotalcites (HTs) are the most common layered double hydroxide (LDH) used for CO_2 capture as their basic nature interacts with the acidity of the gas. They are anionic clays composed of cationic and anionic layers (Ding and Alpay, 2000). HTs can be represented with the following general chemical formula:

$$\left[M^{+2}_{(1-x)} M^{+3}_{x} (OH)_2\right]^{+x} \left[A^{-m}_{\frac{x}{n}} \cdot yH_2O\right]^{-x} \tag{1.2}$$

Where M is a metallic cation, A is an anion and y is the number of water molecules (Miguel *et al.*, 2014). Structurally, they are very similar to brucite (Oliveira *et al.*, 2008), differentiating in that the divalent cations of HTs, generally Mg (although Cu, Ni, Mn, Zn have been used (Ram Reddy *et al.*, 2006; Halabi *et al.*, 2012), are partially substituted by trivalent cations such as Al, Fe, Cr, V (Halabi *et al.*, 2012). To complete the layer, six OH^- ions surround each cation in an octahedron which shares the edges with other stacked sheets. The OH^- form hydrogen bonds, creating a layered network (Baskaran *et al.*, 2015). To balance the cationic layer, anionic interlayers with anions and water molecules are interleaved as shown in Figure 1.2.

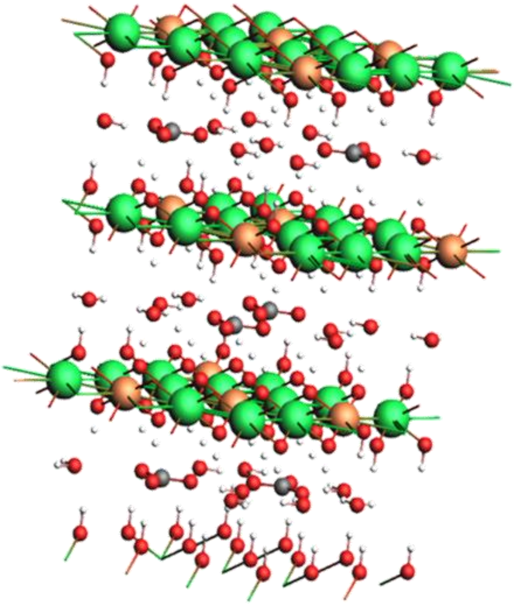

Figure 1.2 Al-Mg-CO_3 HT molecular structure (Costantino *et al.*, 1998).
Mg^{2+} in green, Al^{3+} in orange, O in red, C in grey and H in white.

HTs as CO_2 adsorbents require less energy for regeneration than chemical solvents and can work in a wide range of temperatures, from 200 to 500°C (Wang *et al.*, 2011; Bhatta *et al.*, 2015). Their relatively low heat of adsorption and high CO_2 selectivity (Ram Reddy *et al.*, 2006; Halabi *et al.*, 2012; Miguel *et al.*, 2014) makes them good candidates for scaling the adsorption process. Another advantage is their fast kinetics, which can improve when humidity is present (Miguel *et al.*, 2014). From the economical perspective, HTs are widely available and their cost is lower than the one of alkaline ceramics, although they are more expensive than alkali-meta based oxides (Bhatta *et al.*, 2015).

Despite the promising results, HTs must overcome some challenges for commercial application. First, their adsorption capacity is relatively low in contrast with MOFs or chemical absorbents (Salaudeen *et al.*, 2018). Some authors argue their mechanical stability must be improved (Garcia-Gallastegui *et al.*, 2012). Additionally, the process design must be designed for optimum temperature and pressure conditions.

1.2 Motivation

We selected HTs as the adsorbent material for PCC due to their promising results and wide availability. We were interested in improving their performance by finding innovative ways to study HT's interaction with the flue gases. However, we encountered an important challenge. Due to their polymorphic nature, it is impractical to synthesize each material variation and carry out experimental tests under many possible operating conditions.

Computational tools, more specifically, molecular simulation studies, are complementary to experimental research as they enable researchers to carry out theoretical experiments with fewer physical resources (Wang *et al.*, 2019). Thus, we decided to take advantage of the insights that molecular simulations provide.

1.3 Introduction to molecular simulations

Computational methods are a time- and cost-effective alternative to experimental studies (Pardakhti *et al.*, 2019). They enable a better understanding of materials properties and generate insights into physical and chemical processes (Jensen, 2007). Our interest in molecular simulations originates from the fact that they facilitate the large-scale screening of porous materials and discover useful adsorbents (Wilmer and Snurr, 2011; Pardakhti *et al.*, 2019). To familiarize the reader with molecular simulations techniques, we present some basic concepts. We introduce the different techniques according to the accuracy they provide for the inter-atomic interactions calculation and the type of structural and statistical data they render based on the classification of Greenwell *et al.*, (2006).

1.3.1 Basic concepts

Potential Energy Surface

The potential energy surface (PES) is a function that describes how a molecular system changes with the configuration of its elements (Cramer, 2004; Greenwell *et al.*, 2006). That is to say the PES defines the system's energy as a function of the position of the particles that compose it. Local minima in the PES convey the optimal position of the atoms in the system, which can correspond to isomers. On the other hand, saddle points relate to transition states between them (Cramer, 2004). Figure 1.3 shows a graphic representation of the PES. We can observe there are especial saddle points which represent the progress of a reaction, a) clearly shows that the product is the global minimum similarly to the 3D contour plot in b) (Long, 2020).

When completely calculated, the PES provides information about all the possible chemical structures and all isomerization pathways interconnecting them. Thus, calculating the PES is a key component of simulation techniques.

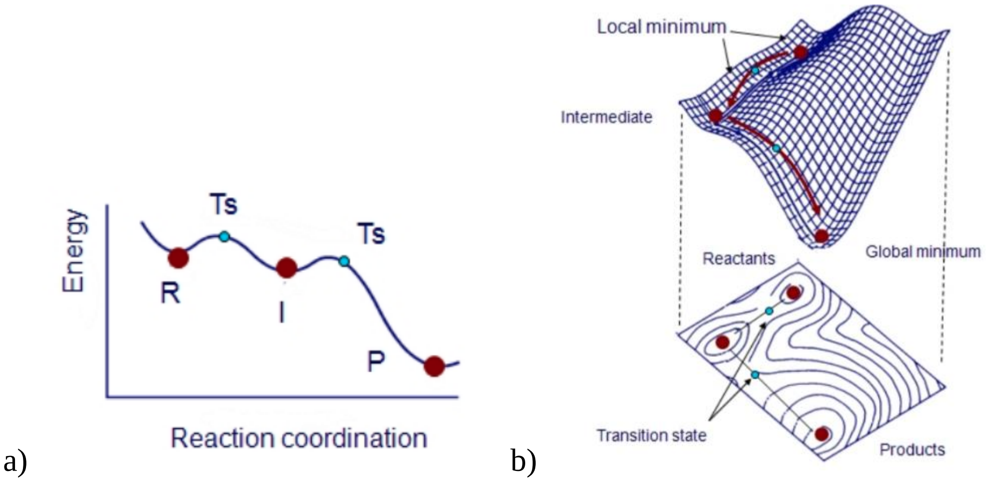

Figure 1.3 PES graphical representation. Obtained from Long (2010).

There are two main approaches for calculating the PES, each with a different level of accuracy: quantum mechanics and classical mechanics also known as molecular mechanics (Greenwell *et al.*, 2006). Quantum mechanical methods can differentiate the atom's nuclei and electrons, whereas classical mechanics take the whole atom as a sole entity. Semi-empirical methods (in-between) also exist (Greenwell *et al.*, 2006), such as ReaxFF (Van Duin *et al.*, 2001).

Quantum Mechanics

Quantum mechanics (QM) describe microscopic systems through wave functions that are capable of explaining all the physical properties of a system (Cramer, 2004). This is possible because QM simulations explicitly model the interactions between the electrons and the nuclei of the atoms in the system (Greenwell *et al.*, 2006). Thus, QM methods can model the making or breaking of bonds, and in consequence, dynamic processes (Leach, 2001). Another advantage of QM is that the only input data required are the atomic number and the initial configuration of the atoms in the system (Greenwell *et al.*, 2006). However, due to the accuracy level, QM simulations can pose a massive computational cost. Only systems with hundreds of atoms can be studied, even with the use of large parallel computers (Greenwell *et al.*, 2006).

There are several quantum theories for treating molecular systems, such as the Molecular Orbital theory, Hückel theory or the Valence Bond theory. An alternative QM approach is the Density Functional Theory (DFT), which has recently gained popularity (Leach, 2001). In this work, we utilised the latter as is a simplified and cost-effective theory.

Molecular mechanics

The classical mechanics or molecular mechanics approach (MM) considers each atom as a particle, disregarding the differences between nuclei and electrons. At the atomic scale, nuclei are so “heavy” that the quantum effects in some cases are almost negligible, and thus, their behaviour can be approximated as classical particles (Jensen, 2007). This simplification also allows MM to overcome the time and size limitations of QM (Aktulga *et al.*, 2012). This approach can handle larger and “realistic” systems up to millions of atoms thanks to the use of simple-interatomic potentials that calculate the potential energy of a system of atoms given their position and model the interaction forces between them based on Newtonian laws (Greenwell *et al.*, 2006; Kamat, van Duin and Yakovlev, 2010).

In MM, the molecules in a system are seen as a “ball and spring” model, with the atoms exhibiting different sizes and “softness”, and the bonds varying in length and “stiffness” (Jensen, 2007). The necessary input data encompass 1) the initial atomic positions and 2) a set of suitable parameters for the interaction potential functions. This set is commonly referred to as force field (FF) (Greenwell *et al.*, 2006).

FFs have both, bonded and non-bonded terms (long-range electrostatic and van der Waals forces) to describe the interaction potential functions. The bonded interactions are usually represented by the bond stretching, bond-angle bending and dihedral angle torsions terms (Suter *et al.*, 2009). A FF is usually selected based on the accuracy, transferability and computational speed (Suter *et al.*, 2009). Selecting an adequate FF is important because there are subtle distinctions in the force constants and geometric parameters for similar atoms when modelled in different environments (Mayo *et al.*, 1990).

This poses a challenge that can become a drawback. MM simulation results rely on the careful parameterization of the atomic interactions, e.g. bonds, valence angles, torsions, van der Waals interactions (Aktulga *et al.*, 2012). The parameters of an FF are usually derived from experimental data and/or QM calculations for a specific system. Thus, it is difficult to predict the performance of the same FF when used for modelling other systems and conditions different to the original ones (Greenwell *et al.*, 2006).

Another drawback of the MM approach is that sub-atomic scale interactions cannot be described (Greenwell *et al.*, 2006). As classical approaches usually rely on static bonds and fixed atomic partial charges, their applicability is limited to non-reactive systems (Aktulga *et al.*, 2012).

Reactive FFs have been developed overcome this limitation, such as ReaxFF (Van Duin *et al.*, 2001), however, in general terms, MM simulations are better used for modelling phenomena predominantly governed by non-bonded interactions (Greenwell *et al.*, 2006).

1.3.2 Molecular simulation types

Geometry optimisation

Geometry optimisation (GO) refers to finding the lowest-energy configuration of a starting structure by the systematic and iterative variation of the bond parameters, following the curvature of the potential energy well until a minimum is reached (Greenwell *et al.*, 2006; Hinchliffe, 2008). In other words, to optimize the geometry or configuration of the position of the particles in the system, several geometries are tried until it is reasonable to assume that the one with the lowest possible energy is found (Cramer, 2004), this is the global PES minimum.

Theoretically, the minimum energy corresponds to the observed molecular structure in reality (Greenwell *et al.*, 2006). Thus, it is useful to do a GO of the structures of the materials analysed to ensure they are the closest to experimental structures. DFT is a popular approach to carry out GO as it renders accurate results at a reasonable computational expense (Yu *et al.*, 2016). A disadvantage of GO calculations is that thermal motion is neglected, thus only local minima of the PES can be searched (Greenwell *et al.*, 2006)

Molecular dynamics

Molecular dynamic (MD) simulations were introduced in 1957 (Alder and Wainwright, 1957), and by the 1960s were used to carry out the first theoretical studies of gas adsorption in porous solids (Konstantakou *et al.*, 2011). MD simulations use the initial configuration of a system and velocities of its atoms to traverse the PES (Greenwell *et al.*, 2006). The trajectory of the particles is calculated with Newtonian laws of motion (Pardakhti *et al.*, 2019), and thus, MD simulations are capable of following the evolution of the system through time, usually measured in femtoseconds (10^{-15} s). This enables the examination of kinetic processes (Suter *et al.*, 2009). Furthermore, non-equilibrium conditions analysed with MD facilitate the study of the rate of adsorption and diffusion properties of adsorbents (Pardakhti *et al.*, 2019). MD simulations can also include the thermal energy when using a thermostat (Greenwell *et al.*, 2006). As the dynamical evolution of the system can be followed, results from MD simulations can be directly contrasted with experimental data from techniques such as nuclear magnetic resonance (NMR) and quasi-elastic neutron scattering (Greenwell *et al.*, 2006).

Most MD simulations use the MM approach. Thus, they require two types of data: the atomic structure of the system, in our case the adsorbent and adsorbate; and the FF potentials to describe the bonding and nonbonded interactions between the phases. In consequence, the use of adequate FF is key to obtaining accurate simulations. This can be challenging, especially when studying novel systems under different conditions. Another important disadvantage of MD simulations is the timescale. It is difficult to simulate a system for more than 1-10 ns (Greenwell *et al.*, 2006), and so, simulation results are hard to contrast with process experimental data. Due to computational power limitations, it is not possible to simulate several minutes of a real adsorption process (Purdue and Qiao, 2018).

Monte Carlo and statistical ensembles

The mathematical Monte Carlo method samples points in a multidimensional space according to a probability distribution, also defined on that space (Hinchliffe, 2008; Theodorou, 2010). The MC method has many different applications, from modelling uncertainty in strategies for CO_2 supply (Melese *et al.*, 2017) to predicting thermodynamic properties of a system based on the principles of statistical mechanics (Theodorou, 2010).

MC was the first technique used to perform a molecular system simulation (Leach, 2001). MC methods search through the PES of the system by sampling different system configurations. These configurations are generated by random changes in the position of one or more atoms according to predefined rules (Greenwell *et al.*, 2006). The changes to the system are accepted based on the system's energy derived from the configuration of the particles. If the potential energy of a certain configuration is lower than the previous one, then the change is directly accepted. If the move is rejected, then the "old" configuration is added to the sampling again and a new change is attempted (Jensen, 2007).

The main variation among the MC simulations is how the random changes to the system are done (Jensen, 2007). The most common algorithm implemented for MC is the one introduced by Metropolis *et al.* (1953). It biases the generation of the system configurations towards those with the most significant probability in the Boltzmann distribution, making the sampling much more computationally efficient (Sekerka, 2015).

The MC Metropolis algorithm satisfies the conditions of a Markov chain; 1) the outcome of each trial only depends on the preceding trial, in this case, on the previous configuration of the system, and 2) each trial belongs to a finite set of possible outcomes (Leach, 2001). This is one of the main differences between MC simulations using the Metropolis algorithm and MD simulations. In MD simulations all the states are connected in time, whereas in MC the outcome of a configuration only depends on the preceding one (Leach, 2001). Moreover, in the Metropolis algorithm, any state can be reached from any other if enough “moves” or changes are made to the system (Metropolis *et al.*, 1953).

The MC method can be used to study different types of systems, which are typically differentiated by the statistical ensemble they represent (Sekerka, 2015). The isobaric-isothermal ensemble is denoted as NPT, where the number of particles in the system (N), the pressure (P) and the temperature (T) are fixed. NPT ensembles best represent experimental conditions where there is constant external pressure (P) and temperature. This is particularly useful to simulate swelling of a structure since the system can stochastically alter its volume (Greenwell *et al.*, 2006). On the other hand, in a canonical ensemble (NVT) the number of particles (N), pressure (P) and temperature (T) are fixed (Greenwell *et al.*, 2006). It represents a system in contact with a heat reservoir that maintains the system’s temperature (Sekerka, 2015). They are useful for studying the interlayer molecular loading of a system with known *d*-spacing obtained through X-ray diffraction (Greenwell *et al.*, 2006).

There are three fixed settings in the grand canonical ensemble: the volume of the simulation cell (V), the temperature of the adsorbate (T) and the chemical potential (μ) (Jensen, 2007). This means that the number of molecules in the gas phase freely fluctuates until the μ of the adsorbent and the adsorbate are the same (Pardakhti *et al.*, 2019). The MC accepted changes to the system are the insertion of new gas molecules, deletion of existing molecules and translation or rotations of the existing molecules in the system (Pardakhti *et al.*, 2019).

Grand Canonical Monte Carlo simulations

Grand Canonical Monte Carlo simulations (GCMC) are one of the most common methods for understanding the molecular interactions during adsorption and separation in crystalline porous materials (Pardakhti *et al.*, 2019). They enable the study of adsorption and transport of fluids through porous materials (Leach, 2001). GMCM simulations can provide information regarding the gas uptake and selectivity of the material at different temperatures and pressures (Konstantakou *et al.*, 2011; Wilmer and Snurr, 2011; Zhang *et al.*, 2014; Pardakhti *et al.*, 2019). Furthermore, GCMC simulations can also provide data on the molecular packing of the adsorbed layers (Konstantakou *et al.*, 2011). Simulations usually consider 7×10^6 configurations, although statistics are not collected during the first 3×10^6 configurations to ensure an adequate convergence (Konstantakou *et al.*, 2011).

Simulation type selection

The selection of the simulation depends on the desired information. GO are typically used to understand the energy of the system based on a specific configuration. MD simulations can provide information on the evolution of the system in time. MC simulations are commonly used to calculate thermodynamic averages. They usually search low energy configurations and find the global energy minimum faster than MD, although MC do not follow a deterministic pathway across the PES (Greenwell *et al.*, 2006). It is better to use MC for simulations at exact temperatures and pressures rather than MD with sometimes ill-defined conditions (Leach, 2001). MC results with low energy configurations can be compared with experimental data from quasi-elastic neutron scattering (QENS) or XRD (Greenwell *et al.*, 2006).

Another important consideration is the type and size of the system studied since it determines the computational cost of the calculations. Gases are the easiest to model of the three states of matter because the particles are so far apart on average that the intermolecular interactions are almost negligible, save for brief collisions. In contrast, liquid state particles are much harder to study and model since they are not in complete order or disorder. Crystalline solids have their particles orderly arranged, and thus provide properties of regular solids (Hinchliffe, 2008).

The computational cost also depends on the approach taken. For a QM-DFT calculation, a moderately sized molecule contains about 15 atoms (Cramer, 2004). Classical methods, on the other hand, can handle thousands. Simulations using over 10^5 atoms can even provide information on phase transitions, elastic and plastic deformations, and defect dynamics that are not possible to observe with smaller systems (Suter *et al.*, 2009). Large systems are considered bulk materials when they contain more than 10^{23} atoms (Hinchliffe, 2008). To reduce the computational cost, they are modelled using relatively small models ($<10^5$ atoms) under the following assumptions (Greenwell *et al.*, 2006):

1) When the original system is a crystalline structure, a unit-cell of the system can be replicated several times to emulate the bulk material. A system derived from several replicas is referred to as a super-cell.
2) Periodic boundary conditions in the simulation cell enable the infinite replication of the super-cell in the three orthogonal space directions.

It is important that the considered super-cell system is large enough to avoid artificial periodicity effects. For example, when a molecule in one simulation cell interacts with its periodic reappearance in neighbouring super-cells or long-range electrostatic interactions are ill-defined (Greenwell *et al.*, 2006). A summary of this introduction to molecular simulation studies is presented in Table 1.2.

Table 1.2 Characteristics of the approaches to calculate the PES.

	Quantum Mechanics	*Molecular Mechanics*	
Accuracy level	• Differentiates atoms nuclei and electrons. • Can describe interactions among electrons.	• The atom is described as a sole entity (Jensen, 2007).	
Advantages	• Can model the creation or braking of bonds (chemical reactions) and dynamic processes (Leach, 2001)	• Lower computational power requirement (Aktulga *et al.*, 2012). • Larger systems can be simulated (up to millions of atoms) thanks to the use of simple-interatomic potentials (Greenwell *et al.*, 2006).	
Disadvantages	• High computational cost. • Better suited for smaller systems (hundreds of atoms) (Greenwell *et al.*, 2006)	• It is difficult to create an adequate FF adapted to the structure and conditions of the simulation (Greenwell *et al.*, 2006).	
Input required	• Atomic number of the elements • Initial configuration of the atoms in the system (Greenwell *et al.*, 2006)	• Force Field (FF) containing the parameters for the interaction potential functions. • Usually derived from experimental data or QM calculations (Greenwell *et al.*, 2006) • Examples of FF used for studying adsorption processes:	
		CLAYFF	(Cygan *et al.*, 2004)
		AMBER	(Billemont *et al.*, 2013)
		TraPPE	(Potoff and Siepmann, 2001; Jin and Firoozabadi, 2013; Lin *et al.*, 2013; Teo *et al.*, 2017)
		UFF	(Rappé *et al.*, 1992; Lin *et al.*, 2013; Addicoat *et al.*, 2014)
		DREIDING	(Mayo *et al.*, 1990)
		ReaxFF	(Van Duin *et al.*, 2001; Huang *et al.*, 2015)
Theory	• Ab initio: Molecular Orbital Theory • Semi-empirical: Hückel, Valence Bond theory, Density Functional Theory DFT (Leach, 2001; Yu *et al.*, 2016)	• Newtonian laws	
Common applications	• Geometry optimisation • Calculation of interaction forces between small pieces of the structure and few gas molecules.	• Molecular dynamics simulations • GCMC simulations	

1.4 Aim and objectives

This research project aims to employ molecular simulations to study CO_2 adsorption on HTs and gain new insight on how to improve their performance. For achieving this, we set the following objectives:

- To develop the geometry of the supercell required to represent the HT during the molecular simulations.
- To develop a reactive FF capable of representing the formation and breaking of molecular bonds in an HT-flue gases environment.
- To carry out MD simulation studies of the calcination of the HT.
- To carry out GCMC simulations for adsorption studies to understand the behaviour of HT in presence of CO_2.

1.5 Novel contributions

The main contributions of this work are:

1) The development of a reactive FF tailored for HT-flue gases systems using ReaxFF.
2) MD simulations showing the changes in the HT during calcination.

1.5.1 ReaxFF FF development

We selected the ReaxFF method to study CO_2 adsorption on HTs because of its capability of simulating both physisorption and chemisorption on large and periodic systems. Despite these important traits, the selection of ReaxFF presented a key challenge. To carry out the simulations, ReaxFF requires an adequate FF. None of the FFs included in the Amsterdam Modelling Suite 2019 software had the necessary parameters to represent the HT structure and its interaction with the flue gases due to the elements involved and the chemical environment.

The development of a FF can be a complex task. Most of the existing FF contain parameters that have been obtained from electronic-structure calculations. An experimental approach to finding these parameters could lead to cumbersome and inconsistent values given the limits of our measurement instruments, as explained in Jensen, (2007). Thus, for this work, we chose to use the information from QM geometry optimization calculations to reparametrize the values of an already existing FF.

Previous FF reported in the literature, such as the modified Dreiding and CLAYFF failed to maintain the structure of the LDH in long MD simulations (Zhang *et al.*, 2012). In the case of the modified Dreiding, this is attributed to the lack of the two minima needed in the PES for modelling the oxygen-metal-oxygen (O-M-O) angle.

On the other hand, since CLAYFF uses a non-bonded model, it relies on the van der Waals and Columbic interactions instead of covalent bonds, which makes it unable to maintain the octahedral structure of the HT layers (Zhang *et al.*, 2012). The LDHFF, which improved on Dreiding's results can hold the octahedral structure of $Mg-Al$ HT for over 2 ns of MD simulations and predict the exchange capability of the interlayer anion. However, it is not compatible with the ReaxFF engine, nor Dreiding or CLAYFF. The lack of an FF compatible with ReaxFF that could describe the HT structure prevented the immediate simulations for the adsorption studies. As consequence, after creating an adequate representation of the HT structure, the next step required for this project was the development of a ReaxFF FF capable of simulating the HT structure and its chemical interaction with the flue gases.

1.5.2 MD simulations of HT calcination.

MD simulations of the calcination of HTs are scarce. The closest study to our work was carried out by Kim *et al.* (2005), who used the consistent-valence force field (CVFF) to study the structural transition of $Mg-Al-CO_3$ HT due to a thermal gradient from 0 to 300 ºC (Kim *et al.*, 2005). However, the FF parameters for the cations were obtained from different sources developed for different conditions, i.e. for representing octahedrally coordinated Mg and tetrahedrally coordinated Al, whereas the simulations used them to represent octahedrally coordinated cations (Kim *et al.*, 2007). Lombardo *et al.* (2008) also carried out MD calcination studies with CLAYFF to understand the effect of the interlayer anion on the stability of the structure. Nevertheless, the HTs employed in their work were $Zn-Al-Cl$ and $Zn-Al-CO_3$. In our work, we carry out MD simulations using a specialised FF for representing a $Mg-Al-CO_3$ HT in ReaxFF, achieving a similar calculated surface area value in the range of experimental measurements for this type of HT.

1.6 Scope of this study

This work focuses on molecular simulations of CO_2 capture on $Mg-Al-CO_3$ HT as adsorbent for PCC as an alternative to commercial MEA chemical absorption as it has shown promising results (Wang *et al.*, 2011). Figure 1.4 is a graphical representation of how this work fits into the PCC landscape. Adsorption-based PCC units usually comprise two columns so that while one is adsorbing, the other is regenerating the adsorbent. For this work, our focus was on the adsorbent material rather than the process. Many studies have focused on improving experimentally HT's adsorption capacity by experimentally varying their composition, synthesis process and operation conditions.

In this project, we chose a different approach and used molecular simulations to study CO_2 adsorption on HTs. Molecular simulations have the advantage of carrying out systematic studies without the need for numerous experiments and providing insights on the interaction between de materials and the flue gases.

We selected the ReaxFF method in the AMS 2019 software to study $Mg - Al - CO_3$ HT due to its capabilities for simulating physical and chemical adsorption in complex periodical systems. Nevertheless, the target adsorption studies required an adequate geometry reflecting the HT structure and a specialised force field to provide useful insights. Thus, we created the geometry based on the results from previous experimental measurements. We also developed a force field that included all the required atom types, for both the hydrotalcite structure and the flue gas molecules. Subsequently, we carried out MD simulations to observe the calcination process at 400ºC, the experimentally recorded ideal temperature to activate the adsorbent. Finally, we did a preliminary GCMC simulation at 200 ºC and 1 bar to observe adsorption in post-combustion conditions. Due to the computational resources available, the simulations of the adsorption were carried out using only one type of HT and CO_2 as flue gas.

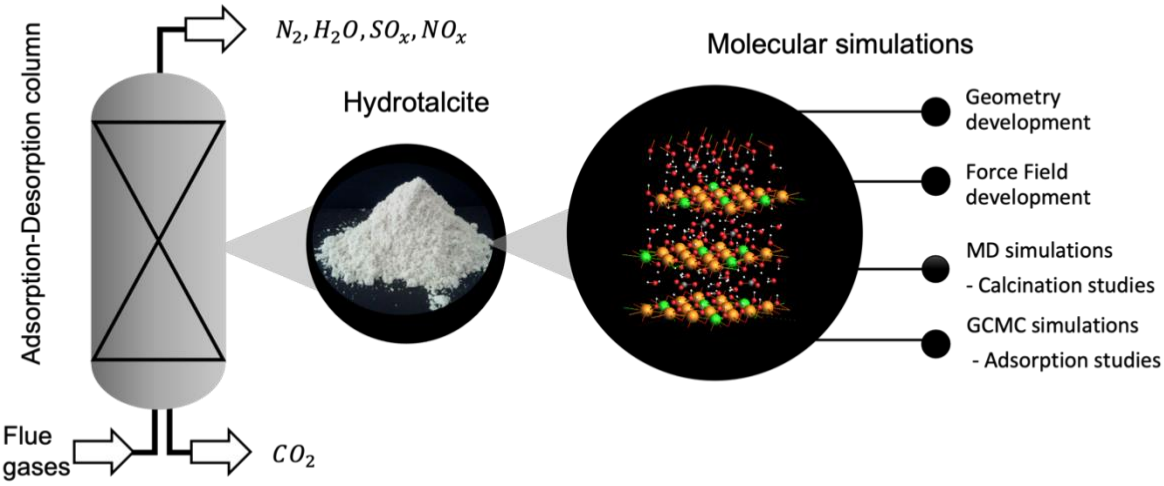

Figure 1.4 Scope of this work.

1.4.4 Research methodology

For this project, we carried out an extensive literature review on adsorption as an alternative technology for CO_2 capture. Next, we developed a geometry that would adequately represent the selected HT. We subsequently developed a specialised ReaxFF force field using the CMA-ES algorithm.

We employed the developed geometry and FF to carry out MD simulations for observing the changes the HT undergo during calcination. Finally, we carried out a preliminary GCMC. The methodology is summarised in Figure 1.5.

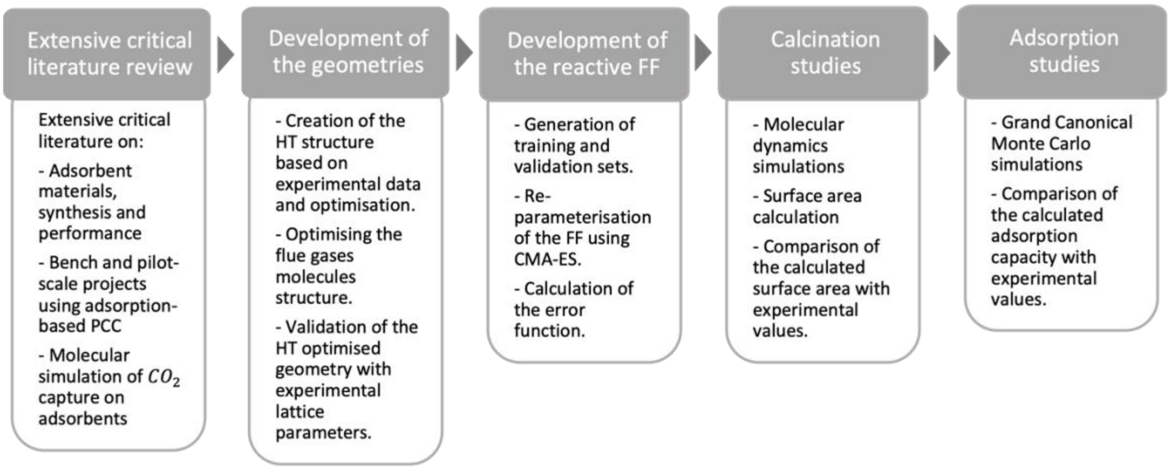

Figure 1.5 Overview of the research methodology.

1.5.6 Software tools used for the study

We selected the Amsterdam Modelling Suite 2019 (AMS) software to carry out the molecular simulations due to its capability for performing both types of calculations, QM and MM. AMS 2019 2019 can represent the formation and breaking of chemical bonds in with large systems (te Velde *et al.*, 2001), a crucial trait for studying the chemisorption process of CO_2 capture in HT. AMS 2019 has been continuously developed since the early seventies for harnessing the computational advantages of DFT (te Velde *et al.*, 2001) and is composed of different "engines" that carry out diverse types of calculations as shown in Figure 1.6.

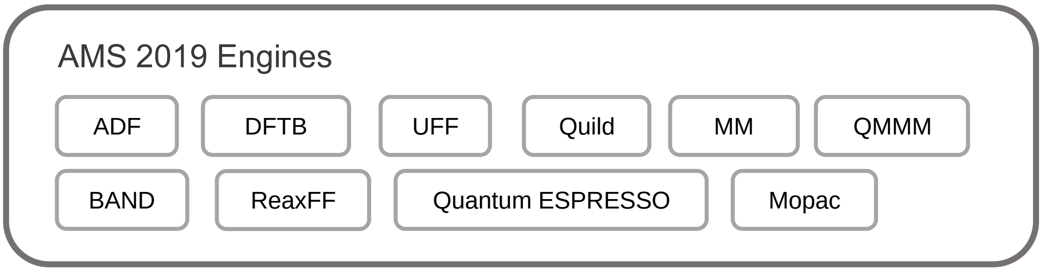

Figure 1.6 Available engines in AMS 2019.

The engines ADF, BAND, DFTB, Quantum ESPRESSO use DFT, whereas MOPAC, ReaxFF and the Universal Force Field UFF implement other semi-empirical methods (SCM, 2018).

AMS capability of using *ab initio* and force-field methods made this software a flexible tool to develop the hydrotalcite geometry and the training set for the specialised FF and test it. Another advantage of this software is the fact that technical support is always available, which is not the case for other molecular simulations open-source software such as Avogadro or RASPA. In this work, we used the engines that better suited the task. An accurate representation of the flue gases and HT structure was required for the simulations. Thus, the DFTB and ADF engines were used to create the geometry and carry out the GO of gas molecules. The BAND engine was employed to develop and optimise the HT structure as it is the only engine capable of carrying out DFT calculations on periodic structures. The GO of the HT ensured that the structure used for calcination and adsorption studies agreed with experimental measurements of the interlayer space and cell parameters.

The MD for simulating the calcination process and the GCMC simulations for carrying out the adsorption studies required an engine capable of representing chemical reactions at a low computational cost. The engines and tools developed to harness DFT have an inherent high computational cost, exacerbated when analysing complex structures, such as HT. The ReaxFF engine was selected because of its capacity for handling a large periodic system, up to 10^6 atoms (Bai *et al*, 2012), and to recreate chemical reactions at a manageable computational cost (van Duin *et al.*, 2019). Table 1.3 enlists the engines used for this work.

Table 1.3 Engines from AMS 2019 used for this project.

Engine	*Approach*	*Theory*	*Type of calculations*	*System capacity*
DFTB	QM	DFTB	Geometry optimisation	Molecules
ADF	QM	DFT	Geometry optimisation	Molecules
BAND	QM	DFT	Geometry optimisation	Periodic systems
ReaxFF	MM	Newtonian*	MD, GCMC	Molecules and periodic systems

*ReaxFF uses bond order and bond energy corrections to represent the formation and breaking of bonds.

1.5.7 Outline of the thesis

Chapter 2 enlists the current bench and pilot-scale PCC projects. We discuss the challenges they have faced, and the solutions proposed. We also provide a literature review on HT synthesis, adsorption experimental studies, and molecular simulation studies on the topic.

Later, Chapter 3 describes the process carried out to develop the HT geometry file that we used in the rest of the work. Chapter 4 explains the development of the FF used to carry out the simulations of HT calcination and CO_2 adsorption. Chapter 5 is about the calcination studies using MD simulations methodology and findings. Next, Chapter 6 contains the adsorption studies using GCMC simulations, detailing the methodology and results. Finally, Chapter 7 states the conclusions drawn from the work carried out and points out the possible direction of further research. A summary of these sections can be found in the proceedings of the 15th International Conference on Greenhouse Gas Control Technologies (GHGT-15) where this work was presented (Bonilla and Wang, 2021).

2. Literature Review: Recent Studies on adsorption-based PCC

2.1 Overview

The purpose of this chapter is to provide an overview of previous work focusing on adsorption as an alternative PCC technology. First, we enlist the current bench and pilot-scale projects for CO_2 capture worldwide and discuss their progress and challenges. Next, we delve into studies of HTs. We offer a literature review of research on the synthesis process and its effect on their adsorption performance. Finally, we present insights gained through molecular simulation studies and how this tool can accelerate our understanding of the adsorption process and improve current adsorbents materials.

2.2 Bench and pilot -scale projects using adsorption-based PCC

Adsorption for PCC is relatively recent in contrast with chemical absorption. The first adsorption applications were carried out in the early 1990s (Wolsky *et al*, 1994; Chue *et al.*, 1995), whereas amine scrubbing to separate CO_2 from natural gas and H_2 was patented in 1930 (Bottoms, 1930; Rochelle, 2009). As consequence, there are fewer studies carried out at a larger scale than laboratory experiments that enable adsorption commercialisation. This section gives an overview of contemporary projects using adsorption for PCC at a larger scale, considering bench-scale as <1 tonCO_2/day and pilot-scale 1 - 200 tonCO_2/day (Just, 2013). We provide information on the organisation leading the project, location, and the main characteristics of the process. Finally, we highlight the challenges faced by the projects and the different paths they took to overcome them.

2.2.1 Completed projects

Pilot scale

The largest adsorption project registered was the pilot **Hadong dry sorbent CO_2 capture system** led by the Korea Electric Power Research Institute (KEPRI) located at the Hadong power plant in South Korea. It operated from April 2014 to 2017, capturing **200 tonCO_2/day** from 35,000 Nm^3/h of flue gas (Park *et al.*, 2014) equivalent to a 10 MW coal-fired ultra-supercritical power plant (Yi, 2015; *Hadong power station*, 2021; Global CCS Institute, 2021). KEPRI developed a specialised adsorbent KEPCO2P2, made of 35% K_2CO_3 and 65% of support material (Global CCS Institute, 2021).

The former reacts with the CO_2 whereas the support material facilitated solids management. In the TSA cycle of the fluidised bed, the adsorption occurred at ~80 °C and regeneration of the sorbent at ~200 ºC (Yi, 2015; Zhao *et al.*, 2018).

TDA Research Inc has completed two adsorption projects and has one more under development. The first one, the **sorbent based post-combustion CO_2 slipstream testing** was realized in collaboration with Porocel and NETL (O'Palko *et al*, 2019). The project started in March 2014 and ended in January 2021 (Elliott and Yi, 2018; NETL, 2020). The project was able to capture **~10 tonCO_2/day** at the National Carbon Capture Center (NCCC) located in Wheat Ridge, Colorado. Testing was carried out using a 0.5 MWe slipstream of flue gas, with 1.5 months for parametric testing and 2 months for steady-state testing (Elliot and Yi, 2020). Alkalised alumina (Al_2O_3) was employed as the adsorbent in a PSA regeneration cycle (O'Palko *et al*, 2019) in multiple beds (2-bed, 3-bed, 4-bed, 10-bed) (Elliot and Yi, 2020). Adsorption takes place at 140-150 ºC and 1 bar, whereas regeneration occurred at the same temperature range, with a pressure increase of 1.11 bar using steam (Elliot and Yi, 2020). The next steps for the projects include upscaling to a 25 MWe slipstream (Elliot and Yi, 2020).

The oldest project of **technology for removing CO_2 from power plant flue gas by the physical adsorption method** was carried out by Tokyo Electric Power company and Mitsubishi Heavy Industries, Ltd. The pilot plant was located at the Yokosuka thermal power station which used a coal and oil mixture (Ishibashi *et al.*, 1996). It operated from October to December 1994 treating 1,000 Nm^3/h of flue gases to capture **~5 tonCO_2/day** using Ca-X zeolite. The capture process consisted of two stages. The first used a PTSA system whereas the second had a PSA cycle, with regeneration conditions of 0.05 – 0.15 bar and 50-100ºC (Ishibashi *et al.*, 1996).

Bench scale

Smaller demonstration facilities have also been built. An example is the **RTI's solid sorbent-based CO_2 capture process** project. It was developed by RTI International in collaboration with the National Energy Technology Laboratory (NETL) from the Department of Energy (DOE) of the United States of America (USA). This test unit was installed in North Carolina and operated 100 hours in 2016. The unit was capable of treating up to 15,000 Nm^3/h and captured about **0.15 tonCO_2/day** from synthetic coal-fired flue gas (Nelson *et al.*, 2017). The TSA process in a fluidised moving-bed reactor (FMGR) used an adsorbent comprised of polyethyleneimine (PEI) on silica as a support material.

Adsorption was carried out at 50 - 90 °C and regeneration at >110 °C in a (Nelson *et al.*, 2017). Due to the promising results, the process was analysed for its implementation in coal-fired power plants and natural gas combined cycle (NGCC) power plants and cement plants (Nelson *et al.*, 2017). An additional prototype of the RTI's solid sorbent-based CO_2 capture process was installed at the cement plant Norcem in Brevik, Norway. The system operated for over 150 hours and showed a ~30% reduction in the adsorption capacity after 100 cycles due to the 100 ppm of SO_2 present in the flue gas. This indicated deep scrubbing is necessary upstream of the capture unit (Nelson *et al.*, 2017).

The second project of TDA Research Inc is a **new sorbent process for transformational carbon capture process**, made in collaboration with Membrane Technology & Research Inc. from July 2018 to August 2021(Lang *et al*, 2019). Located too in Wheat Ridge, Colorado, this project had the capacity of treating ~8 Nm^3/h of pulverised-coal power plant flue gas, capturing **0.06 ton$\boldsymbol{CO_2}$/day**. The tested adsorbent comprised amine-functionalised resin beads in a VSA cycle, with adsorption at 1.1 bar and 60 ºC and counter-current desorption at 0.2 bar, with the same temperature (Lang *et al*, 2019). An important difference of the configuration of the process is that the capture units are engineered structures that can be integrated into modules, facilitating the upscaling process (NETL, 2020).

An innovative project for PCC adsorption is the **VeloxoTherm^{TM} CO_2 capture process demonstration** led by Inventys Thermal Technologies Inc in collaboration with Svante and Electricore Inc. The project facilities are located in Lashburn, Saskatchewan, Canada (Government of Canada, 2018). The rotary adsorption VTSA process employs amine-appended MOFs, specially developed by the Lawrence Berkeley National Laboratory (LBNL) in collaboration with DOCCSS and Mosaic Materials. The scale-up production was carried out by Inventis (NETL, 2019; Long, 2020). Tests were carried out in a slipstream flue gas of a 10 MWe coal-fired unit (Bui *et al.*, 2018) and captured **0.01 ton$\boldsymbol{CO_2}$/day** (NETL, 2020). The project started in August 2017 and finished in July 2021 (Neaton, Long and Haranczyk, 2019; NETL, 2020). An advantage of the rotating bed reactor is the reduction of cycle time and energy consumption (Svante, 2020). It has achieved a 60 s/cycle time, in which the adsorption temperature starts around 50 ºC and increases to ~80 ºC to the exothermic reaction in the bed, (Long, 2020). Desorption occurs at ~110ºC (Neaton *et al*, 2020).

2.2.2 Current projects

Pilot scale

In addition to power plants and the cement industry, adsorption for PCC can be applied in other industrial settings. The most recent example is **DISPLACE**, a project from the C4U initiative coordinated by Imperial College London (CORDIS, 2020).

The project aims at capturing the CO_2 emissions from oxy-combustion walking beam furnaces for producing steel at the industrial CCS cluster in North Sea Port, Gent, Belgium. The process includes a calcium looping unit and an adsorption unit using HTs since the blast furnace gas has a higher temperature than the one at power plants, 400ºC. The adsorption unit uses fixed beds with PSA regeneration. The desorption pressure varies between 1 to 5 bar (Cobden and Abanades, 2021). The project has over 2,000 h of operation (Cobden and Abanades, 2021), showing an 83% carbon capture rate (Spallina *et al.*, 2021) from the treated 400 Nm^3/h (Mahgerefteh, 2021), calculated in **~3.6 ton$\boldsymbol{CO_2}$/day**.

Bench scale

The **transformational sorbent-based process for a substantial reduction in the cost of $\boldsymbol{CO_2}$ capture** can treat 136 – 170 Nm^3/h from a 400 MW coal-fired utility plant (Jain, 2019b) and capture **0.89 ton$\boldsymbol{CO_2}$/day**. The project is managed by InnoSepra, LLC in collaboration with Main Line Engineering, Plant Process Equipment, Arizona State University and the Technology Center Mongstad (TCM) (Jones *et al*, 2019). The project started in May 2019 and will be completed in April 2022. The regeneration of the specially designed adsorbent is carried out using a TSA process and a specialised adsorbent in fixed beds. The project is currently working on the second generation of their technology. After demonstrating that the first generation used up to 50% less energy than amine solvent capture (Jain, 2019a), the second generation succeeded in reducing the heating requirement from 1.3 GJ/MT to 0.7 GJ/MT. Their process carries out adsorption at 25-32 ºC and 1.15 bar, and desorption at 100 ºC and 0.3 – 1.0 bar (Jones and Jain, 2020).

The third project by TDA Research Inc focuses on a **transformational sorbent system for PCC**, in collaboration with the University of Alberta and the University of California, Irvine (O'Palko, Hanucu and Alptekin, 2019). The project started in June 2019 and will be completed in May 2022. Testing is carried out at the Wyoming Integrated Test Center at Wheat Ridge, Colorado.

The final field-testing prototype will be able to treat up to 8 Nm^3/h of coal-fired power plant flue gas and capture **~0.04 tonCO_2/day** (NETL, 2020) with SIFSIX-2-Cu-I MOF as adsorbent (O'Palko and Alptekin, 2020). The process uses a vacuum-concentration swing adsorption (VCSA) multistage system. Adsorption at 30 - 50ºC under mild vacuum (~0.2 – 0.3 bar) precedes desorption, which occurs in two steps. During the first one, a vacuum (0.05 bar) is used to recover the CO_2 and purge using the boiler intake air. Then, the CO_2-loaded gas goes back to the boiler. This benefits the adsorption process while reducing the auxiliary load of the vacuum pump (NETL, 2020; O'Palko and Alptekin, 2020)

Another innovative project under development is the **high-efficiency PCC system** by Precision Combustion, Inc (PCI) in collaboration with the University of Florida and CSIRO (NETL, 2018). This collaboration started in February 2017 and is set to finish in April 2022. Current prototypes treating ~3.6 Nm^3/h can capture **~0.015 tonCO_2/day** with a 44% capture rate (Palko *et al*, 2020). The project is installed at the test bay of the NCCC (O'Palko *et al.*, 2020). The selected adsorbent is a MOF, which is deposited on Microlith, a tailorable mesh substrate (Loebick and Weisman, 2017) with openings of 600 µm (O'Palko *et al.*, 2020). Due to the coil configuration of the Microlith in the reactor, the TSA system has a low-pressure drop, high mass transfer and lower energy penalty. Adsorption occurs at 30°C and desorption at 80°C, with waste heat or steam (Loebick *et al.*, 2018).

2.2.3 Projects under development

The project by the Rensselaer Polytechnic Institute (RPI) located in Troy, New York in collaboration with the University of South Carolina (USC) and the Gas Technology Institute is denominated **transformational molecular layer deposition (MLD) tailor-made size sieving sorbents for PCC**. The project started in October 2019 and will end in September 2022. During this project, RPI will oversee sorbent performance testing and design, construction, and optimisation of the PSA process. Once this stage finishes, the University of South Carolina and the Gas Technology Institute will construct a testing skid and transport it to the NCCC in Wilsonville, Alabama for field testing under coal-fired power plant conditions (Oneil, Hancu and Yu, 2019). The contribution of this project is the new manufacturing process. MLD consists of a scalable vapour phase deposition technique that homogeneously places ultrathin coating (< 20 nm) layers of Al_2O_3 on an adsorbent, e.g. 5A or 13X zeolite (Yu *et al.*, 2019). The composite adsorbent has shown a CO_2/N_2 selectivity 130 times higher than zeolite 13X alone under similar conditions (Gollakota and Yu, 2020). The PCC adsorption unit is designed to work for a 550 MWe power plant but testing is pending.

Adsorption is intended to happen at 20 ºC and 0.01 bar and desorption at 0.05 bar, at the same temperature in a system of 8 parallel beds. The process is designed to reduce energy consumption by using the light product of the PSA system and ambient air to regenerate the desiccant wheels for water vapour removal (Gollakota and Yu, 2020).

There are other upcoming up-scaled adsorption projects. The **Haifeng carbon capture test platform** led by the Guangdong Electric Power Design Institute in collaboration with the UK-China (Guangdong) CCUS Centre will be located at the CRP Haifeng Power plant, Haifeng, China. The testing platform started operations in January 2018 using flue gas from a 1,000 MW unit. In the first stage of the project, amine-solvent and membrane technologies will be tested, and adsorption during the second stage (UK-Guangdong CCUS Centre, 2017).

Industrial applications of adsorption PCC are also on the horizon, with the **MOF4Air** initiative planning on using MOFs in different settings, i.e. for a refinery furnace-boiler plant (Izmit, Turkey), a waste incineration plant (Marseille, France) and a combined heat and power plant and refinery (Mongstad, Norway) (MOF4Air, 2019). Currently, different MOFs (MIL53(Al)-X, UIO(Zr)-X and X-MOF-74) are being investigated to determine their tolerance towards impurities such as H_2O, SO_2, NO_x and H_2S. Due to the application variation, there are two different process configurations considered, a VPSA system with fixed beds and a TSA with moving beds (MBTSA) (MOF4Air, 2019).

It can be noted that adsorption in precombustion settings has projects are in later stages of development. Examples are Sinopec's integrated gasification combined cycle (IGCC) plant in China (Alptekin *et al.*, 2019; O'Palko, Hancu and Alptekin, 2019) and the Port Arthur Project in Texas, a hydrogen production facility (Baade *et al.*, 2012; Folger, 2014; MIT, 2016; Office of Fossil Energy, 2016). On the other hand, Automated Sorbent Test Rig (ASTR) and COURSE 50 (JFE Group, 2019; Global CCS Institute, 2021) projects focus on industrial settings for cement and steel respectively.

Table 2.1 and Table 2.2 show a summary of the process characteristics of the different completed and current projects previously described.

Table 2.1 Bench and pilot-scale adsorption PCC completed projects.

Project	***Leading organisation***	***Location***	***Adsorbent Material***	***Material cost ($USD/kg)***	***Capture Scale (tonCO_2/day)***	***Process***	***Reactor type***	***Sources***
Pilot scale								
Pilot Hadong Dry-sorbent CO_2 Capture System Test	KEPRI	Hadong power plant, South Korea	KEPCO2P2	2.70	200	TSA	Fluidised bed	(Yi, 2015; *Hadong power station*, 2021; Global CCS Institute, 2021)
Sorbent Based Post-Combustion CO_2 Slipstream testing	TDA Research Inc	Wheat Ridge, Colorado, USA	Alkalised alumina Al_2O_3	13.23	10	PSA	Multiple fixed bed	(Elliott and Copeland, 2016; Elliott and Yi, 2018; O'Palko, Hancu and Elliot, 2019)
Technology for removing CO_2 from power plant flue gas by the physical adsorption method	Tokyo Electric Power Company Mitsubishi Heavy Industries, Ltd.	Yokosuka, Kanagawa, Japan	Ca-X Zeolite	N/A	~5	2-Stages PTSA + PSA	Fixed bed	(Ishibashi *et al.*, 1996).
Bench scale								
RTI's solid sorbent-based CO_2 capture process	RTI International	North Carolina, USA	Poly-Amine (PEI) on support material (silica)	> 10	0.15	TSA	Fluidised moving bed	(Nelson *et al.*, 2017)
A New Sorbent Process for Transformational Carbon Capture Process	TDA Research Inc	Wheat Ridge, Colorado, USA	Amine-based ion exchange polymeric resin	<20	0.06	VSA	Spiral-wound and planar modules	(Alptekin *et al.*, 2018; Alptekin and Jayaraman, 2019a; Lang *et al.*2019; Alptekin, 2020)
VeloxoTherm^{TM} CO_2 capture process demonstration	Inventys Thermal Technologies Inc	Lashburn, Saskatchewan, Canada	Amine-Appended MOF	N/A	0.01	TSA	Rotating bed reactor VeloxoTherm^{TM}	(Government of Canada, 2018; Neaton *et al.*, 2019; NETL, 2019; Long, 2020; Svante, 2020)

Table 2.2 Bench and pilot-scale adsorption PCC current projects.

Project	*Leading organisation*	*Location*	*Adsorbent Material*	*Estimated capture cost (USD/tCO_2$)*	*Capture Scale (tonCO_2/day)*	*Process*	*Reactor type*	*Sources*
Pilot scale								
DISPLACE	Imperial College London	North Sea Port, Gent, Belgium	Hydrotalcites	$60.00*	~3.6	PSA	Fixed bed	(Cobden and Abanades, 2021)
Bench scale								
Transformational Sorbent-Based Process for a Substantial Reduction in the Cost of CO_2 capture	InnoSepra, LLC	Bridgewater, New Jersey, USA	Inno Sepra, LLC especially developed adsorbent	$31.00	~0.89	TSA	Fixed bed	(Jain, 2019a, 2019b; Jones, Hancu and Jain, 2019; Jones and Jain, 2020)
Transformational Sorbent System for PCC	TDA Research Inc	Wheat Ridge, Colorado, USA	SIFSIX-2-Cu-I MOF	$30.00	0.04	VCSA	Fixed-bed radial flow reactors	(Alptekin and Jayaraman, 2019b; O'Palko *et al*, 2019; O'Palko and Alptekin, 2020)
High-Efficiency PCC System	Precision Combustion Inc	North Haven, Connecticut, USA	MOF on Microlith mesh in adsorption modules	$30.00	0.015	TSA	Microlith unit	(Loebick and Weisman, 2017; Loebick *et al*., 2018; NETL, 2018; O'Palko *et al*., 2020; Palko, Zoican-Loebick and Baird, 2020)

2.2.4 Insights from the projects

The described projects prove that adsorption as an alternative PCC technology is feasible. However, the number of developments working at a larger scale than laboratory studies is still small in contrast with other alternatives, especially absorption with solvents. For example, from the +60 PCC projects for power plants registered in the CO2Re database (Global CCS Institute, 2021), an extensive international database by the Global CCS Institute, only four projects mention the use of solid adsorbents. Although the number of adsorption projects has increased, particularly in the last decade, current and future projects are not considering commercial deployment yet. As seen throughout the projects previously described, adsorption PCC technology faces four main challenges: 1) the continuous large-scale production of the adsorbent material, 2) heat management and temperature control, 3) solids handling and circulation control and 4) the adsorbent tolerance towards impurities.

The **continuous large-scale production of the adsorbent** with consistent characteristics has not been achieved in all projects. Although progress has been made in this area, the adsorbent production scale is still minor in contrast with the possible demand. For example, during the TDA Research Inc project employing SIFSIX-2-Cu-I MOF, the production of MOF pellets is still in the 0.5 kg per batch (Alptekin and Jayaraman, 2019b). A potential bypass is the use of commercially available materials, even if their performance is not as good as tailored adsorbents. Interestingly, the only commercial-scale project, in Hadong, employed potassium carbonate instead of a specialised adsorbent. The K_2CO_3 carbonation reaction rate was considered too slow to be practical at a large scale until recently (Wang *et al.*, 2011).

Heat management and temperature control are crucial to ensure an optimum working adsorption capacity. Results from the RTI’s tests showed that the heat management in the adsorber is more relevant than the kinetics of the CO_2 capture reaction (Nelson *et al.*, 2017). Researchers attributed this to the fact that a temperature increase in the reactor reduces the working capacity due to the exothermic nature of adsorption. Heat management can also affect the length of the process, as seen in the project of Inventys Thermal Technologies Inc. When CO_2 was used as the desorption gas, the heat transfer between the hot gas and the adsorbent was very slow, resulting in a long cycle of 633 s. On the other hand, if steam was used for desorption the heat transfer was faster, leading to a cycle time of 100 s, which is preferred to reduce energy consumption (Long, 2020).

Solids handling and circulation control are important considerations for the design of the process. High pressure drop and dust formation are common problems in conventional dry sorbent systems using fixed beds (Alptekin and Jayaraman, 2019a). A possible solution is to pelletise the adsorbents, vary the size of the pellets or change the design of the reactor. In the TDA Research Inc project using polymeric resin, the small size of the resin beads makes their use impractical in fixed beds due to a high pressure drop, thus, researchers used ceramic and polymeric binders with high permeability to pelletise them (Alptekin *et al.*, 2018) and improve the rate of the adsorption (kinetics). However, this process can sometimes have an impact in the adsorption capacity of the material. In the TDA Research Inc project using MOFs, the adsorbent had a marginal loss in CO_2 adsorption when pelletised, balanced by a slight improvement of kinetics (Alptekin and Jayaraman, 2019b). Changing the disposition of the adsorbent in the process can improve the performance of the capture unit. Microlith, the substrate mesh, patented by PCI, has a higher surface area per unit and a larger mass and heat transfer coefficient contrasted to monoliths or pellets. This results in a superior CO_2 capture rate and reduced regeneration energy as the pressure drop decreases (NETL, 2018). Another advantage of using Microlith is the flexibility it provides for the design of the reactor, either planar or radial (Loebick *et al.*, 2018).

The **presence of other pollutants** in the flue gases can also impact the performance of the adsorption PCC unit. Preliminary tests of the RTIs project showed that a content of 100 ppm of SO_2 in the flue gas can cause a reduction of 30% in the initial loading capacity over 100 adsorption/regeneration cycles (Nelson *et al.*, 2017). It must be noted that this issue is material specific. As a counterexample, the TDA Research Inc project using SIFSIX-2-Cu-I MOF showed that the exposure to NO and SO_x did not degrade the CO_2 adsorption capacity of the material. Furthermore, the adsorbent does not hold any NO and only retains about 0.24% wt of SO_2 (Alptekin and Jayaraman, 2019b). In another TDA Research Inc project employing polymeric resin beads, the presence of water vapour improved the adsorption capacity (Alptekin *et al.*, 2018).

2.2.5 Summary

Adsorption can be a potential alternative to solvent absorption for PCC. However, its large-scale application must overcome four main challenges: 1) the continuous large-scale production of the adsorbent material, 2) heat management and temperature control, 3) solids handling and circulation control and 4) the adsorbent tolerance towards impurities.

More research is needed to find an optimum combination of the adsorption material and process design for specific applications. It is crucial to further the development of adsorbent materials that can sustain their adsorption capacity after several cycles and that are tolerant to impurities in the flue gases. Nevertheless, careful consideration of the desired process conditions is key for achieving large-scale implementation. Even if the development of an adsorbent achieves a significant adsorption capacity at lab-scale experiments, it does not imply that it will hold at real conditions. Additionally, the competitivity of the adsorption PCC unit largely depends on the design of the regeneration process. A significant energy consumption reduction can be achieved by using adsorbents that work with a reduced temperature or pressure swing, using pellets or fluidised beds for improving solids management or by taking advantage of waste heat and innovating the reactor type and configuration.

2.3 Experimental studies of HT synthesis

HTs are usually produced by co-precipitation of metallic salts containing the cations that will create the layers. For example, when $Mg(NO_3)_2 \cdot 6H_2O$ and $Al(NO_3)_3 \cdot 9H_2O$ are used, dissolved in deionized water, they create an Mg-Al cationic layer. Unitary hydroxides ($Mg(OH)_2$ and $Al(OH)_2$) are alternative and basic precursors in contrast with the acid metallic salts (Manohara *et al.*, 2021). The anions are also added in a solution, e.g. Na_2CO_3 for creating carbonates in the interlayer, jointly with a precipitation agent, commonly $NaOH$ or Na_2CO_3 (Hutson *et al.*, 2004; Ram Reddy *et al.*, 2006; Garcia-Gallastegui *et al.*, 2012; Muñoz *et al.* 2015; Silva *et al.*, 2017). Urea can also be utilized in urea hydrolysis processes (Othman *et al.*, 2009). The precipitation agent plays a key role in controlling the pH of the reaction, and thus, the final cationic ratio R (Wang *et al.*, 2011) and the crystallinity of the produced HT (Bhatta *et al.*, 2015). In turn, R affects the number of needed anions in the interlayer to counterbalance the layer charge (Trave *et al.*, 2002). The cationic ratio for Mg-Al HTs has been observed in the range of $1.3 \leq R \leq 5$, whereas Mg-Ga HTs are more stable, $1.0 \leq R \leq 12.9$ presumably due to the smaller difference of ionic radii (Trave *et al.*, 2002). Finally, the precipitate is filtered, washed and dried (Hutson and Attwood, 2008). Additional post-synthesis washing with organic solvents has been used to increase the final HT surface area (Manohara *et al.*, 2021). Another variation to the coprecipitation synthesis is microwave radiation. This occurs before washing the precipitate and can increase specific surface area by reducing the average size of the crystallites. Microwave radiation reduces the ageing period and removes the need of washing (Othman *et al.*, 2009).

There are other less popular but still effective processes to produce HTs, e.g. homogeneous precipitation from solution (HPFS) (Manohara *et al.*, 2018), aqueous exfoliation, modified amide hydrolysis (Manohara *et al.*, 2021), urea hydrolysis, hydrothermal synthesis, microwave irradiation and sol-gel (Baskaran *et al.*, 2015). The reader is referred to (Othman *et al.*, 2009) for a more detailed description of the later methods.

The synthesis process heavily influences the final properties of the HTs, such as the morphology, the lateral size, typically 0.48 nm (Hutson *et al.*, 2004), and the degree of stacking of the layers (Winter *et al.*, 2005), with the interlayer varying from 0.3 nm to 3 nm (Othman *et al.*, 2009). For example, coprecipitation synthesis usually results in submicron crystallites with ill-defined hexagonal morphology, whereas HPFS renders micron-size hexagonal crystallites (Manohara *et al.*, 2018). On the other hand, urea hydrolysis produces smaller particles and the sol-gel method originates highly pure HTs (Othman *et al.*, 2009).

In addition to the synthesis type, the conditions at which synthesis is carried out also affect the physicochemical properties of the HTs. As previously mentioned, pH plays a key role during synthesis. Tuning it can aid to achieve solution supersaturation, promoting the HT precipitation. A very low pH value could impede the precipitation of all different metal ions, whereas a very high value could result in the dissolution of the metal ions (Othman et al., 2009). In acid conditions, $Mg(OH)_2$ dissociates into Mg^{2+} and OH^- anions, preventing the formation of the layered structure and resulting in an amorphous product, $AlOOH$ (Wang *et al.*, 2011).

If pH $\geq$ 8, the crystallinity of the material increases with the increase in the pH. For instance, a pH=9 produces an HT with an Mg/Al ratio of 2.3 and pore size of 3.7 nm, whereas a pH=14 results in pores of 18.3 nm (Wang *et al.*, 2011). A condition with pH=10 has been reported to provide HTs with better adsorption capacities (Bhatta *et al.*, 2015).

The used metallic salts and the M^{+2}/M^{+3} ratio also affect the CO_2 adsorption capacity and kinetics, adsorbent regenerability and cyclic stability (Bhatta *et al.*, 2015). Experimental studies investigating the effect of the anions found changes in the morphology and consequently in the BET surface area. For example, HT containing CO_3^- had a “sand rose” morphology, with the “rose” or sphere measuring ~400 – 450 nm with each “petal” between 24 and 25 nm of width and 30-32 layers like brucite. On the other hand, HTs with NO_2, SO_4, Cl and HCO_3 as anions resulted in non-porous particles with a “stone” morphology that varied from several to several-tenths µm of radius (Wang *et al.*, 2011). Furthermore, it has been observed that larger anions produce a greater interlayer space (Bhatta, *et al.*, 2015).

2.3.1 Calcination

After synthesis, HTs undergo a thermal treatment denominated calcination (Wang *et al.*, 2011). If the precipitate is used in the crystalline phase, the CO_2 sorption process is driven by its reaction with the basic Mg-OH in the adsorbent. The reaction results in $Mg(HCO_3)_2$ that is irreversibly chemisorbed (Ram Reddy *et al.*, 2006), making regeneration increasingly difficult. Thus, calcination is used to produce mixed metallic oxides (MMO). During calcination, HTs undergo three main stages: dehydration of the interlayer water (~100ºC), dehydroxylation of the cationic layer (200-210ºC) and decarboxylation, if interlayer anions are carbonates (>300ºC) (Wang *et al.*, 2011). The temperature at which these stages occur can shift slightly depending on the size of the sample and the atmosphere used, e.g. He, N_2 or CO_2 (Hutson *et al.*, 2004).

The changes in the composition result in a progressive collapse of the layered structure of the HT due to the migration of the Al^{3+} from the octahedral cationic layer to the tetrahedral sites in the interlayer (Hutson *et al.*, 2004). As consequence, Mg^{2+} ions form the $Mg-O$ active basic sites fit for CO_2 capture (Wang *et al.*, 2011). The resulting mixed metallic oxides (MMO) are thermally stable and possess a higher surface area (Muñoz *et al*, 2015). The maximum calcination temperature has an important effect on the final characteristics of the adsorbent. If it is not high enough, not all sites will be activated, but if the HT is calcined at a very high temperature, crystalline MgO (Ram Reddy *et al.*, 2006) and Al_2O_3 (Bhatta *et al.*, 2015) are formed, reducing the number of active sites of Mg-O. In the case of Mg-Al-CO_3 HT, the optimum temperature is considered 400°C (Wang *et al.*, 2011). Table 2.3 shows information on the synthesis process and resulting adsorption capacity of HTs with Mg and Al as cations and carbonates as interlayer anions. Figure 2.1 plots these results and suggests that an increase in adsorption temperature is unfavourable for the adsorption capacity.

2.3.2 Summary

The **synthesis** process has a significant impact on the final adsorption properties of the adsorbent. HT modifications to improve its adsorption performance, such as adding functional groups or carrying out complicated synthesis processes raise their production cost. The **composition** of the adsorbent also plays a key role in the adsorption properties. The complementing **cation**, the **cationic rate** and **selected anions** in the interlayers significantly influence the size of the crystal cells and the adsorption capacity. It must be noted that most of the adsorption experimental studies for CO_2 capture have been carried out at a lab-scale.

Table 2.3 Synthesis and resulting adsorption capacity of HTs.

Adsorbent	Synthesis	Calcination		$Mg\!:\!Al$	Surface area	Adsorption					Source
	Modification	Time [h]	T [°C]	Ratio	BET [m^2/g]	Method	Capacity [mol/kg]	T [°C]	P_{CO2} [bar]	Total pressure [bar]	
HT-MG30	Mg 30%	4	400		200.0	Column	**0.9**	**398.85**	0.4	2	(Oliveira *et al.*, 2008)
HT-MG50	MG 50%	4	400		160.0	Column	**0.1**	**398.85**	0.4	2	
HT-MG70	Mg 70%	4	400		145.0	Column	**0.12**	**398.85**	0.4	2	
CH (MG-AL-CO3)	None	4	400	1.63	77.5	Column	**0.26**	**300**	0.1	1.0	(Bhatta *et al.*, 2015)
HTA-CP	None - Coprecipitation	10	450	1.85	54.6	TGA	**0.56**	**300**		1	(Hanif *et al.*, 2014)
HTA-US	Ultrasonication	10	450	1.74	123.4	TGA	**0.57**	**300**		1	
HTA-MV	Microwave radiation	10	450	1.51	257.8	TGA	**0.72**	**300**		1	
HTA-CP	None - Coprecipitation	10	450	1.85	54.6	TGA	**0.44**	**350**		1	
HTA-US	Ultrasonication	10	450	1.74	123.4	TGA	**0.52**	**350**		1	
HTA-MV	Microwave radiation	10	450	1.51	257.8	TGA	**0.56**	**350**		1	
HTA-CP	None - Coprecipitation	10	450	1.85	54.6	TGA	**0.36**	**400**		1	
HTA-US	Ultrasonication	10	450	1.74	123.4	TGA	**0.37**	**400**		1	
HTA-MV	Microwave radiation	10	450	1.51	257.8	TGA	**0.48**	**400**		1	
HTA-CP	None - Coprecipitation	10	450	1.85	54.6	TGA	**0.72**	**300**		2	
HTA-US	Ultrasonication	10	450	1.74	123.4	TGA	**0.76**	**300**		2	
HTA-MV	Microwave radiation	10	450	1.51	257.8	TGA	**0.92**	**300**		2	
HTA-CP	None - Coprecipitation	10	450	1.85	54.6	TGA	**0.52**	**350**		2	
HTA-US	Ultrasonication	10	450	1.74	123.4	TGA	**0.56**	**350**		2	
HTA-MV	Microwave radiation	10	450	1.51	257.8	TGA	**0.72**	**350**		2	
HTA-CP	None - Coprecipitation	10	450	1.85	54.6	TGA	**0.48**	**400**		2	
HTA-US	Ultrasonication	10	450	1.74	123.4	TGA	**0.49**	**400**		2	
HTA-MV	Microwave radiation	10	450	1.51	257.8	TGA	**0.52**	**400**		2	

Adsorbent	**Synthesis**	**Calcination**		**$Mg:Al$**	**Surface area**	**Adsorption**					**Source**
	Modification	**Time [h]**	**T [°C]**	**Ratio**	**BET [m^2/g]**	**Method**	**Capacity [mol/kg]**	**T [°C]**	**P_{CO2} [bar]**	**Total pressure [bar]**	
HTLC-200	None - Coprecipitation		200	0.73/0.27/0.135	66.1	TGA	**0.274**	**200**		1.07	(Hutson *et al.*, 2004)
HTLC-400	None - Coprecipitation		400	0.73/0.27/0.135	183.7	TGA	**0.731**	**200**		1.07	
MG3AL1–CO3	None	5	400	3 to q	239.0	TGA	**0.53**	**200**		1.01325	(Wang *et al.*, 2011)
MG3AL1–CO3	None	4	400	3 to 1	167.0	Autosorb TGA	**0.231**	**100**	1	1	(Ram Reddy *et al.*, 2006)
MG3AL1–CO3	None	4	400	3 to 1	167.0	Autosorb TGA	**0.486**	**200**	1	1	
MG3AL1–CO3	None	4	400	3 to 1	167.0	Autosorb TGA	**0.249**	**300**	1	1	
MG3AL1–CO3	None	4	400	3 to 1	167.0	Autosorb TGA	**0.169**	**400**	1	1	

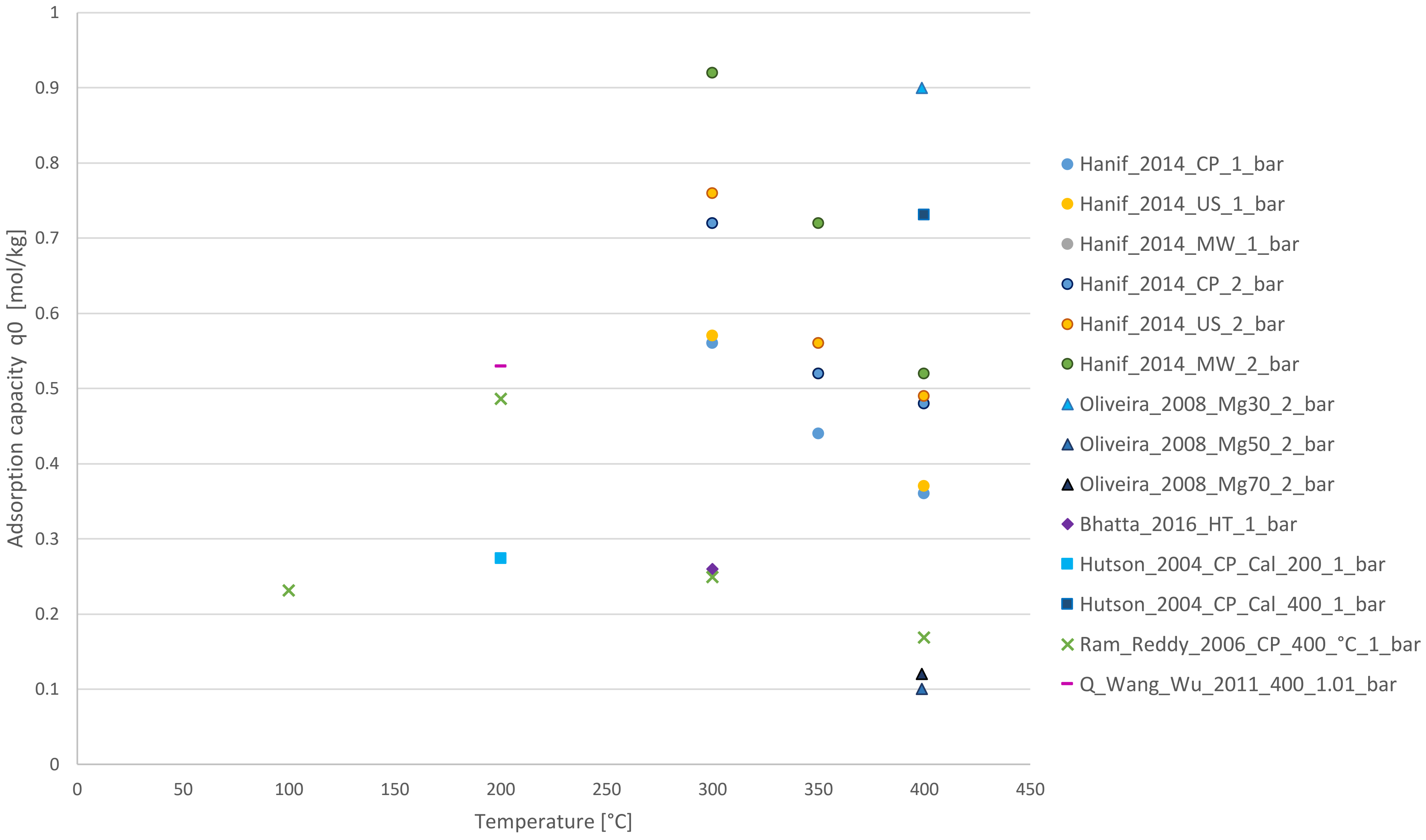

Figure 2.1 Adsorption capacity of $Mg - Al - CO_3$ HTs.

2.4 Experimental studies of HT for PCC

Adsorption studies using HTs have shown these adsorbents are capable of working on a wider temperature range than other materials, 100ºC to 400ºC (Hutson *et al.*, 2004; Ram Reddy *et al.*, 2006; Oliveira *et al.*, 2008a; Wang *et al.*, 2011; Hanif *et al.*, 2014; Bhatta *et al.*, 2015a). However, their adsorption capacity is relatively low. For example, depending on the synthesis method and the calcination temperature, the adsorption capacity of Mg-Al-CO_3 HTs can vary from 0.1 – 0.92 mmol/g and can exhibit a BET surface area of ~55 to ~258 m^2/g. Thus, most of the HTs adsorption studies focus on improving the adsorption capacity and can be classified on synthesis variations, composition variations, impregnation with alkali metals and those using supporting materials. Regarding synthesis variations, co-precipitation remains the main method due to its simplicity and the fact that it provides the opportunity to tune the characteristics of the HT. By varying the supersaturation and the pH, the crystallinity and the M^{2+}/M^{3+} ratio can be controlled correspondingly (Othman *et al.*, 2009).

2.4.1 Varying HTs composition

Studies analysing the effect of the anions in the interlayer on the adsorption capacity point out that CO_3^- has the best results. At 300ºC and 1 bar HT with this anion exhibited 0.5 mmol/g, whereas OH^- HT only achieved 0.2 mmol/g at the same conditions (Choi *et al*, 2009). This is supported by the findings of (Wang *et al.*, 2011) in which $Mg_3Al_1 - CO_3$ had the highest CO_2 capture capacity of 0.53 mmol/g, in contrast with $Mg_3Al_1 - NO_3$ (0.21 mmol/g), $Mg_3Al_1 - Cl$ (0.18 mmol/g), $Mg_3Al_1 - HCO_3$ (0.18 mmol/g), and $Mg_3Al_1 - SO_4$ (0.10 mmol/g). On the other hand, studies focusing on the effect of the cations showed that the structural evolution of the material after calcination is determined by the trivalent cations (Wang, *et al.*, 2011). Although the maximum adsorption capacity of HTs using Al (0.41 $mmol/g$), Fe (0.46 $mmol/g$) and Mn (0.42 $mmol/g$) were similar, HTs with Al had superior thermal stability and showed lower sensibility towards calcination temperature (Wang *et al.*, 2010). Furthermore, when Be^{+2} or Cd^{+2} are used as divalent cations, the obtained precipitates are not HTs (Othman *et al.*, 2009).

2.4.2 Impregnation

Interestingly, a specific and strong affinity for the CO_2 is more relevant than the available surface area or the pore volume. For instance, HTs impregnated with K_2CO_3 at a 20% load increased their adsorption capacity by more than 50% compared with non-impregnated samples even if their surface area was smaller (Silva *et al.*, 2017).

Researchers explain this by an increase in the basicity of the material (Hanif *et al.*, 2014) and the blocking of the pores by the impregnated material respectively (Hanif *et al.*, 2014; Miguel *et al.*, 2014; Bhatta *et al.*, 2015). Some disadvantages of this method to increase HTs adsorption capacity is the energy penalty for regeneration, poor durability and lower kinetics (Silva *et al.*, 2017). Alternative studies using Cs for impregnation found a higher adsorption capacity (0.35 – 0.44 mol/kg) than pure HTs (0.10 mol/kg), although not as high in contrast with K impregnation (0.76 mol/kg) (Oliveira *et al.*, 2008).

2.4.3 Supporting materials

Several supporting materials have been studied for improving the performance of HTs for CO_2 capture. Examples are zeolites (Bhatta *et al.*, 2015), CNT (Bhatta *et al.*, 2015), carbon nanofibers (CNFs) which have achieved an adsorption capacity of 0.75 mmol/g in contrast with the 0.16 mmol/g of unsupported HTs (Winter *et al.*, 2005), GOx which reported an increase of 62% with a 7%wt load (Garcia-Gallastegui *et al.*, 2012), coal-derived graphitic material (Bhatta *et al.*, 2015a), and SBA-15 silica that achieved 2.404 mmol/g in contrast with 1.79 mmol/g of unsupported HT (Pramod *et al.*, 2015). The supporting material confers mechanical stability to the composite besides the increase in the adsorption capacity. However, the adsorbent production cost increases, and so does the bed volume and operational costs. In some cases, the HT coating is lost after several cycles (Bhatta *et al.*, 2015a).

Interestingly, most of the experimental studies of HTs in PCC conditions focus on the adsorption capacity rather than on the regeneration stage. Lab-scale experiments considering regeneration did so by changing the feed gas. It has been reported that K-promoted hydrotalcites with intercalated carboxyl in the interlayer (K-Mg3-Al-C18) showed an adsorption capacity of 1.97 mmol/g at 300ºC and 1 atm, with an isosteric heat of 54.3 kJ/mol, which is expected to be advantageous for PSA processes (Li *et al.*, 2017). More recent projects that include the regeneration process are under development, such as DISPLACE in which flue gases from steel ovens will be treated (Spallina *et al.*, 2021). Studies in precombustion conditions using HTs have shown that K-promoted HTs regenerated through TSA can lose up to ~7% of their adsorption capacity after a few cycles. Researchers attributed this to the irreversible conversion of K_2O (the promoter) into K_2CO_3 (Wu *et al.*, 2013). Another approach to study hydrotalcite regeneration is by modelling the desorption isotherms. It has been used to analyse K-promoted HT modified with Ga. The results suggest that these HTs can be expected to perform well in a PSA process (Silva *et al.*, 2017).

2.4.4 Summary

The selected **synthesis process** heavily influences the final properties of the HTs, such as the morphology, the lateral size (Hutson *et al.*, 2004) and the degree of stacking of the layers (Winter *et al.*, 2005). The used metallic-salts and the M^{2+}/M^{3+} ratio affect the CO_2 adsorption capacity and kinetics, adsorbent regenerability and cyclic stability (Bhatta *et al.*, 2015b). Other modifications with promising results for improving the adsorption capacity of HTs include K_2CO_3 impregnation and the use of supporting materials.

2.5 Molecular simulation studies of PCC with HT

Understanding and predicting the properties of HTs requires a meticulous analysis of the structure. However, as in the case of CMs, the characterization of HTs is often problematic due to their polymorphic nature and the variability of their composition (Suter *et al.*, 2009; Zhang *et al.*, 2012). HTs materials often present polytypism (defects in a crystal as stacking faults), turbostraticity (random orientation of the layers) and interstratification (intergrowth of motifs with different interlayer spacing) (Costa *et al.*, 2010). Experimental data from techniques that elucidate their structure, such as X-ray diffraction, have a limited resolution due to the structural disorder and small particle size (Wang *et al.*, 2001). Molecular simulations can complement experimental findings by contributing insights into how the elements in the structure affect adsorption. Different approaches have been considered for studying these materials with computational tools. From the systematic analysis of small clusters with DFT to MD simulations of the calcination process and GCMC simulations for studying their adsorption capabilities. Each approach has revealed different characteristics of these adsorbents and the factors affecting their structure and behaviour. This section describes molecular simulation studies carried out for HT that have shown promising results for PCC. We remark the approach taken, the type of simulations used, and the insights obtained.

2.5.1 QM studies

Structure

To better understand CO_2 adsorption on HTs, the first step is to get a realistic representation of the structure. Due to the complexity and size of the structure of HTs, the use of QM based methods is mostly focused on studying the interactions between small cells and reactive groups on the clay sheets (Suter *et al.*, 2009).

The most common method used to carry out QM simulations of HT is DFT. For example, systematic DFT calculations of simplified clusters have shown that the **electronic structure of the cations is more relevant than their ionic size** (Yan *et al.*, 2009). Although there were some discrepancies of the length of the metal-oxygen (M-O) and metal-metal (M…M) interatomic distances, probably because the interaction between layers was not accounted for, their simulations were able to predict match experimental results (Yan *et al.*, 2009). DFT calculations of Mg-Al-CO_3 LDH of 3R1 polytype suggested that the **interlayer anions and their orientation affect the stacking sequence and thermodynamic potentials** of the material (Costa *et al.*, 2010).

Calcination

Once the initial layered HT geometry has been created, the next challenge is to study its structural changes during calcination. DFT calculations were also used to analyse the transformation of an Mg-Al-CO_3 HT in the temperature range of 25 to 350°C, i.e. the early stages of the thermal evolution (Costa *et al.*, 2012). Computational studies of the calcination of the material were scarce up to the 2010s, and no studies using QM methods had been applied directly to this problem previously (Costa *et al.*, 2012). In the DFT study of calcination, the van der Waals effects were neglected since it was previously reported that they did not have a significant influence on the structure of HTs. Results showed that at 180°C the HT transforms due to the **loss of interlayer water**. Next, at 280°C, the lamellar structure exhibits **monodentate CO_3^- grafted into the layers**. Finally, at 350°C, **bidentate bonds between the CO_3^- anions with the cationic layer are formed**. These results and mechanism agree better with experimental results than the previously proposed mechanisms (López *et al.*, 1997; Rives, 1999), which stated that at intermediate temperatures, the released hydroxyls from the structure reacted with the CO_3^- to form CO_2 and H_2O (Costa *et al.*, 2012).

A subsequent DFT Mg-Al HT study supports these results, pointing out that at 330°C, the **decomposition of the CO_3^- into CO_2 and residual O_2 occurs via a monodentate intermediate**, thermodynamically favoured over bidentate in agreement with (Costa *et al.*, 2012). This means that only one of the oxygen atoms of the CO_3^- attaches to the cationic layer. In consequence, a OH^- of the layer detaches and forms a water molecule (Zhang *et al.*, 2016). The simulations showed that the CO_2 molecule detaches from the structure only after the water molecules evaporate. In the following stage, after the layered structure is heated at 450ºC, a significant migration of the cations in the c-axis, i.e. perpendicular to the layers is observed despite the structure holding its layers.

Al atoms displayed much lower mobility than the Mg atoms, attributed to the stronger electrostatic interaction between the Al^{3+} and the O^{2-} and OH^{-} (Zhang *et al.*, 2016). Based on this, the researchers suggested that the Al^{3+} can stabilize the layered structure when present in a higher ratio. Finally, a complete collapse of the layered structure was observed at 800ºC generating a totally disordered cation distribution. The resulting amorphous mixed metallic oxides (MMO) show many holes and exhibited a higher surface area of 125.5 m^2/g in comparison with the pristine HT surface area of 71.8 m^2/g (Zhang *et al.*, 2016).

Although the comparison of simulation results and experimental data showed the same trends, the calculated XRD patterns disagreed more as the temperature increased. This was attributed to the fact that the modelled structures do not reflect all the different ways in which the HT can collapse, nor the pore size and distribution (Zhang *et al.*, 2016).

2.5.2 MM studies

Structure

MM studies have been used to study HTs at a lower computational expense. However, the initial challenge to carry out these simulations was the creation of an adequate FF.

Initial attempts to create a FF capable of modelling clay minerals, as is the case of HTs, showed that **hydrated clays are very sensitive to the model used to represent the water molecules**, **since they must reproduce properties for both bulk water and the interacting energies of the interlayer spacing and hydration energies** (Teppen *et al.*, 1997).

An alternative approach to study $Mg-Al-Cl, Mg-Al-OH$ and $Mg-Ga-OH$ HTs was to use first-principle molecular dynamics (FPMD), combined with DFT for obtaining the interatomic forces (Trave *et al.*, 2002). When comparing the structures, it was found that energetically favoured configurations of the cationic layers had the **$\boldsymbol{Al}$ cations non-adjacently placed, minimizing the cation-cation repulsive interactions** (Trave *et al.*, 2002). Interestingly, Cl^{-} anions preferred sites in the interlayer vertically aligned with the Al. In contrast OH^{-} anions favour sites at the centre of a square formed by two pairs of H atoms facing each other across the interlayer region. This suggests a stronger interaction with the OH^{-} groups in the layers rather than with the underlying electrostatic potential of the layers (Trave *et al.*, 2002).

A key work for achieving the computational representation of clays was the development of a general FF for clay materials referred to as CLAYFF (Cygan *et al.*, 2004). Previous empirical FFs used a constrained clay lattice, which spared computing time by reducing the degrees of freedom as the motion of the atoms in the solids was disregarded. In consequence, the exchange of energy and momentum of the interaction atoms of the clay and the fluid were not modelled (Cygan *et al.*, 2004). CLAYFF represents the atoms as point charges (with parameters optimized with DFT calculations), capable of interacting. Thus, the oxygen and hydroxyl charges vary depending on their occurrence in different environments, such as water molecules, hydroxyl groups or bridging and substitution. This enabled more flexibility when simulating complex or ill-defined crystal structures.

Another important trait of CLAYFF for modelling HTs is that it can **distinguish between tetrahedral and octahedral Al** (Cygan *et al.*, 2004). Unsurprisingly, many simulation studies of clays use CLAYFF as the FF or a modified version of it. For example, hydration studies of HTs were now possible. MD studies of $Ni - Al$ HT with different anions carried out in a NPT ensemble, at 25 ºC and 1 bar, showed that **hydrated structures have larger-inter layer spacing**, resulting in a lower electrostatic interaction between the adjacent sheets. The study also found that the $Al - O$ bonds are longer when the anions are monovalent in contrast with bivalent anions (Li *et al.*, 2006). The authors modelled the LDH structure based on an Mg-Al model, exchanging the cations with the only constraints of avoiding two neighbouring AlO_6 octahedrons. They used a variety of parameters to create a modified FF, using as basis different FF, including cff91and CLAYFF (Li *et al.*, 2006). The researchers observed three different types of distributions of the inter-layer anions and water molecules (Li *et al.*, 2006).

1. When anions are smaller, the H_2O molecules have their bonds parallel to the cationic layers.
2. The H_2O molecules are tilted since there is more inter-layer space due to the anion diameter.
3. Systems with even larger interlayer spacing give place to a double layer of H_2O molecules, with their bonds parallel to the closest cationic layer.

These observations agree with experimental measurements of the interlayer distance and anion content (Li *et al.*, 2006). The study also compared the binding energies of the different anions. The strongest bonds was found for carbonates; $CO_3^{2-} > SO_4^{2-} > OH^- > F^- > Cl^- > Br^- > NO_3^-$, as corroborated in later studies (Costa *et al.*, 2010).

The large binding energy of CO_3^{2-} could explain why some HTs get polluted with CO_3 generated when in contact with the CO_2 of the atmosphere when stored, even if they have different interlayer anions. In general, results suggest that larger atomic charges and smaller interatomic distances result in larger binding energies (Li *et al.*, 2006).

Later, a specialised FF for modelling layered double hydroxides (LDH), i.e. the group of minerals to which HTs belong, was developed (Zhang *et al.*, 2012). It combined parameters from the polymer consistent force field (PCFF) to reproduce the octahedral coordination caused by $O - M -$O bending and DFT calculations of small, representative cluster models (Zhang *et al.*, 2012). Previous FFs, such as the modified Dreiding and CLAYFF, failed to maintain the structure of the LDH in long MD simulations (Zhang *et al.*, 2012). The new layered double hydroxides force field (LDHFF) could hold the octahedral structure of the LDHs for over 2 ns of MD simulations. Furthermore, it was able to predict the exchange capability of the interlayer anions in agreement with experimental results for $Mg - Al - A$ HTs ($anion\ A: CO_3^{2-} > OH^- > Cl^- > Br^- > NO_3^-$ (Zhang *et al.*, 2012) and previous simulations (Li *et al.*, 2006).

LDHFF has been used for later studies (Geng *et al.*, 2013; Kaassis *et al.*, 2015; Tavares *et al.*, 2020; Zhao *et al.*, 2020), although none of them focused on the capture of CO_2. For example, Zhao et al (2020) studied the anion exchange behaviour of $M^{II}Al$ HT using DFT calculations and LDHFF MD simulations. They observed that the interlayer distance depends not only on the size and arrangement of the anions, as seen by experimental measurements, but also on the charges the anions carry. When the hydrogen bonding between the anion and the host is strong, the charge transfer increases. On the other hand, when the anion has a small electronegativity, it becomes more difficult for the anion to be exchanged (Zhao *et al.*, 2020).

Calcination

MD simulations using the consistent-valence force field (CVFF) were used to study the structural transition of HT due to a thermal gradient from 0 to 300 ºC (Kim *et al.*, 2005). The main goal was to develop an accurate model which could be later used to calculate the isotherms of the material. The calculated x-ray diffraction properties of the resulting structures achieved a range of 7% error in contrast with experimental data (Kim *et al.*, 2005). The deviation can be partially explained by the fact that the FF parameters for the cations were obtained from different sources developed for different conditions, i.e. for representing octahedrally coordinated Mg and tetrahedrally coordinated Al whereas the simulations used them to represent octahedrally coordinated cations (Kim *et al.*, 2007).

On the other hand, MD studies with CLAYFF of $Zn - Al - Cl$ and $Zn - Al - CO_3$ undergoing calcination showed that the **interlayer anion affects the stability of the structure** (Lombardo *et al.*, 2008). It was observed that $Zn - Al - CO_3$ loses its layered arrangement at ~150-180 °C but can restore it upon hydration, similarly to $Mg - Al - CO_3$ HT. On the other side, $Zn - Al - Cl$ was still stable at 200 °C, until 500 - 900 °C when $ZnCl$ evaporates (Lombardo *et al.*, 2008). An interesting feature of this study was the use of several MD structure models to calculate the XRPD pattern of the materials, allowing the description of the polycrystalline HT.

Adsorption

Early studies of CO_2 adsorption on $Mg - Al - CO_3$ HT used energy minimization and equilibrium MD simulations with the CVFF. The calculated isotherms were in agreement with experimental Langmuir isotherms at 200ºC, but differed at 220ºC, especially at high loadings to up to 30% (Kim *et al.*, 2007). In the same study, simulations for studying CO_2 diffusivity showed that it weakly depends on the adsorbate concentration. The researchers also observed a gap between computed and experimental results. Simulations best fitted experimental data at higher temperature ~250ºC, when simulations yielded values only 15% higher than experimental values (Kim *et al.*, 2007). The discrepancy was attributed to two factors. First, computational models consider a single crystal structure, whereas HT synthesis creates polycrystalline materials. As a result, diffusion takes place in the inter-particle regions, rather than in the interlayer space as expected in a single crystal. Second, the computational method used for calculating the diffusivities is an unsteady state method, whereas experimental techniques are steady-state and equilibrium techniques (Kim et al., 2007).

More complete and recent work on CO_2 adsorption on HT was carried out using an $Mg - Al - Cl$ structure. First, MM-MD simulations with CLAYFF were performed to calcinate the pristine layered structure (Gao *et al.*, 2018). After cooling it down, the structure was used then to carry out the adsorption analysis at room temperature conditions. GCMC simulations for static adsorption showed there is no significant difference in the adsorption capacity of structures with altered Mg/Al ratio. The calculated isotherm was recognised as type II, indicating a multilayer adsorption (Gao *et al.*, 2018). However, MD simulations, capable of calculating the residence time of the CO_2 molecules, disagreed. In these simulations, the **dynamic adsorption behaviour was sensitive to the $\boldsymbol{Mg/Al}$ ratio**.

The adsorption capacity increased with the Al content, with a maximum when $R = 3.0$. This ratio also showed the highest diffusion barrier. The discrepancy between the adsorption capacity of experimental studies of the same group and the MD simulations was attributed to physisorption representation by columbic and van der Waals interactions, whereas chemisorption that takes place during experiments was excluded (Gao *et al.*, 2018).

In addition to the effect of the cations ratio, the role of H_2O molecules in the intercalation of CO_2 has also been investigated with MD simulations employing CLAYFF. In this study, the calcination of the material was not carried out. Instead, the HT still exhibited its layered structure and was represented by different cells with a variation in the number of H_2O and CO_2 molecules. Simulations of $Mg-Al-Cl$ HT at ambient pressure and temperature achieved a **high loading**, of 3.85 $mmol/g$, **when the concentration of water was low or negligible** (Khorshidi *et al.*, 2018). Interestingly, when the H_2O concentration increased to 2 molecules per simulation cell (the maximum water concentration experimentally found) the CO_2 load was similar, but the structure had a larger interlayer spacing, from 23.0 Å without H_2O to 28.5 Å with H_2O. The authors observed that at low H_2O concentration, CO_2 molecules are mostly parallel to the mineral surface, but at higher H_2O concentration, CO_2 molecules had different orientations; mostly perpendicular to the layered structure in accordance to previous studies of hydration in $Ni-Al$ HT (Li *et al.*, 2006). This phenomenon was attributed to the dipole interaction between H_2O and CO_2 molecules and the reduced interaction between the OH^- groups of the HT and the CO_2. Additionally, they proposed that the water molecules create an extensive hydrogen bond network, which changes the orientation of the interlayer carbonates and increases the diffusivity of CO_2 in the adsorbent.

A posterior study of $Mg-Al-CO_3$ HT suggests that the **CO_2 adsorption occurs mainly due to the attraction between the O atoms in the gas molecule and the Mg ions**. The random arrangement of ions in the amorphous oxide, product of calcination, was pointed out as a factor to generate a stronger heterogeneous electric potential resulting in a higher overall adsorption capacity (Khalkhali *et al.*, 2020). The way in which researchers obtained the HT calcined structure was unusual. They carried out MD simulations using FF parameters from different sources, including the CLAYFF. The HT structure was heated up to 3,226.85 °C to obtain a homogeneous liquid structure. Then, it was cooled down to obtain layered double oxides (LDO) (Khalkhali *et al.*, 2020).

This temperature is much higher than the 400ºC considered as optimum for calcination (Wang *et al.*, 2011). The authors observed that the $Al-O$ bond is shorter than $Mg-O$, in both amorphous and crystalline LDO, which had not been reported before (Khalkhali *et al.*, 2020).

2.5.3 Summary

Molecular simulations of HTs are very useful to understand their structure and behaviour both during calcination and CO_2 adsorption. The systematic study of the effect of the cation and anion nature has shown that the $Mg-Al-CO_3$ has the most stable structure for CO_2 capture, which agrees with experimental findings. Structural molecular studies of HT have shown that:

- The electronic structure of the cations is more relevant than their ionic size.
- Interlayer anions and their orientation affect the stacking sequence and thermodynamic potentials
- Hydrated structures have larger inter-layer spacing.
- Hydrated clays are very sensitive to the model used to represent the water molecules since they must reproduce properties for both bulk water and the interacting energies of the interlayer spacing and hydration energies.
- The Al cations in $Mg-Al-CO_3$ HT are non-adjacently placed, minimizing the cation-cation repulsive interactions.
- FFs used must be able to distinguish between tetrahedral and octahedral Al.

On the other hand, studies focusing on the calcination of the HT have shown the same stages reported in experiments. In addition, they suggest that the interlayer anion affects the stability of the structure. Finally, molecular simulations of the adsorption have shown the following points, although it must be pointed out that most of the studies mentioned use a non-reactive environment and thus cannot account for chemisorption.

- Dynamic adsorption behaviour is sensitive to the Mg/Al ratio.
- High loading of CO_2 is achieved at low or negligible water concentration.
- CO_2 adsorption occurs mainly due to the attraction between the O atoms in the gas molecule and the Mg ions.

2.6 Summary

Adsorption-based PCC shows promising results. Projects around the world have already passed the proof of concept stage and have provided insights into the challenges to implement it at a large scale: 1) the continuous scalable production of the adsorbent material, 2) heat management and temperature control, 3) solids handling and circulation control and 4) the adsorbent tolerance towards impurities.

HTs are an adsorbent material with good performance for CO_2 capture, widely available and relatively cheap. However, research on how to increase their adsorption capabilities to compete with chemical absorption PCC is still ongoing. Experimental studies have found that the synthesis process has a significant impact on the final adsorption properties of the adsorbent. Their composition, i.e. the cations and anions, and the calcination temperature are key factors influencing their capture performance. K_2CO_3 impregnation and the use of supporting materials have shown promising results for further improvement.

Due to the many possible combinations for their composition and preparation, in addition to the operating conditions, experimental and systematic studies are impractical. Molecular simulations can help overcome this challenge. Their use to systematically study the effects of the cations and anions have shown $Mg - Al - CO_3$ has the most stable structure for CO_2 capture. These studies have also shown that the simulations results are very sensitive to the cationic ratio and the FF utilised to represent the HT structure. Most of the studies have been carried out using non-reactive environments, a serious limitation for investigating the role of chemisorption during CO_2 adsorption on HTs. Our work tackles this challenge by developing a tailored reactive FF for ReaxFF, a semiempirical method capable of representing both the long-range interactions of the physisorption and the formation of chemical bonds of chemisorption.

3. Geometry development

3.1 Overview

In this chapter, we describe the process for the development of the HT geometry used in the development of the FF and in the subsequent molecular simulations. Generating a structure that adequately represented the HT was crucial to carry out the simulations and to develop a tailored force field. The geometry was optimised to ensure the manual modifications were adequate and that the geometry still reflected the HT from experimental measurements. The calculation of the PES function was carried out with a QM-DFT approach and thus, a brief introduction to DFT is provided. We aim at helping the reader to better understand the simulations settings, what the calculations represent and what factors influence the results. Finally, we discuss the challenges we faced as well as the limitations of our approach for generating this geometry.

3.2 Introduction to DFT

Density Functional Theory (DFT) is the most popular choice for QM calculations as it is computationally affordable and renders reasonably reliable and accurate results (Yu *et al.*, 2016). The underlying theory of DFT are the theorems by Hohenberg and Kohn (1964), and Kohn and Sham (1965). The key ideas, oversimplified, are the following:

1. The ground-state properties of a many-electron system only depend on the electronic density, i.e. the electrons arrangement in the system (Hohenberg and Kohn, 1964).
2. A system's total energy calculation requires an approximation of the exchange-correlation energy (Kohn and Sham, 1965).

In other words, by calculating the arrangement and interactions of the electrons in the system, the ground-state properties of the said system can be known. The arrangement of the system is known in many cases where the initial atom coordinates are provided. Thus, the next challenge is to calculate the electronic density of the system $E[\rho(r)]$. In DFT this is carried out with the following expression (Wolters, 2016):

$$E[\rho(r)] = T_s[\rho(r)] + E_{Ne}[\rho(r)] + E_C[\rho(r)] + E_{XC}[\rho(r)] \tag{3.1}$$

Where $\boldsymbol{T_s[\rho(r)]}$ is the kinetic energy of the electrons assuming a non-interacting reference system (Kohn and Sham, 1965). $\boldsymbol{E_{Ne}[\rho(r)]}$ represents the potential energy or the electrostatic attraction between the nuclei and the electron density in the system whereas $\boldsymbol{E_C[\rho(r)]}$ is the

Coulomb electron repulsion of the charges in the system. Finally, $\boldsymbol{E_{XC}}[\boldsymbol{\rho}(\boldsymbol{r})]$ is the exchange-correlation energy term that amends the deficiencies of the kinetic energy and Coulomb terms.

The calculation of the Coulomb terms for the interaction between nuclei and orbiting electrons is relatively simple since nuclei are regarded as stationary from the perspective of the electrons. Current theories can exactly calculate the kinetic, potential, and electrostatic energies. Nevertheless, the exchange-correlation energy term cannot be calculated exactly and is very difficult to describe. Some authors even catalogue the challenge of finding a universal exchange-correlation functional to a "Quantum Merlin Arthur" (QMA) complexity, equivalent of the non-deterministic polynomial-time hard (NP-hard) mathematical problem (Yu *et al.*, 2016). Many exchange-correlation functionals have been developed for DFT, each one bringing more accuracy, but also increasing the computational power demand. The simplest functional is the Local Density Approximation (LDA) while the most accurate and computationally expensive are hybrid functionals. The progression has been associated this progression to "Jacob's ladder" as a path towards the "heaven of chemical accuracy" (Jacobsen and Cavallo, 2017). Figure 3.1 shows examples of functionals in increasing accuracy level. The HF model is the simplest way to describe a system (Earth), and the functionals increase in complexity from left to right. It is considered that the goal would be achieving chemical accuracy, whcich is why it is considered "heaven".It is important to note that the final geometry of the DFT-optimized structures can vary depending on the functional used. Thus, caution must be exercised in selecting a functional to represent the studied system as accurately at an accessible computational expense.

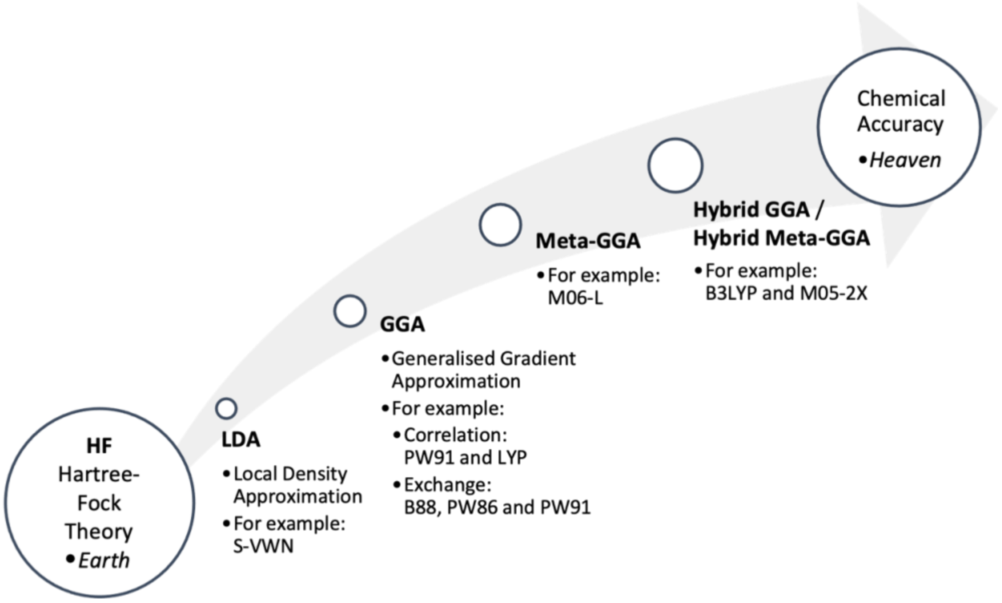

Figure 3.1 DFT exchange-correlation functionals diagram based on Jacobsen and Cavallo (2017).

3.3 Methodology

3.3.1 HT supercell development

To represent the selected adsorbent, an $Mg - Al - CO_3$ HT, the geometry drawn in the simulation box had to agree with experimental data. Thus, the atoms coordinates were obtained from a crystallographic information file (.cif) derived from X-ray powder diffraction measurements results (Costantino *et al*, 1998) available at the Inorganic Crystal Structure Database (ICSD) with the ID 86655. The original .cif file contained information of the basic structural unit (BSU) of the HT, a single "column" of the periodic structure, Figure 3.2.

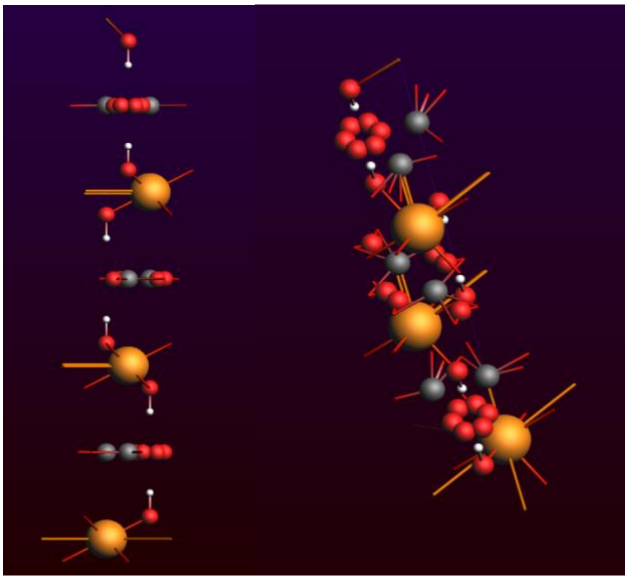

Figure 3.2 BSU of the HT with the original atom coordinates of the 86655.cif. Side view on the left, view from a different persective to the right. O atoms in red, H in white, carbon in black and Mg in orange.

As previously mentioned, HTs present polymorphism, meaning that the location of the interlayer atoms does not follow a strict pattern. As a result, H_2O and CO_3 molecules can vary their position and orientation. To represent this, the .cif file provides useful information about the probability of these atoms being present at certain positions, i.e., the occupancy. Early attempts using the "Supercell" software to automatically create BSUs failed as the number of possible supercells ($\sim 9.8 \times 10^8$ for $2 \times 2 \times 1$ BSUs) was too large for computing a representative sample. An attempt of creating the SC1 in the RASPA software made possible the replacement of the Mg atoms with Al. However, the allocation of the H_2O and CO_3 molecules was inadequate.

The creation of the HT geometry in AMS 2019 allowed for the manual editing and the geometry optimisation of an SC1. Nevertheless, the AMS 2019 software was not capable of interpreting the occupancy information and thus placed an atom at every possible location.

Therefore, the structure showed more atoms than necessary, as seen in Figure 3.2 where O atoms form rings. To correct this, the geometry was manually edited. First, a supercell of $4 \times 4 \times 1$ BSU was created similar to the work of Hutson *et al.* (2004). We will refer to it as supercell 1 (SC1). It comprised three cationic layers and the required number of H_2O and CO_3^- molecules to ensure the composition of the adsorbent followed the chemical formula 3.1.

$$Mg_6Al_2(CO_3)(OH)_{16} \cdot 4(H_2O) \tag{3.1}$$

Care was taken to reflect the $Mg{:}Al$ ratio of $3{:}1$ by replacing the Mg atoms for Al. This ratio has been considered as optimum for CO_2 capture applications according to Khorshidi *et al.* (2018). Al cations were placed non-adjacently to minimise cation-cation repulsive interactions (Trave et al., 2002) as in previous studies (Li *et al.*, 2006; Kim *et al.*, 2007; Sideris *et al.*, 2012). The surplus H_2O molecules in the interlayer were deleted. The final SC1 is shown in Figure 3.3.

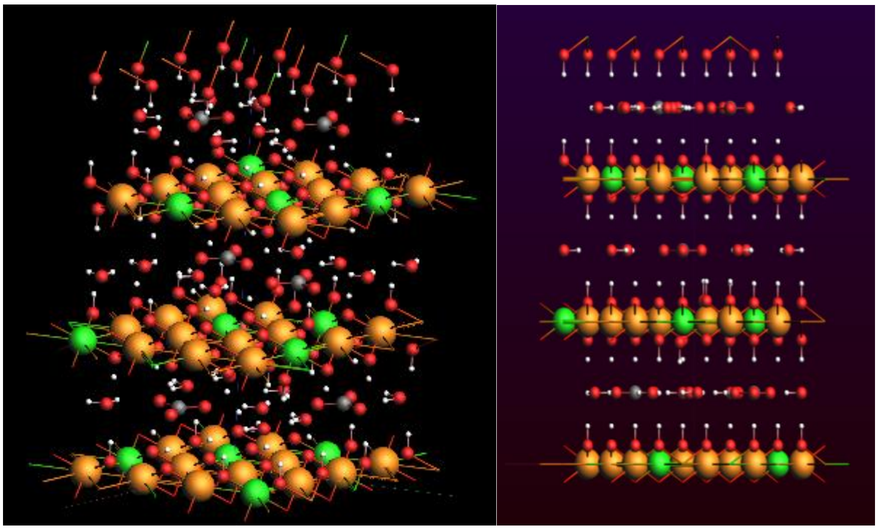

Figure 3.3 SC1 from two different perspectives, side view on the right. Mg atoms in orange, Al in green, O in red, C in grey and H in white.

3.2.2 Geometry Optimisation

After the creation of the HT geometry, it was necessary to ensure the coordinates of the atoms still represented adequately the adsorbent. That is, to obtain the global minimum of the PES function. We employed the QM approach for this since there were no FFs capable of representing HT. The geometry optimisation (GO) was carried out using the BAND engine of AMS 2019 as it is the only engine capable of performing DFT calculations for periodic structures. The exchange-correlation functional selected was the Perdew-Burke-Ernzerhof (PBE) functional from the Generalized Gradient Approximation (GGA) approach, similar to the work of Costa *et al.* (2010). PBE was selected because it shows good performance for the description of simple metals, solids, and hydrogen bonds (Ernzerhof and Scuseria, 1999). The basis set selected was triple ζ (TZP) with one polarization function to account for the polarisation effects present due to C and H atoms. Table 3.1 shows the main settings used for the GO of SC1.

Table 3.1 BAND Settings for the SC1's GO.

Main Settings	
Task	Geometry optimization
Followed by	Nothing
Periodicity	Bulk
Unrestricted	Unselected
XC functional	GGA: PBE
Relativity	None
Basis set	TZP
Frozen core	Large
Numerical quality	Normal

The optimised SC1 geometry was used as the building block to create a larger structure, the supercell 2 (SC2). This was done to obtain a geometry that represented more adequately the HT. As mentioned earlier, HT is prone to defects in the structure, which are difficult to depict with small systems. Thus, the optimised SC1 was multiplied $3 \times 3 \times 1$, creating the SC2 shown in Figure 3.4.

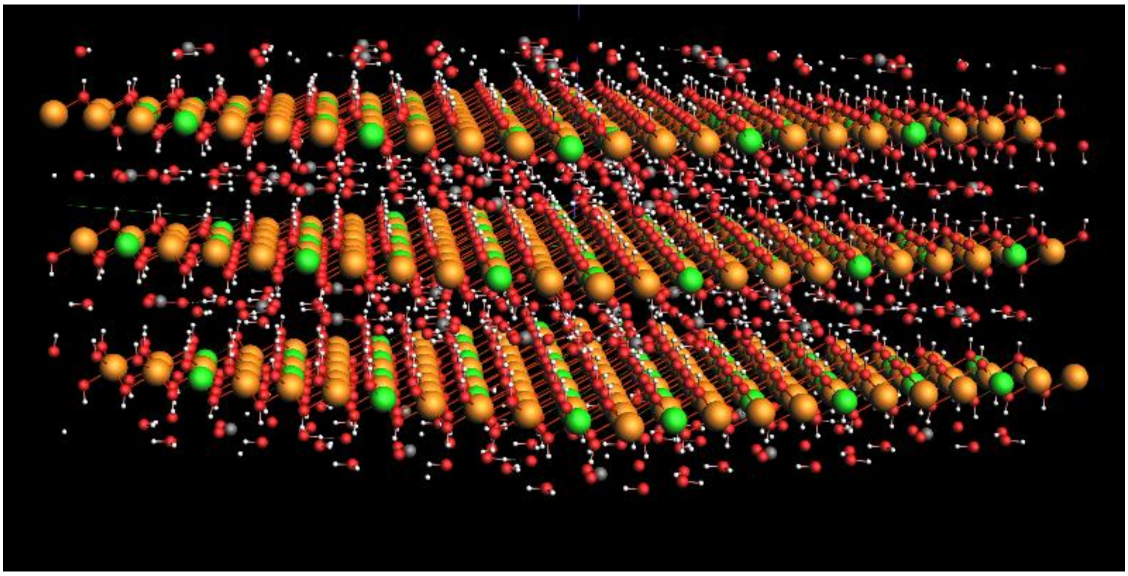

Figure 3.4 SC2. Mg atoms in orange, Al in green, O in red, C in grey and H in white.

3.4 Results and discussion –comparison with experimental data of the HT

3.4.1 HT supercell development

The BSU from Costantino *et al.* (1998) provided the coordinates of the atoms required to develop the HT supercell geometries. The SC1 created for the HT showed the expected layered structure, as seen in Figure 3.3. This configuration is similar to HT structures described in the literature in which the cationic layers are intercalated with anionic layers (López *et al.*, 1997; Rives, 1999). The cationic ratio and the H_2O and CO_3^- content were suitably corrected to match the $Mg - Al - CO_3$ HT composition. It must be noted, however, that the selected sites for the Al atoms, as well as the H_2O and CO_3^- molecules, could vary in real structures. The polymorphism of the HT is not easily represented in SC1 as it is too small in comparison with real samples. The use of a single SC in the simulations can limit the observation of different calcination and adsorption patterns. Due to the computational resources' constraints, we only worked with this structure.

3.4.2 Geometry Optimisation

Since the edition of SC1 was carried out manually, it was crucial to validate it. The first step towards this aim was to carry out a GO. The results showed the optimised structure achieved slightly lower energy of formation (-42,731.04175 $kcal/mol$), indicating a more stable geometry than the non-optimised SC1 (-41,789.14641 $kcal/mol$) as shown in Figure 3.5.

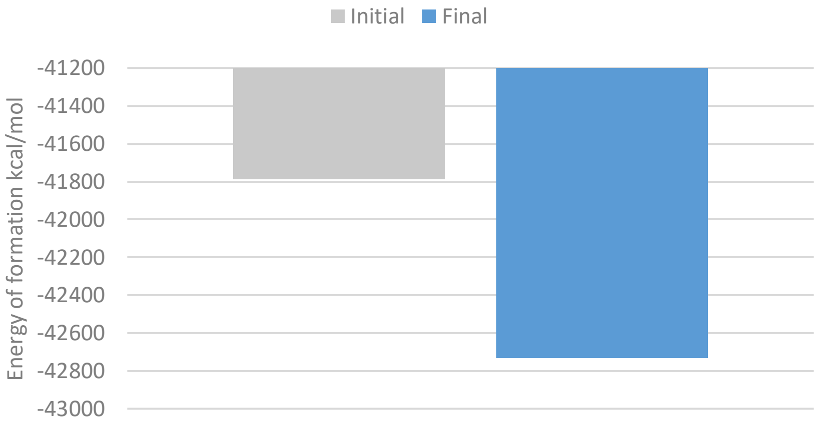

Figure 3.5 Energy of formation of SC1 after GO.

The optimised SC1 is represented in a ".xyz" that contains the coordinates of the atoms as shown in the 9. Appendix. The geometry preserved its typical layered structure, which was passed on to the SC2 as seen in Figure 3.4. The file representing SC2 is lengthy as it contains 3024 atoms. It can be accessed and downloaded directly from the GitHub repository of the project. https://github.com/PheLiBoP/ghgt-15_Molecular_simulation_of_CO2_capture_using_HT.

To validate the optimised SC2 geometry, we contrasted its lattice parameters against the original data from Costantino *et al.* (1998) as shown in Table 3.2. We divided SC2 length by the number of BSUs present in the structure to be able to compare the values. The results were in a range of under 1% error. Figure 3.6 is included as a reference of the meaning of each parameter.

Table 3.2 Lattice parameters of the original .cif file and the obtained SC2.

Lattice parameter	*Original .cif*	*Optimized structure*	*% Error*
a	3.04535(9)	3.0546	-0.30
b	3.04535(9)	3.0694	-0.79
c	22.7010(13)	22.5693	0.58
α	90	90.0776	-0.09
β	120	119.7696	0.19
γ	90	89.9205	0.09

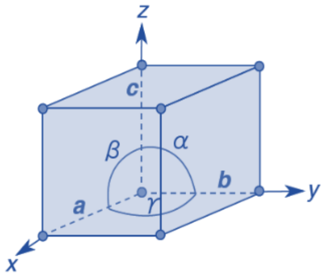

Figure 3.6 Lattice parameters. Image from LibreTexts^{TM} (2020).

It must be mentioned that the GO of SC1 was interrupted due to the computational power available. The PES optimization ran for about a month, however, it stopped as there was no space in the hard drive partition allocated for the simulation for it to continue. This could imply that the obtained SC1 could still be further refined, although we are comfortable with using the results of the last iteration since the difference in the total energy comparing with the previous iteration structure is low. In future work, it is advised to carry out the GO until the convergence criteria are met. In addition, the creation of other SC with different positions for the interlayer anions could enrich the study as these variations could represent the defects naturally found in the HT real structure.

3.5 Summary

The HT geometry was developed using data from experimental measurements. It was manually edited to adequately reflect the composition of the $Mg - Al - CO_3$ HT selected for the adsorption studies. Next, the structure was optimized using DFT to ensure the modifications agreed with the original lattice parameters. The structure exhibited the expected layered structure and lattice parameters. This structure was employed for the development of the FF, as well as for the MD and GCMC simulations in the calcination and adsorption studies, respectively.

4. Force field development

4.1 Overview

The molecular simulation studies of the selected $Mg - Al - CO_3$ HT required a specialised ReaxFF FF as input. None of the available FFs in the AMS 2019 software could reflect the HT interaction with flue gases. An initial approach to the problem was to create a new FF based on the parameters of existing FFs. Unlike traditional FFs, in a ReaxFF, each element is described using a single atom type and can be used in different chemical environments (Zhang *et al*, 2014). There are two branches of the type of environments analysed with ReaxFF, combustion and aqueous. These branches differentiate mainly in how accurately they describe water molecules, as a gas-phase or in a liquid-phase respectively (SCM, 2017). As this work aimed at studying CO_2 adsorption from flue gases, we initially considered using parameters from FFs included in the combustion branch. However, it became clear it was not possible to carry out the simulations with the available FFs. Even if they contained some parameters for the elements included in the HT system, they were missing information about the bonds and interactions. Thus, it was decided to do a re-parameterization of an existing ReaxFF FF using the Covariance Matrix Adaptation Evolutionary Strategy (CMA-ES). In this section, we provide a brief introduction to CMA-ES to facilitate understanding the FF development process. We describe the steps taken and finally, we discuss the limitations of our resulting FF.

4.2 Introduction to CMA-ES

The CMA-ES is a stochastic mathematical method for real-parameter optimization of non-linear, non-convex functions with little user interference (Sadeghi and Kalantar, 2014). In other words, this method can find the optimum parameters for functions, even for those with more than one minimum, using a small amount of information as a starting point. It was designed to reduce the number of required generations to converge to the optimum (Hansen *et al*, 2003), which makes it a robust optimization method even in "rugged landscapes", where discontinuities and local optima are common (Hansen, 2016).

In ReaxFF, the total energy of the system is calculated with the PES function. However, the parameters that represent the behaviour of each atom type of atom are needed. The CMA-ES method is useful to find these parameters. As a strategy, CMA-ES has shown better results in contrast with other FF re-parameterization methodologies used in computer science for optimization problems, such as the Monte Carlo Force Field (MCFF) optimizer (Iype, 2013) and Genetic Algorithms (Shchygol *et al.*, 2018). CMA-ES achieves the lowest error function value with fewer steps and less dependence on the initial guess in contrast with MCFF (Shchygol *et al.*, 2018). Additionally, CMA-ES has a lower chance of being trapped into a local optimum instead of finding the global because it generates sets of search points according to a multivariate normal distribution, which prevents biasing the points in any direction (Sadeghi and Kalantar, 2014).The optimization happens after the mean and covariance matrix of the searching points of both a Training Set (TS) and a Validation Set (VS) are updated and compared with the objective function (Sadeghi and Kalantar, 2014):

$$Error = \sum_{i=1}^{n} \left[\frac{x_{i,TS} - x_{i,ReaxFF}}{\sigma_i} \right]^2 \tag{4.1}$$

Where the sum encompasses the square of the difference between the results of each one of the entries of the TS ($x_{i,TS}$) and the entries generated by the reparametrized FF ($x_{i,ReaxFF}$). The difference between the values generated by the TS and the ReaxFF new FF is “weighted” according to the value of σ_i, which can be manually assigned. The value of σ_i can be used to highlight a relevant feature of the FF, e.g. bond distance, angle, or energy terms in contrast with the other entries. The new FF is then compared with the values generated by the VS in order to observe how well it represents the system.

In summary, when implementing the CMA-ES for optimising the new FF parameters, the challenge is to find the minimum error function between the results obtained with reference data in the TS, and the ones created with the new modified FF. A global minimum hence reveals the best set of new FF parameters, which are then compared against a validation set (VS). Thus, for obtaining well-fitted parameters, a sound TS is required. In this work, we describe how we generated our TS and its limitations. The implementation of the CMA-ES algorithm in AMS 2019 consists of four main stages as shown in Figure 4.1. In the next section, we describe in detail each stage and the tasks performed.

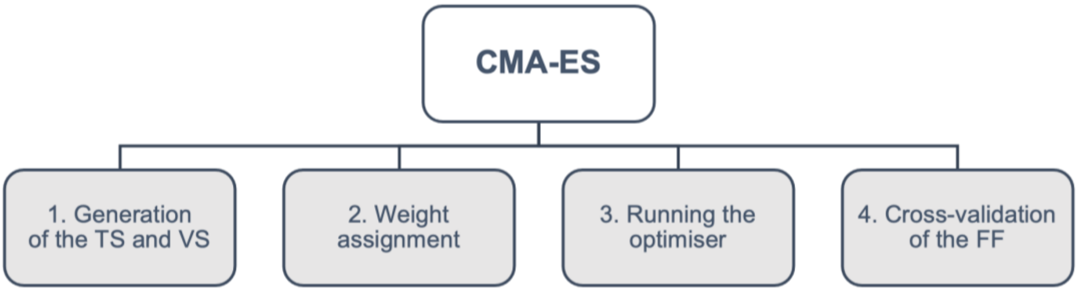

Figure 4.1 Stages for the implementation of the CMA-ES algorithm.

4.3 Generation of the TS and VS

The generation of the TS and VS is the most complex step in the process of using CMA-ES for developing the ReaxFF. Both data sets comprise four entry types:

a. **Optimized Geometry** of the structure of the different systems that are involved in the studied phenomena. For this work, it meant the optimised geometries of the HT structure and the flue gases (CO, CO_2, O_2, H_2, H_2O, N_2, NO, NO_2).

b. **Potential Energy Surface** scans (PES). The bond scans of the bonds that are expected to break and/or form during the studied reactions. These are performed to locate the initial guess of the Transition States energies.

c. **Conformers** or alternative configurations of the studied systems. For example, some organic molecules can have the same atoms and structures but with varying bond angles or dihedral angles. They ought to be considered in the TS to generate FF values capable of representing them.

d. **Transition States** provide information on the changes in bond energies when a reaction takes place. Transition states are snapshots of the bond trajectories and give an approximate energy profile of the expected reactions (SCM, 2018b). This information can be extracted from trajectory snapshots from reference MD simulations employing an existing FF.

Next, the entries are divided into the TS and the validation set (VS) used for step 4. Cross-validation of the FF. Figure 4.2 shows a summary of the CMA-ES process. The next section describes the work done to obtain each one of the entries for the TS.

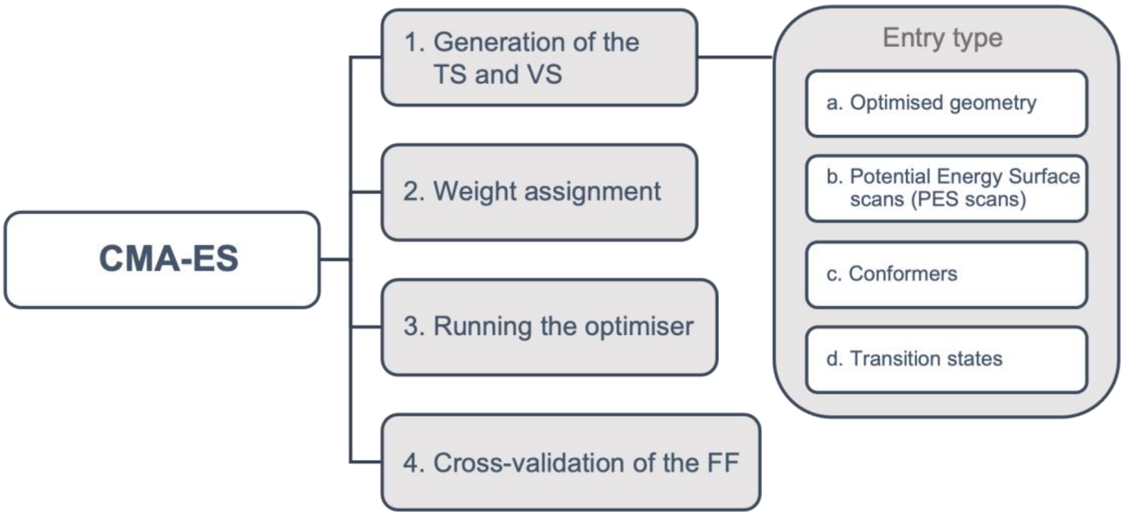

Figure 4.2 CMA-ES process and the entry types for the TS and VS.

4.3.1 Optimised geometry

HT

As mentioned in section 3.2.2 Geometry Optimisation, the HT geometry was optimised with a QM-DFT approach. For the TS, the GGA-PBE functional was used, as in the work of Hjertenaes *et al.* (2016). PBE has shown good performance for the description of simple metals, solids, and hydrogen bonds at a suitable computational cost (Ernzerhof and Scuseria, 1999). According to Rappoport *et al.* (2011), the PBE functional is the most "universal" functional which can be both applied for molecules and solids. It might not be the best fit for either, however, it can handle both types of systems and is good for describing 3D elements. Its main disadvantages are the overestimation of the bonding distance and lattice constants of extended solids by about 7.6 pm, and the underestimation of vibrational frequencies (Rappoport *et al.*, 2011).

We employed the PBEsol functional to generate the HT structure for the VS. This functional is a modified version of PBE to enhance solids representation (Haas *et al*, 2011; Rappoport *et al.*, 2011). It is less accurate when representing the molecular bond energies. However, it exhibits a better lattice constant and other equilibrium properties for densely packed solids. The molecular bond distances are comparable to the ones of PBE. The optimised geometry using PBEsol was expected to better represent the HT, which is why it was used for the VS.

In both cases, for the TS and VS, the settings of the GO job for the HT structure employed a TZP basis set (triple ζ), with one polarization function for building the Slater-type orbitals used by AMS 2019. According to te Velde *et al.* (2001), these orbitals present correct short and long-range behaviour, as well as a cusp behaviour and appropriate long-range decay allowing the generation of high-quality basis sets in exchange of a higher computational cost. A large frozen core was chosen to reduce computational expense (SCM, 2018a). No relativity effects were considered as the HT structure does not contain heavy elements. The Quasi-Newton optimization method was selected due to its capacity to treat large periodic systems in cartesian coordinates. The AMS 2019 engine used was BAND as it is capable of handling periodical structures. The GO settings for the HT structure for the TS and VS are shown in Table 4.1 and Table 4.2 respectively.

Table 4.1 GO settings for the HT structure for the TS.

BAND Main		*Geometry Optimization*	
Task:	Geometry Optimization	*Optimization method:*	Quasi-Newton
Followed by:	Nothing	*Optimization space:*	Auto
Periodicity:	Bulk	*Optimize lattice:*	Yes
Unrestricted:	Unselected	*Maximum number of iterations:*	-
XC functional:	**GGA:PBE**	*Gradient convergence*	1e-3 $Ha/Å$
Relativity:	None	*Energy convergence*	1e-5 Ha
Basis set:	TZP	*Step convergence*	1e-3 Å
Frozen core:	Large	*Initial Hessian*	Auto
Numerical quality:	Normal	*Pressure*	0.0 Pa
Calculate:	Unselected		

Table 4.2 GO settings for the HT structure for the VS.

BAND Main		*Geometry Optimization*	
Task:	Geometry Optimization	*Optimization method:*	Quasi-Newton
Followed by:	Nothing	*Optimization space:*	Auto
Periodicity:	Bulk	*Optimize lattice:*	Yes
Unrestricted:	Unselected	*Maximum number of iterations:*	-
XC functional:	**GGA:PBE**	*Gradient convergence*	1e-3 $Ha/Å$
Relativity:	None	*Energy convergence*	1e-5 Ha
Basis set:	TZP	*Step convergence*	1e-3 Å
Frozen core:	Large	*Initial Hessian*	Auto
Numerical quality:	Normal	*Pressure*	0.0 Pa
Calculate:	Unselected		

Flue gases

The GO of the gas molecules was carried out for all the flue gases expected as a result of the combustion or the chemisorption processes: CO_2, CO, O_2, N_2, NO, NO_2, H_2 and H_2O. The geometry of the flue gas molecules was imported from the AMS 2019 database. This allowed a reduction in the computational time of optimization. The molecules of NO and NO_2 were obtained from a SMILES string since they were not available in the database. The geometries are shown in Figure 4.3

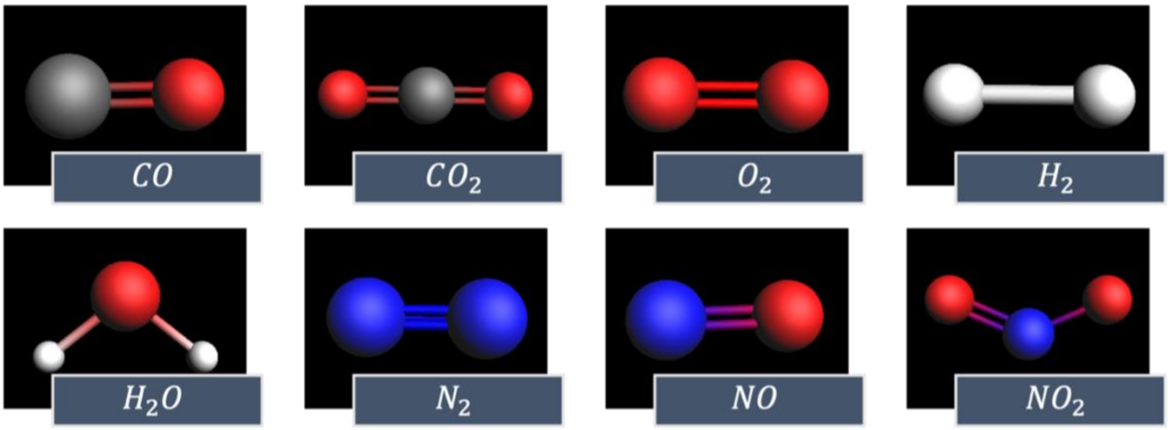

Figure 4.3 Structures of the flue gases molecules.

The geometry optimization of the flue gas molecules of the TS was carried out with the DFTB engine, whereas the VS structures were optimised using the ADF engine. The geometries created for the TS were imported, pre-optimized with the Universal Force Field (UFF), and then optimized with density functional based tight-binding method (DFTB). DFTB is a modification from DFT, based on a second-order expansion of the Kohn-Sham total energy as a function of the charge density variations (dftb.org, 2021). The DFTB3 model with the dispersion correction D3-BJ and the parameter directory DFT.org/3ob-3-1 was selected. DFTB3 is a model usually applied to biomolecules as it improves the description of charged systems. The summary of the settings for the GO of the TS are detailed in Table 4.3.

Table 4.3 GO settings for the flue gases geometries for the TS.

DFTB Main		*Geometry Optimization*	
Task:	Geometry Optimization	*Optimization method:*	Quasi-Newton
Followed by:	Nothing	*Optimization space:*	Auto
Model:	DFTB3	*Optimize lattice:*	Unselected
Dispersion correction:	D3-BJ	*Maximum number of iterations:*	-
Periodicity	None	*Gradient convergence*	1e-3 $Ha/Å$
Total charge:	0.0	*Energy convergence*	1e-5 Ha
Occupation:	Auto	*Step convergence*	1e-3 Å
Parameter directory:	DFT.org/3ob-3-1	*Initial Hessian*	Auto
k-space sampling:	Gamma only (default)		
Spin polarization:	0		
Unrestricted:	Unselected (default)		
Fermi Temperature:	300 K (default)		

The molecules were optimised with DFT in the ADF engine for the VS, using the GGA-PBE functional and the TZP basis set, the same settings used for the HT. Some modifications of the settings were necessary for the GO of the NO and NO_2 molecules. For these molecules, the Unrestricted setting was changed to a spin polarization 1 as each molecule has one unpaired electron. Table 4.4 shows the settings for optimising the flue gas molecules for the VS.

Table 4.4 GO settings for the flue gases geometries for the VS.

ADF Main Settings		*Geometry Optimization Details*	
Task:	Geometry Optimization	**Coordinates used for optimization:**	Delocalized
Total charge:	0	**Optimization method:**	AUTO (Quasi-Newton)
Spin polarization:	0 (default)	**Energy convergence:**	1e-3 $Ha/\text{Å}$
Unrestricted:	Unselected	**Gradient convergence:**	1e-5 Ha
XC functional:	**GGA:PBE**		
Relativity:	None		
Basis set:	TZP		
Frozen core:	Small		
Numerical quality:	Normal		

4.3.2 Potential Energy Surface scans (PES scans)

The purpose of adding PES scans to the TS is to improve the approximation of the energy gradient in the bonds involved in the expected chemical reactions of the studied system (SCM, 2018b). The PES scans for the TS were created using DFTB theory in the DFTB engine with the settings described in Table 4.5.

Table 4.5 Settings for generating the PES scans of the flue gases in the TS.

DFTB Main Settings

Task:	PES scan	*Total charge:*	0.0 (default)
Followed by:	Nothing	*Spin polarization:*	0 (default)
Model:	DFTB3	*Unrestricted:*	Default
Dispersion	D3-BJ	*Occupation:*	Auto
Periodicity:	None	*Fermi temperature:*	300.0 K (default)
k-space:	Gamma only (default)	*Parameter directory:*	DFT.org/3ob-3-1

The PES scans for the VS were calculated with DFT theory in the ADF engine with the same functional as the HT. The settings are described in Table 4.6.

Table 4.6 Settings for generating the PES scans of the flue gases in the VS.

ADF Main Settings

Task:	PES scan	*Relativity:*	None
Total charge:	0	*Basis set:*	TZP
Spin polarization:	0 (default)	*Frozen core:*	Small
Unrestricted:	Unselected	*Numerical quality:*	Normal
XC functional:	GGA: PBE		

Additional settings for carrying out the PES scans were customised for each flue gas molecule. The behaviour of two atoms that are linked by a bond can be modelled as a harmonic oscillation, analogous to a simple spring ideal model. In a more accurate depiction, molecules follow an-harmonic behaviour due to the dissipation of energy. The PES scans settings were customised for each molecule to obtain an energy curve that reflected this phenomenon. In the settings, the bond distance at which the scan was performed, i.e. the minimum and maximum distances, as well as the number of iterations, were tailored to capture the start of the anharmonicity of the curve. The parameters values were based on previous trials for generating the energy curves shown in Figure 4.4.

a) CO_2

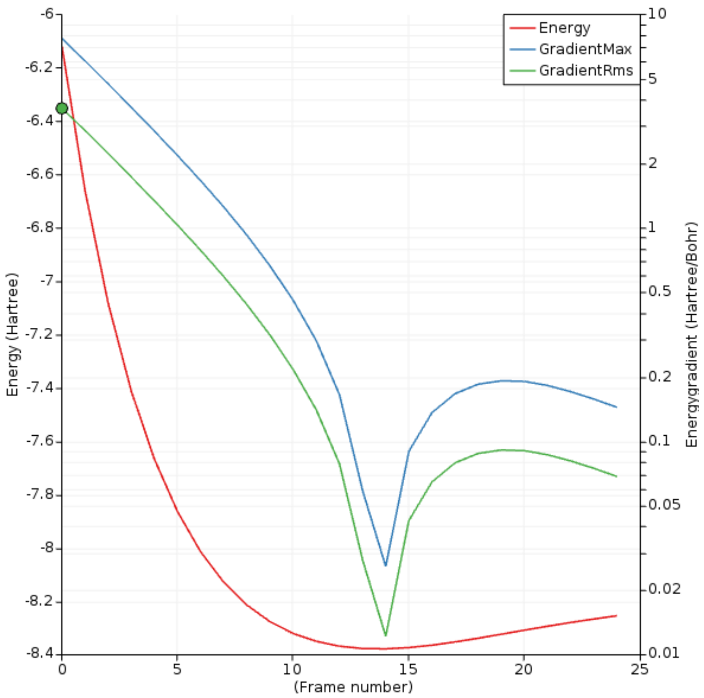

b) CO

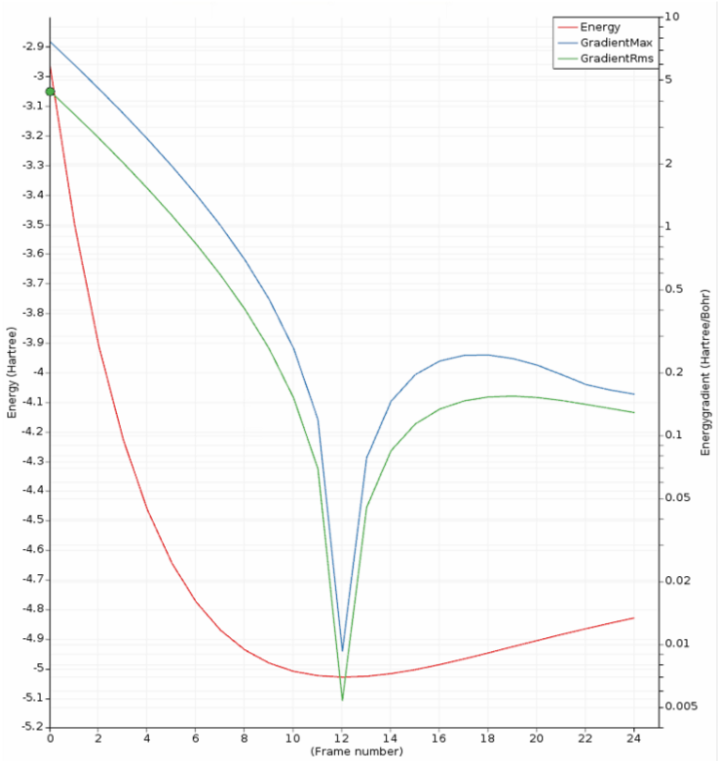
Energy
GradientMax
GradientRms
Energy (Hartree)
Energygradient (Hartree/Bohr)
(Frame number)
-2.9
-3
-3.1
-3.2
-3.3
-3.4
-3.5
-3.6
-3.7
-3.8
-3.9
-4
-4.1
-4.2
-4.3
-4.4
-4.5
-4.6
-4.7
-4.8
-4.9
-5
-5.1
-5.2
0
2
4
6
8
10
12
14
16
18
20
22
24
10
5
2
1
0.5
0.2
0.1
0.05
0.02
0.01
0.005

c) H_2

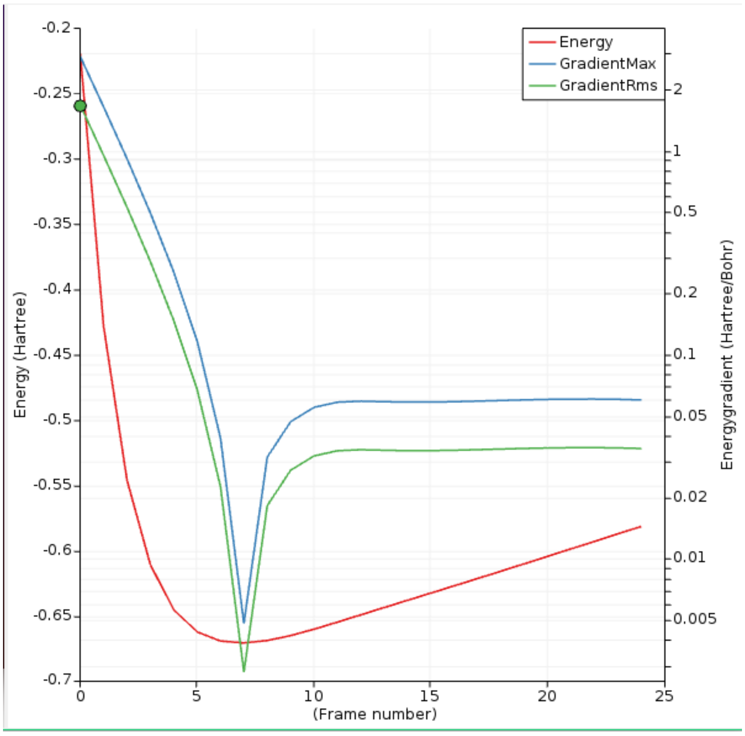
Energy
GradientMax
GradientRms
Energy (Hartree)
Energygradient (Hartree/Bohr)
(Frame number)
-0.2
-0.25
-0.3
-0.35
-0.4
-0.45
-0.5
-0.55
-0.6
-0.65
-0.7
0
5
10
15
20
25
2
1
0.5
0.2
0.1
0.05
0.02
0.01
0.005

d) H_2O

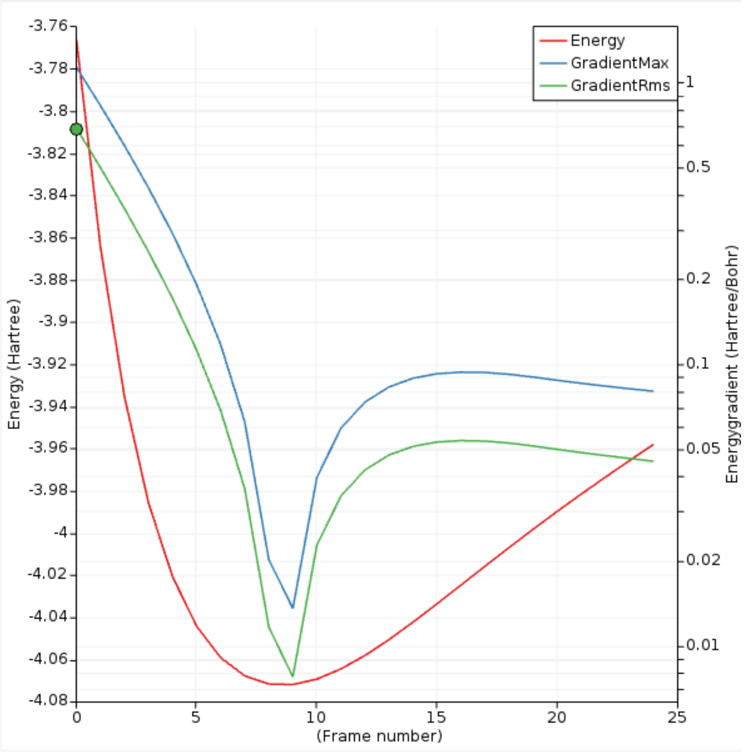
Energy
GradientMax
GradientRms
Energy (Hartree)
Energygradient (Hartree/Bohr)
(Frame number)
-3.76
-3.78
-3.8
-3.82
-3.84
-3.86
-3.88
-3.9
-3.92
-3.94
-3.96
-3.98
-4
-4.02
-4.04
-4.06
-4.08
0
5
10
15
20
25
1
0.5
0.2
0.1
0.05
0.02
0.01

e) N_2

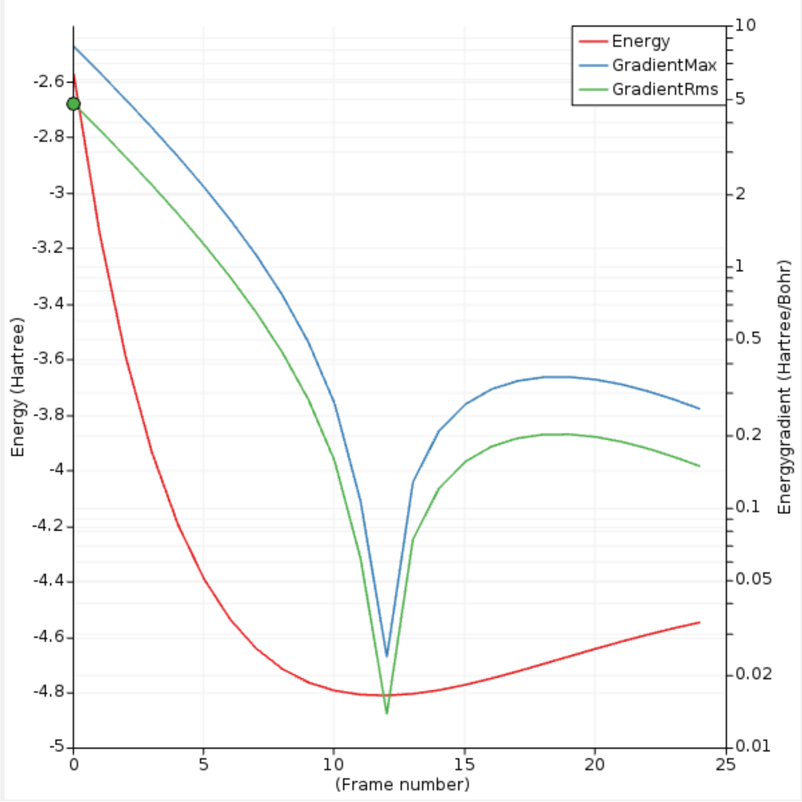
Energy
GradientMax
GradientRms
Energy (Hartree)
Energygradient (Hartree/Bohr)
(Frame number)
-2.6
-2.8
-3
-3.2
-3.4
-3.6
-3.8
-4
-4.2
-4.4
-4.6
-4.8
-5
0
5
10
15
20
25
10
5
2
1
0.5
0.2
0.1
0.05
0.02
0.01

f) NO

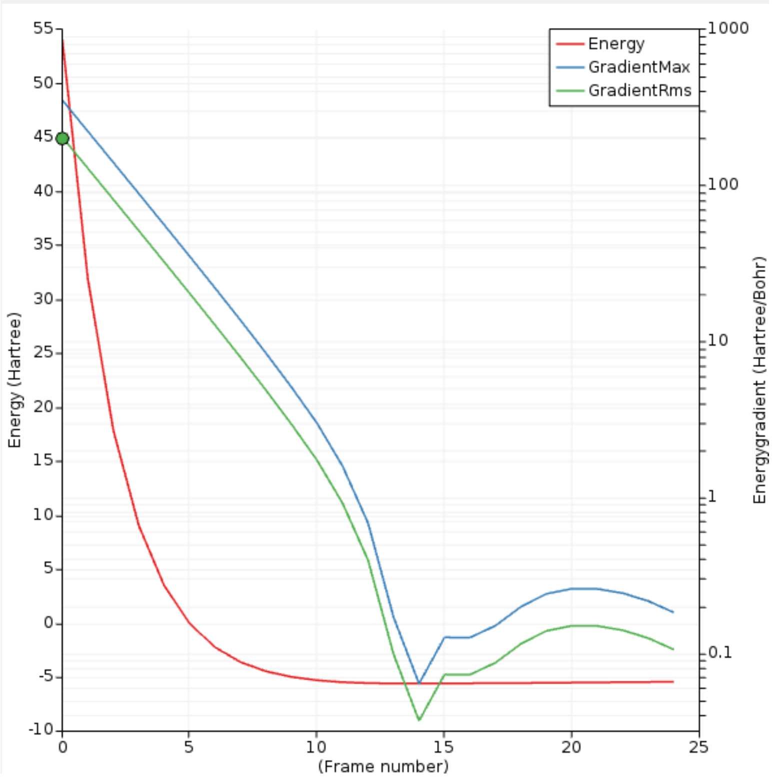
Energy
GradientMax
GradientRms
Energy (Hartree)
55
50
45
40
35
30
25
20
15
10
5
0
-5
-10
1000
100
10
1
0.1
Energygradient (Hartree/Bohr)
0
5
10
15
20
25
(Frame number)

g) NO_2

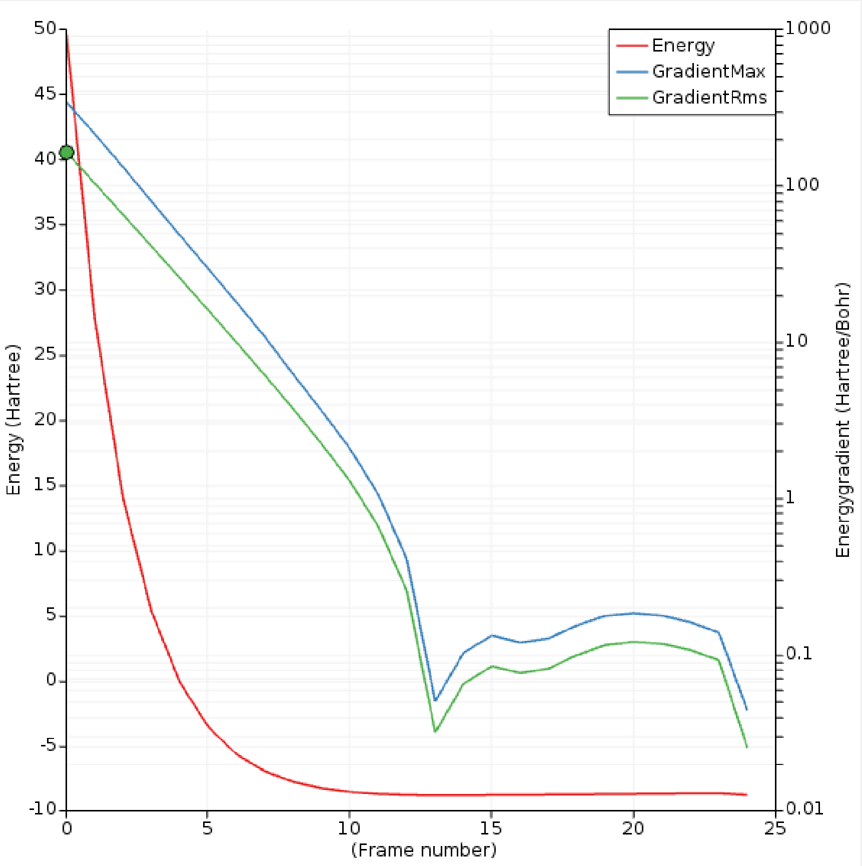
Energy
GradientMax
GradientRms
Energy (Hartree)
50
45
40
35
30
25
20
15
10
5
0
-5
-10
1000
100
10
1
0.1
0.01
Energygradient (Hartree/Bohr)
0
5
10
15
20
25
(Frame number)

h) O_2

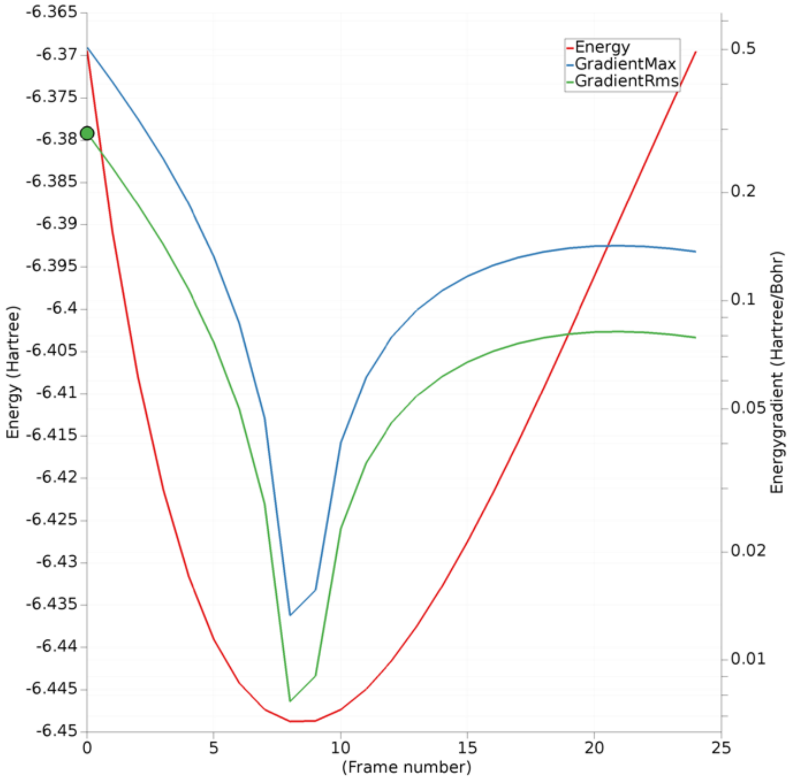

Figure 4.4 PES scans from the ADF engine.

Some runs with MgO and AlO were also attempted to try to include information for the metallic oxides as a simplified version of the HT. However, it was not possible to obtain a clear energy curve due to the periodicity of the structures found in the databases and the computational power available. In addition, there are no tested Slater-Koster parameters available for Al. Thus, it was not possible to represent the electronic part of the DFTB model or the repulsive energy contribution (dftb.org, 2021). In the case of Mg, the run using the self-consistent charge (SCC) system did not converge, which is why it was not included. The final values used for obtaining the PES scans are summarised in Table 4.7.

Table 4.7 Bond distances scanned for the PES.

Engine	*TS [Å]*		*VS [Å]*		*Engine*	*TS [Å]*		*VS [Å]*	
Molecule	**Min**	**Max**	**Min**	**Max**	*Molecule*	**Min**	**Max**	**Min**	**Max**
CO_2	0.9	1.6	1.1	1.6	NO	0.9	1.6	0.9	1.6
CO	0.9	1.6	0.9	1.6	NO_2	1.0	1.6	1.0	1.6
O_2	1.0	1.6	0.6	1.6	H_2	0.5	1.0	0.5	1.0
N_2	0.8	1.6	0.9	1.6	H_2O	0.7	1.6	0.9	1.6

4.3.3 Conformers

Conformers are other possible geometries representing the same molecule but with slight differences in bond distance, angle, or dihedral angle. In the case of the flue gases, only one geometry configuration was generated, meaning that the optimized geometry only had a global minimum. We attribute this to the fact that the molecules are diatomic or triatomic systems. Unfortunately, it was not possible to represent the polymorphism of the HT due to the computational power available. Only SC1 was employed for the TS and VS, optimised with a PBE or PBEsol functional respectively. Consequently, no conformers were used for the development of the new FF.

4.3.4 Transition States

The transition states MD snapshots for the flue gases were obtained from simulations using the ReaxFF engine and an existing FF developed by Zhang *et al.* (2014) for the simulation of the interaction between carbon dioxide with ionic liquid tetrabutyl-phosphonium glycinate through physical and chemical absorption. This FF is included in the software under the name CHONSSiNaP.ff. It belongs to the combustion branch, which means that the parameters included in the FF are potentially transferable to other systems with a similar chemical environment. As it can be deducted from the FF's name, it does not include the metallic elements present in the HT structure. Thus, this FF was only utilized to simulate the oxidation of the flue gases. The reactions simulated considered molecular oxygen and the remaining flue gases available in the system to generate CO_2, NO, NO_2 and H_2O. The reactions included in the TS and VS are the following:

$$O_2 + 2CO \rightarrow 2CO_2 \tag{4.2}$$

$$O_2 + N_2 \rightarrow 2NO \tag{4.3}$$

$$O_2 + 2NO \rightarrow 2NO_2 \tag{4.4}$$

$$O_2 + 2H_2 \rightarrow 2H_2O \tag{4.5}$$

The formation and breaking of bonds was analysed in the simulation box for each reaction containing single molecules. Only the relevant frames of the simulation were added to the TS for efficiency reasons. For example, Figure 4.5 shows some of the included frames in the TS that describe the formation of CO_2.

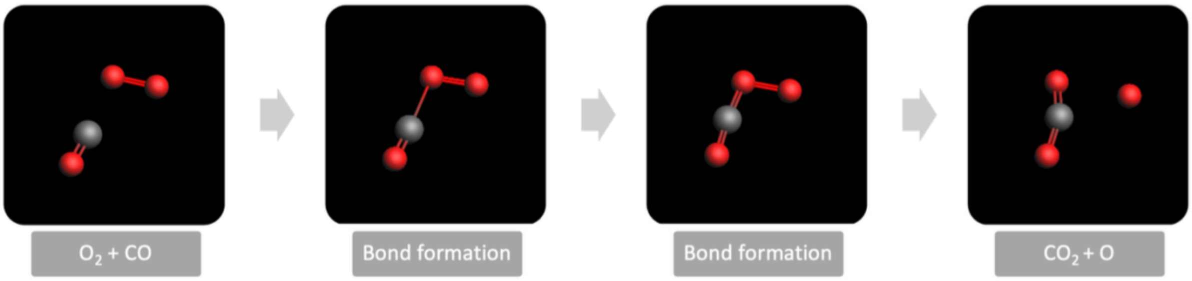

Figure 4.5 Transition state of the formation of CO_2.

The ReaxFF settings to carry out the MD simulations to generate the transition states are shown in Table 4.8. The selected frames, which showed the process of the reaction of interest, were then added to the TS to generate a single point calculation using the ADF engine. The settings employed GGA PBE, with the TZP as the basis set, with a large frozen core.

Table 4.8 ReaxFF settings for obtaining the transition states of the flue gases reactions.

ReaxFF Main Settings	
Task:	Molecular Dynamics
Periodicity:	Bulk
Force Field:	CHONSSiNaP.ff
Corrected torsions	Unselected
Number of iterations	40,000
Start with	0 non-reactive iterations
Time step	0.25
Method	NVT Berendsen
Temperature	298 K
Damping constant	100.0 fs

Once all the entries were ready, the ADFtrain tool in AMS 2019 was used to allocate them in the TS and the VS. As in the case of the tutorials available on the SCM website, the transition state snapshots were used only for the TS. On the other hand, the VS should include the geometries of the products of the reactions. However, in this work, the VS includes the optimized geometry of the HT. It was not possible to include the mixed metallic oxides' structure resulting from HT calcination in this work. Attempts of using MgO and Al_2O structures failed. Table 4.9 summarises the entries type used for the TS and VS.

Table 4.9 TS and VS entries used to develop the FF.

Set	*Engine*	*Task*	*Configuration*		*System*	
Training	DFTB	GO	*Model*:	DFT3	CO	CO_2
		PES	*Dispersion Correction*:	D3-BJ	O_2	N_2
			Parameter directory:	DFT.org/3ob-3-1	NO	NO_2
			Optimization method:	Quasi-Newton	H_2	H_2O
	BAND	GO	*XC functional*:	GGA-PBE		
			Basis Set:	TZP	HT	
			Geometry:	Periodic system		
	ReaxFF	MD	*Periodicity*:	Bulk	$O_2 + CO$	
			Force Field:	CHONSSiNaP.ff	$O_2 + N_2$	
			No. of iterations:	20,000	$O_2 + NO$	
			Time step:	0.25	$O_2 + H_2$	
			Method:	NVT Berendsen		
			Temperature:	298 K		
			Damping constant:	100.0 fs		
Validation	ADF	GO	*XC functional:*	GGA-PBEsol	CO	CO_2
		PES	*Basis Set*:	TZP	O_2	N_2
			Frozen core:	Small	NO	NO_2
					H_2	H_2O
	BAND	GO	*XC functional:*	GGA-PBE		
			Basis Set:	TZP	HT	
			Geometry:	Periodic system		

4.4 Weight assignment

The next step in the CMA-ES algorithm after completing the TS and VS is to assign a weight or "importance" to each entry for calculating the error function in equation (4.1). Weight assignment must consider how much the entry is expected to influence the outcome of the studied reactions and how many entries of the TS are representing it.

In this work, the bond distance between the atoms of the optimized geometry of the flue gases was assigned a weight of 0.2. The atomic bonds in the optimized geometry of the HT were assigned a value of 0.1, except for the metallic oxides and the bonds in the carbonates which also were assigned a weight of 0.2 since they were expected to take part in the calcination and chemisorption processes. The angles formed between three atoms were assigned a value of 0.5, the PES and TS were given 0.1.

The weight values were assigned to balance the number of entries with their frequency in the TS based on the values provided in the tutorials for AMS 2019. The values of the weights are summarized in Table 4.10.

Table 4.10 Assigned weights of the TS entries.

Block	*Type*	*System*	*Weight σ*
Geometry	Angle	Gas molecules	0.5
		HT	0.5
Geometry	Distance	Gas molecules	0.2
		HT (OH- bonds)	0.1
		HT (M-O, M-M, CO)	0.1
Energy	Bond scans	All PES	0.1
Energy	Other	All TSt	0.1

4.5 Running the optimiser

4.5.1 Initialisation mode

There are two modes to run the CMA-ES optimizer in AMS 2019. The first one is to initialize the optimizer from values of an existing FF as the initial “guess” of the new FF values expected to render an adequate representation of the studied system. The second one is to use random values as the initial “guess”. In this work, we employed both modes and compared the results.

- **FF initialisation:** The first approach we took was to create a tailored HT-FF by using the values of the parameters from other available FFs (Kamat *et al.*, 201*0; Liu et al*, 2011; Bai *et al.*, 2012; Newsome *et al.*, 2012; Pitman and Van Duin, 2012; Iype *et al*, 2013; Huygh *et al.*, 2014; Zhang *et al.*, 2014; Psofogiannakis *et al.*, 2015). Interestingly, we did not find any combustion-branch FF that included the required parameters for Al. Thus, the missing parameters were taken from FF from the water branch, from studies that involved $O_n - Al - OH -$ bonds derived from clay and zeolite structures (Pitman and Van Duin, 2012).
- **Random initialisation:** The CMA-ES algorithm is well suited to operate with a random initial guess. It automatically generates the random values used to do the optimisation.

4.5.2 Input files preparation

In addition to the initial values of the new FF, an important file to run the optimizer is the *params* file. It contains the list of parameters that will be reparametrized and the minimum and maximum possible values for each parameter to guide the algorithm. This range was based on the values of the FFs used to create the HT-FF. The parameters included for reparameterization were the missing bonds and angles in existing FFs required to run the simulations. They are listed in Table 4.11 and the limit values can be consulted in the Params file. Once the training set entries, the initialisation values, system geometry and the params files were ready, the CMA-ES algorithm was executed.

Table 4.11 Reparametrized bond and angle parameters.

Bonds		*Angles*		*H-bonds*
C-O	C-O off diag.	C-C-N	H-N-H	O-H-N
C-N	C-N off diag.	O-C-N	C-O-C	N-H-O
N-H	N-H off diag.	C-N-H	C-C-O	N-H-N
		H-C-O		

4.6 Cross-validation of the FF

The error function value was analysed to validate the new FFs produced by the CMA-ES algorithm. Lower errors imply that the difference between the values generated by the FF and the information in the TS is smaller, and thus, the FF better represents the system. The error function value was calculated for the CMA-ES generated FFs.

In addition to the value of the error objective function in (4.1), the root mean square deviation (RMSD) errors for the bonds, angles, and energies can be obtained from the different FF generated by the CMA-ES algorithm. This is useful to understand which entries of the FF render the highest error and modify either their weight or their values. The RMSD were only calculated for the bonds and angles since the energy entries were excluded in the final runs.

4.7 Results and discussion

4.7.1 Generation of the TS and VS

Optimised geometry

The optimized HT geometry for the TS was obtained from a GO job, which ran for over a month in a 24-core computer. The job stopped at the 36th iteration due to an error in which the engine was not able to produce the results necessary to continue. We attribute this to the lack of available memory space in the hard drive at that moment. It was advised by the SCM developers to use the last geometry available. Thus, the geometry implemented in the following steps was the one of the 35th iteration. Figure 4.6 shows the energy of formation of the system during geometry optimisation.

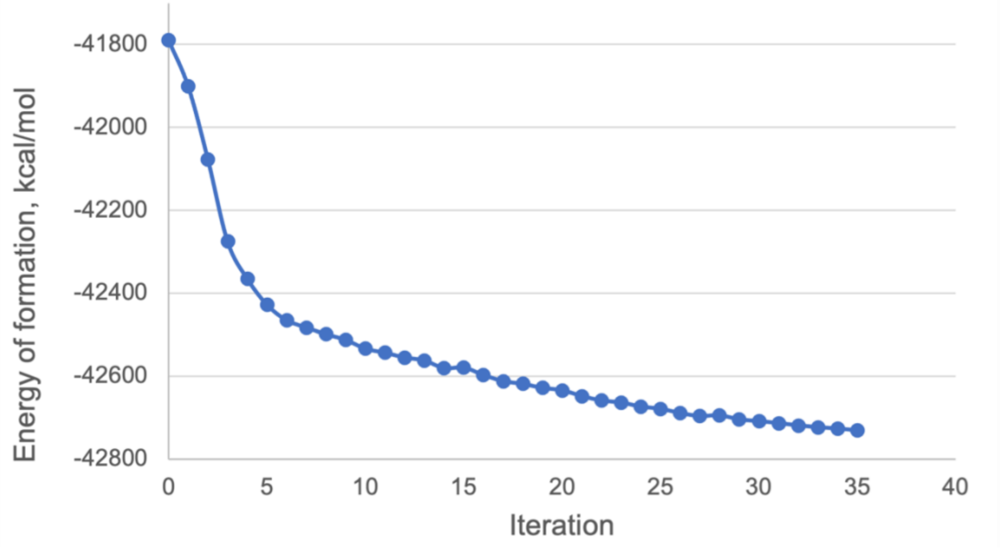

Figure 4.6 Energy of formation of SC1 during GO using PBE.

On the other hand, the PBEsol-optimised SC1 for the VS rendered a more stable geometry with lower total energy in contrast with the HT structure optimised with the PBE functional, as shown in Table 4.12.

Table 4.12 Energy of the optimized geometry of the HT SC1.

Set	*Functional*	*Energy [kcal/mol]*
Training	PBE	-42,721.300
Validation	PBEsol	-43,384.096

After the geometry optimisation of the flue gases molecules, the energy of the optimized geometries with DFTB was much lower than the ones optimized with ADF as shown in Table 4.13. However, since DFT is regarded as a more accurate approach, the ADF optimized geometries were used for the VS.

Table 4.13 Final energy of formation of the gas molecules.

	Total Energy [kcal/mol]			*Total Energy [kcal/mol]*	
Molecule	**DFTB**	**ADF**	*Molecule*	**DFTB**	**ADF**
CO_2	-5,436.57	-527.505	**O_2**	-4,124.84	-197.786
CO	-3,291.24	-340.233	**N_2**	-3,018.85	-382.679
H_2	-426.94	-155.622	**NO**	-3,507.18	-280.335
H_2O	-2,593.54	-326.166	**NO_2**	-5,558.03	-419.968

Potential Energy Surface scans (PES scans)

The resulting PES scans of the flue gases molecules for the TS are shown in Figure 4.7. Figure 4.8 presents the PES scans included in the VS. As in the case of the geometry optimization, DFTB results exhibited much lower energies than the ADF PESs. Interestingly, the H_2 PESs obtained in both engines were very similar. This can be a consequence of using the PBE functional. It provides accurate yet sometimes too small atomization energies due to the self-correlation energy of the one-electron in the hydrogen atom (Ernzerhof and Scuseria, 1999). The functional selection could affect the H_2 molecules PES scan, as well as the OH^- bonds in the HT structure.

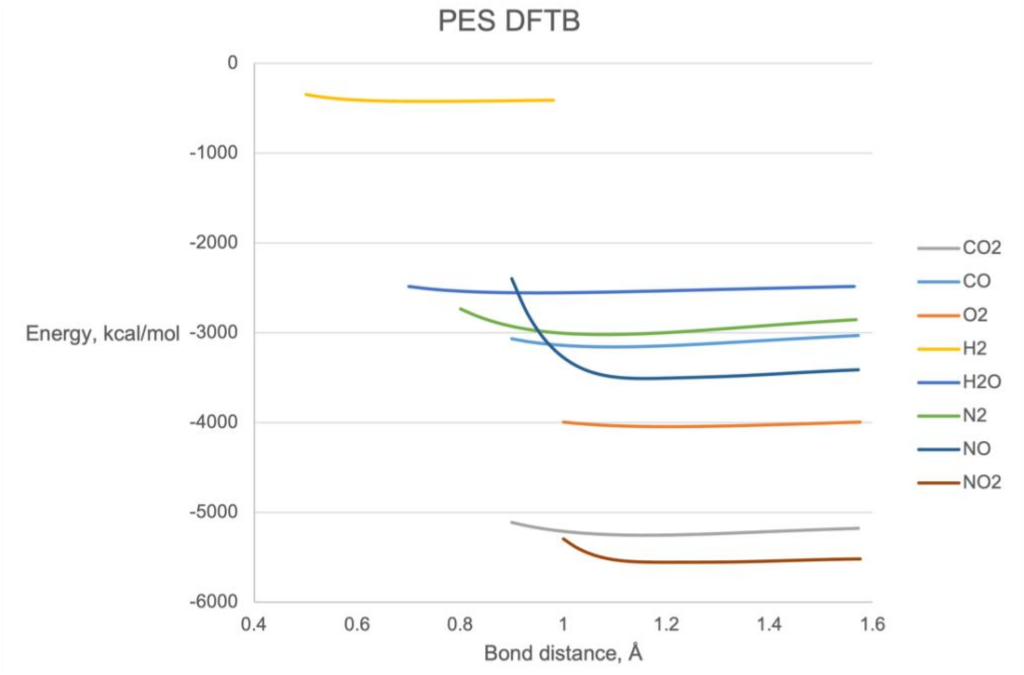

Figure 4.7 DFTB PES scans of the flue gases.

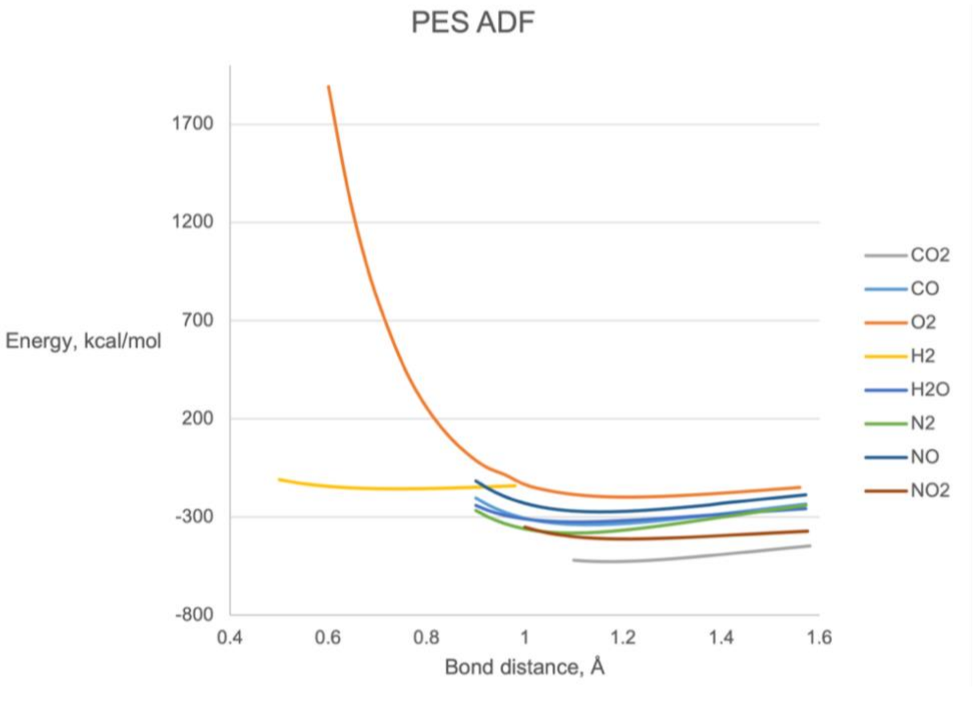

Figure 4.8 ADF PES scans of the flue gases.

Conformers

As mentioned in section 4.3.3 Conformers, no other conformers were included in the TS or VS. The algorithm implemented in AMS 2019 to produce conformers did not generate any, which we attribute to the simplicity of the flue gas molecules. In the case of the HT, it was not possible to create various differentiated SCs due to time and computational power constraints.

Transition States

The transition states were obtained from the MD simulations using a different FF and the same settings, save for the number of iterations. The reaction resulting in CO_2 was obtained in 20,000 iterations, whereas the rest required 40,000 iterations.

TS and VS

Once the TS was ready for running the CMA-ES optimiser it comprised 1,371 entries, most corresponding to geometry, i.e. bond distances and angles, entries due to the large HT structure as presented in Figure 4.9.

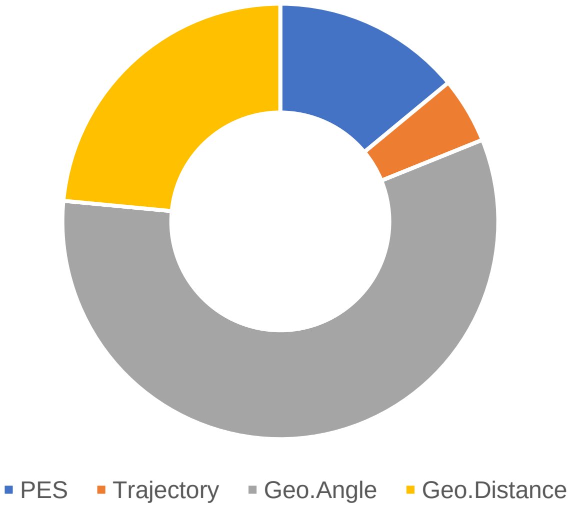

Figure 4.9 TS composition.

The created TS has several caveats. First, during the creation of the optimised geometries, SC1 was not completely optimised. Furthermore, only one configuration of the HT structure was included, making it difficult for the CMA-ES algorithm to allow for more variations to occur with the new values of the generated FF. These variations would play the roles of HT conformers. In addition, it was not possible to include information on the calcination product, the mixed metallic oxides observed experimentally, which should be included to better reflect the products of the expected reactions.

Regarding the optimized geometry for the VS, due to time constraints, the GO job for the HT was left to run only for one iteration considering that the energy difference between the two systems, PBE and PBEsol optimized was substantial. It must be pointed out that at the time of developing the FF we did not understand that the differences between functionals and theories would have a significant impact on the final FF result. Thus, the energy difference was due to the change of functional, more than an increase in the accuracy of the model. It is now clear to the author that mixing these different bases is fundamentally mistaken. We urge the readers to avoid mixing theories. In the case of this work, it would mean to carry out the GO of the HT and flue gases using DFT, for both the TS and the VS, varying the convergence criteria. The same applies to the PES scans and the transition states, which were the main source of the high RMSD for the energy entries. A possible alternative is to carry out MD simulations in the ADF engine with the molecules of the flue gases.

4.7.2 Weight assignment

Weight assignment considered the importance of the entries and the number of entries represented. It must be pointed out, however, that the σ values employed in this work gave preference to the geometry. This is reflective of the number of angles in the systems, the flue gas molecules and the HT. On the other hand, the σ of the PES and transition states was very small, which was advantageous since these entries generated larger errors in the cross-validation step as will be discussed in the next section.

4.7.3 Running the optimiser

After the TS and VS were ready, the CMA-ES algorithm implemented in AMS 2019 was executed. In preliminary runs, we encountered a bug in the code. This issue was corrected after several interactions with the SCM developers. The algorithm was run several times to iteratively improve the results with variations in the training set and initial FF values.

The CMA-ES corrected algorithm was set to produce five different FF in each run. It was initially believed that initialising the algorithm with the values from HT-FF would result in a better FF. This was assumed since the available FF have already been validated and have resulted in insightful simulations. However, when comparing the error function values of the FF generated with HT-FF and the ones that originated with the random initialisation, it was observed that a lower error function value was obtained for the latter. We attribute this to many factors; the values in the HT-FF could have a tighter restriction in agreement with other systems, which had a different energy base and a different chemical environment, and the available data provided by the TS.

4.7.4 Cross-validation of the FF

Initial results of the CMA-ES optimiser showed extremely high values for the error function. Figure 4.10 shows the lowest value of the function error obtained from each trial.

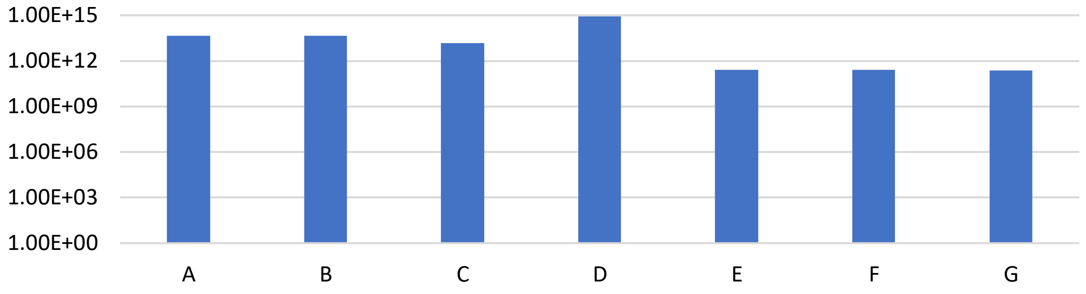

Figure 4.10 Error function values for initial CMA-ES runs.

Different corrections to the TS were applied to reduce them. By using the revised TS, in which the transition states were not included, a lower error function value was achieved in the CMA-ES-9 Run 5: 9.5538e09. Table 4.14 provides a summary of the issues encountered in the different runs and how they were solved.

Table 4.14 Issues summary of running the CMA-ES algorithm.

CMA-ES run	*Issue*
1	The FF file had values outside the range given in the params file. It was edited.
2	The geometry of the HT had atoms “too close”. The geometry was revised.
3	Error “Atoms were too close”. SCM developers found a bug. A patch for AMS 2019 was installed.
4	Some of the intervals in the params file were zero. The params were edited.
5	“Atoms too close”. Decided to use a random initial value.
5 random	“Atoms too close”. Thus, it was not due to the initial FF guess. SCM developers found a bug in the conversion of the coordinates of the periodic system of the HT. Another patch was installed for AMS 2019.
6	Replaced the coordinates in the geometry file in the input data. Same error function value was obtained.
7	The same error function value was obtained. We replaced the coordinates also in the validation set geometry file. The params file was edited again. PES entries weight was reduced to lower the energy error. There was also an error with the algorithm not generating numerical values .
8	Revised coordinates of the files. Same numerical values problem. The SCM developers found another bug. A new patch was installed for AMS 2019.
9	Atom index out of range. When the geometry file of the validation set it was observed that the gases coordinates were missing and included them.

To better understand the problematic entries, the RMSDs were calculated for the bond, angle, and energy entries. From the results obtained in the different runs, it was observed that the bugs in the algorithm had a significant effect on the geometry. The errors of “Atoms too close” was due to the wrong conversion of the periodicity of the system, and was reflected in a larger RMSD both in the bonds and angles as can be observed in the runs 2 to 8 in Figure 4.11 and Figure 4.12 respectively. The runs 1, 2, 5 and 9 error calculation did not generate the required data to do the graph due to the issues mentioned earlier. Once the geometry was corrected, both errors diminished. Nevertheless, it was seen that the RMSD of the energy entries was constant, shown in Figure 4.13, even when the weight was lowered.

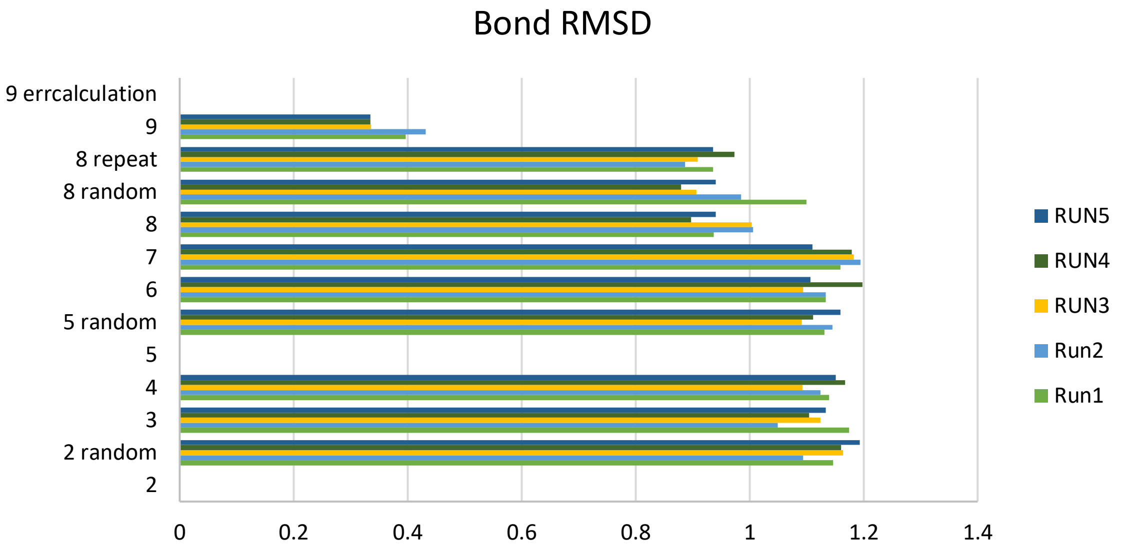

Figure 4.11 Bond RMSD of the CMA-ES FF optimisation.

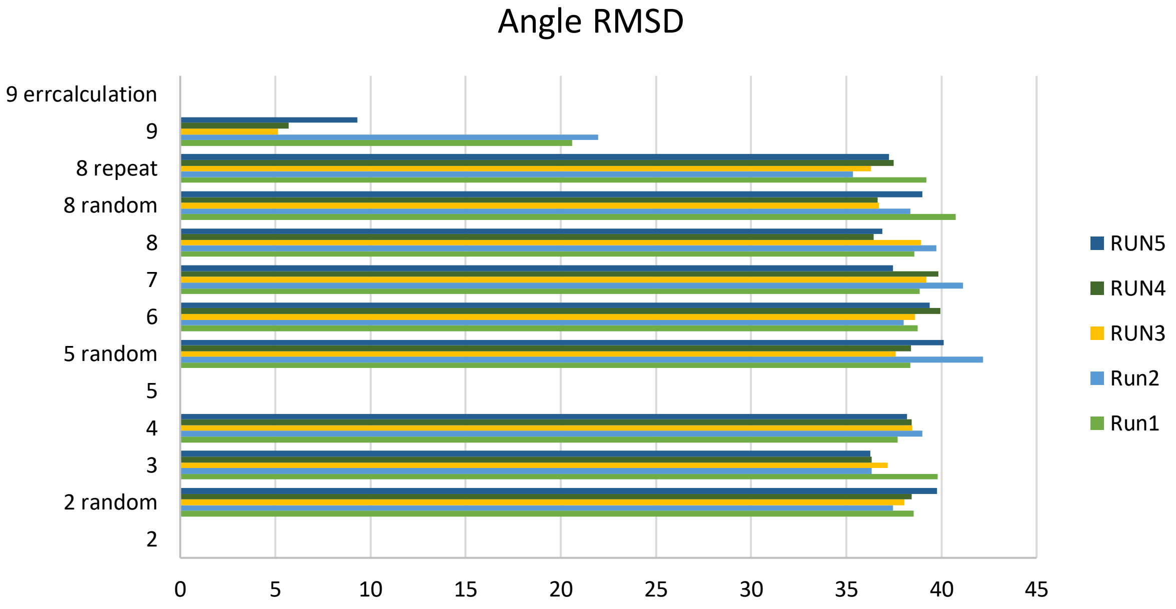

Figure 4.12 Angle RMSD of the CMA-ES FF optimisation.

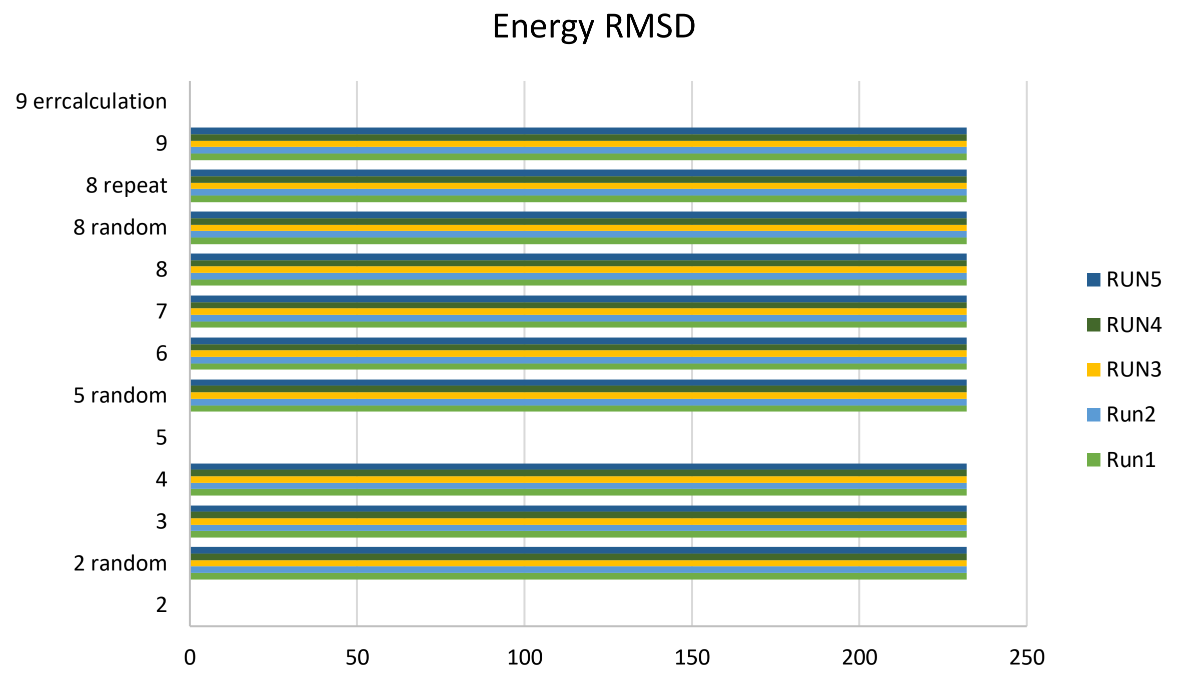

Figure 4.13 Energy RMSD of the CMA-ES FF optimisation.

A suggestion by the developers to further reduce the error function value was to completely erase the entries of energy (such as the PES and the transition states). With this modification, the error function value was reduced to 200.551. However, the resulting MD simulations with the generated FF exhibit a geometry too different from the expected. Thus, the FFs produced with this TS were not used for the simulations.

4.8 Summary

In this section, we described how the FF was developed using the CMA-ES algorithm. First, a TS and a VS were generated, comprising four types of entries: optimised geometries, PES scans, conformers, and transition states. Each entry was assigned a weight value to be used for calculating the error function. The best results after running the optimiser, i.e. with the lowest value of the error function value, were obtained when the algorithm was initialised with random values. The five FFs generated in the run with the best performance were selected to carry out MD simulation tests.

5. MD simulations – Calcination Studies

5.1 Overview

When HTs are used as an adsorbent for capturing CO_2, they must undergo a thermal activation treatment denominated calcination, which produces mixed metallic oxides with increased surface area and capture capacity (Miguel *et al.*, 2014). If the HT is not calcined, the CO_2 adsorption would be driven by the acid-base reaction with the $Mg-OH$, resulting in irreversibly chemisorbed $Mg(HCO_3)_2$ (Ram Reddy *et al.*, 2006).

To understand the influencing factors in the CO_2 adsorption on calcined HT, we required the calcined structure geometry. Ideally, this geometry would reflect the changes the adsorbent undergoes during calcination and thus, represent more adequately the adsorption process in the adsorption studies with GCMC simulations. Thus, we carried out calcination simulations on the generated HT structure.

In this chapter, we introduce the ReaxFF method used to help the reader understand the role of the FF and its importance. Next, we describe the process carried out for doing the calcination studies, including the refinement of the simulation settings, selection of the FF and the comparison of the surface area of the resulting calcined HT with experimental measurements.

5.2 Introduction to ReaxFF

The ReaxFF method was developed to make MD simulations more practical, especially when using large-scale reactive chemical systems of hydrocarbon components (Van Duin *et al.*, 2001). ReaxFF can emulate chemical reactions and the non-bonded long-range interaction between atoms (Iype *et al.*, 2013), important features for simulating chemisorption and physisorption of CO_2 in HT.

ReaxFF uses the interatomic potential of the molecules to describe the reactive events in a system during a simulation. The method takes advantage of a bond order formalism, in which the electronic interactions of the chemical bonding are implicit (Senftle *et al.*, 2016). The bond order is calculated in each step, based on the interatomic distances of the particles in the system (Zhang *et al*, 2014). By using the relationship between the bond distance and bond order; and the bond order and bond energy, the program is able to adequately predict the disassociation of the bonds (Van Duin *et al.*, 2001). In consequence, the program does not need previously reaction site or connectivity information (Zhang *et al*, 2014).

ReaxFF can also account for non-bonded interactions. Van der Waals and Coulomb interactions are described by calculating the pair-interaction of all the atoms in the system, even if they are not directly connected (Zhang *et al*, 2014). To elude the creation of overly close-range non-bonded interactions, ReaxFF utilizes a shielding term (Zhang *et al*, 2014). The total energy of the system (E_{system}) is calculated in the ReaxFF engine of AMS 2019 with the following expression (van Duin *et al.*, 2019):

$$\begin{split} E_{system} = E_{bond} + E_{lp} + E_{over} + E_{under} + E_{val} + E_{pen} + E_{coa} + E_{C2} + E_{tors} \\ + E_{conj} + E_{H-bond} + E_{vdWaals} + E_{Fe-dim} + E_{Coulomb} \end{split} \tag{5.1}$$

Where

$\boldsymbol{E_{bond}}$	is the bond energy.
$\boldsymbol{E_{lp}}$	represents the energy derived from the presence of a lone electron pair.
$\boldsymbol{E_{over}}$	refers to the energies that arise from the over-coordination of the atoms with respect to their valence.
$\boldsymbol{E_{under}}$	denotes to the energies that result from the under-coordination of the atoms with respect to their valence.
$\boldsymbol{E_{val}}$	signifies the valence angle energy contribution.
$\boldsymbol{E_{pen}}$	represents the penalty energy imposed for systems with two double bonds sharing an atom in a valency angle.
$\boldsymbol{E_{coa}}$	is the 3-body conjugation term (e.g. NO_2^-).
$\boldsymbol{E_{C2}}$	is a term for correcting the behaviour of the bond formed between the C in a $-C_2-$ molecule (i.e. as a double bond, instead of a triple one).
$\boldsymbol{E_{tors}}$	is the term that ensures that the dependence of the energy of torsion angle is considered.
$\boldsymbol{E_{conj}}$	describes the contribution of the conjugation effects (e.g. in benzene and other aromatics).
$\boldsymbol{E_{H-bond}}$	depicts the H bond interactions.
$\boldsymbol{E_{vdWaals}}$	accounts for the van der Waals interactions.
$\boldsymbol{E_{Coulomb}}$	represents the Coulomb energy.

It must be noted that the calculation of these energy terms has as basis the bond order and bond distances between the atoms of the system. Thus, having an accurate geometry to start the simulations and an FF capable of adequately predicting these distances is crucial for having useful results and insights.

5.3 Methodology

The calcination studies comprised four steps as seen in Figure 5.1. First, we refined the simulation settings by doing short calcination simulations using FF1, which we will discuss in section 5.3.1 Settings refinement. In this thesis, we report the simulation with the optimised settings. Next, we carried out preliminary calcination simulations to test the produced FF with CMA-ES and selected the one with the best performance based on the value of the error function 4.1. We then carried out a long calcination simulation using the chosen FF and the refined settings. Finally, we calculated the surface area of the calcined structure to compare it with experimental measurements calcinating HT at similar conditions (Hutson *et al*, 2004; Winter *et al.*, 2005; Ram Reddy *et al.*, 2006; Wang, *et al.*, 2011; Bhatta *et al.*, 2015).

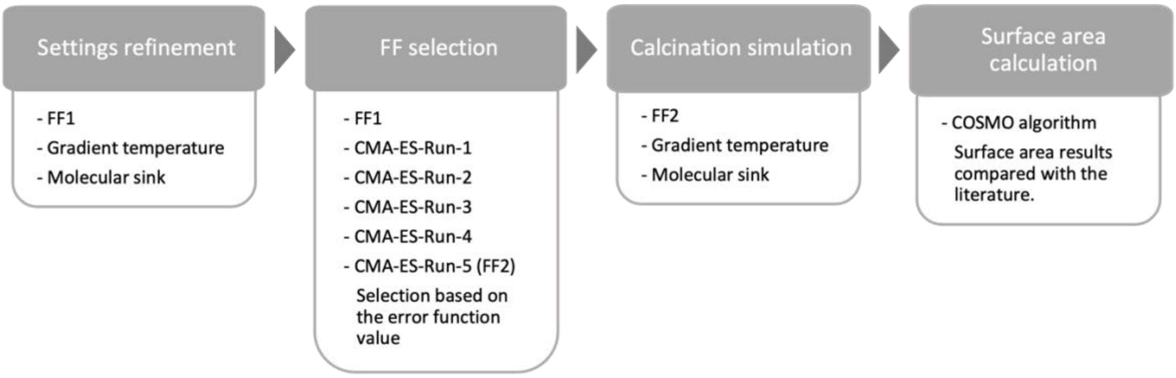

Figure 5.1 Methodology for the calcination studies.

5.3.1 Settings refinement

To make the calcination simulations as realistic as possible, we aimed at using the pressure and temperature conditions of calcination experiments. Literature shows that the optimum temperature for the calcination of the selected $Mg-Al-CO_3$ HT is 400°C in atmospheric pressure (Ram Reddy *et al.*, 2006; Bhatta *et al.*, 2015). Initial simulations using only these parameters as a reference showed that further refinements were needed to improve the representation of the calcination process. First, a gradient temperature better reflected the process as the material starts at room temperature and requires time to heat up. Second, a molecular sink was needed to allow the produced gas molecules to “escape” the simulation box as would happen in experimental settings for water evaporation.

The refined settings are shown for a short simulation of 100 000 steps. The temperature gradient was set from room temperature, 25 ºC (298.15 K), to the optimum calcination temperature of 400 ºC (673.15 K). A molecular sink for H_2O and CO_2 was included every 200 iterations. We used SC1 for the simulations to economise time and computational power.

We employed an FF developed by Dr Mathew Aneke from our research group, which we will refer to as FF1. This FF is based on the work of (Psofogiannakis *et al.*, 2015), modifying their FF to include the missing parameters required to simulate an HT system. The Mg and Al atoms in FF1 are described using the same values and do not faithfully represent the HT structure which is why we developed a new FF. The FF file can be found in the project's repository and the 9. Appendix. The MD settings used for the settings-refinement calcination simulation are shown in Table 5.1.

Table 5.1 MD refined settings for the calcination studies.

ReaxAMS Main Settings*		*Model MD*		*Thermostat*		*Molecule sink*	
Task:	Molecular Dynamics	*Number of steps*	100,000	*Thermostat:*	NHC for all	*Formula:*	$H_2O \mid CO_2$
Followed by:	Nothing	*Time step:*	0.1 fs	*Damping constant:*	100 fs	*Frequency:*	200 | 200
Periodicity:	Bulk	*Sample frequency:*	100	*NHC chain length:*	10	*Start step:*	0
Force Field:	FF1	*Initial velocities:*	Random	*For N steps:*	20,000	*Stop Step:*	-
Torsions:	Original	*Initial temperature*	298.15 K	*Temperature:*	298.15 – 673.15 K		
Non-reactive:	Unselected	*Preserve*	Total and Angular momentum	*Until end:*	673		

*The ReaxFF engine was updated in AMS 2019 and renamed ReaxAMS.

5.3.2 FF selection

To test which FF had the best performance, we carried out preliminary MD simulations using the SC2 structure. We used FF1 and the five FFs generated by the trial CMA-ES-Run-9. The simulations had a fixed number of particles (N) and pressure (P). The temperature of the system (T) was set to 400ºC (673.15 K) with a Berendsen thermostat and damping constant of 100 fs. A molecular sink for H_2O and CO_2 was set every 200 iterations and another one for CO every 400 iterations. The simulation ran 1 million iterations equivalent to 0.1 ns to observe if the structures held after a longer period thanks to the used FF. Table 5.2 shows the settings used for the simulations used to select a FF.

Table 5.2 MD settings for selecting the FF.

ReaxAMS Main Settings*		*Model MD*		*Thermostat*		*Molecule sink*	
Task:	Molecular Dynamics	*Number of steps*	100,000	*Thermostat:*	NHC for all	*Formula:*	$H_2O \mid CO_2 \mid CO$
Followed by:	Nothing	*Time step:*	0.1 fs	*Damping constant:*	100 fs	*Frequency:*	200 | 200 | 400
Periodicity:	Bulk	*Sample frequency:*	100	*NHC chain length:*	10	*Start step:*	0
Force Field:	FF1 CMA-ES-Run-1 CMA-ES-Run-2 CMA-ES-Run-3 CMA-ES-Run-4 CMA-ES-Run-5	*Initial velocities:*	Random	*For N steps:*	20,000	*Stop Step:*	-
Torsions:	Original	*Initial temperature*	298.15 K	*Temperature:*	298.15 – 673.15 K		
Non-reactive:	Unselected	*Preserve*	Total and Angular momentum	*Until end:*	673		

5.3.3 Calcination simulation

After refining the simulation settings and selecting the FF produced by CMA-9-RUN5, which we will refer to as FF2, we set the main calcination simulation with SC2. It represents 1.2 ns with a time step of 0.1 fs. Other studies have used 2 ns simulations for HT calcination (Gao *et al.*, 2018). The length of the simulation allowed for 0.2 ns for initial geometry relaxation, similar to Khalkhali *et al.* (2020).

We used a Nosé-Hoover thermostat with a damping constant of 100 fs and a chain length of 10. The temperature was increased during the following 0.4 ns from 26.85 ºC (300 K), close to room temperature until 400 ºC (673.15 K) which is considered as optimum calcination temperature at a rate of 1000 K/ns. A cautionary note, this heating rate is not possible in experimental settings. Thus, results must not be compared “second by second”, but for analysing trends. The temperature remained constant for 0.2 ns. The temperature was then decreased for the next 0.3 ns until it reached ambient temperature again and remained there for the rest of the simulation. These last 0.5 ns of the simulation represent the cool-down process of experimental calcination. Figure 5.2 shows the temperature settings as a function of time.

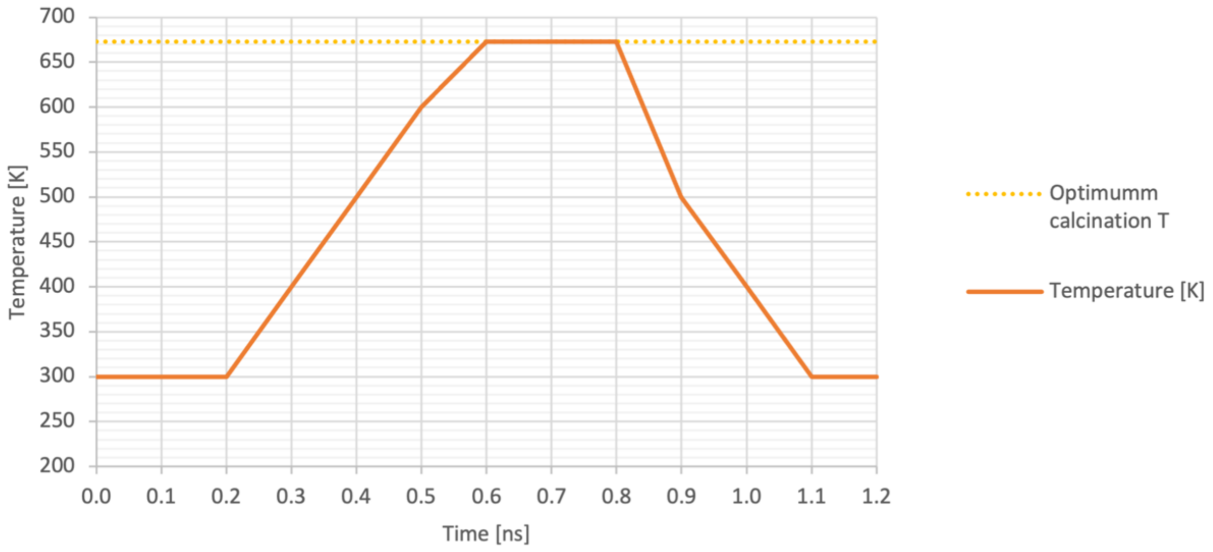

Figure 5.2 Temperature gradient settings for the calcination study.

The barostat used was Berendsen which is recommended for systems far from equilibrium (SCM, 2018a). The molecular sink was set to allow the H_2O and CO_2 molecules to escape the simulation box. The complete simulation settings are presented in Table 5.3 and

Table 5.4

Table 5.3 MD settings for the calcination studies.

ReaxAMS Main Settings		*Model MD*		*Barostat*		*Molecular sink*	
Task:	Molecular Dynamics	*Number of steps:*	12,000,000	*Barostat:*	Berendsen	*Formula:*	$H_2O \mid CO_2$
Followed by:	Nothing	*Time step:*	0.1 fs	*Damping constant:*	300 fs	*Frequency:*	200,000
Periodicity:	Bulk	*Sample frequency:*	10,000	*Scale:*	XYZ	*Start step:*	0
Force Field:	FF2	*Initial velocities:*	Random	*Equal:*	None	*Stop Step:*	-
Torsions:	Original	*Initial temperature:*	300 K	*Pressure:*	101325.0 Pa		
Non-reactive:	Unselected	*Preserve*	Total and Angular momentum				

Table 5.4 Thermostat settings for the calcination simulation.

Thermostat		*Gradient*	
Thermostat:	NHC for all	*For N steps:*	*Temperature:*
		2 000 000	300 – 300
		1 000 000	300 – 400
		1 000 000	400 – 500
		1 000 000	500 – 600
Damping constant:	100 fs	*1 000 000*	600 – 673.15
		2 000 000	673.15 – 673.15
		1 000 000	673.15 – 500
		1 000 000	500 – 400
		1 000 000	400 – 300
NHC chain length:	10	*Until end:*	300

5.3.4 Surface area calculation

To validate the obtained calcined structure, we calculated its surface area at different moments of the calcination process and compared the results with the values reported in the literature. In experimental studies, the surface area of the HT, either fresh or calcined, is usually calculated with the BET method. In this procedure, the volume of nitrogen gas adsorbed on the surface of particles is measured at -196°C, the boiling point of N_2. The reason for this is that at this temperature, N_2 is below the critical temperature and so, it condenses on the surface of the particles. N_2 is presumably inert, and thus, only the kinetic diameter matters when measuring the surface area. In the case of our focus of interest, its kinetic diameter is very close to that of the CO_2 molecule, with 364 pm for N_2 and 330 pm for CO_2 (Ismail *et al.*, 2015). In a BET measurement, it is assumed that the adsorption is done in a monolayer. Thus, using the size of the gas molecule, the amount of adsorbed gas is correlated to the total surface area of the particles, including pores at the surface. The caveat of this approach to measure the surface area is that inaccessible pores are not detected and that other types of adsorption (non-monolayer) are neglected (Rouquerol *et al*, 1998).

The surface area of the simulated calcined HT structure was calculated with the Conductor-like Screening Model for Realistic Solvents (COSMO) algorithm (Klamt and Schüürmann, 1993), available in the BAND engine of AMS 2019. Although the primary use of the COSMO algorithm to predict the chemical potentials of liquids, during its first step, it carries out the construction and segmentation of the suitable solvent-accessible surface (SAS). Calculating the SAS allows computing the surface area of a molecular structure using a desired probe molecule. In this work, nitrogen was set as the probe molecule to resemble the BET method for experimentally measuring the surface area (Silva *et al.*, 2017). The settings for running the COSMO tool are displayed in Table 5.5. The area was then divided by the adsorbent mass to obtain the results in m^2/g , the units used to report experimental data.

Table 5.5 Settings for calculating the surface area.

BAND Main Settings		*Model Solvation (COSMO)*	
Task:	Single Point	*Include COSMO solvation:*	Yes
Followed by:	Nothing	*Solvent:*	Nitrogen
Periodicity:	Slab	*Surface type:*	Asurf
Unrestricted:	-unselected-	*Change determination method:*	CONJ
XC functional:	GGA:PBEsol	*Correct for outlying charge:*	Yes
Relativity:	None	*Calculate Coulomb interaction:*	EXACT
Basis set:	SZ	*Handle charges:*	VAR
Frozen core:	Large	*N Star:*	4
Numerical quality:	Basic	*Only above slab:*	Yes
Calculate:	Band structure		

5.4 Results and discussion

5.4.1 Settings refinement

The simulation carried out to refine the settings for the calcination exhibited similar behaviour as the reported in the literature. Previous experimental studies describing the changes the HT undergoes during calcination mention three main stages.

First, the dehydration of the interlayer water and loss of hydroxyls of the cationic layer occurs after 120-210°C, with a later decarboxylation above 200-300°C which causes the layered structure to collapse (Hutson *et al.*, 2004; Winter *et al.*, 2005; Ram Reddy *et al.*, 2006; Wang, *et al.*, 2011; Bhatta *et al.*, 2015). The described stages can be observed in Figure 5.3.

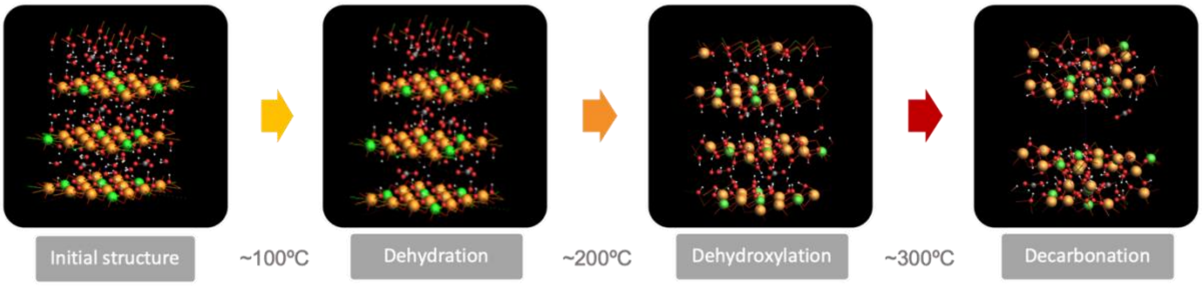

Figure 5.3 Stages of HT calcination. Mg^{2+} in green, Al^{3+} in orange, O in red, C in grey and H in white.

Preliminary calcination simulations of SC1 with FF1 allowed us to observe an increase in the lattice in the c axis, as in the case of hydrating clays, which we attribute to the presence of the trapped gases molecules in the interlayer. However, the simulation did not represent experimental settings for calcination as water molecules were not able to leave the simulation box. Consequently, for posterior simulations, we decided to include the molecular sink. It can be mentioned that this deformation of the lattice has been observed in other studies, where the c axis also showed a decompression in contrast with experimental values, leading to a slight overestimation of the distance between the two planes where intra-layer oxygens are situated and an underestimation of the a axis too (Trave *et al.*, 2002).

Figure 5.4 shows the “evaporation” of the H_2O molecules and the decomposition of the carbonates into CO_2 and CO in a preliminary simulation. The reduction in the number of OH^- correlates to small increases in the number of H_2O molecules during the calcination. As expected, water molecules were formed after dehydroxylation of the structure.

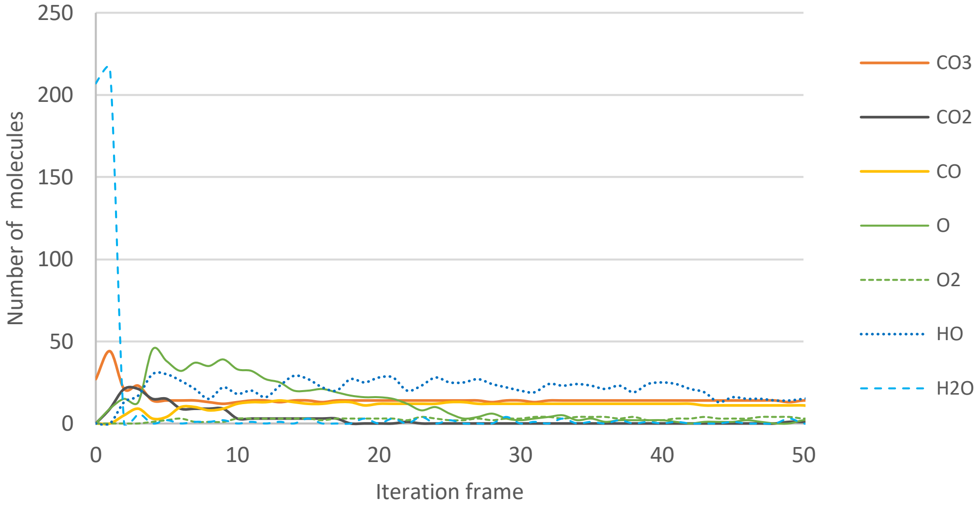

Figure 5.4 Molecules generated during the calcination simulation of SC1 with FF1.

The results suggest that the presence of H_2O molecules is necessary to transform the interlayer carbonates into CO_2. Zhang et al (2016) reached similar conclusions. In their work when simulating HT calcination at 330°C, their results showed that the decomposition of the carbonates into CO_2 and residual O_2 occurs via a monodentate intermediate, i.e., attached to the cationic layer only by one oxygen. Monodentate intermediates were thermodynamically favoured over bidentate intermediates, in which the two oxygen atoms are attached (Zhang *et al.*, 2016). When a monodentate attaches to the cationic layer, a OH^- of the layer consequently separates itself and can form a water molecule. This would explain why the CO_2 detaches from the structure only after evaporation of water.

Another insight from the refinement of the simulation settings was the need for a period of geometry relaxation at the selected temperatures. The settings for this short simulation did not consider room temperature conditions, and thus, in the main simulation, we decided to implement it.

5.4.2 FF Selection

We employed FF1 as the baseline to compare the performance of the other FFs. It must be mentioned that not all the FFs from CMA-ES-9 could carry out the simulations, only the ones from runs 1, 4 and 5. Thus, the next results correspond to the working simulations.

FF1

Using FF1 resulted in a structure collapse as predicted, after the loss of water and carbonates in the interlayer. However, not all the hydroxyls were lost as expected. The final structure can is presented in Figure 5.5.

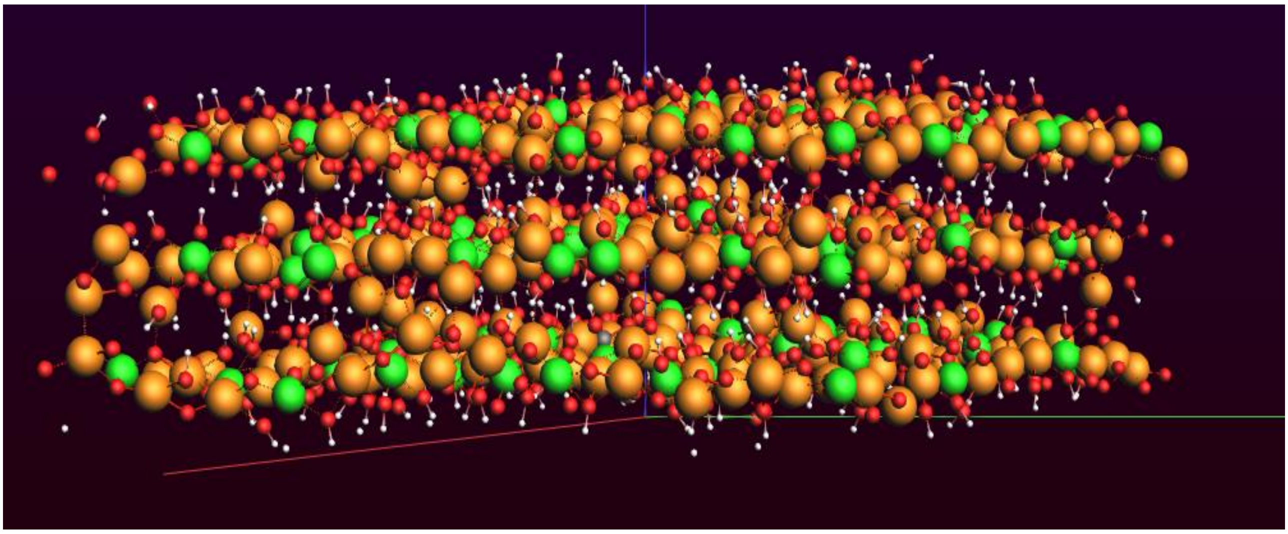

Figure 5.5 Calcined HT structure using FF1. Mg^{2+} in green, Al^{3+} in orange, O in red, C in grey and H in white.

CMA-ES-9 Run 1

In this case, the disappearance of the interlayer anions also triggered the layered structure collapse. It was observed that the frequency of the water molecules sink affects the oxidation of the carbonates. If the water molecules are quickly "evaporated", the CO_3^- do not transform into CO_2 as readily. It can be observed in Figure 5.6 that the collapsed cationic layers agglomerate in a random position, which creates "tunnels" due to the periodicity of the structure when the SC2 is repeated.

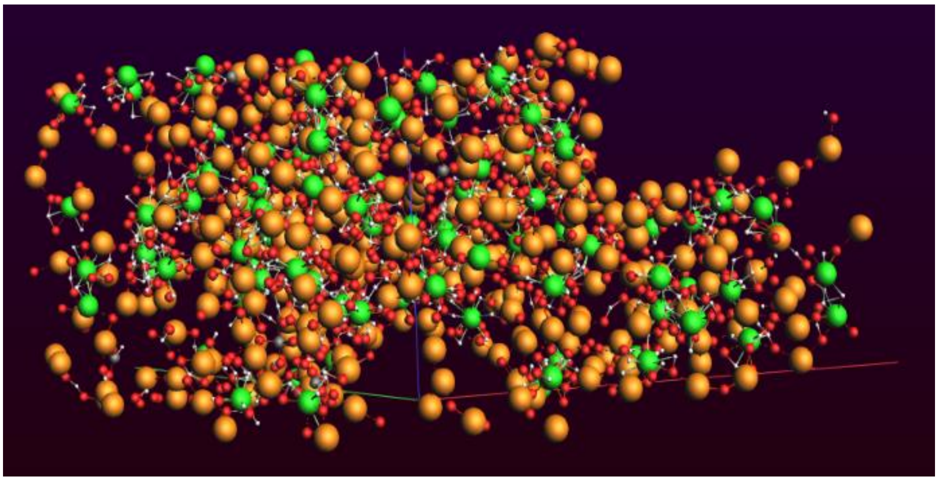

Figure 5.6 Calcined HT structure using the FF from CMA-9 Run 1.
Mg^{2+} in green, Al^{3+} in orange, O in red, C in grey and H in white.

CMA-ES-9 Run 4

During this simulations, the carbonates had similar behaviour to CMA-9 Run 1. The agglomeration of the metallic oxides at the top and bottom of the simulation box created layers, shown in Figure 5.7, which is unrealistic in contrast with the bulk metallic oxides resulting from calcination in experiments.

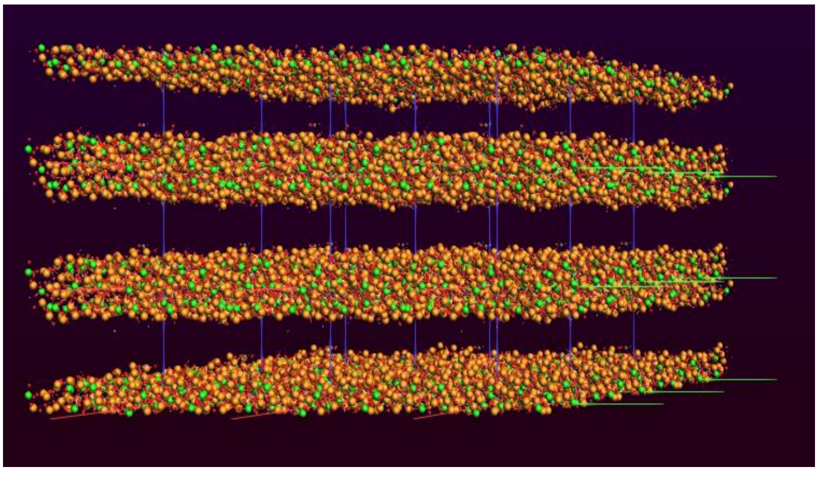

Figure 5.7 Calcined HT structure using the FF from CMA-9 Run 4.
Mg^{2+} in green, Al^{3+} in orange, O in red, C in grey and H in white.

CMA-ES-9 Run 5 (FF2)

The carbonates presented a similar behaviour as in previous runs. However, the metallic oxides generated with this FF have a better distribution over the simulation box and better correspond to the descriptions mentioned in the literature. Thus, this was the FF selected to carry out the long calcination study and the adsorption studies.

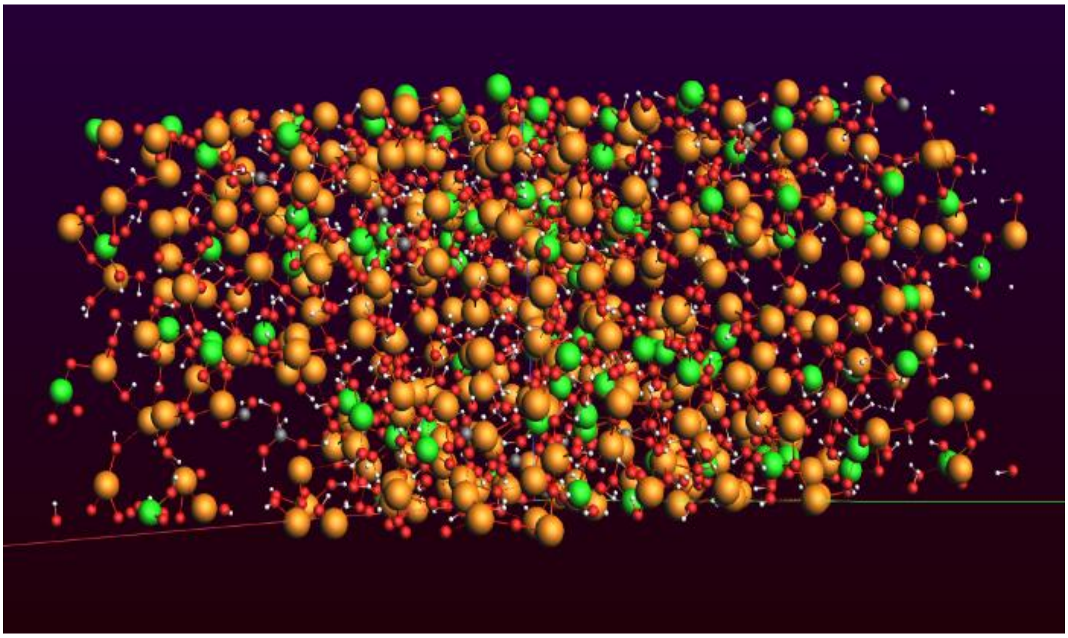

Figure 5.8 Calcined HT structure using the FF from FF2.
Mg^{2+} in green, Al^{3+} in orange, O in red, C in grey and H in white.

The calcined structure closest to the expected one was obtained with the FF from CMA-ES-9 Run 5, Figure 5.8. We attribute this to the fact that the CMA-ES-9 trial had the lowest error function value and the most complete TS among the different attempts. Thus, this FF was used for the following simulations. It can be mentioned that further FFs generated using CMA-ES and a TS in which the energy entries were eliminated resulted in unrealistic structures.

5.4.3 Calcination simulation

The decomposition of the HT followed the behaviour reported in the literature: dehydration, dihydroxylation and decarbonation (Wang *et al.*, 2011) as explained in 2.3.1 Calcination. The most important changes to the structure occurred at the beginning of the simulation. The transformation of the layered HT structure into a network of mixed metallic oxides can be observed in Figure 5.9.

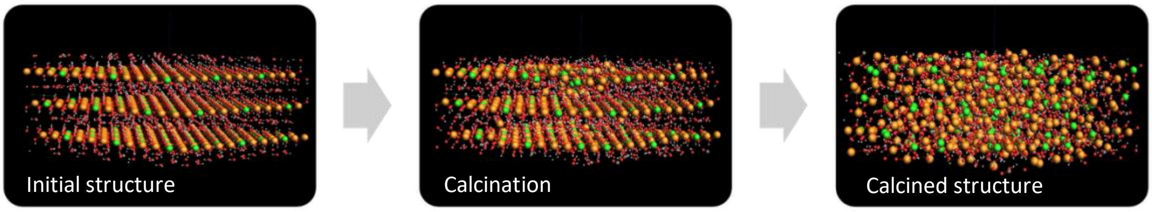

Figure 5.9 Structure of the HT during the calcination simulation. Mg^{2+} in green, Al^{3+} in orange, O in red, C in grey and H in white.

Figure 5.10 shows the reduction of the number of water molecules, reflecting the dehydration as part of the molecular sink. The number of hydroxyls and carbonates fluctuated and reduced as expected due to the formation of water and carbon dioxide. Interestingly, the generation of H_2O molecules is not directly related to the number of carbonates that remain on the surface. The carbonates transform or graft during the initial 0.025 ns of the simulation.

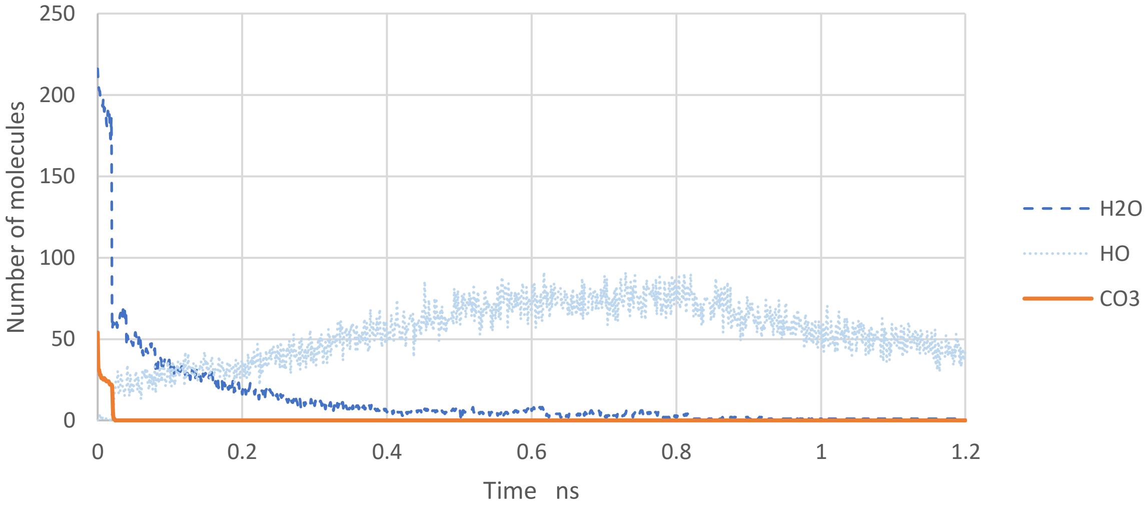

Figure 5.10 Molecules generated during the calcination of SC2 with FF2.

Another cautionary note must be considered regarding the molecular sink. This function requires the user to select which molecules will be deleted and how frequently. The removed molecules were selected because of comparing the simulation with experimental conditions. However, the frequency at which they are removed was set to allow the water molecules enough time in the simulation to react with the carbonates, but not too long to hydrate the structure and generate swelling. The frequency was qualitatively adjusted according to the results of previous simulations and the water molecule behaviour and could play a more important role. In further studies, it is advised to examine its effect on the final calcinated structure. The settings for representing the experimental conditions could also be revised. The thermostat selection can affect the accuracy of the thermodynamic average of the ensemble.

For example, the velocity-rescaling method has been criticised as inadequate for maintaining the system in a true constant-temperature statistical ensemble (Kim *et al.*, 2007) and the Noosé-Hover (NH) algorithm can be inefficient at high temperatures (e.g. 400ºC). Both give the same total energy, but NH has larger temperature fluctuations (Kim *et al.*, 2007). Additionally, we recommend using more time for geometry relaxation at all stages. Our relaxation time was based on the simulations of Khalkhali *et al.*, (2020), however, it has been pointed out to us that 0.1 ns is not enough to allow the structure to settle. This could explain why the layered structure collapsed in the first relaxation iterations at room temperature, showing unnecessary bonds between H and cationic atoms in some cases. When revising the generated molecules, CHO formation was found in the first 200 iteration frames, which could be attributed to the nature of the ReaxFF method, originally developed to represent hydrocarbons.

5.4.4 Surface area

When calculating the surface area of the calcinated structure at different points of the simulation an increase was observed, as reported in the literature. Preliminary calculations using SC1 and FF1 during 100,000 iterations, showed an increase in the surface area from187.40 m^2/g to 269.24 m^2/g. The 1.2 ns long simulation of SC2 with FF2 exhibited an initial surface area of 198.88 m^2/g, a maximum of 270.68 m^2/g at the optimum calcination temperature, and 247.63 m^2/g as the final surface area after cooling down. The described behaviour can be observed in Figure 5.11, which also provides information regarding the maximum and minimum surface area reported in the literature for $Mg - Al - CO_3$ HT, from 54.6 m^2/g to 257.8 m^2/g (Hanif *et al.*, 2014; Bhatta *et al.*, 2015).

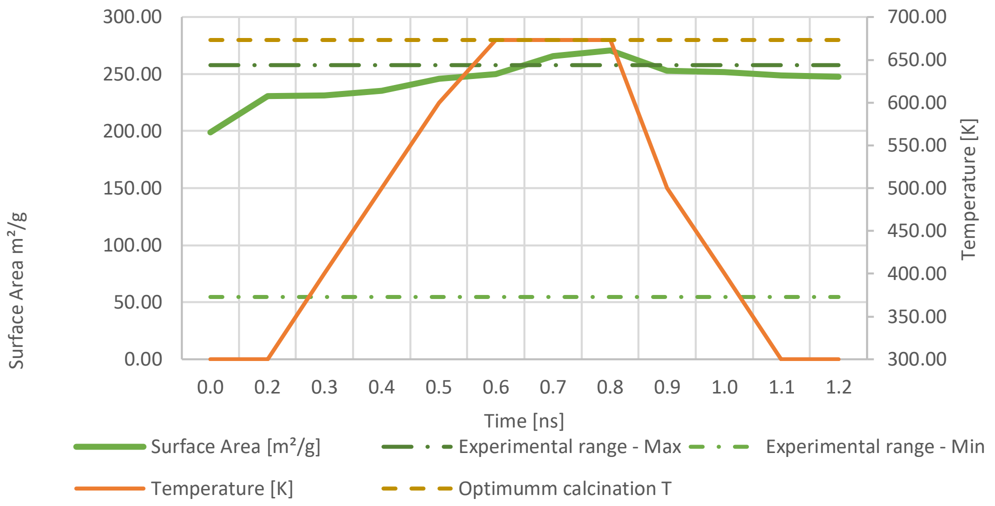

Figure 5.11 Surface area correlation to calcination temperature

The simulation shows a constant increase in the surface area with the increase in the calcination temperature. Interestingly, when the optimum calcination temperature was sustained, the surface area still increased. This suggests that the simulation time was insufficient to settle the atoms in their optimum position. For future work, it is advised to carry out longer simulations. The surface area obtained after the temperature reduction is in the range of experimental values, being closer to the upper boundary. The adsorption capacity related to the resulting surface area is around 0.36 $molCO_2/kgHT$ to 0.92 $molCO_2/kgHT$ (Hanif *et al.*, 2014), depending on the HT synthesis, composition and calcination temperature.

The surface area obtained for the short simulation was slightly lower than the one for the calcinated structure of SC2 with FF2, which could be the result of FF1 and FF2 having very similar values. This was an encouraging sign since the parameters for FF1 were obtained from a validated FF (Psofogiannakis *et al.*, 2015). The surface area of SC2 during calcination showed the expected trend. Nevertheless, it is not clear if the final surface area, which is lower in contrast with the observed at optimum calcination temperature, is due to the reduction in the temperature or because of the simulation time. It must be noted that the simulated structure of HT is a very small cell, and thus, it is not able to reflect all the possible paths for the collapse of the layered structure nor the pore distribution. This can be a source of inaccuracy as in the case of the work of Zhang et al (2016) in which the comparison of the simulated structure with experimental values disagreed more as the temperature increased (Zhang *et al.*, 2016).

5.5 Summary

In this section we discussed the results of the first MD simulations using the ReaxFF method to analyse the HT structural transformation during calcination. The results show the same structural changes reported by experiments; dehydration, dehydroxylation and carbonation. The development of different simulations with modified settings enabled us to better understand the parameters affecting the results, such as the FF, thermostat, type of ensemble and duration of each stage of the simulation. Our results suggest that the presence of the H_2O molecules enable the transformation of the carbonates into CO_2, avoiding the attachment of the C atoms onto the metallic oxides. Further analysis of the structure in future work could provide information regarding the attachment mechanism of the C atoms reported by other authors. The calculated surface area of the calcined structure is in the upper limit of the surface areas reported by experimental studies, suggesting that the simulation closely represents the calcined structure.

6. Molecular simulation – Adsorption studies

6.1 Overview

To evaluate the adsorption capacity of the simulated HT structure we carried out GCMC simulations, which are particularly useful to calculate the adsorption capacity of a material and isotherms. In this chapter, we provide a brief introduction to the GCMC algorithm used in AMS 2019. Its code has been recently modified by Hans von Shoot in collaboration with Thomas Senftle for AMS to support 3D periodic boundary conditions, as is the case of SC1 (SCM, 2019). Next, we present the preliminary adsorption studies carried out with SC1. Finally, we discuss the challenges that must be overcome for obtaining useful results in future work.

6.2 Introduction to GCMC algorithm

GCMC simulations allow the study of adsorption through the insertion or deletion of molecules or particles into a system. The GCMC simulation generates trial moves according to the number of iterations and trials allowed. The "moves" are then accepted or rejected based on the energy in the system E_{old}^{AMS} produced by the optimised geometry. Moves that decrease the energy of the system are always accepted, whereas moves that increase the energy are only accepted under a probability criterion. The possible moves are (SCM, 2019):

- **Insert**: This move changes the coordinates of the atoms by inserting a new molecule or atom, resulting in rotations and random positioning. The insertion can occur within a range between a minimum or maximum radius, R_{min} and R_{max} respectively. The new value for the energy of the system is the previous energy plus the chemical potential (μ_{MC}) added by the new molecule in the system.

$$E_{old}^{MC} = E_{old}^{AMS} + \mu_{MC} \tag{6.1}$$

- **Delete**: This modification of the atom's coordinates erases a molecule or particle. The new value for the energy of the system is the previous energy minus the chemical potential of the deleted molecules or atoms.

$$E_{old}^{MC} = E_{old}^{AMS} - \mu_{MC} \tag{6.2}$$

- **Displace**: This change to the coordinates of the atoms also results in rotations, random position assignment according to R_{min} and R_{max} by displacing an existing molecule or atom. Since the number of particles is the same, there is no change in the energy of the system.

$$E_{old}^{MC} = E_{old}^{AMS} \tag{6.3}$$

- **Change volume**: This move is only available when a modification of the lattice is desired. The energy of the system is thus calculated based on the energy of the previous configuration, minus the difference in volumes multiplied by the pressure, plus the number of new molecules multiplying the natural logarithm of the available volumes ratio and the temperature.

$$E_{old}^{MC} = E_{old}^{AMS} - P(V_{new} - V_{old}) + N_{inserted} \ln{(V_{new}^{avail}/V_{old}^{avail})} kT \tag{6.4}$$

6.3 Methodology

The GCMC simulation was carried out using the ReaxFF engine, SC1 and FF1. Simulations using SC2 and FF2 did not converge and terminated with errors and thus are not reported. The simulation box considered SC1 as a μPT ensemble, with fixed chemical potential, pressure, and temperature respectively. The simulation pressure and temperature were set similar to experimental conditions, at 200ºC (473.15 K) and 1 bar (Hutson *et al.*, 2004; Ram Reddy *et al.*, 2006; Wang *et al.*, 2011).

Table 6.1 Settings for the GCMC simulations.

ReaxAMS Main Settings		*Minimisation Details*	
Task:	GCMC	*Method:*	Quasi-Newton
Periodicity:	Bulk	*Max No of steps:*	1 000
Force field:	FF1	*Convergence:*	1.0 $(kcal/mol)/Å$
Stress:	Off	*Add molecules within:*	3.0 Å
MC ensemble:	*μPT*	*Add molecules no closer than:*	0.3 Å
Temperature	*473.15 K*	*Max tries*	3 000
Pressure	*0.0 GPa*	*Molecule to add:*	CO_2
No. of GCMC iterations	*10 000*	*Chemical potential:*	-400 $kcal/mol$

Table 6.1 shows the settings for the adsorption studies. We carried out four simulations, each job ran for 10,000 GCMC iterations with a convergence of 1.0 (kcal/mol)/Å. The CO_2 molecules were inserted within $R_{min} = 0.3$ and $R_{max} = 3.0$ Å. The chemical potential $\mu = -400\ kcal/mol$ was assigned based on several preliminary runs and suggestions of empirical results from the software developers.

SC1 was set as the support structure for the adsorption in which the CO_2 molecules were inserted. The final system contained the initial support structure and ideally, the number of CO_2 molecules the HT could adsorb. The inserted molecules that formed chemical bonds with the HT structure were classified as chemisorbed. On the other hand, CO_2 molecules which did not create chemical bonds with the original HT were considered as physisorbed. Finally, we calculated the HT adsorption capacity in $molCO_2/kgHT$, the commonly reported unit in literature, by dividing the number of inserted CO_2 molecules over the molecular weight of the HT structure.

6.4 Results and discussion

The results of the adsorption capacity studies using SC1 and FF1 showed a very high adsorption capacity, significantly different from the reported in the literature. The average chemisorbed CO_2 molecules imply an adsorption capacity of 9.86 $molCO_2/kgHT$ as represented in Figure 6.1. On the other hand, physisorption varied considerably, with an average value of 24.92 $molCO_2/kgHT$. Thus, the total CO_2 adsorption capacity results in 34.78 $molCO_2/kgHT$ using a chemical potential of -400 kcal/mol.

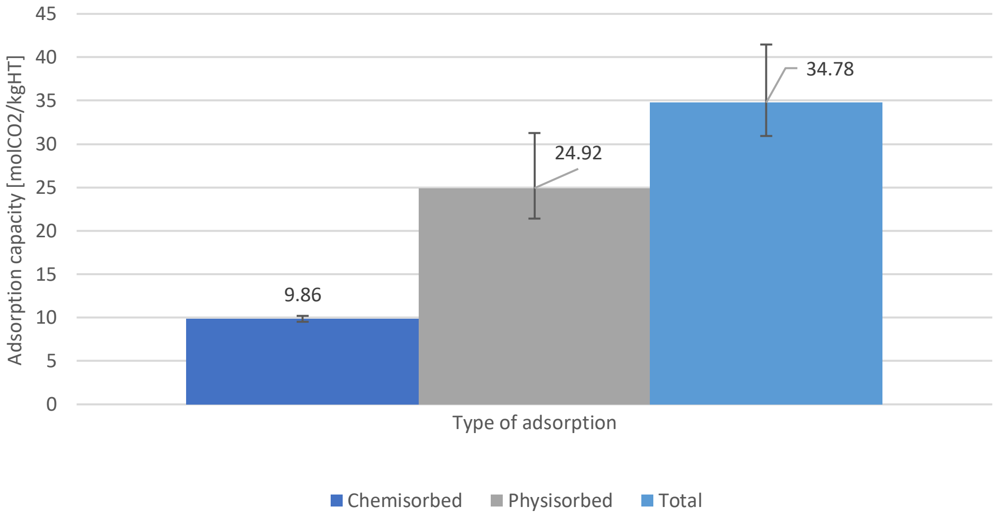

Figure 6.1 Adsorption capacity of SC1.

The fraction of CO_2 adsorbed through chemisorption was ~28%, higher than the 18.4% reported in experimental studies of HT calcination at 400°C (Hutson *et al.*, 2004). Although the proportion of the physisorption is encouraging, the total adsorption capacity is over significantly larger than the reported in the literature, which is between 0.1 – 2.29 $molCO_2/kgHT$ (Hutson and Attwood, 2008; Oliveira *et al*, 2008).

The poor results of the adsorption studies are attributed to several factors influencing the GCMC simulations discussed next.

Input

HT structure. SC1 represents a “fresh” HT structure, thus this preliminary study is not directly comparable with experimental data. Further attempts to run the GCMC simulations with the calcined structures from the calcination studies resulted in errors that have not been clarified but that we attribute to the used FF and the computational power available for this project.

Size of the system. The size of the simulated system, i.e. the number of atoms, greatly influences the computational cost. Larger supercells significantly increase the computation time and cost Attempts of carrying out the adsorption studies with the calcined SC2 structure with few iterations terminated with errors after running for one week.

Force Field. FF1 is a FF that does not differentiate the cations atoms. It is capable of holding the SC2 structure for over 9,500 iterations during a geometry optimization, however, it does not reflect the HT structure adequately. Attempts of using FF2 resulted in simulations that did not converge, highlighting the importance of improving the FF obtained with the CMA-ES method and its TS.

Settings

Radius of proximity. $R_{min} = 0.3$ Å and $R_{max} = 3.0$ Å also influence the number of inserted molecules. Our range could be too small, creating charge equilibration overlaps and thus reducing the opportunities for CO_2 insertions.

Chemical potential μ. The chemical potential μ is one of the most significant parameters for setting a GCMC simulation as can be deduced from section 5.1.1. It represents the change in the internal energy of the system when an additional particle is added while holding the volume and the entropy constant (Cook and Dickerson, 1995). Unfortunately, experimental values cannot be employed for simulations since the values of the internal energy of the system correspond to different temperature and pressure conditions.

Furthermore, the μ of a system also depends on the force field. The used value for our work is an empirical approximation suggested by the software developers, -400 kcal/mol, after several failed attempts to calculate it using FF1 and FF2. It can be noted that runs with a reduced μ value resulted in lower adsorption capacity. However, our preliminary results fail to clarify if the difference between adsorption capacities is due to the μ value or because of the number of iterations. The variation between results using the same μ is almost the same as the variation between simulations with a different one. Further work requires longer runs to ensure the system has reached an equilibrium and calculate the average adsorption capacity based on it. Presumably, the average adsorption capacity of the simulations should converge to the same value after enough iterations when using the same μ.

Length of simulation. As in the case of the MD simulations, the length of the GCMC simulation can also influence the result if the convergence criteria are not met. The number of iterations for our work is insufficient to achieve a steady-state in the system. For example, other authors consider in their simulations 1×10^6 steps to equilibrate the system and another 2×10^6 to calculate the average adsorption capacity of the system (Gao *et al.*, 2018). Alternatively, the use of 2×10^5 test particles has been used to compute the energy and calculate the average in simulations where only ~1% of insertions were successful, a rate considered to provide reliable statistics (Kim *et al.*, 2007). In our work, simulations had an average of 10% accepted moves with 2% corresponding to insertions pointing towards more accepted moves than expected. Furthermore, we set 10,000 iterations due to computational and time constrictions, with each simulation taking at least 3 days to complete in a 32-cores computer, more frequently than not, a week. A simulation of 100,000 iterations only achieved one iteration after 28 days and we decided to terminate it. In consequence, the calculation of a full isotherm was not in our capabilities.

Output

Adsorption capacity calculation. Our calculated total adsorption capacity depends only on the mass of the atoms in the system. Some authors prefer to normalise the adsorption capacity to the total surface area and pore volume (Hutson *et al*, 2004). Experimental studies suggest the number of active sites (Bhatta *et al.*, 2015) and surface area also influence the adsorption capacity (Wang *et al.*, 2011). Unfortunately, SC1 is still very small in contrast with experimental samples, thus pore size and distribution cannot be represented. These characteristics are in principle determined by the calcination process. Future simulations should use the calcined SC2 structure.

Flue gases: The adsorption process could be described more accurately in future simulations by including other flue gases besides the CO_2 molecules. In realistic settings, other flue gases might compete with the CO_2 with the HT for active adsorption spaces, or in the case of H_2O, affect the structure due to the memory effect.

6.5 Summary

In this section, we described the process to carry out the adsorption studies. The results of our GCMC simulations exhibited very high adsorption capacity values in contrast with experimental data. Most of the inserted CO_2 molecules were physisorbed, i.e. attached to the HT structure by nonbonded interactions. This is an encouraging result, which could be translated to a low energy requirement for the regeneration of the adsorbent. Nevertheless, the total adsorption capacity obtained, 33.77 $molCO_2/kgHT$, is significantly higher than expected (Hutson and Attwood, 2008). We attribute the inaccuracy of the simulation to several factors, such as the input system and FF, the insertion proximity radius, chemical potential and length of the simulation in the settings, and the method followed to calculate the adsorption capacity. Further studies require improved FF, input system and longer simulations using a more appropriate chemical potential.

7. Conclusions and recommendations

7.1 Conclusions

In this work, we focused on HTs for their promising advantages, such as wide availability, low cost, and fast kinetics. Experimental studies on the synthesis of HT and its adsorption performance highlight the importance of the **composition**, i.e. the cations, cationic rate and anions in the interlayers which significantly influence the size of the crystal cells and the adsorption capacity. However, the study of HTs using an experimental approach was impractical for systematic research of all the possible HT composition and operation conditions. Molecular simulations offer an alternative methodology to gain insights into CO_2 adsorption on HTs and how to improve their performance. Previous molecular simulation studies of HT have shown that their structure is sensitive to the electronic structure of the cations and their ratio, to the representation of the water molecules and the FF values used to distinguish between tetrahedral and octahedral Al. With this work, we aimed at taking the first steps towards simulations using the ReaxFF method which enabled a better representation of the adsorption, both physisorption and chemisorption, which is mostly neglected, by using a reactive and specialised FF.

Before this work, there were no ReaxFF FFs available that could carry out the simulations of CO_2 adsorption on HT. The development of the FF using the CMA-ES optimiser enabled the calcination and adsorption studies. To run the CMA-ES optimiser implemented in the AMS 2019 software it was necessary to create a TS that would provide information on the studied system. The importance of a complete and robust TS cannot be understated as the resulting FF values completely depend on the input provided. The selection of an appropriate weight of each TS entry should also be carefully considered to reduce the error function value according to what is most useful for the user.

The results of the MD simulations show the same structural changes reported in the literature; dehydration, dehydroxylation and decarbonation. The calculated surface area of the calcined structure is close to the highest value reported by experimental studies, suggesting that the simulation can represent the calcined structure despite the limitations of the FF. The settings for the calcination of SC2 using FF2 were improved based on the insights from preliminary simulation results. However, the calcination simulation could still benefit from a longer period for each step, i.e. a higher number of iterations in each stage: initial temperature, increasing temperature, optimum temperature and cooling down.

Finally, we carried out a preliminary GCMC simulation to calculate the adsorption capacity of SC1. The results showed very high adsorption capacity values in contrast with experimental data, 33.77 $molCO_2/kgHT$ (Hutson and Attwood, 2008). Most of the inserted CO_2 molecules were physisorbed as expected. We explain the total adsorption capacity being so high to several factors: the input geometry, developed FF's limitations, insertion proximity radius, the chemical potential employed, length of the simulation.

7.2 Recommendation for Future Work

Molecular simulations are a useful and powerful tool to develop and improve adsorbent materials and to test them systematically and efficiently. Despite the time scale difference in contrast with adsorption experiments, molecular simulations can provide insights on the transformation of the adsorbent during activation, the specific position of active sites for CO_2 capture and even provide isotherms. In this work, the simulations carried out provided preliminary results on the behaviour of CO_2 on $Mg - Al - CO_3$ HT. To enhance the results, the following aspects should be considered:

To improve the HT geometry optimisation

The optimisation of the HT geometry SC1 did not converge due to computational constraints. A complete convergence, even with a more relaxed convergence criterion is desirable. In addition, the selected functional must remain consistent when obtaining the PES scans and transition states. Furthermore, the addition of more variations of SC1 to account for the natural polymorphism of HT is advised. Different functionals could also be considered. Time and equipment constraints should be carefully considered as they considerably affected our studies.

To refine the developed FF

For the development of the FF, the CMA-ES optimiser is a practical method. However, users should include the HT variation structures as the inclusion of different variations of SC1 could better capture the polymorphism of the HTs. Changes in the position of the interlayer anions or even of the position of the Al atoms could provide more information for the FF reparameterization. Data from calcined HT structures should also be considered for the VS. In this work, in the final CMA-ES optimisation, the energy entries were later excluded as they were a source of the large values of the error function. It is advised to improve the quality of the energy entries and assign them a higher weight, i.e. the PES scans and transition states.

Additional caution must be taken regarding the software. The existence of undetected bugs could be an issue hard to detect for researchers new to the area of computational chemistry.

To carry out longer MD simulations of the HT calcination

Carrying out the calcination studies is still recommended. If the FF is improved and more computational power is available, longer calcination simulations can be carried out to verify the influence of the simulation time. A larger system could also be useful to observe different ways in which the layered structure collapses. The settings for representing the experimental conditions could also be revised. The thermostat selection can affect the accuracy of the thermodynamic average of the ensemble. Further analysis of the structure in future work could provide information regarding the attachment mechanism of the C atoms reported by other authors. The ability to carry out a molecular simulation study of the HT structure calcination opens possibilities to manipulate different aspects of the process and study them in a more efficient way than experimentally. The composition of the HT and the temperature and pressure conditions could be changed to produce better adsorbents when the FF is validated.

To perform GCMC simulations for obtaining an isotherm

The adsorption studies require an improved FF, and in turn, a more adequate calcined HT structure. Careful consideration of the insertion proximity radius, μ and length of the simulation in the settings is required to improve the obtained results. With a better FF, structure, and more computational resources it should be possible to calculate the isotherm and evaluate the performance of the HT at different conditions.

8. References

Abanades, J. C., Arias, B., Lyngfelt, A., Mattisson, T. , Wiley, D. E., Li, H., Ho, M. T., Mangano, E., Brandani, S. (2015) 'Emerging CO_2 capture systems', *International Journal of Greenhouse Gas Control*, 40, pp. 126–166. doi: 10.1016/j.ijggc.2015.04.018.

Addicoat, M. A., Vankova, N., Farjana, I. A., Heine, T. (2014) 'Extension of the Universal Force Field to Metal-Organic Frameworks', *Journal of Chemical Theory and Computation*, 10(2), pp. 880–891. doi: 10.1021/ct400952t.

Aktulga, H. M. , Fogarty, J.C., Pandit, S. A., Grama, A. Y. (2012) 'Parallel reactive molecular dynamics: Numerical methods and algorithmic techniques', *Parallel Computing*, 38(4–5), pp. 245–259. doi: 10.1016/j.parco.2011.08.005.

Alder, B. J. and Wainwright, T. E. (1957) 'Phase transition for a hard sphere system', *The Journal of Chemical Physics*, 27(5), pp. 1208–1209. doi: 10.1063/1.1743957.

Alptekin, G., Jayaraman, A., DeVoss, S., Jonska-Muteba, E. (2018) *A New Sorbent Process for Transformational Carbon Capture Process*. Wheat Ridge. Available at: https://netl.doe.gov/projects/files/A New Sorbent Process for Transformational Carbon Capture Process.pdf.

Alptekin, G. Jayaraman, A., Cates, M., Bonnema, M., Dippo, J., Gribble, D., Libberton, K. (2019) *Pilot Testing of a Highly Efficient Pre-combustion*. Wheat Ridge, CO. Available at: https://netl.doe.gov/projects/files/Pilot Testing of a Highly Effective Pre-Combustion Sorbent-Based Carbon Capture System (FE0013105).pdf.

Alptekin, G. (2020) *A New Sorbent Process for Transformational Carbon Capture Process*. Available at: https://netl.doe.gov/projects/files/SC0018682_TDA_Amine Sorbent_tech sheet.pdf.

Alptekin, G. and Jayaraman, A. (2019a) *A New Sorbent Process for Transformational Carbon Capture Process*. Wheat Ridge. Available at: https://netl.doe.gov/projects/files/Phase II_Project_Kickoff_DE-SC0018682_082119_NonConfidential.pdf.

Alptekin, G. and Jayaraman, A. (2019b) *Transformational Sorbent System for Post Combustion Carbon Capture (Contract No. DE-FE-0031734)*. Wheat Ridge, CO. Available at: https://netl.doe.gov/projects/files/Slides TDA FE0031734 Kickoff Mtg 081519 Public.pdf.

Areeprasert, C., Zhao, P., Ma, D., Shen, Y., Yoshikawa, K. (2014) 'Alternative solid fuel production from paper sludge employing hydrothermal treatment', *Energy and Fuels*, 28(2), pp. 1198–1206. doi: 10.1021/ef402371h.

Baade, W., Farnand, S., Hutchison, R., Welch, K. (2012) *CO_2 capture from SMRs : A demonstration project*. Allentown, Pennsylvania. Available at: http://www.h2alliance.com/pdf/Air-Products-tech-paper-CO2-capture.pdf.

Bahamon, D. Díaz-Márquez, A., Gamallo, P., Vega, L. F. (2018) 'Energetic evaluation of swing adsorption processes for CO_2 capture in selected MOFs and zeolites: Effect of impurities', *Chemical Engineering Journal*, 342 (December 2017), pp. 458–473. doi: 10.1016/j.cej.2018.02.094.

Bai, C., Liu, L. and Sun, H. (2012) 'Molecular dynamics simulations of methanol to olefin reactions in HZSM-5 zeolite using a ReaxFF force field', *Journal of Physical Chemistry C*, 116(12), pp. 7029–7039. doi: 10.1021/jp300221j.

Baskaran, T., Christopher, J. and Sakthivel, A. (2015) 'Progress on layered hydrotalcite (HT) materials as potential support and catalytic materials', *RSC Adv.*, 5(120), pp. 98853–98875. doi: 10.1039/C5RA19909C.

Ben-Mansour, R., Habib, M. A., Bamidele, O. E., Basha, M., Qasem, N. A.A., Peedikakkal, A., Laoui, T., Ali, M. (2016) 'Carbon capture by physical adsorption: Materials, experimental investigations and numerical modeling and simulations - A review', *Applied Energy*, 161, pp. 225–255. doi: 10.1016/j.apenergy.2015.10.011.

Bhatta, L., Subramanyam, S., Chengala, M. D., Bhatta, U. M., Venkathesh, K.. (2015a) 'Enhancement in CO_2 Adsorption on Hydrotalcite-based Material by Novel Carbon Support Combined with K_2CO_3 Impregnation', *Industrial and Engineering Chemistry Research*, 54(43), pp. 10876–10884. doi: 10.1021/acs.iecr.5b02020.

Bhatta, L., Subramanyam, S., Chengala, M. D., Olivera, S., Venkatesh, K. (2015b) 'Progress in hydrotalcite like compounds and metal-based oxides for CO_2 capture: A review', *Journal of Cleaner Production*, 103, pp. 171–196. doi: 10.1016/j.jclepro.2014.12.059.

Di Biase, E. and Sarkisov, L. (2013) 'Systematic development of predictive molecular models of high surface area activated carbons for adsorption applications', *Carbon*, 64, pp. 262–280. doi: 10.1016/j.carbon.2013.07.061.

Billemont, P., Coasne, B. and De Weireld, G. (2013) 'Adsorption of Carbon Dioxide, Methane, and Their Mixtures in Porous Carbons: Effect of Surface Chemistry, Water Content, and Pore Disorder', *Langmuir*, 29(10), pp. 3328–3338. doi: Doi 10.1021/La3048938.

Bogel-Burroughs, N., McDonnell Nieto del Rio, G. and Paybarah, A. (2021) *Texas Winter Storm: What to Know, The New York Times*. Available at: https://www.nytimes.com/2021/02/20/us/texas-winter-storm-explainer.html (Accessed: 5 April 2021).

Bonilla, P. and Wang, M. (2021) 'Molecular Simulation of Post-combustion Carbon Capture using Hydrotalcites', in *15th International Conference on Greenhouse Gas Control Technologies, GHGT-15*. GHGT-15. Available at: https://papers.ssrn.com/sol3/papers.cfm?abstract_id=3811404.

Bottoms, R. R. (1930) 'Process for separating acidic gases, United States Patent office', *Us1783901*. Available at: https://patentimages.storage.googleapis.com/21/dc/33/8f7f493bfaae75/US1783901.pdf.

BP (2020) *Statistical Review of World Energy 2020*. 69th edn. London. Available at: https://www.bp.com/content/dam/bp/business-sites/en/global/corporate/pdfs/energy-economics/statistical-review/bp-stats-review-2020-full-report.pdf.

BP (2021) *Statistical Review of World Energy globally consistent data on world energy markets*. Available at: https://www.bp.com/content/dam/bp/business-sites/en/global/corporate/pdfs/energy-economics/statistical-review/bp-stats-review-2021-full-report.pdf.

Bui, M. Adjiman, C. S., Bardow, A., Anthony, E. J., Boston, A., Brown, S., Fennell, P. S., Fuss, S., Galindo, A., Hackett, L. A., Hallett, J. P., Herzog, H. J., Jackson, G., Kemper, J., Krevor, S., Maitland, G. C., Matuszewski, M., Metcalfe, I.S., Petit, C., Puxty, G., Reimer, J., Reiner, D. M., Rubin, E. S., Scott, S. A., Shah, N., Smit, B., Trusler, J. P.M., Webley, P., Wilcox, J., Mac Dowell, N. (2018) 'Carbon capture and storage (CCS): The way forward', *Energy and Environmental Science*, 11(5), pp. 1062–1176. doi: 10.1039/c7ee02342a.

Cheung, O. and Hedin, N. (2014) 'Zeolites and related sorbents with narrow pores for $\mathrm{CO_2}$ separation from flue gas', *RSC Adv.*, 4(28), pp. 14480–14494. doi: 10.1039/C3RA48052F.

Choi, S., Drese, J. H. and Jones, C. W. (2009) 'Adsorbent materials for carbon dioxide capture from large anthropogenic point sources', *ChemSusChem*, 2(9), pp. 796–854. doi: 10.1002/cssc.200900036.

Chue, K. T. Kim, J. N., Yoo, Y. J., Cho, S. H., Yang, R. T. (1995) 'Comparison of Activated Carbon and Zeolite 13X for $\mathrm{CO_2}$ Recovery from Flue Gas by Pressure Swing Adsorption', *Industrial and Engineering Chemistry Research*, 34(2), pp. 591–598. doi: 10.1021/ie00041a020.

Cobden, P. and Abanades, C. (2021) *International Workshop on $\mathrm{CO_2}$ Capture and Utilization Pilot preparation for demonstration in the C4U project Post-combustion Capture*. Available at: https://c4u-project.eu/wp-content/uploads/2021/05/20210217-Pilot-Preparation-for-Demonstration-in-C4U.pdf (Accessed: 10 June 2021).

Cook, G. and Dickerson, R. H. (1995) 'Understanding the chemical potential', *American Journal of Physics*, 63(8), pp. 737–742. doi: 10.1119/1.17844.

COP26 (2021) *UN Climate Change Conference*. Available at: https://ukcop26.org/ (Accessed: 15 November 2021).

CORDIS, E. C. (2020) *Advanced Carbon Capture for steel industries integrated in CCUS Clusters, C4U Project*. Available at: https://c4u-project.eu/wp-content/uploads/2021/04/C4U-General-Overview-27-April-21.pdf (Accessed: 10 June 2021).

Costa, D. G. Rocha, A. B., Diniz, R., Souza, W.F, Chiaro, S. S. X., Leitão, A. A. (2010) 'Structural Model Proposition and Thermodynamic and Vibrational Analysis of Hydrotalcite-Like Compounds by DFT Calculations', *Phisical Chemistry C*, 114(33), pp. 14133–14140. doi: 10.1021/jp1033646.

Costa, D. G. Rocha, A. B., Souza, W. F., Chiaro, S. S. X., Leitão, A. A. (2012) 'Ab initio study of reaction pathways related to initial steps of thermal decomposition of the layered double hydroxide compounds', *Journal of Physical Chemistry C*, 116(25), pp. 13679–13687. doi: 10.1021/jp303529y.

Costantino, U., Marmottini, F., Nocchetti, M., Vivani, R. (1998) 'New Synthetic Routes to Hydrotalcite-Like Compounds − Characterisation and Properties of the Obtained Materials', *European Journal of Inorganic Chemistry*, 1998(10), pp. 1439–1446. doi: 10.1002/(sici)1099-0682(199810)1998:10<1439::aid-ejic1439>3.3.co;2-t.

Cramer, C. J. (2004) *Essentials of Computational Chemistry Theories and Models*, *Essentials of Computational Chemistry*. doi: 10.1021/ci010445m.

Cygan, R. T., Liang, J.-J. and Kalinichev, A. G. (2004) 'Molecular Models of Hydroxide, Oxyhydroxide, and Clay Phases and the Development of a General Force Field', *The Journal of Physical Chemistry B*, 108(4), pp. 1255–1266. doi: 10.1021/jp0363287.

Dantas, T. L. P. Luna, F. M. T, Silva Jr, I. J, Torres, A. E. B, de Azevedo, D. C. S., Rodrigues, A. E., Moreira, R. F.P.M (2011) 'Modeling of the fixed - bed adsorption of carbon dioxide and a carbon dioxide - nitrogen mixture on zeolite 13X', *Brazilian Journal of Chemical Engineering*, 28(3), pp. 533–544. doi: 10.1590/S0104-66322011000300018.

dftb.org (2021) *DFTB, Download of Slater-Koster files*. Available at: https://dftb.org/parameters/download (Accessed: 29 September 2021).

Ding, Y. and Alpay, E. (2000) 'Equilibria and kinetics of $\mathrm{CO_2}$ adsorption on hydrotalcite adsorbent', *Chemical Engineering Science*, 55(17), pp. 3461–3474. doi: 10.1016/S0009-2509(99)00596-5.

van Duin, A. C. T. Goddard, W.A., Islam, M.M., van Schoot, H., Trnka, T., Yakovlev, A.L. (2019) 'ReaxFF'. Amsterdam: SCM and Vrije Universiteit.

Van Duin, A. C. T., Dasgupta, S., Lorant, F., Goddard, W. A. (2001) 'ReaxFF: A reactive force field for hydrocarbons', *Journal of Physical Chemistry A*, 105(41), pp. 9396–9409. doi: 10.1021/jp004368u.

Elliot, J. and Yi, F. (2020) *Pilot Unit Testing at NCCC of Sorbent based* $\mathrm{CO_2}$ *Capture Project # DE-FE0012870*. Available at: https://netl.doe.gov/projects/files/Sorbent Based Post-Combustion CO2 Slipstream Testing (FE0012870).pdf (Accessed: 3 June 2021).

Elliott, J. and Copeland, B. (2016) *Post-Combustion* $\mathrm{CO_2}$ *Capture with Low Cost Solid Sorbent Slipstream Testing*. Pittsburgh. Available at: https://netl.doe.gov/projects/files/J-Elliott-TDA-Slipstream-Test-of-Sorbent-Based-Capture.pdf.

Elliott, J. and Yi, F. (2018) *Update on Pilot Unit of Sorbent Based Post-Combustion* $\mathrm{CO_2}$ *Capture Project # DE-FE0012870*. Pittsburgh. Available at: https://netl.doe.gov/projects/files/J-Elliott-TDAR-Pilot-Unit-Sorbent-Based-Capture.pdf.

Ernzerhof, M. and Scuseria, G. E. (1999) 'Assessment of the Perdew-Burke-Ernzerhof exchange-correlation functional', *Journal of Chemical Physics*, 110(11), pp. 5029–5036. doi: 10.1063/1.478401.

Fakhroleslam, M. and Fatemi, S. (2016) ‘Comparative simulation study of PSA, VSA, and TSA processes for purification of methane from CO_2 via SAPO-34 core-shell adsorbent’, *Separation Science and Technology (Philadelphia)*, 51(14), pp. 2326–2338. doi: 10.1080/01496395.2016.1210640.

Fan, L. S., Zeng, L., Wang, W., Luo, S. (2012) ‘Chemical looping processes for CO_2 capture and carbonaceous fuel conversion - Prospect and opportunity’, *Energy and Environmental Science*, 5(6), pp. 7254–7280. doi: 10.1039/c2ee03198a.

Folger, P. (2014) *Carbon capture and sequestration: Research, developement, and demonstration at the U.S. Department of Energy, Congressional Research Service*.

Fradette, L., Lefebvre, S. and Carley, J. (2017) ‘Demonstration Results of Enzyme-Accelerated CO_2 Capture’, *Energy Procedia*, 114, pp. 1100–1109. doi: 10.1016/j.egypro.2017.03.1263.

Gao, M., Khalkhali, M., Beck, S., Choi, P., Zhang, H. (2018) ‘Study of Thermal Stability of Hydrotalcite and Carbon Dioxide Adsorption Behavior on Hydrotalcite-Derived Mixed Oxides Using Atomistic Simulations’, *ACS Omega*, 3(9), pp. 12041–12051. doi: 10.1021/acsomega.8b01498.

Garcés-Polo, S. I. Villarroel-Rocha, J., Sapag, K., Korili, S.A., Gil, A. (2017) ‘Adsorption of CO_2 on mixed oxides derived from hydrotalcites at several temperatures and high pressures’, *Chemical Engineering Journal*, 332(September 2017), pp. 24–32. doi: 10.1016/j.cej.2017.09.056.

Garcés, S. I. Villarroel-Rocha, J., Sapag, K, Korili, S A, Gil, A. (2013) ‘Comparative Study of the Adsorption Equilibrium of CO_2 on Microporous Commercial Materials at Low Pressures’, *Industrial & Engineering Chemistry Research*, 52, pp. 6785–6793. doi: dx.doi.org/10.1021/ie400380w.

Garcia-Gallastegui, A. Iruretagoyena, D., Gouvea, V., Mokhtar, M., Asiri, A. M., Basahel, S. N., Al-Thabaiti, S. A., Alyoubi, A. O., Chadwick, D., Shaffer, M. S.P. (2012) ‘Graphene oxide as support for layered double hydroxides: Enhancing the CO_2 adsorption capacity’, *Chemistry of Materials*, 24(23), pp. 4531–4539. doi: 10.1021/cm3018264.

Geng, C. Xu, T., Li, Y., Chang, Z., Sun, X., Lei, X.(2013) ‘Effect of synthesis method on selective adsorption of thiosulfate by calcined MgAl-layered double hydroxides’, *Chemical Engineering Journal*, 232, pp. 510–518. doi: 10.1016/j.cej.2013.08.010.

Global CCS Institute (2021) *Facilities, CO2Re Facility Data*. Available at: https://co2re.co/FacilityData (Accessed: 16 July 2021).

Gollakota, S. and Yu, M. (2020) *Transformational Molecular Layer Deposition Tailor-Made Size-Sieving Sorbents for Post- Combustion CO_2 Capture Project Information, Technology sheet*. Available at: https://netl.doe.gov/projects/files/FE0031730_RPI_tech sheet.pdf (Accessed: 8 June 2021).

Government of Canada (2018) *VeloxoTherm^{TM} CO_2 Capture Process Demonstration, Current Investments*. Available at: https://www.nrcan.gc.ca/science-and-data/funding-partnerships/funding-opportunities/current-investments/veloxothermtm-co2-capture-process-demonstration/20424 (Accessed: 30 June 2020).

Grande, C. A. (2012) ‘Advances in Pressure Swing Adsorption for Gas Separation’, *ISRN Chemical Engineering*. Edited by D. Cazorla-Amoros, T. M. Aminabhavi, and X. Feng, 2012, p. 982934. doi: 10.5402/2012/982934.

Grande, C. A. and Rodrigues, A. E. (2008) ‘Electric Swing Adsorption for CO_2 removal from flue gases’, *International Journal of Greenhouse Gas Control*, 2(2), pp. 194–202. doi: 10.1016/S1750-5836(07)00116-8.

Greenwell, H. C., Jones, W., Coveney, P. V., Stackhouse, S. (2006) ‘On the application of computer simulation techniques to anionic and cationic clays: A materials chemistry perspective’, *Journal of Materials Chemistry*, pp. 708–723. doi: 10.1039/b506932g.

Haas, P., Tran, F., Blaha, P., Schwarz, K. (2011) ‘Construction of an optimal GGA functional for molecules and solids’, *Physical Review B - Condensed Matter and Materials Physics*, 83(20), pp. 1–6. doi: 10.1103/PhysRevB.83.205117.

Hadong power station (2021) *Global Energy Monitor Wiki*. Available at: https://www.gem.wiki/Hadong_power_station#cite_note-2 (Accessed: 31 May 2021).

Halabi, M. H., De Croon, M. H. J. M., Van Der Schaaf, J., Cobden, P. D., Schouten, J. C. (2012) ‘High capacity potassium-promoted hydrotalcite for CO_2 capture in H_2 production’, *International Journal of Hydrogen Energy*, 37(5), pp. 4516–4525. doi: 10.1016/j.ijhydene.2011.12.003.

Hallenbeck, A. P. and Kitchin, J. R. (2013) ‘Effects of O_2 and SO_2 on the capture capacity of a primary-amine based polymeric CO_2 sorbent’, *Industrial and Engineering Chemistry Research*, 52(31), pp. 10788–10794. doi: 10.1021/ie400582a.

Hanif, A., Dasgupta, S., Divekar, S., Arya, A., Garg, M. O., Nanoti, A. (2014) ‘A study on high temperature CO_2 capture by improved hydrotalcite sorbents’, *Chemical Engineering Journal*, 236, pp. 91–99. doi: 10.1016/j.cej.2013.09.076.

Hansen, N. (2016) *The CMA Evolution Strategy: A Tutorial*. Cornell: Cornell University. Available at: http://arxiv.org/abs/1604.00772 (Accessed: 4 September 2019).

Hansen, N., Müller, S. D. and Koumoutsakos, P. (2003) ‘Reducing the time complexity of the derandomized evolution strategy with covariance matrix adaptation CMA-ES’, *Evolutionary Computation*, 1(11), pp. 1–18. Available at: http://delivery.acm.org/10.1145/780000/772376/106365603321828970.pdf?ip=143.167.56.177&id=772376&acc=ACTIVE SERVICE&key=BF07A2EE685417C5.33526737E11CAFEF.4D4702B0C3E38B35.4D4702B0C3E38B35&__acm__=1563285199_a49f0fff553117e2e3b5e4d79cba1a6c#URLTOKE (Accessed: 1 August 2019).

Hinchliffe, A. (2008) *Molecular Modelling for Beginners*. 2nd edn. Chichester: Wiley.

Hjertenaes, E., Quynh Nguyen, A. and Koch, H. (2016) ‘A ReaxFF force field for sodium intrusion in graphitic cathodes’, *Phys. Chem. Chem. Phys.*, 18, pp. 31431–31440. doi:

10.1039/c6cp06774c.

Hohenberg, P. and Kohn, W. (1964) ‘Inhomogeneous Electron Gas’, *Physical Review*, 136(3B), pp. B864–B871. Available at: https://journals.aps.org/pr/pdf/10.1103/PhysRev.136.B864 (Accessed: 5 August 2019).

Huang, Y., Cannon, F. S., Watson, J. K., Reznik, B., Mathews, J. P. (2015) ‘Activated carbon efficient atomistic model construction that depicts experimentally-determined characteristics’, *Carbon*, 83, pp. 1–14. doi: 10.1016/j.carbon.2014.11.012.

Hutson, N. D. and Attwood, B. C. (2008) ‘High temperature adsorption of CO_2 on various hydrotalcite-like compounds’, *Adsorption*, 14(6), pp. 781–789. doi: 10.1007/s10450-007-9085-6.

Hutson, N. D., Speakman, S. A. and Payzant, E. A. (2004) ‘Structural effects on the high temperature adsorption of CO2 on a synthetic hydrotalcite’, *Chemistry of Materials*, 16(21), pp. 4135–4143. doi: 10.1021/cm040060u.

Huygh, S., Bogaerts, A., Van Duin, A. C. T., Neyts, E. C. (2014) ‘Development of a ReaxFF reactive force field for intrinsic point defects in titanium dioxide’, *Computational Materials Science*, 95, pp. 579–591. doi: 10.1016/j.commatsci.2014.07.056.

IPCC (2014) *Climate Change 2014: Synthesis Report, 5th Assessment Report: Mitigation of Climate Change*. doi: 10.1017/CBO9781107415324.

IPCC (2018) *IPCC special report on the impacts of global warming of 1.5 °C - Summary for policy makers*. Incheon. Available at: http://report.ipcc.ch/sr15/pdf/sr15_spm_final.pdf (Accessed: 5 November 2018).

Ishibashi, M., Ota, H., Akutsu, N., Umeda, S., Tajika, M., Izumi, J., Yasutake, A., Kabata, T., Kageyama, Y.(1996) ‘Technology for removing carbon dioxide from power plant flue gas by the physical adsorption method’, *Energy Conversion and Management*, 37(6–8), pp. 929–933. doi: 10.1016/0196-8904(95)00279-0.

Ismail, A. F., Chandra Khulbe, K. and Matsuura, T. (2015) *Gas Separation Membranes*. Cham: Springer International Publishing. doi: 10.1007/978-3-319-01095-3.

Iype, E. Hütter, M., Jansen, A. P. J., Nedea, S. V., Rindt, C. C. M. (2013) ‘Parameterization of a reactive force field using a Monte Carlo algorithm’, *Journal of Computational Chemistry*, 34(13), pp. 1143–1154. doi: 10.1002/jcc.23246.

Jacobsen, H. and Cavallo, L. (2017) ‘Directions for Use of Density Functional Theory : A Short Instruction Manual for Chemists’, in Kaczmarek-Kedziera, J. L. et al. (eds) *Handbook of Computational Chemistry*. 2nd edn. Springer, pp. 225–267.

Jain, R. (2019a) *Transformational Sorbent-Based Processes for a Substantial Reduction in the Cost of* CO_2 *Capture*. Pittsburgh (Pennsylvania). Available at: https://netl.doe.gov/projects/files/Transformational Sorbent-Based Process for a Substantial Reduction in the Cost of CO_2 Capture (FE0031722).pdf.

Jain, R. (2019b) *Transformational Sorbent-Based Processes for a Substantial Reduction in the*

Cost of CO2 Capture Kick-off meeting (DE-0031722). Pittsburgh (Pennsylvania). Available at: https://netl.doe.gov/projects/files/FE0031722_InnoSepra Kickoff_09-30-19.pdf.

Jensen, F. (2007) *Introduction to Computational Chemistry*. 2nd edn, *Annual Reports on the Progress of Chemistry - Section C*. 2nd edn. Odense, Denmark: Wiley. doi: 10.1039/PC9939000045.

JFE Group (2019) *Protecting the Global Environment: Climate Change Mitigation, JFE Holdings Inc.* Available at: https://www.jfe-holdings.co.jp/en/csr/pdf/2019/2019_09_04.pdf (Accessed: 23 April 2020).

Jiang, N., Shen, Y., Liu, B., Zhang, D., Tang, Z., Li, G., Fu, B. (2020) '$\mathrm{CO_2}$ capture from dry flue gas by means of VPSA, TSA and TVSA', *Journal of CO2 Utilization*, 35, pp. 153–168. doi: 10.1016/j.jcou.2019.09.012.

Jin, Z. and Firoozabadi, A. (2013) 'Fluid Phase Equilibria Methane and carbon dioxide adsorption in clay-like slit pores by Monte Carlo simulations', *Fluid Phase Equilibria*, 360, pp. 456–465. doi: 10.1016/j.fluid.2013.09.047.

Jones, A., Hancu, D. and Jain, R. (2019) *Transformational Sorbent-Based Process for a Substantial Reduction in the Cost of CO2 Capture Project Information*. Pittsburgh (Pennsylvania). Available at: https://netl.doe.gov/project-information?p=FE0031722.

Jones, A. and Jain, R. (2020) *Transformational Sorbent- Based Process for a Substantial Reduction in the Cost of* $\mathrm{CO_2}$ *Capture*. Available at: https://netl.doe.gov/projects/files/FE0031722_InnoSepra_Sorbent_tech sheet.pdf (Accessed: 8 June 2021).

Just, P. E. (2013) 'Shell Cansolv - Deploying CCS Worldwide', *PCCC-2, Bergen, Norway*, (September).

Kaassis, A. Y. A., Xu, S. M., Evans, D.G., Williams, G. R., Wei, M., Duan, X. (2015) 'Combined In Situ and In Silico Studies of Guest Intercalation into the Layered Double Hydroxide $[\mathrm{LiAl_2(OH)_6}]\mathrm{X \cdot yH_2O}$', *Journal of Physical Chemistry C*, 119(32), pp. 18729–18740. doi: 10.1021/acs.jpcc.5b04203.

Kamat, A. M., van Duin, A. C. and Yakovlev, A. (2010) 'Molecular dynamics simulations of laser-induced incandescence of soot using an extended ReaxFF reactive force field', *Journal of Physical Chemistry A Molecules, Spectroscopy, Kinetics, Environment & General Theory*, 114(48), pp. 12561–12572. doi: http://dx.doi.org/10.1021/jp1080302.

Kamran, U. and Park, S. J. (2021) 'Chemically modified carbonaceous adsorbents for enhanced $\mathrm{CO_2}$ capture: A review', *Journal of Cleaner Production*, 290, p. 125776. doi: 10.1016/j.jclepro.2020.125776.

Kemter, M., Fischer, M., Luna, L.V., Schönfeldt, E., Vogel, J., Banerjee, A., Korup, O., Thonicke, K. (2021) 'Cascading hazards in the aftermath of Australia's 2019/2020 Black Summer wildfires', *Earth's Future*, (Figure 1), pp. 1–7. doi: 10.1029/2020ef001884.

Khalkhali, M., Zhu, X., Shi, Y., Liu, Q., Choi, P., Zhang, H. (2020) 'Structure and CO_2 physisorption capacity of hydrotalcite-derived oxide', *Journal of CO2 Utilization*, 36(September 2019), pp. 64–75. doi: 10.1016/j.jcou.2019.10.019.

Khorshidi, Z. N., Khalkhali, M., Zhang, H., Choi, P. (2018) 'Molecular Dynamics Study of the Role of Water in the Carbon Dioxide Intercalation in Chloride Ions Bearing Hydrotalcite', *The Journal of Physical Chemistry C*, p. acs.jpcc.8b01691. doi: 10.1021/acs.jpcc.8b01691.

Kim, N., Kim, Y., Tsotsis, T. T., Sahimi, M. (2005) 'Atomistic simulation of nanoporous layered double hydroxide materials and their properties. I. Structural modeling', *Journal of Chemical Physics*, 122(21). doi: 10.1063/1.1902945.

Kim, N., Harale, A., Tsotsis, T. T., Sahimi, M. (2007) 'Atomistic simulation of nanoporous layered double hydroxide materials and their properties. II. Adsorption and diffusion', *Journal of Chemical Physics*, 127(22). doi: 10.1063/1.2799985.

Klamt, A. and Schüürmann, G. (1993) 'COSMO: A new approach to dielectric screening in solvents with explicit expressions for the screening energy and its gradient', *Journal of the Chemical Society, Perkin Transactions 2*, (5), pp. 799–805. doi: 10.1039/P29930000799.

Kohn, W. and Sham, L. J. (1965) 'Self-Consistent Equations Including Exchange and Correlation Effects', *Physical Review A*, 140(4A), pp. A1133–A1138. doi: 10.1046/j.1365-4362.2002.01376.x.

Konstantakou, M., Gotzias, A., Kainourgiakis, M., Stubos, A. K., Steriotis, T. A. (2011) 'GCMC Simulations of Gas Adsorption in Carbon Pore Structures', in Mordechai, S. (ed.) *Applications of Monte Carlo Method in Science and Engineering*. IntechOpen. doi: 10.5772/15988.

Lang, D., Hancu, D. and Alptekin, G. (2019) *A New Sorbent Process for Transformational Carbon Capture Process, Project Landing Page - National Energy Technology Laboratory*. Available at: https://netl.doe.gov/project-information?p=SC0018682 (Accessed: 8 June 2020).

Lawal, A., Wang, M., Stephenson, P., Koumpouras, G., Yeung, H. (2010) 'Dynamic modelling and analysis of post-combustion CO_2 chemical absorption process for coal-fired power plants', *Fuel*, 89(10), pp. 2791–2801. doi: 10.1016/j.fuel.2010.05.030.

Leach, A. R. (2001) *Molecular modelling Principles and applications*. 2nd edn. Dorchester: Prentice Hall.

León, M., Díaz, E., Bennici, S., Vega, A., Ordóñez, S., Auroux, A. (2010) 'Adsorption of CO_2 on hydrotalcite-derived mixed oxides: Sorption mechanisms and consequences for adsorption irreversibility', *Industrial and Engineering Chemistry Research*, 49(8), pp. 3663–3671. doi: 10.1021/ie902072a.

Li, H., Ma, J., Evans, D. G., Zhou, T., Li, F., Duan, X. (2006) 'Molecular Dynamics Modeling of the Structures and Binding Energies of α-Nickel Hydroxides and Nickel - Aluminum Layered Double Hydroxides Containing Various Interlayer Guest Anions', 1(2), pp. 4405–4414. doi: 10.1021/cm060867h.

Li, L., Zhao, N., Wei, W., Sun, Y. (2013) ‘A review of research progress on CO_2 capture, storage, and utilization in Chinese Academy of Sciences’, *Fuel*, 108, pp. 112–130. doi: 10.1016/j.fuel.2011.08.022.

Li, S., Shi, Y., Zeng, H., Cai, N. (2017) ‘Development of carboxyl-layered double hydrotalcites of enhanced CO_2 capture capacity by K_2CO_3 promotion’, *Adsorption*, 23(2–3), pp. 239–248. doi: 10.1007/s10450-016-9844-3.

LibreTexts^{TM} (2020) *15.4 Lattice Geometry*. 26 November 2020. Available at: https://eng.libretexts.org/Bookshelves/Materials_Science/TLP_Library_I/15%3A_Crystallography/15.04%3A_Section_4- (Accessed 27 January 2020)

Lian, Y., Deng, S., Li, S., Guo, Z., Zhao, L., Yuan, X. (2019) ‘Numerical analysis on CO_2 capture process of temperature swing adsorption (TSA): Optimization of reactor geometry’, *International Journal of Greenhouse Gas Control*, 85(April), pp. 187–198. doi: 10.1016/j.ijggc.2019.03.029.

Lillia, S. *et al.* (2018) ‘A comprehensive modeling of the hybrid temperature electric swing adsorption process for CO_2 capture’, *International Journal of Greenhouse Gas Control*, 74(April), pp. 155–173. doi: 10.1016/j.ijggc.2018.04.012.

Lin, L. C., Kim, J., Kong, X., Scott, E., McDonald, T. M., Long, J. R., Reimer, J. A., Smit, B. (2013) ‘Understanding CO_2 dynamics in metal-organic frameworks with open metal sites’, *Angewandte Chemie - International Edition*, 52(16), pp. 4410–4413. doi: 10.1002/anie.201300446.

Liu, L., Liu, Y., Zybin, S. V., Sun, H., Goddard, W. A. (2011) ‘ReaxFF-lg: Correction of the ReaxFF reactive force field for London dispersion, with applications to the equations of state for energetic materials’, *Journal of Physical Chemistry A*, 115(40), pp. 11016–11022. doi: 10.1021/jp201599t.

Liu, Z., Grande, C. A., Li, P., Yu, J., Rodrigues, A. E. (2011) ‘Multi-bed Vacuum Pressure Swing Adsorption for carbon dioxide capture from flue gas’, *Separation and Purification Technology*, 81(3), pp. 307–317. doi: https://doi.org/10.1016/j.seppur.2011.07.037.

Loebick, C., Weissman, J., Baird, B., Roux, S., Ryan, E. (2018) *High-Efficiency Post Combustion Carbon Capture System DOE SBIR Phase 2 Contract # DE-SC0017221*. Available at: https://netl.doe.gov/projects/files/High-Efficiency Post Combustion Carbon Capture System Nov 2018.pdf.

Loebick, C. and Weisman, J. (2017) *High-Efficiency Post Combustion Carbon Capture System DOE SBIR Phase 1 Contract # DE-SC0017221*. Available at: https://netl.doe.gov/projects/files/High-Efficiency Post Combustion Carbon Capture System Dec 2017.pdf.

Lombardo, G. M., Pappalardo, G. C., Costantino, F., Costantino, U., Sisani, M. (2008) ‘Thermal Effects on Mixed Metal (Zn / Al) Layered Double Hydroxides : Direct Modeling of the X-Ray Powder Diffraction Line Shape Through Molecular Dynamics Simulations’, *Chemistry of Materials*, 20, pp. 5585–5592. doi: 10.1021/cm801053d.

Long, J. (2010) "*Use of potential energy surfaces (PES) in spectroscopy and reaction dynamics*". University of Iceland. Available at: https://notendur.hi.is/agust/kennsla/ee10/ees10/Seminars/ees-LongTHESIS-10.pdf (Accessed 18 June 2021.)

Long, J. R. (2020) *Amine-appended Metal-Organic Frameworks as switch-like adsorbents for energy-efficient carbon capture, National Energy Technology Laboratory Carbon Capture 2020 - Integrated Review Webinar - October 5-7.* Available at: https://netl.doe.gov/projects/files/Amine-Appended Metal-Organic Frameworks as Switch-Like Adsorbents for Energy Efficient Carbon Capture (FWP-FP0006194).pdf (Accessed: 3 June 2021).

López, T., Bosch, P., Asomoza, M., Gómez, R., Ramos, E (1997) 'DTA-TG14 and FTIR spectroscopies of sol-gel hydrotalcites : aluminum source effect on physicochemical properties', *Materials Letters*, 31(June), pp. 311–316.

Lu, X., Jin, D., Wei, S., Zhang, M., Zhu, Q., Shi, X., Deng, Z., Guo, W., Shen, W. (2015) 'Competitive adsorption of a binary $\mathrm{CO_2}$ - $\mathrm{CH_2}$ mixture in nanoporous carbons: effects of edge-functionalization', *Nanoscale*, 7(3), pp. 1002–1012. doi: 10.1039/C4NR05128A.

Mahgerefteh, H. (2021) *C4U*. Available at: https://c4u-project.eu/work-packages/#et_pb_accordion_item_0 (Accessed: 23 August 2021).

Manohara, G. V., Li, L., Whiting, A., Greenwell, H. C. (2018) 'Ultra-high aspect ratio hybrid materials: The role of organic guest and synthesis method', *Dalton Transactions*, 47(9), pp. 2933–2938. doi: 10.1039/c7dt04312k.

Manohara, G. V., Norris, D., Maroto-Valer, M. M., Garcia, S. (2021) 'Acetate intercalated Mg-Al layered double hydroxides (LDHs) through modified amide hydrolysis: a new route to synthesize novel mixed metal oxides (MMOs) for $\mathrm{CO_2}$ capture', *Dalton Transactions*, 50(21), pp. 7474–7483. doi: 10.1039/d1dt00602a.

Mayo, S. L., Olafson, B. D. and Goddard, W. A. (1990) 'DREIDING: A generic force field for molecular simulations', *Journal of Physical Chemistry*, 94(26), pp. 8897–8909. doi: 10.1021/j100389a010.

Melese, Y., Heijnen, P., Stikkelman, R., Herder, P. (2017) 'An approach for flexible design of infrastructure networks via a risk sharing contract: The case of CO2 transport infrastructure', *International Journal of Greenhouse Gas Control*, 63(July), pp. 401–411. doi: 10.1016/j.ijggc.2017.06.006.

Metropolis, N., Rosenbluth, A. W., Rosenbluth, M. N., Teller, A. H., Teller, E. (1953) 'Equation of state calculations by fast computing machines', *The Journal of Chemical Physics*, 21(6), pp. 1087–1092. doi: 10.1063/1.1699114.

Miguel, C. V., Trujillano, R., Rives, V., Vicente, M. A., Ferreira, A. F. P., Rodrigues, A. E. Mendes, A., Madeira, L. M. (2014) 'High temperature $\mathrm{CO_2}$ sorption with gallium-substituted and promoted hydrotalcites', *Separation and Purification Technology*, 127, pp. 202–211. doi: 10.1016/j.seppur.2014.03.007.

MIT (2016) *Port Arthur Fact Sheet: Carbon Dioxide Capture and Storage Project*, *Carbon Capture & Sequestration Technologies @ MIT*. Available at: https://sequestration.mit.edu/tools/projects/port_arthur.html (Accessed: 1 June 2020).

MOF4Air (2019) *The MOF4AIR Project, Metal Organic Frameworks for carbon dioxide Adsorption processes in power production and energy Intensive industRies*. Available at: https://www.mof4air.eu/wp-content/uploads/2019/11/MOF4AIR-presentation-disclosable-20191106.pdf (Accessed: 11 June 2021).

Moreira, D. and Pires, J. C. M. (2016) 'Atmospheric $\mathrm{CO_2}$ capture by algae: Negative carbon dioxide emission path', *Bioresource Technology*, 215, pp. 371–379. doi: 10.1016/j.biortech.2016.03.060.

Muñoz, V., Zotin, F. M. Z. and Palacio, L. A. (2015) 'Copper–aluminum hydrotalcite type precursors for NOx abatement', *Catalysis Today*, 250(x), pp. 173–179. doi: 10.1016/j.cattod.2014.06.004.

Neaton, J. B., Long, J. R. and Haranczyk, M. (2019) *Amine-Appended Metal-Organic Frameworks as Switch-Like Adsorbents for Energy-Efficient Carbon Capture*. Pittsburgh (Pennsylvania). Available at: https://netl.doe.gov/projects/files/Amine-Appended Metal-Organic Frameworks as Switch-Like Adsorbents for Energy-Efficient Carbon Capture (FWP-FP00006194).pdf (Accessed: 2 June 2020).

Neaton, J. B., Long, J. R. and Haranczyk, M. (2020) *Amine-Appended Metal-Organic Frameworks as switch-like adsorbents for energy-efficient carbon capture*, *May 2020 NETL CO2 Capture Technology Tech-Sheet*. Available at: https://netl.doe.gov/projects/files/FWP-FP00006194_LBNL_tech sheet.pdf (Accessed: 3 June 2021).

Nelson, T. O., Kataria, A., Mobley, P., Soukri, M., Tanthana, J. (2017) 'RTI's Solid Sorbent-Based $\mathrm{CO_2}$ Capture Process: Technical and Economic Lessons Learned for Application in Coal-fired, NGCC, and Cement Plants', *Energy Procedia*, 114(November 2016), pp. 2506–2524. doi: 10.1016/j.egypro.2017.03.1409.

NETL (2018) *High-Efficiency Post Combustion Carbon Capture System*, *Project Landing Page - National Energy Technology Laboratory*. Available at: https://netl.doe.gov/project-information?p=SC0017221 (Accessed: 2 June 2020).

NETL (2019) *Amine-Appended Metal-Organic Frameworks as Switch-Like Adsorbents for Energy Efficient Carbon Capture Project Information*. Available at: https://netl.doe.gov/project-information?p=FWP-FP00006194 (Accessed: 2 June 2020).

NETL (2020) *2020 Carbon Capture Program R&D - Compendium of Carbon Capture Technology*. Available at: https://www.netl.doe.gov/sites/default/files/2020-07/Carbon-Capture-Technology-Compendium-2020.pdf (Accessed: 21 June 2021).

Newsome, D. A., Sengupta, D., Foroutan, H., Russo, M. F., van Duin, A.C. T. (2012) 'Oxidation of Silicon Carbide by $\mathrm{O_2}$ and $\mathrm{H_2O}$: A ReaxFF Reactive Molecular Dynamics Study, Part I', *The Journal of Physical Chemistry C*, 116(30), pp. 16111–16121. doi: 10.1021/jp306391p.

NOAA (2021) *Trends in Atmospheric Carbon Dioxide, Data from Launa Moa, Hawaii*. Available at: https://www.esrl.noaa.gov/gmd/ccgg/trends/mlo.html (Accessed: 2 April 2021).

Norahim, N., Yaisanga, P., Faungnawakij, K., Charinpanitkul, T., Klaysom, C. (2018) 'Recent Membrane Developments for CO_2 Separation and Capture', *Chemical Engineering & Technology*, (2), pp. 211–223. doi: 10.1002/ceat.201700406.

O'Palko, A., Loebick, C., Baird, B., Weissman, J., Anderson, A.(2020) *High-Efficiency Post Combustion Carbon Capture System, Phase ll Project Review Meeting*. Available at: https://netl.doe.gov/projects/files/Slides PCI SC0017221 Project Review Mtg 2020-06-09 Non-Proprietary.pdf (Accessed: 3 June 2021).

O'Palko, A. and Alptekin, G. (2020) *Transformational Sorbent System for Post Combustion Carbon Capture*. Available at: https://netl.doe.gov/projects/files/FE0031734_TDA_MOF Sorbent_tech sheet.pdf.

O'Palko, A., Hancu, D. and Alptekin, G. (2019) *Pilot Testing of a Highly Effective Pre-Combustion Sorbent-Based Carbon Capture System*. Available at: https://netl.doe.gov/project-information?p=FE0013105 (Accessed: 18 June 2020).

O'Palko, A., Hancu, D. and Elliot, J. (2019) *Sorbent Based Post-Combustion* CO_2 *Slipstream Testing, Project Landing Page - National Energy Technology Laboratory*. Available at: https://netl.doe.gov/projects/files/Pilot-Scale Slipstream Testing of Sorbent-Based CO_2 Capture Process (FE0012870).pdf (Accessed: 2 June 2020).

O'Palko, A., Hanucu, D. and Alptekin, G. (2019) *Transformational Sorbent System for Post-Combustion Carbon Capture, Project Landing Page - National Energy Technology Laboratory*. Available at: https://netl.doe.gov/project-information?p=FE0031734 (Accessed: 10 June 2020).

Office of Fossil Energy (2016) *Texas* CO_2 *Capture Demonstration Project Hits Three Million Metric Ton Milestone, Articles*. Available at: https://www.energy.gov/fe/articles/texas-co2-capture-demonstration-project-hits-three-million-metric-ton-milestone (Accessed: 1 June 2020).

Oliveira, E. L. G., Grande, C. A. and Rodrigues, A. E. (2008) 'CO_2 sorption on hydrotalcite and alkali-modified (K and Cs) hydrotalcites at high temperatures', *Separation and Purification Technology*, 62(1), pp. 137–147. doi: 10.1016/j.seppur.2008.01.011.

Oneil, N., Hancu, D. and Yu, M. (2019) *Transformational Molecular Layer Deposition Tailor-Made Size-Sieving Sorbents for Post- Combustion CO2 Capture Project Information*. Pittsburgh (Pennsylvania). Available at: https://netl.doe.gov/project-information?p=FE0031730.

Othman, M. R., Helwani, Z., Martunus, Fernando, W. J. N. (2009) 'Synthetic hydrotalcites from different routes and their application as catalysts and gas adsorbents: A review', *Applied Organometallic Chemistry*, 23(9), pp. 235–246. doi: 10.1002/aoc.1517.

Page, B., Turan, G. and Zapantis, A. (2020) *Global Status of CCS 2020, Global CCS Institute*.

Available at: https://www.globalccsinstitute.com/resources/global-status-report/.

Palko, A. O., Zoican-Loebick, C. and Baird, B. (2020) *High-Efficiency Post Combustion Carbon Capture System*. Washington. doi: https://www.nationalcarboncapturecenter.com/wp-content/uploads/2021/05/DE-SC0017221-Precision-Combustion-Report.pdf.

Pardakhti, M., Jafari, T., Tobin, Z., Dutta, B., Moharreri, E., Shemshaki, N. S., Suib, S., Srivastava, R.(2019) 'Trends in Solid Adsorbent Materials Development for CO_2 Capture', *ACS Applied Materials and Interfaces*, 11(38), pp. 34533–34559. doi: 10.1021/acsami.9b08487.

Park, Y. C., Jo, Sung H., Kyung, D. H., Kim, J. Y., Yi, C. K., Ryu, C. K., Shin, M. S. (2014) 'Test operation results of the 10 MWe-scale dry-sorbent CO_2 capture process integrated with a real coal-fired power plant in Korea', *Energy Procedia*, 63, pp. 2261–2265. doi: 10.1016/j.egypro.2014.11.245.

Pitman, M. C. and Van Duin, A. C. T. (2012) 'Dynamics of confined reactive water in smectite clay-zeolite composites', *Journal of the American Chemical Society*, 134(6), pp. 3042–3053. doi: 10.1021/ja208894m.

Plaza, M. G. and Rubiera, F. (2019) 'Evaluation of a novel multibed heat-integrated vacuum and temperature swing adsorption post-combustion CO_2 capture process', *Applied Energy*, 250(May), pp. 916–925. doi: 10.1016/j.apenergy.2019.05.079.

Potoff, J. J. and Siepmann, J. I. (2001) 'Vapor-liquid equilibria of mixtures containing alkanes, carbon dioxide, and nitrogen', *AIChE Journal*, 47(7), pp. 1676–1682. doi: 10.1002/aic.690490826.

Pramod, C. V, Upendar, K., Mohan, V., Sarma, D. S., Dhar, G. M., Prasad, P. S. S., Raju, B. D., Rao, K. S. R. (2015) 'Hydrotalcite-SBA-15 composite material for efficient carbondioxide capture', *Journal of CO_2 Utilization*, 12, pp. 109–115. doi: 10.1016/j.jcou.2015.05.002.

Psofogiannakis, G. M., McCleerey, J. F., Jaramillo, E., Van Duin, A. C. T. (2015) 'ReaxFF reactive molecular dynamics simulation of the hydration of Cu-SSZ-13 zeolite and the formation of Cu dimers', *Journal of Physical Chemistry C*, 119(12), pp. 6678–6686. doi: 10.1021/acs.jpcc.5b00699.

Purdue, M. J. and Qiao, Z. (2018) 'Molecular simulation study of wet flue gas adsorption on zeolite 13X', *Microporous and Mesoporous Materials*, 261(October 2017), pp. 181–197. doi: 10.1016/j.micromeso.2017.10.059.

Ram Reddy, M. K., Xu, Z. P., Lu, G. Q., da Costa, J. C. D. (2006) 'Layered Double Hydroxides for CO_2 Capture: Structure Evolution and Regeneration', *Industrial & Engineering Chemistry Research*, 45(22), pp. 7504–7509. doi: 10.1021/ie060757k.

Rappé, A. K., Casewit, C. J., Colwell, K. S., Goddard, W. A., Skiff, W. M. (1992) 'UFF, a Full Periodic Table Force Field for Molecular Mechanics and Molecular Dynamics Simulations', *Journal of the American Chemical Society*, 114(25), pp. 10024–10035. doi: 10.1021/ja00051a040.

Rappoport, D., Crawford, N. R. M., Furche, F., Burke, K. (2011) ‘Approximate Density Functionals: Which Should I Choose?’, *Encyclopedia of Inorganic and Bioinorganic Chemistry*. doi: 10.1002/9781119951438.eibc0380.

Rashidi, N. A. and Yusup, S. (2016) ‘An overview of activated carbons utilization for the post-combustion carbon dioxide capture’, *Journal of* CO_2 *Utilization*, 13, pp. 1–16. doi: 10.1016/j.jcou.2015.11.002.

Riboldi, L. and Bolland, O. (2015) ‘Evaluating Pressure Swing Adsorption as a CO_2 separation technique in coal-fired power plants’, *International Journal of Greenhouse Gas Control*, 39, pp. 1–16. doi: https://doi.org/10.1016/j.ijggc.2015.02.001.

Riboldi, L. and Bolland, O. (2017) ‘Overview on Pressure Swing Adsorption (PSA) as CO_2 Capture Technology: State-of-the-Art, Limits and Potentials’, *Energy Procedia*, 114, pp. 2390–2400. doi: https://doi.org/10.1016/j.egypro.2017.03.1385.

Ritchie, H. and Roser, M. (2020) *Energy mix, Our World in Data*. Available at: https://ourworldindata.org/energy-mix (Accessed: 12 July 2012).

Rives, V. (1999) ‘Comment on “ Direct Observation of a Metastable Solid Phase of Mg / Al / CO_3 -Layered Double Hydroxide by Means of High-Temperature in Situ Powder XRD and DTA/TG"’, *Inorganic Chemistry*, 38(2), pp. 406–407. doi: 10.1021/ic980739y.

Rochelle, G. T. (2009) ‘Amine Scrubbing for CO_2 Capture’, *Science*, 325(September 2009), pp. 1652–1654. doi: 10.1126/science.1176731.

Rouquerol, F., Rouquerol, J. and Sing, K. S. W. (1998) ‘Assessment of Surface Area’, in *Chapter 6. Adsorption by Powders and Porous Solids : Principles, Methodology, and Applications*. Marseille: Elsevier Science & Technology, Academic Press. Available at: https://ebookcentral.proquest.com/lib/sheffield/detail.action?docID=311285#.

Sadeghi, M. and Kalantar, M. (2014) ‘Multi types DG expansion dynamic planning in distribution system under stochastic conditions using Covariance Matrix Adaptation Evolutionary Strategy and Monte-Carlo simulation’, *Energy Conversion and Management*, 87, pp. 455–471. doi: 10.1016/J.ENCONMAN.2014.07.010.

Salaudeen, S. A., Acharya, B. and Dutta, A. (2018) ‘CaO-based CO_2 sorbents: A review on screening, enhancement, cyclic stability, regeneration and kinetics modelling’, *Journal of* CO_2 *Utilization*, 23(July 2017), pp. 179–199. doi: 10.1016/j.jcou.2017.11.012.

SCM (2017) ‘ReaxFF Manual’, pp. 1–60. doi: 10.1210/jc.2003-032149.

SCM (2018a) *AMS Manual - ADF Modeling Suite 2018*. Amsterdam. Available at: www.scm.com.

SCM (2018b) *Reparametrizing ReaxFF with the CMA-ES optimizer*, *ReaxFF advanced tutorials*. Available at: https://www.scm.com/doc/Tutorials/Advanced/ReaxFF_parametrization_hands_on_tutorial.html#reparametrizing-reaxff-with-the-cma-es-optimizer (Accessed: 20 August 2019).

SCM (2019) *Grand Canonical Monte Carlo (GCMC), Documentation*. Available at: https://www.scm.com/doc/AMS/Tasks/GCMC.html?highlight=GCMC (Accessed: 21 May 2020).

Sekerka, R. F. (2015) *Thermal Physics: Thermal Physics for Scientists and Engineers*. Pittsburgh: Carnegie Mellon University / Elsevier.

Senftle, T. P., Hong, S., Islam, M. M., Kylasa, S. B., Zheng, Y., Shin, Y. K., Junkermeier, C. Engel-Herbert, R., Janik, Michael J., Aktulga, H. M., Verstraelen, T., Grama, A., Van Duin, A. C.T. (2016) 'The ReaxFF reactive force-field: Development, applications and future directions', *npj Computational Materials*, 2(November 2015). doi: 10.1038/npjcompumats.2015.11.

Shaw, R. A. and Hatton, T. A. (2020) 'Electrochemical CO_2 capture thermodynamics', *International Journal of Greenhouse Gas Control*, 95(January), p. 102878. doi: 10.1016/j.ijggc.2019.102878.

Shchygol, G., Yakovlev, A., Trnka, T., van Duin, A. C. T. (2018) 'Systematic comparison of Monte Carlo Annealing and Covariance Matrix Adaptation for the optimization of ReaxFF parameters', *ChemRxviv*. doi: doi.org/10.26434/chemrxiv.6606668.v1.

Shen, C., Liu, Z., Li, P., Yu, J. (2012) 'Two-Stage VPSA Process for CO_2 Capture from Flue Gas Using Activated Carbon Beads', *Industrial & Engineering Chemistry Research*, 51(13), pp. 5011–5021. doi: 10.1021/ie202097y.

Sideris, P. J., Blanc, F., Gan, Z., Grey, C. (2012) 'Identification of cation clustering in Mg-Al layered double hydroxides using multinuclear solid state nuclear magnetic resonance spectroscopy', *Chemistry of Materials*, 24(13), pp. 2449–2461. doi: 10.1021/cm300386d.

Siegelman, R. L., Milner, P.J., Kim, E. J., Weston, S. C, Long, J. R. (2019) 'Challenges and opportunities for adsorption-based CO_2 capture from natural gas combined cycle emissions', *Energy and Environmental Science*, 12(7), pp. 2161–2173. doi: 10.1039/c9ee00505f.

Silva, J. M., Trujillano, R., Rives, V., Soria, M.A., Madeira, L.M. (2017) 'High temperature CO_2 sorption over modified hydrotalcites', *Chemical Engineering Journal*, 325, pp. 25–34. doi: 10.1016/j.cej.2017.05.032.

Spallina, V., Martynov, S., Porter, R., Mahgerefteh, H. (2021) *System simulation for integration of CO_2 capture technologies into steelworks and CCUS clusters Advanced Carbon Capture for Steel Industries Integrated in CCUS Clusters*. Available at: https://c4u-project.eu/wp-content/uploads/2021/05/IWCCU-C4U-Presentation-Spallina-1A_2.pdf (Accessed: 10 June 2021).

Suter, J. L., Anderson, R. L., Greenwell, H. C., Coveney, P. V. (2009) 'Recent advances in large-scale atomistic and coarse-grained molecular dynamics simulation of clay minerals', *Journal of Materials Chemistry*, 19(17), pp. 2482–2493. doi: 10.1039/b820445d.

Svante (2020) *A Center For Testing and Innovation*. Available at: https://svanteinc.com/carbon-capture-technology/ (Accessed: 30 June 2020).

Tavares, S. R., Haddad, J. F.S., Moraes, P. I. R., Leitão, A. A. (2020) 'Computational exploration of the anion exchange on the basal surface of layered double hydroxides by molecular dynamics', *Applied Surface Science*, 513(November 2019), p. 145743. doi: 10.1016/j.apsusc.2020.145743.

Teo, H. W. B., Chakraborty, A. and Kayal, S. (2017) 'Evaluation of CH_4 and CO_2 adsorption on HKUST-1 and MIL-101(Cr) MOFs employing Monte Carlo simulation and comparison with experimental data', *Applied Thermal Engineering*, 110, pp. 891–900. doi: 10.1016/j.applthermaleng.2016.08.126.

Teppen, B. J., Rasmussen, K., Bertsch, P. M., Miller, D. M., Schäfer, L. (1997) 'Molecular dynamics modeling of clay minerals. 1. gibbsite, kaolinite, pyrophyllite, and beidellite', *Journal of Physical Chemistry B*, 101(9), pp. 1579–1587. doi: 10.1021/jp961577z.

Theodorou, D. N. (2010) 'Progress and outlook in Monte Carlo simulations', *Industrial and Engineering Chemistry Research*, 49(7), pp. 3047–3058. doi: 10.1021/ie9019006.

Townsend, A., Raji, N. and Zapantis, A. (2020) *The Value of Carbon Capture and Storage (CCS)*. Global CCS institute. Available at: https://www.globalccsinstitute.com/resources/publications-reports-research/the-value-of-carbon-capture-ccs/ (Accessed: 16 November 2021).

Trave, A., Selloni, A., Goursot, A., Tichit, D., Weber, J. (2002) 'First principles study of the structure and chemistry of Mg-based hydrotalcite-like anionic clays', *Journal of Physical Chemistry B*, 106(47), pp. 12291–12296. doi: 10.1021/jp026339k.

Tuinier, M. J., van Sint Annaland, M., Kramer, G. J., Kuipers, J. A M (2010) 'Cryogenic CO_2 capture using dynamically operated packed beds', *Chemical Engineering Science*, 65(1), pp. 114–119. doi: 10.1016/j.ces.2009.01.055.

UK-Guangdong CCUS Centre (2017) *Haifeng CO_2 Capture Testing Platform Contract Signed: Project Enters Engineering Stage*, *News*. Available at: http://www.gdccus.org/en/nd.jsp?id=560 (Accessed: 29 June 2020).

UNFCCC (2015) 'Paris Agreement', in *Conference of the Parties on its twenty-first session*. Paris: United Nations Framework Convention on Climate Change, p. 25. doi: FCCC/CP/2015/L.9/Rev.1.

te Velde, G., Bickelhaupt, F. M., Baerends, E. J., Fonseca Guerra, C., van Gisbergen, S. J.A. Snijders, J. G., Ziegler, T. (2001) 'Chemistry with ADF', *Journal of Computational Chemistry*, 22(9), pp. 931–967. doi: 10.1002/jcc.1056.

Wang, J., Kalinichev, A. G., Kirkpatrick, R. J., Hou, X. (2001) 'Molecular modeling of the structure and energetics of hydrotalcite hydration', *Chemistry of Materials*, 13(1), pp. 145–150. doi: 10.1021/cm000441h.

Wang, L., Yang, Y., Shen, W., Kong, X., Li, P., Yu, J., Rodrigues, A. E. (2013) 'CO_2 capture from flue gas in an existing coal-fired power plant by two successive pilot-scale VPSA units', *Industrial and Engineering Chemistry Research*, 52(23), pp. 7947–7955. doi: 10.1021/ie4009716.

Wang, Q., Tay, H. H., Ng, D. J. W., Chen, L., Liu, Y., Chang, J., Zhong, Z., Luo, J., Borgna, A. (2010) 'The Effect of Trivalent Cations on the Performance of Mg-M-CO_3 Layered Double Hydroxides for High-Temperature CO_2 Capture', *ChemSusChem*, 3(8), pp. 965–973. doi: 10.1002/cssc.201000099.

Wang, Q., Luo, J., Zhong, Z., Borgna, A. (2011) 'CO_2 capture by solid adsorbents and their applications: current status and new trends', *Energy Environ. Sci.*, 4, pp. 42–55. doi: 10.1039/C0EE00064G.

Wang, Q., Wu, Z., Wu, Z., Tay, H. H., Chen, L., Liu, Y., Chang, J., Zhong, Z., Luo, J., Borgna, A. (2011) 'High temperature adsorption of CO_2 on Mg-Al hydrotalcite: Effect of the charge compensating anions and the synthesis pH', *Catalysis Today*, 164(1), pp. 198–203. doi: 10.1016/j.cattod.2010.10.042.

Wang, Y., Li, Z., Otto, A., Robinius, M., Stolten, D., (2017) 'A review of Post-combusstion CO_2 Capture Technologies from Coal-fired Power Plants', *Energy Procedia*, 114, pp. 650 – 665. doi:10.1016/j.egypro.2017.03.1209.

Wang, Y., Hu, X., Hao, J., Ma, R., Guo, Q., Gao, H., Bai, H. (2019) 'Nitrogen and Oxygen Codoped Porous Carbon with Superior CO_2 Adsorption Performance: A Combined Experimental and DFT Calculation Study', *Industrial and Engineering Chemistry Research*, 58(29), pp. 13390–13400. doi: 10.1021/acs.iecr.9b01454.

Webley, P. A. (2014) 'Adsorption technology for CO_2 separation and capture: a perspective', *Adsorption*, 20(2), pp. 225–231. doi: 10.1007/s10450-014-9603-2.

Wilmer, C. E. and Snurr, R. Q. (2011) 'Towards rapid computational screening of metal-organic frameworks for carbon dioxide capture: Calculation of framework charges via charge equilibration', *Chemical Engineering Journal*, 171(3), pp. 775–781. doi: 10.1016/j.cej.2010.10.035.

Winter, F., Koot, V., Van Dillen, A. J., Geus, J. W., de Jong, K. P. (2005) 'Hydrotalcites supported on carbon nanofibers as solid base catalysts for the synthesis of MIBK', *Journal of Catalysis*, 236(1), pp. 91–100. doi: 10.1016/j.jcat.2005.09.020.

Wolsky, A. M., Daniels, E. J. and Jody, B. J. (1994) 'CO_2 capture from the flue gas of conventional fossil-fuel-fired power plants', *Environmental Progress*, 13(3), pp. 214–219. doi: 10.1002/ep.670130320.

Wolters, L. P. (2016) *Molecular Orbital Perspectives on Catalyst Design and Halogen Bonds - Molecular Orbital Perspectives on Catalyst Design and Halogen Bonds*. Vrije. Available at: https://www.scm.com/wp-content/uploads/Chemical_Bonding_and_Catalysis_thesis_Wolters.pdf.

Wu, Y. J., Li, P., Yu, J. G., Cunha, A. F., Rodrigues, A. E. (2013) 'K-Promoted Hydrotalcites for CO_2 Capture in Sorption Enhanced Reactions', *Chemical Engineering and Technology*, 36(4), pp. 567–574. doi: 10.1002/ceat.201200694.

Yaghi, O. M., Li, G. and Li, H. (1995) 'Selective binding and removal of guests in a microporous metal–organic framework', *Nature*, 378(6558), pp. 703–706. doi:

10.1038/378703a0.

Yan, H., Wei, M., Jing, M., Li, F., Evans, D. G., Duan, X. (2009) ‘Theoretical study on the structural properties and relative stability of M(II)-Al layered double hydroxides based on a cluster model’, *Journal of Physical Chemistry A*, 113(21), pp. 6133–6141. doi: 10.1021/jp810129h.

Yi, C. K. (2015) *Dry Solid Sorbent* CO_2 *Capture Project of 10 MWe scale*, *Carbon Sequestration Leadership Forum*. Available at: https://www.cslforum.org/cslf/sites/default/files/documents/riyadh2015/Yi-DrySolidSorbentProject-TG-Riyadh1115.pdf (Accessed: 22 April 2020).

Younas, M., Sohail, M., Leong, L. K., Bashir, M. J. K., Sumathi, S. (2016) ‘Feasibility of CO_2 adsorption by solid adsorbents: a review on low-temperature systems’, *International Journal of Environmental Science and Technology*, 13(7), pp. 1839–1860. doi: 10.1007/s13762-016-1008-1.

Yu, H. S., Li, S. L. and Truhlar, D. G. (2016) ‘Perspective: Kohn-Sham density functional theory descending a staircase’, *Journal of Chemical Physics*, 145(13). doi: 10.1063/1.4963168.

Yu, M., Underhill, P., Ritter, J., Sexton, A., Morton, F. (2019) *Transformational Molecular Layer Deposition Tailor-made Size-sieving Sorbents for Post-Combustion* CO_2 *Capture DOE Contract No. DE-FE0031730*. Morgantown, WV. Available at: https://netl.doe.gov/projects/files/2019 DE-FE0031730_Kickoff Meeting_updated_1122.pdf.

Zhang, B., Van Duin, A. C. T. and Johnson, J. K. (2014) ‘Development of a ReaxFF reactive force field for tetrabutylphosphonium glycinate/CO_2 mixtures’, *Journal of Physical Chemistry B*, 118(41), pp. 12008–12016. doi: 10.1021/jp5054277.

Zhang, J., Burke, N., Zhang, S., Liu, K.,Pervukhina, M. (2014) ‘Thermodynamic analysis of molecular simulations of CO_2 and CH_4 adsorption in FAU zeolites’, *Chemical Engineering Science*, 113, pp. 54–61. doi: 10.1016/j.ces.2014.04.001.

Zhang, S. T., Yan, H., Wei, M., Evans, D. G., Duan, X. (2012) ‘Valence force field for layered double hydroxide materials based on the parameterization of octahedrally coordinated metal cations’, *Journal of Physical Chemistry C*, 116(5), pp. 3421–3431. doi: 10.1021/jp211194w.

Zhang, S. T., Dou, Y., Zhou, J., Pu, M., Yan, H., Wei, M., Evans, D. G., Duan, Xue (2016) ‘DFT-Based Simulation and Experimental Validation of the Topotactic Transformation of MgAl Layered Double Hydroxides’, *ChemPhysChem*, (17), pp. 2754–2766. doi: 10.1002/cphc.201600354.

Zhao, H., Luo, X., Zhang, H., Sun, N., Wei, W., Sun, Yuhan (2018) ‘Carbon-based adsorbents for post-combustion capture: a review’, *Greenhouse Gases: Science and Technology*, 8(1), pp. 11–36. doi: 10.1002/ghg.1758.

Zhao, R., Zhao, L., Deng, S., Song, C., He, J., Shao, Y., Li, S. (2017) ‘A comparative study on CO_2 capture performance of vacuum-pressure swing adsorption and pressure-temperature swing adsorption based on carbon pump cycle’, *Energy*, 137, pp. 495–509. doi: 10.1016/j.energy.2017.01.158.

Zhao, X.-J., Zhu, Y.-Q., Xu, S., Liu, H.-M., Yin, P., Feng, Y.-L., Yan, H. (2020) 'Anion Exchange Behavior of M II Al Layered Double Hydroxides: a Molecular Dynamics and DFT Study', *Physical Chemistry Chemical Physics*, (3). doi: 10.1039/d0cp02537b.

Zhao, Y., Liu, X. and Han, Y. (2015) 'Microporous carbonaceous adsorbents for CO_2 separation via selective adsorption', *RSC Adv.*, 5(38), pp. 30310–30330. doi: 10.1039/C5RA00569H.

Zhu, X., Shi, Y., Li, S., Cai, N. (2018) 'Elevated temperature pressure swing adsorption process for reactive separation of CO/CO_2 in H_2-rich gas', *International Journal of Hydrogen Energy*, 43(29), pp. 13305–13317. doi: 10.1016/j.ijhydene.2018.05.030.

9. Appendix

a. Geometry file for SC1

```
336

Frame 0: Geometry 1, Energy: -69.13694 Hartree

H -6.852037499986984 3.956025699992485 18.93112059996404

H 0.5610993699989341 -3.840418159992705 18.92997495996404

H -1.017455029998067 -1.822207309996539 18.92279036996405

H -6.852037499986984 3.956025699992485 9.579821999981803

H 0.7613374999985537 -3.956025699992485 9.579821999981803

H 3.806687499992769 -3.956025699992485 18.93112059996404

H 5.329362499989877 -3.076908869994155 20.6881779999607

H 0.7613374999985537 1.318675229997495 18.93112059996404

H -0.5726079799989123 -1.427638269997288 9.700745399981573

H -2.284012499995661 1.536601309997081 9.700745399981573

H 5.329362499989877 -1.318675229997495 18.93112059996404

H 3.806687499992769 1.318675229997495 18.93112059996404

H 2.284012499995661 3.956025699992485 18.93112059996404

H -2.284012499995661 -3.956025699992485 3.769879399992839

H 6.852037499986984 -3.956025699992485 9.579821999981803

O 4.638061679991189 -3.476031589993397 18.92636397996405

H -6.852037499986984 3.956025699992485 3.769879399992839

H 0.7613374999985537 -3.956025699992485 3.769879399992839

O 3.496447709993358 -0.6186754399988248 18.92537749996405

H -2.284012499995661 1.318675229997495 3.769879399992839

H -0.7613374999985537 4.173951779992072 9.700745399981573

H 0.7613374999985537 -2.197792049995825 2.012821999996176

H 2.284012499995661 5.714259339989145 5.55417799998945

H 0.7613374999985537 1.318675229997495 3.769879399992839

H -0.1972071599996254 3.926063949992542 3.778209629992823

H 6.852037499986984 -3.956025699992485 3.769879399992839

H 0.7613374999985537 -0.439558409999165 20.6881779999607

O 6.160736679988298 -0.8386811199984068 18.92636397996405

H 2.284012499995661 3.956025699992485 3.769879399992839
```

H	-1.325467839997482	-3.046947119994212	3.788790369992803
H	-1.975999689996246	0.03401191999993539	3.788790369992803
H	-0.7613374999985537	-3.076908869994155	17.14682199996743
H	-5.893492839988805	4.865104269990758	3.788790369992803
H	1.719882159996733	-3.046947119994212	3.788790369992803
H	0.9500670199981952	3.185871909993948	5.433254599989678
H	-0.5052199699990403	1.694259969996782	3.788790369992803
H	-3.806687499992769	0.439558409999165	5.55417799998945
H	5.45342446998964	-3.305267109993721	3.794124499992793
H	-2.284012499995661	-0.439558409999165	20.6881779999607
H	-2.224016949995775	3.111547319994089	5.515737449989522
H	0.7613374999985537	4.835142519990815	3.797120599992787
H	5.329362499989877	-1.318675229997495	9.579821999981803
H	8.37471249998409	-3.076908869994155	20.6881779999607
O	2.284012499995661	-2.509878519995232	18.92521833996405
H	3.550569969993255	4.331610429991771	3.788790369992803
Mg	-2.284012499995661	-3.956025699992485	0.0
Mg	-3.806687499992769	-1.318675229997495	0.0
Al	-5.329362499989877	1.318675229997495	0.0
Mg	-6.852037499986984	3.956025699992485	0.0
Mg	0.7613374999985537	-3.956025699992485	0.0
Al	-0.7613374999985537	-1.318675229997495	0.0
Mg	-2.284012499995661	1.318675229997495	0.0
Mg	-3.806687499992769	3.956025699992485	0.0
Al	3.806687499992769	-3.956025699992485	0.0
Mg	2.284012499995661	-1.318675229997495	0.0
Mg	0.7613374999985537	1.318675229997495	0.0
Mg	-0.7613374999985537	3.956025699992485	0.0
Mg	6.852037499986984	-3.956025699992485	0.0
Mg	5.329362499989877	-1.318675229997495	0.0
Mg	3.806687499992769	1.318675229997495	0.0
Al	2.284012499995661	3.956025699992485	0.0
Mg	-0.7613374999985537	-3.076908869994155	7.566999999985626
Mg	-2.284012499995661	-0.439558409999165	7.566999999985626

Al	-3.806687499992769	2.197792049995825	7.566999999985626
Mg	-5.329362499989877	4.835142519990815	7.566999999985626
Mg	2.284012499995661	-3.076908869994155	7.566999999985626
Al	0.7613374999985537	-0.439558409999165	7.566999999985626
Mg	-0.7613374999985537	2.197792049995825	7.566999999985626
Mg	-2.284012499995661	4.835142519990815	7.566999999985626
Mg	5.329362499989877	-3.076908869994155	7.566999999985626
Mg	3.806687499992769	-0.439558409999165	7.566999999985626
Mg	2.284012499995661	2.197792049995825	7.566999999985626
Al	0.7613374999985537	4.835142519990815	7.566999999985626
Al	8.37471249998409	-3.076908869994155	7.566999999985626
Mg	6.852037499986984	-0.439558409999165	7.566999999985626
Mg	5.329362499989877	2.197792049995825	7.566999999985626
Mg	3.806687499992769	4.835142519990815	7.566999999985626
Al	-2.284012499995661	-2.197792049995825	15.13399999997125
Mg	-3.806687499992769	0.439558409999165	15.13399999997125
Mg	-5.329362499989877	3.076908869994155	15.13399999997125
Mg	-6.852037499986984	5.714259339989145	15.13399999997125
Mg	0.7613374999985537	-2.197792049995825	15.13399999997125
Mg	-0.7613374999985537	0.439558409999165	15.13399999997125
Mg	-2.284012499995661	3.076908869994155	15.13399999997125
Al	-3.806687499992769	5.714259339989145	15.13399999997125
Mg	3.806687499992769	-2.197792049995825	15.13399999997125
Mg	2.284012499995661	0.439558409999165	15.13399999997125
Al	0.7613374999985537	3.076908869994155	15.13399999997125
Mg	-0.7613374999985537	5.714259339989145	15.13399999997125
Mg	6.852037499986984	-2.197792049995825	15.13399999997125
Al	5.329362499989877	0.439558409999165	15.13399999997125
Mg	3.806687499992769	3.076908869994155	15.13399999997125
Mg	2.284012499995661	5.714259339989145	15.13399999997125
O	-2.284012499995661	-3.956025699992485	14.15838668997311
O	-3.806687499992769	-1.318675229997495	14.15838668997311
O	-5.329362499989877	1.318675229997495	14.15838668997311
O	-6.852037499986984	3.956025699992485	14.15838668997311

O	0.7613374999985537	-3.956025699992485	14.15838668997311
O	-0.7613374999985537	-1.318675229997495	14.15838668997311
O	-2.284012499995661	1.318675229997495	14.15838668997311
O	-3.806687499992769	3.956025699992485	14.15838668997311
O	3.806687499992769	-3.956025699992485	14.15838668997311
O	2.284012499995661	-1.318675229997495	14.15838668997311
O	0.7613374999985537	1.318675229997495	14.15838668997311
O	-0.7613374999985537	3.956025699992485	14.15838668997311
O	6.852037499986984	-3.956025699992485	14.15838668997311
O	5.329362499989877	-1.318675229997495	14.15838668997311
O	3.806687499992769	1.318675229997495	14.15838668997311
O	2.284012499995661	3.956025699992485	14.15838668997311
O	-2.284012499995661	-3.956025699992485	8.542613309983771
O	-3.806687499992769	-1.318675229997495	8.542613309983771
O	-5.329362499989877	1.318675229997495	8.542613309983771
O	-6.852037499986984	3.956025699992485	8.542613309983771
O	0.7613374999985537	-3.956025699992485	8.542613309983771
O	-0.5726079799989123	-1.427638269997288	8.663536709983543
O	-2.284012499995661	1.536601309997081	8.663536709983543
O	-3.806687499992769	3.956025699992485	8.542613309983771
O	3.806687499992769	-3.956025699992485	8.542613309983771
O	2.284012499995661	-1.318675229997495	8.542613309983771
O	0.7613374999985537	1.318675229997495	8.542613309983771
O	-0.7613374999985537	4.173951779992072	8.663536709983543
O	6.852037499986984	-3.956025699992485	8.542613309983771
O	5.329362499989877	-1.318675229997495	8.542613309983771
O	3.806687499992769	1.318675229997495	8.542613309983771
O	2.284012499995661	3.956025699992485	8.542613309983771
O	-0.7613374999985537	-3.076908869994155	21.72538668995873
O	-2.284012499995661	-0.439558409999165	21.72538668995873
O	-3.806687499992769	2.197792049995825	21.72538668995873
O	-5.329362499989877	4.835142519990815	21.72538668995873
O	2.284012499995661	-3.076908869994155	21.72538668995873
O	0.7613374999985537	-0.439558409999165	21.72538668995873

```
O -0.7613374999985537 2.197792049995825 21.72538668995873

O -2.284012499995661 4.835142519990815 21.72538668995873

O 5.329362499989877 -3.076908869994155 21.72538668995873

O 3.806687499992769 -0.439558409999165 21.72538668995873

O 2.284012499995661 2.197792049995825 21.72538668995873

O 0.7613374999985537 4.835142519990815 21.72538668995873

O 8.37471249998409 -3.076908869994155 21.72538668995873

O 6.852037499986984 -0.439558409999165 21.72538668995873

O 5.329362499989877 2.197792049995825 21.72538668995873

O 3.806687499992769 4.835142519990815 21.72538668995873

O -0.7613374999985537 -3.076908869994155 16.1096133099694

O -2.284012499995661 -0.439558409999165 16.1096133099694

O -3.806687499992769 2.197792049995825 16.1096133099694

O -5.329362499989877 4.835142519990815 16.1096133099694

O 2.284012499995661 -3.076908869994155 16.1096133099694

O 0.7613374999985537 -0.439558409999165 16.1096133099694

O -0.7613374999985537 2.197792049995825 16.1096133099694

O -2.284012499995661 4.835142519990815 16.1096133099694

O 5.329362499989877 -3.076908869994155 16.1096133099694

O 3.806687499992769 -0.439558409999165 16.1096133099694

O 2.284012499995661 2.197792049995825 16.1096133099694

O 0.7613374999985537 4.835142519990815 16.1096133099694

O 8.37471249998409 -3.076908869994155 16.1096133099694

O 6.852037499986984 -0.439558409999165 16.1096133099694

O 5.329362499989877 2.197792049995825 16.1096133099694

O 3.806687499992769 4.835142519990815 16.1096133099694

O -2.284012499995661 -2.197792049995825 6.591386689987479

O -3.806687499992769 0.439558409999165 6.591386689987479

O -5.329362499989877 3.076908869994155 6.591386689987479

O -6.852037499986984 5.714259339989145 6.591386689987479

O 0.7613374999985537 -2.197792049995825 6.591386689987479

O -0.7613374999985537 0.439558409999165 6.591386689987479

O -2.224016949995775 3.111547319994089 6.552946139987553

O -3.806687499992769 5.714259339989145 6.591386689987479
```

```
O 3.806687499992769 -2.197792049995825 6.591386689987479

O 2.284012499995661 0.439558409999165 6.591386689987479

O 0.9500670199981952 3.185871909993948 6.470463289987708

O -0.7613374999985537 5.714259339989145 6.591386689987479

O 6.852037499986984 -2.197792049995825 6.591386689987479

O 5.329362499989877 0.439558409999165 6.591386689987479

O 3.806687499992769 3.076908869994155 6.591386689987479

O 2.284012499995661 5.714259339989145 6.591386689987479

O -2.284012499995661 -2.197792049995825 0.9756133099981467

O -3.806687499992769 0.439558409999165 0.9756133099981467

O -5.329362499989877 3.076908869994155 0.9756133099981467

O -6.852037499986984 5.714259339989145 0.9756133099981467

O 0.7613374999985537 -2.197792049995825 0.9756133099981467

O -0.7613374999985537 0.439558409999165 0.9756133099981467

O -2.284012499995661 3.076908869994155 0.9756133099981467

O -3.806687499992769 5.714259339989145 0.9756133099981467

O 3.806687499992769 -2.197792049995825 0.9756133099981467

O 2.284012499995661 0.439558409999165 0.9756133099981467

O 0.7613374999985537 3.076908869994155 0.9756133099981467

O -0.7613374999985537 5.714259339989145 0.9756133099981467

O 6.852037499986984 -2.197792049995825 0.9756133099981467

O 5.329362499989877 0.439558409999165 0.9756133099981467

O 3.806687499992769 3.076908869994155 0.9756133099981467

O 2.284012499995661 5.714259339989145 0.9756133099981467

H -2.284012499995661 -2.197792049995825 2.012821999996176

O -1.848829219996488 -1.34221320999745 18.91803374996406

O 2.594252289995072 0.2604413899995053 3.791377499992798

H -3.806687499992769 0.439558409999165 2.012821999996176

H 0.7613374999985537 -3.956025699992485 13.12117799997507

O -0.4510977099991431 -1.139558209997835 11.34262249997845

H -0.7613374999985537 2.197792049995825 20.6881779999607

H -2.284012499995661 1.318675229997495 13.12117799997507

H -2.284012499995661 4.835142519990815 20.6881779999607

O -0.1972071599996254 4.886052159990718 3.782966249992814
```

```
O 6.393785689987854 -3.112531289994088 3.780946179992818
O -0.4510977099991431 4.135142719992145 11.34262249997845
H 4.000966949992399 -2.758022789994761 18.91318564996407
O -2.807373869994668 0.5140060299990236 3.784033749992812
H -0.7613374999985537 -3.076908869994155 20.6881779999607
H 2.284012499995661 -1.318675229997495 13.12117799997507
H -6.719461559987236 5.331796289989871 18.91043836996408
H 0.7613374999985537 3.076908869994155 2.012821999996176
H -6.852037499986984 5.714259339989145 11.36412059997841
O -6.852037499986984 4.916013909990662 3.77463601999283
O -2.284012499995661 -2.996037479994309 3.77463601999283
O 0.7613374999985537 0.9604411799981756 11.34262249997845
H 3.806687499992769 1.318675229997495 13.12117799997507
H 8.37471249998409 -3.076908869994155 17.14682199996743
O 5.329362499989877 -1.885705579996418 11.34278165997845
H -2.471808689995304 0.1244154399997636 11.34504000997845
H 0.7613374999985537 1.318675229997495 13.12117799997507
O 0.7613374999985537 6.026345809988552 11.34278165997845
O 8.37471249998409 -1.885705579996418 11.34278165997845
H 4.389001269991661 -2.078441399996052 11.35595998997843
O 5.329362499989877 3.388995349993562 11.34278165997845
H 2.284012499995661 3.956025699992485 9.579821999981803
H -0.7613374999985537 -1.318675229997495 13.12117799997507
H 6.852037499986984 -0.439558409999165 20.6881779999607
C -2.284012499995661 3.076908869994155 18.91068969996407
H -3.806687499992769 5.714259339989145 2.012821999996176
O 0.7613374999985537 -2.996037479994309 3.77463601999283
O 1.973772709996251 -1.139558209997835 11.34262249997845
H -2.284012499995661 -3.956025699992485 13.12117799997507
H 2.284012499995661 3.956025699992485 13.12117799997507
C 0.7613374999985537 4.835142519990815 11.34368969997845
O -6.12256083998837 4.580065399991299 18.92493652996405
H -3.618891309993125 2.761765899994754 11.34504000997845
O 1.973772709996251 4.135142719992145 11.34262249997845
```

H	-2.284012499995661	4.835142519990815	17.14682199996743
H	-2.471808689995304	5.399116359989743	11.34504000997845
C	0.7613374999985537	-0.439558409999165	11.34368969997845
H	3.806687499992769	3.076908869994155	2.012821999996176
H	-0.7613374999985537	2.197792049995825	17.14682199996743
O	-2.775075189994729	1.035160059998034	11.35821833997842
H	3.806687499992769	-2.197792049995825	2.012821999996176
O	-6.020663319988563	6.194253449988232	11.35936397997842
H	-2.284012499995661	-0.439558409999165	17.14682199996743
H	-3.806687499992769	-1.318675229997495	13.12117799997507
H	-2.284012499995661	-3.956025699992485	9.579821999981803
O	-2.775075189994729	6.309860979988013	11.35821833997842
H	-0.7613374999985537	5.714259339989145	5.55417799998945
H	3.806687499992769	1.318675229997495	9.579821999981803
H	-0.7613374999985537	3.956025699992485	13.12117799997507
H	-3.806687499992769	3.956025699992485	13.12117799997507
C	2.284012499995661	-1.318675229997495	18.92431029996405
H	8.37471249998409	-2.845693799994594	11.33802503997846
H	2.284012499995661	5.714259339989145	2.012821999996176
O	-2.594252289995072	3.256025899993815	3.775622499992828
O	0.3261542199993804	2.17425407999587	3.784033749992812
H	6.59591996998747	-1.694259969996782	18.91220962996407
H	6.852037499986984	-2.197792049995825	2.012821999996176
O	-0.2702748099994866	-3.360424049993617	18.92521833996405
H	0.7613374999985537	4.835142519990815	17.14682199996743
O	-4.838299809990809	3.360424049993617	3.775781659992827
H	-0.7613374999985537	5.714259339989145	2.012821999996176
H	2.284012499995661	0.439558409999165	2.012821999996176
C	-3.806687499992769	3.956025699992485	3.776689699992826
H	5.129124369990257	0.5551659499989454	11.36297495997841
H	-5.329362499989877	1.318675229997495	13.12117799997507
H	-3.806687499992769	-1.318675229997495	9.579821999981803
O	-3.806687499992769	5.147228989990222	3.775781659992827
O	2.719195779994835	4.81160453999086	3.784033749992812

```
H -5.58548002998939 5.338674599989858 11.34520962997845

H 6.852037499986984 -3.956025699992485 13.12117799997507

H -3.806687499992769 2.197792049995825 17.14682199996743

H 5.329362499989877 0.439558409999165 2.012821999996176

H -0.7613374999985537 0.439558409999165 2.012821999996176

O 3.806687499992769 -1.839557999996505 3.791377499992798

H 6.852037499986984 -2.197792049995825 5.55417799998945

H 5.329362499989877 2.429007129995386 11.33802503997846

O -3.315624809993702 3.672510519993023 11.35821833997842

H 4.389001269991661 3.196259519993928 11.35595998997843

C 3.806687499992769 -0.439558409999165 3.790310299992799

H -6.852037499986984 3.956025699992485 13.12117799997507

H -5.329362499989877 1.318675229997495 9.579821999981803

O 1.071577289997965 -0.6186754399988248 18.92537749996405

H -3.606449369993149 0.5551659499989454 11.36297495997841

O 4.297750189991836 1.035160059998034 11.35821833997842

H 5.329362499989877 -1.318675229997495 13.12117799997507

H 3.806687499992769 -3.956025699992485 13.12117799997507

H 6.852037499986984 -0.439558409999165 17.14682199996743

H -5.329362499989877 3.076908869994155 5.55417799998945

O -3.496447709993358 2.376909079995484 18.90962249996408

H 3.806687499992769 -0.439558409999165 20.6881779999607

H 5.329362499989877 -2.845693799994594 11.33802503997846

O 5.019122709990466 0.2604413899995053 3.791377499992798

H 0.3668199199993032 -2.64241524999498 18.91204000996407

H -3.806687499992769 3.956025699992485 9.579821999981803

H 5.329362499989877 -3.076908869994155 17.14682199996743

H -2.284012499995661 3.076908869994155 2.012821999996176

H -5.329362499989877 3.076908869994155 2.012821999996176

O 1.760651129996655 4.760694899990956 18.91696624996407

H -3.806687499992769 2.197792049995825 20.6881779999607

H -5.329362499989877 4.835142519990815 17.14682199996743

H 5.329362499989877 2.197792049995825 20.6881779999607

H -3.806687499992769 5.714259339989145 5.55417799998945
```

H	5.329362499989877	2.197792049995825	17.14682199996743
H	-6.852037499986984	5.714259339989145	5.55417799998945
H	3.612408049993138	2.516678139995219	18.91318564996407
H	2.284012499995661	2.197792049995825	20.6881779999607
H	-2.484250629995281	3.192516409993936	11.36297495997841
H	-2.284012499995661	-2.197792049995825	18.90387939996409
H	3.806687499992769	-3.956025699992485	9.579821999981803
O	-2.284012499995661	4.476908469991495	18.90962249996408
H	3.806687499992769	-0.439558409999165	17.14682199996743
H	3.994483689992412	0.1244154399997636	11.34504000997845
H	-6.852037499986984	5.714259339989145	2.012821999996176
H	5.329362499989877	0.439558409999165	5.55417799998945
H	-5.329362499989877	4.835142519990815	20.6881779999607
H	2.284012499995661	-3.076908869994155	17.14682199996743
H	3.806687499992769	4.835142519990815	20.6881779999607
H	3.806687499992769	-2.197792049995825	5.55417799998945
H	3.806687499992769	4.835142519990815	17.14682199996743
H	0.7613374999985537	-2.197792049995825	5.55417799998945
H	2.592025309995076	5.240689009990044	18.91220962996407
H	0.7613374999985537	4.835142519990815	20.6881779999607
H	-3.606449369993149	5.829866879988925	11.36297495997841
H	2.284012499995661	-1.318675229997495	9.579821999981803
O	-1.071577289997965	2.376909079995484	18.90962249996408
H	0.5670580499989228	2.516678139995219	18.91318564996407
H	2.284012499995661	2.197792049995825	17.14682199996743
H	7.434351269985878	-2.078441399996052	11.35595998997843
O	1.398432229997344	2.036684029996131	18.91794226996407
H	3.806687499992769	3.076908869994155	5.55417799998945
H	2.284012499995661	-3.076908869994155	20.6881779999607
H	0.7613374999985537	-0.439558409999165	17.14682199996743
O	4.443782229991559	2.036684029996131	18.91794226996407
H	2.284012499995661	0.439558409999165	5.55417799998945
H	-2.284012499995661	-2.197792049995825	5.55417799998945
H	-0.7613374999985537	0.439558409999165	5.55417799998945

```
H 0.7613374999985537 1.318675229997495 9.579821999981803
VEC1 12.1814 0.0 0.0
VEC2 -6.0907 10.54940185 0.0
VEC3 0.0 0.0 22.701
```

b. Params file

```
#---------------------------------------------------

3 4 1   0.5   0.0000   300.0  #

3 4 2   0.5  -0.020    250.0  #

3 4 3   0.5   0.0000   200.0  #

3 4 4   0.1  -2.0000     1.0  #

3 4 5   0.1  -1.5000     0.5  #

3 4 7   0.1   0.0000    55.0  #       C-O bond params

3 4 8   0.1  -1.0000     1.5  #

3 4 9   0.1  -2.0000    25.0  #

3 4 10  0.1  -1.0000     1.0  #

3 4 11  0.1   0.0000    30.0  #

3 4 13  0.1  -1.0000   -0.02  #

3 4 14  0.1   0.0000    15.0  #

#---------------------------------------------------

4 2 1   0.05   0.0000     1.0   #

4 2 2   0.05   1.0000     4.0   #

4 2 3   0.1    1.0000    20.0   #       C-O off diag.

4 2 4   0.05  -1.0000     4.0   #

4 2 5   0.05  -2.0000     4.0   #

4 2 6   0.05  -2.0000     2.0   #

#---------------------------------------------------

3 7 1   0.5   0.0000   300.0   #

3 7 2   0.5  -0.020    250.0   #

3 7 3   0.5   0.0000   200.0   #

3 7 4   0.1  -2.0000     1.0   #

3 7 5   0.1  -1.5000     0.5   #

3 7 7   0.1   0.0000    55.0   #        C-N bond params

3 7 8   0.1  -1.0000     1.5   #

3 7 9   0.1  -2.0000    25.0   #

3 7 10  0.1  -1.0000     1.0   #

3 7 11  0.1   0.0000    30.0   #

3 7 13  0.1  -1.0000   -0.02   #

3 7 14  0.1   0.0000    15.0   #
```

```
#--------------------------------------------------
4 4 1  0.05   0.0000     1.0     #
4 4 2  0.05   1.0000     4.0     #
4 4 3  0.1    1.0000    20.0     #       C-N off diag.
4 4 4  0.05  -1.0000     4.0     #
4 4 5  0.05  -2.0000     4.0     #
4 4 6  0.05  -2.0000     2.0     #
#--------------------------------------------------
3 10 1   0.5   0.0000   300.0    #
3 10 2   0.5  -0.020    250.0    #
3 10 3   0.5   0.0000   200.0    #
3 10 4   0.1  -2.0000     1.0    #
3 10 5   0.1  -1.5000     0.5    #
3 10 7   0.1   0.0000    55.0    #        N-H bond params
3 10 8   0.1  -1.0000     1.5    #
3 10 9   0.1  -2.0000    25.0    #
3 10 10  0.1  -1.0000     1.0    #
3 10 11  0.1   0.0000    30.0    #
3 10 13  0.1  -1.0000   -0.02    #
3 10 14  0.1   0.0000    15.0    #
#--------------------------------------------------
4 5 1 0.05   0.0000     1.0     #
4 5 2 0.05   1.0000     4.0     #
4 5 3 0.1    1.0000    20.0     #       N-H off diag.
4 5 4 0.05  -1.0000     4.0     #
4 5 5 0.05  -2.0000     4.0     #
4 5 6 0.05  -2.0000     2.0     #
#--------------------------------------------------
5 9 1   0.5      0.00  180.0     #
5 9 2   0.1   -40.00   67.0     #
5 9 3   0.1      0.01   30.0     #       C-C-N
5 9 7   0.05     0.83    5.0     #
#--------------------------------------------------
5 34 1   0.5      0.00  180.0        #
```

```
5 34 2   0.1   -40.00   67.0        #
5 34 3   0.1     0.01   30.0        #       H-N-H
5 34 7   0.05    0.83    5.0        #
#--------------------------------------------------
5 10 1    0.5     0.00  180.0        #
5 10 2    0.1   -40.00   67.0        #
5 10 3    0.1     0.01   30.0        #       O-C-N
5 10 7    0.05    0.83    5.0        #
#--------------------------------------------------
5 15 1    0.5     0.00  180.0     #
5 15 2    0.1   -40.00   67.0     #
5 15 3    0.1     0.01   30.0     #       C-O-C
5 15 7    0.05    0.83    5.0     #
#--------------------------------------------------
5 31 1    0.5     0.00  180.0    #
5 31 2    0.1   -40.00   67.0    #
5 31 3    0.1     0.01   30.0    #       C-N-H
5 31 7    0.05    0.83    5.0    #
#--------------------------------------------------
5 7 1    0.5     0.00  180.0           #
5 7 2    0.1   -40.00   67.0           #
5 7 3    0.1     0.01   30.0           #       C-C-O
5 7 7    0.05    0.83    5.0           #
#--------------------------------------------------
5 12 1    0.5     0.00  180.0     #
5 12 2    0.1   -40.00   67.0     #
5 12 3    0.1     0.01   30.0     #       H-C-O
5 12 7    0.05    0.83    5.0     #
#--------------------------------------------------
7 2 1   0.05   1.0   2.5         #
7 2 2   0.05  -7.0  -1.0      #       O-H-N (H-Bonds)
#--------------------------------------------------
7 3 1    0.05   1.0   2.5        #
7 3 2    0.05  -7.0  -1.0        #       N-H-O (H-Bonds)
```

```
#---------------------------------------------------

7 4 1    0.05   1.0   2.5    #

7 4 2    0.05  -7.0  -1.0    #       N-H-N (H-Bonds)

#---------------------------------------------------
```

c. FF1 file

```
Reactive MD-force field: H/O/Si/Al/Cu, G.M. Psofogiannakis et al., J. Phys. Chem. C,
2015, 119 (12), pp 6678-6686, http://dx.doi.org/10.1021/acs.jpcc.5b00699
 39       ! Number of general parameters
   50.0000 !Overcoordination parameter
    9.5469 !Overcoordination parameter
   26.5405 !Valency angle conjugation parameter
    1.7224 !Triple bond stabilisation parameter
    6.8702 !Triple bond stabilisation parameter
   60.4850 !C2-correction
    1.0588 !Undercoordination parameter
    4.6000 !Triple bond stabilisation parameter
   12.1176 !Undercoordination parameter
   13.3056 !Undercoordination parameter
  -70.5044 !Triple bond stabilization energy
    0.0000 !Lower Taper-radius
   10.0000 !Upper Taper-radius
    2.8793 !Not used
   33.8667 !Valency undercoordination
    6.0891 !Valency angle/lone pair parameter
    1.0563 !Valency angle
    2.0384 !Valency angle parameter
    6.1431 !Not used
    6.9290 !Double bond/angle parameter
    0.3989 !Double bond/angle parameter: overcoord
    3.9954 !Double bond/angle parameter: overcoord
   -2.4837 !Not used
    5.7796 !Torsion/BO parameter
   10.0000 !Torsion overcoordination
    1.9487 !Torsion overcoordination
   -1.2327 !Conjugation 0 (not used)
    2.1645 !Conjugation
    1.5591 !vdWaals shielding
    0.1000 !Cutoff for bond order (*100)
```

```
   2.1365 !Valency angle conjugation parameter
   0.6991 !Overcoordination parameter
  50.0000 !Overcoordination parameter
   1.8512 !Valency/lone pair parameter
   0.5000 !Not used
  20.0000 !Not used
   5.0000 !Molecular energy (not used)
   0.0000 !Molecular energy (not used)
   2.6962 !Valency angle conjugation parameter
15    ! Nr of atoms; cov.r; valency;a.m;Rvdw;Evdw;gammaEEM;cov.r2;#
            alfa;gammavdW;valency;Eunder;Eover;chiEEM;etaEEM;n.u.
            cov r3;Elp;Heat inc.;n.u.;n.u.;n.u.;n.u.
            ov/un;val1;n.u.;val3,vval4
C    1.3817   4.0000  12.0000   1.8903   0.1838   0.9000   1.1341   4.0000
     9.7559   2.1346   4.0000  34.9350  79.5548   5.9666   7.0000   0.0000
     1.2114   0.0000 202.5551   8.9539  34.9289  13.5366   0.8563   0.0000
    -2.8983   2.5000   1.0564   4.0000   2.9663   0.0000   0.0000   0.0000
H    0.8930   1.0000   1.0080   1.3550   0.0930   0.8203  -0.1000   1.0000
     8.2230  33.2894   1.0000   0.0000 121.1250   3.7248   9.6093   1.0000
    -0.1000   0.0000  61.6606   3.0408   2.4197   0.0003   1.0698   0.0000
   -19.4571   4.2733   1.0338   1.0000   2.8793   0.0000   0.0000   0.0000
O    1.2450   2.0000  15.9990   2.3890   0.1000   1.0898   1.0548   6.0000
     9.7300  13.8449   4.0000  37.5000 116.0768   8.5000   8.3122   2.0000
     0.9049   0.4056  59.0626   3.5027   0.7640   0.0021   0.9745   0.0000
    -3.5500   2.9000   1.0493   4.0000   2.9225   0.0000   0.0000   0.0000
N    1.2333   3.0000  14.0000   1.9324   0.1376   0.8596   1.1748   5.0000
    10.0667   7.8431   4.0000  32.2482 100.0000   6.8418   6.3404   2.0000
     1.0433  13.7673 119.9837   2.1961   3.0696   2.7683   0.9745   0.0000
    -4.3875   2.6192   1.0183   4.0000   2.8793   0.0000   0.0000   0.0000
S    1.9405   2.0000  32.0600   2.0677   0.2099   1.0336   1.5479   6.0000
     9.9575   4.9055   4.0000  52.9998 112.1416   6.5000   8.2545   2.0000
     1.4601   9.7177  71.1843   5.7487  23.2859  12.7147   0.9745   0.0000
   -11.0000   2.7466   1.0338   6.2998   2.8793   0.0000   0.0000   0.0000
Si   2.0175   4.0000  28.0600   2.0473   0.1835   0.8925   1.2962   4.0000
```

```
    12.3588   1.2523   4.0000  21.7115 139.9309   4.6988   6.0000   0.0000
    -1.0000   0.0000 128.2031   8.7895  23.9298   0.8381   0.8563   0.0000
    -4.7525   2.1607   1.0338   4.0000   2.5791   0.0000   0.0000   0.0000
Ca   1.9927   2.0000  40.0870   2.7005   0.1848   0.7939   1.0000   2.0000
    10.6123  27.5993   3.0000  38.0000   0.0000  -1.9372   6.5275   0.0000
    -1.3000   0.0000 220.0000  49.9248   0.3370   0.0000   0.0000   0.0000
    -2.0000   4.0000   1.0564   6.2998   2.9663   1.4000   0.0100  13.0000
Cs   2.5411   1.0000 132.9054   2.1409   0.3507   0.9824  -1.0000   1.0000
    14.0000   2.5000   1.0000   0.0000   0.0000  -4.1130   8.7265   0.0000
    -1.0000   0.0000  23.0445 100.0000   1.0000   0.0000   0.8563   0.0000
    -2.5000   3.9900   1.0338   8.0000   2.5791   1.0000   0.0100  13.0000
K    2.1000   1.0000  39.0983   2.6480   0.1676   0.3343  -1.0000   1.0000
     9.0047   2.5000   1.0000   0.0000   0.0000  -5.0000  10.4546   0.0000
    -1.0000   0.0000  23.0445 100.0000   1.0000   0.0000   0.8563   0.0000
    -2.5000   3.9900   1.0338   8.0000   2.5791   1.0000   0.0100  13.0000
Sr   2.1997   2.0000  87.6200   2.5141   0.3839   0.3983   1.0000   2.0000
    11.1452  27.5993   3.0000   0.0000   0.0000  -4.2868   6.5000   0.0000
    -1.3000   0.0000 220.0000  49.9248   0.3370   0.0000   0.0000   0.0000
   -25.0000   4.0000   1.0564   6.2998   2.9663   1.0000   0.1000  13.0000
Na   1.8000   1.0000  22.9898   2.8270   0.1872   0.4000  -1.0000   1.0000
    10.0000   2.5000   1.0000   0.0000   0.0000  -0.9871   6.7728   0.0000
    -1.0000   0.0000  23.0445 100.0000   1.0000   0.0000   0.8563   0.0000
    -2.5000   3.9900   1.0338   8.0000   2.5791   0.0000   0.0000   0.0000
Mg   1.8278   2.0000  24.3050   2.2494   0.1830   0.4805   1.0000   2.0000
    10.8448   4.4030   3.0000  38.0000   0.0000   0.1595   6.1918   0.0000
    -1.3000   0.0000  34.5160  49.9248   0.3370   0.0000   0.0000   0.0000
   -16.6849   2.3663   1.0564   6.0000   2.9663   0.0000   0.0000   0.0000
Al   2.1967   3.0000  26.9820   2.3738   0.2328   0.4873  -1.6836   3.0000
     9.4002   2.6409   3.0000   0.0076  16.5151  -0.7626   6.4941   0.0000
    -1.0000   0.0000  78.4675  20.0000   0.2500   0.0000   0.8563   0.0000
   -23.1826   1.5000   1.0338   8.0000   2.5791   1.4000   0.2000  13.0000
Cu   1.9202   2.0000  63.5460   1.9221   0.2826   1.0000   0.1000   1.0000
    10.9889 100.0000   1.0000   0.0000   0.0000   2.7875   6.0000   0.0000
    -1.0000   0.0000  80.7000  34.9555   0.4988   0.0000   0.8563   0.0000
```

```
    -5.1872   3.1491   1.0000   4.0000   2.5791   0.0000   0.0000   0.0000
X   -0.1000   2.0000   1.0080   2.0000   0.0000   1.0000  -0.1000   6.0000
    10.0000   2.5000   4.0000   0.0000   0.0000   8.5000   1.5000   0.0000
    -0.1000   0.0000 127.6226   8.7410  13.3640   0.6690   0.9745   0.0000
   -11.0000   2.7466   1.0338   6.2998   2.8793   0.0000   0.0000   0.0000
74    ! Nr of bonds; Edis1;LPpen;n.u.;pbe1;pbo5;13corr;pbo6
                     pbe2;pbo3;pbo4;n.u.;pbo1;pbo2;ovcorr
 1  1 158.2004  99.1897  78.0000  -0.7738  -0.4550   1.0000  37.6117   0.4147
        0.4590  -0.1000   9.1628   1.0000  -0.0777   6.7268   1.0000   0.0000
 1  2 169.4760   0.0000   0.0000  -0.6083   0.0000   1.0000   6.0000   0.7652
        5.2290   1.0000   0.0000   1.0000  -0.0500   6.9136   0.0000   0.0000
 2  2 153.3934   0.0000   0.0000  -0.4600   0.0000   1.0000   6.0000   0.7300
        6.2500   1.0000   0.0000   1.0000  -0.0790   6.0552   0.0000   0.0000
 1  3 158.6946 107.4583  23.3136  -0.4240  -0.1743   1.0000  10.8209   1.0000
        0.5322  -0.3113   7.0000   1.0000  -0.1447   5.2450   0.0000   0.0000
 3  3 142.2858 145.0000  50.8293   0.2506  -0.1000   1.0000  29.7503   0.6051
        0.3451  -0.1055   9.0000   1.0000  -0.1225   5.5000   1.0000   0.0000
 1  4 134.1215 140.2179  79.9745   0.0163  -0.1428   1.0000  27.0617   0.2000
        0.1387  -0.3681   7.1611   1.0000  -0.1000   5.0825   1.0000   0.0000
 3  4 130.8596 169.4551  40.0000   0.3837  -0.1639   1.0000  35.0000   0.2000
        1.0000  -0.3579   7.0004   1.0000  -0.1193   6.8773   1.0000   0.0000
 4  4 157.9384  82.5526 152.5336   0.4010  -0.1034   1.0000  12.4261   0.5828
        0.1578  -0.1509  11.9186   1.0000  -0.0861   5.4271   1.0000   0.0000
 2  3 160.0000   0.0000   0.0000  -0.5725   0.0000   1.0000   6.0000   0.5626
        1.1150   1.0000   0.0000   1.0000  -0.0920   4.2790   0.0000   0.0000
 2  4 231.8173   0.0000   0.0000  -0.3364   0.0000   1.0000   6.0000   0.4402
        8.8910   1.0000   0.0000   1.0000  -0.0327   6.5754   0.0000   0.0000
 1  5 128.9942  74.5848  55.2528   0.1035  -0.5211   1.0000  18.9617   0.6000
        0.2949  -0.2398   8.1175   1.0000  -0.1029   5.6731   1.0000   0.0000
 2  5 151.5159   0.0000   0.0000  -0.4721   0.0000   1.0000   6.0000   0.6000
        9.4366   1.0000   0.0000   1.0000  -0.0290   7.0050   1.0000   0.0000
 3  5   0.0000   0.0000   0.0000   0.5563  -0.4038   1.0000  49.5611   0.6000
        0.4259  -0.4577  12.7569   1.0000  -0.1100   7.1145   1.0000   0.0000
 4  5   0.0000   0.0000   0.0000   0.4438  -0.2034   1.0000  40.3399   0.6000
```

```
       0.3296  -0.3153   9.1227   1.0000  -0.1805   5.6864   1.0000   0.0000
5  5  96.1871  93.7006  68.6860   0.0955  -0.4781   1.0000  17.8574   0.6000
       0.2723  -0.2373   9.7875   1.0000  -0.0950   6.4757   1.0000   0.0000
1  6 108.3910  95.0233   0.0000   0.1129  -0.5558   1.0000  17.2117   0.4568
       0.2424  -0.2378  10.1163   1.0000  -0.1020   5.7156   1.0000   0.0000
2  6 250.0000   0.0000   0.0000  -0.7128   0.0000   1.0000   6.0000   0.1186
      18.5790   1.0000   0.0000   1.0000  -0.0731   7.4983   0.0000   0.0000
3  6 272.8709  18.4462   0.0000  -0.6107  -0.3000   1.0000  36.0000   0.8270
      10.2334  -0.5495  29.9954   1.0000  -0.1277   7.5863   1.0000   0.0000
4  6 119.7136  41.2405  43.3991  -0.2060  -0.3000   1.0000  36.0000   0.7957
       0.8189  -0.2614   9.4060   1.0000  -0.1245   6.1856   1.0000   0.0000
6  6  78.0276  54.0531  30.0000   0.5398  -0.3000   1.0000  16.0000   0.0476
       0.2865  -0.8055   7.1248   1.0000  -0.0681   8.6957   0.0000   0.0000
2  7   0.0000   0.0000   0.0000  -0.0203  -0.1418   1.0000  13.1260   0.0230
       8.2136  -0.1310   0.0000   1.0000  -0.2692   6.4254   0.0000  24.4461
3  7  50.8757   0.0000  43.3991   1.0000  -0.3000   1.0000  36.0000   0.0025
       0.7609  -0.2500  12.0000   1.0000  -0.0515   8.9041   1.0000  24.4461
5  7   0.0000   0.0000   0.0000   0.5000  -0.3000   1.0000  16.0000   0.5000
       0.5000  -0.2500  15.0000   1.0000  -0.1000   9.0000   0.0000   0.0000
6  7   0.0000   0.0000   0.0000   0.5000  -0.3000   1.0000  16.0000   0.5000
       0.5000  -0.2500  15.0000   1.0000  -0.1000   9.0000   0.0000   0.0000
7  7  36.9494   0.0000   0.0000  -0.0412  -0.2000   0.0000  16.0000   0.3233
       0.3708  -0.2000  10.0000   1.0000  -0.0822   4.2104   0.0000   0.0000
2  8   0.0000   0.0000   0.0000  -0.0203  -0.1418   1.0000  13.1260   0.0230
       8.2136  -0.1310   0.0000   1.0000  -0.2692   6.4254   0.0000  24.4461
3  8  20.2042   0.0000  43.0000   0.8725  -0.3000   1.0000  36.0000   0.9891
       1.1717  -0.3500  25.0000   1.0000  -0.0535   7.4006   1.0000   0.0000
8  8  23.4317   0.0000   0.0000   0.0743   0.3000   0.0000  25.0000   0.5292
       0.7716  -0.4000  12.0000   1.0000  -0.0584   4.5750   0.0000   0.0000
2  9   0.0000   0.0000   0.0000  -1.0000  -0.3000   1.0000  36.0000   0.7000
      10.1151  -0.3500  25.0000   1.0000  -0.1053   8.2003   1.0000   0.0000
3  9  22.6146   0.0000  43.0000   0.6651  -0.3000   1.0000  36.0000   1.0000
       0.9166  -0.3500  25.0000   1.0000  -0.0583   7.3861   1.0000   0.0000
9  9  22.6628   0.0000   0.0000   0.3272   0.3000   0.0000  25.0000   0.5944
```

```
         0.9915  -0.4000  12.0000   1.0000  -0.0517   4.5075   0.0000   0.0000
  2 10   0.0000   0.0000   0.0000  -0.0203  -0.1418   1.0000  13.1260   0.0230
         8.2136  -0.1310   0.0000   1.0000  -0.2692   6.4254   0.0000  24.4461
  3 10  40.0000   0.0000  43.3991   1.0000  -0.3000   1.0000  36.0000   1.0000
         0.9111  -0.2500  12.0000   1.0000  -0.0746   8.2827   1.0000  24.4461
 10 10  25.4008   0.0000   0.0000   0.2399  -0.2000   0.0000  16.0000   0.4158
         0.5220  -0.2000  10.0000   1.0000  -0.0848   4.0000   0.0000   0.0000
  4  7   0.0000   0.0000   0.0000   0.5000  -0.3000   1.0000  16.0000   0.5000
         0.5000  -0.2500  15.0000   1.0000  -0.1000   9.0000   0.0000   0.0000
  4  8   0.0000   0.0000   0.0000   0.5000  -0.3000   1.0000  16.0000   0.5000
         0.5000  -0.2500  15.0000   1.0000  -0.1000   9.0000   0.0000   0.0000
  4  9   0.0000   0.0000   0.0000   0.5000  -0.3000   1.0000  16.0000   0.5000
         0.5000  -0.2500  15.0000   1.0000  -0.1000   9.0000   0.0000   0.0000
  4 10   0.0000   0.0000   0.0000   0.5000  -0.3000   1.0000  16.0000   0.5000
         0.5000  -0.2500  15.0000   1.0000  -0.1000   9.0000   0.0000   0.0000
  5  8   0.0000   0.0000   0.0000   0.5000  -0.3000   1.0000  16.0000   0.5000
         0.5000  -0.2500  15.0000   1.0000  -0.1000   9.0000   0.0000   0.0000
  5  9   0.0000   0.0000   0.0000   0.5000  -0.3000   1.0000  16.0000   0.5000
         0.5000  -0.2500  15.0000   1.0000  -0.1000   9.0000   0.0000   0.0000
  5 10   0.0000   0.0000   0.0000   0.5000  -0.3000   1.0000  16.0000   0.5000
         0.5000  -0.2500  15.0000   1.0000  -0.1000   9.0000   0.0000   0.0000
  6  8   0.0000   0.0000   0.0000   0.5000  -0.3000   1.0000  16.0000   0.5000
         0.5000  -0.2500  15.0000   1.0000  -0.1000   9.0000   0.0000   0.0000
  6  9   0.0000   0.0000   0.0000   0.5000  -0.3000   1.0000  16.0000   0.5000
         0.5000  -0.2500  15.0000   1.0000  -0.1000   9.0000   0.0000   0.0000
  6 10   0.0000   0.0000   0.0000   0.5000  -0.3000   1.0000  16.0000   0.5000
         0.5000  -0.2500  15.0000   1.0000  -0.1000   9.0000   0.0000   0.0000
  7  8   0.0000   0.0000   0.0000   0.5000  -0.3000   1.0000  16.0000   0.5000
         0.5000  -0.2500  15.0000   1.0000  -0.1000   9.0000   0.0000   0.0000
  7  9   0.0000   0.0000   0.0000   0.5000  -0.3000   1.0000  16.0000   0.5000
         0.5000  -0.2500  15.0000   1.0000  -0.1000   9.0000   0.0000   0.0000
  7 10   0.0000   0.0000   0.0000   0.5000  -0.3000   1.0000  16.0000   0.5000
         0.5000  -0.2500  15.0000   1.0000  -0.1000   9.0000   0.0000   0.0000
  8  9   0.0000   0.0000   0.0000   0.5000  -0.3000   1.0000  16.0000   0.5000
```

```
          0.5000   -0.2500   15.0000    1.0000   -0.1000    9.0000    0.0000    0.0000
  8 10    0.0000    0.0000    0.0000    0.5000   -0.3000    1.0000   16.0000    0.5000
          0.5000   -0.2500   15.0000    1.0000   -0.1000    9.0000    0.0000    0.0000
  9 10    0.0000    0.0000    0.0000    0.5000   -0.3000    1.0000   16.0000    0.5000
          0.5000   -0.2500   15.0000    1.0000   -0.1000    9.0000    0.0000    0.0000
  2 11    0.0000    0.0000    0.0000   -1.0000   -0.3000    1.0000   36.0000    0.7000
         10.1151   -0.3500   25.0000    1.0000   -0.1053    8.2003    1.0000    0.0000
  3 11   45.8933    0.0000    0.0000   -0.1511   -0.3000    1.0000   36.0000    0.3105
          5.8448   -0.3500   25.0000    1.0000   -0.0659    7.9140    1.0000    0.0000
  6 11    0.1000    0.0000    0.0000    0.2500   -0.5000    1.0000   35.0000    0.6000
          0.5000   -0.5000   20.0000    1.0000   -0.2000   10.0000    1.0000    0.0000
 11 11   60.0000    0.0000    0.0000   -0.3458    0.3000    0.0000   25.0000    0.2477
          2.4578   -0.4000   12.0000    1.0000   -0.0513    4.5180    0.0000    0.0000
  2 12   58.6896    0.0000    0.0000   -0.0203   -0.1418    1.0000   13.1260    0.0230
          8.2136   -0.1310    0.0000    1.0000   -0.2692    6.4254    0.0000   24.4461
  3 12   60.0341    0.0000   43.3991    1.0000   -0.3000    1.0000   36.0000    0.0038
          1.0000   -0.2500   12.0000    1.0000   -0.0884    6.7572    1.0000   24.4461
 12 12   27.2865    0.0000    0.0000    0.3694   -0.2000    0.0000   16.0000    0.2631
          0.7983   -0.2000   10.0000    1.0000   -0.1135    4.5200    0.0000    0.0000
  2 13   92.8579    0.0000    0.0000   -0.6528   -0.3000    0.0000   36.0000    0.1551
         10.0663   -0.3500   25.0000    1.0000   -0.0842    7.1758    0.0000    0.0000
  3 13  182.0654    0.0000    0.0000   -0.0920   -0.3000    0.0000   36.0000    0.1688
          0.0010   -0.3500   25.0000    1.0000   -0.1959    6.0894    0.0000    0.0000
  6 13    0.0000    0.0000    0.0000    1.0000    0.3000    0.0000   26.0000    1.0000
          0.5000    0.0000   12.0000    1.0000   -0.2000   10.0000    0.0000    0.0000
  7 13    0.0000    0.0000    0.0000    0.5000   -0.3000    1.0000   16.0000    0.5000
          0.5000   -0.2500   15.0000    1.0000   -0.1000    9.0000    0.0000    0.0000
  8 13    0.0000    0.0000    0.0000    0.5000   -0.3000    1.0000   16.0000    0.5000
          0.5000   -0.2500   15.0000    1.0000   -0.1000    9.0000    0.0000    0.0000
  9 13    0.0000    0.0000    0.0000    0.5000   -0.3000    1.0000   16.0000    0.5000
          0.5000   -0.2500   15.0000    1.0000   -0.1000    9.0000    0.0000    0.0000
 10 13    0.0000    0.0000    0.0000    0.5000   -0.3000    1.0000   16.0000    0.5000
          0.5000   -0.2500   15.0000    1.0000   -0.1000    9.0000    0.0000    0.0000
 11 13    0.0000    0.0000    0.0000    0.5000   -0.3000    1.0000   16.0000    0.5000
```

```
           0.5000  -0.2500  15.0000   1.0000  -0.1000   9.0000   0.0000   0.0000
 12 13     0.0000   0.0000   0.0000   0.5000  -0.3000   1.0000  16.0000   0.5000
           0.5000  -0.2500  15.0000   1.0000  -0.1000   9.0000   0.0000   0.0000
 13 13    34.0777   0.0000   0.0000   0.4832  -0.3000   0.0000  16.0000   0.5154
           6.4631  -0.4197  14.3085   1.0000  -0.1463   6.1608   0.0000   0.0000
  2 14     0.0000   0.0000   0.0000   0.2000  -0.1418   1.0000  13.1260   0.5000
           0.5000  -0.2000  20.0000   1.0000  -0.1000   9.0000   0.0000   0.0000
  3 14    81.4346   0.0000   0.0000  -0.1594  -0.3000   1.0000  36.0000   0.0025
           0.2904  -0.2500  12.0000   1.0000  -0.0742   9.3638   0.0000   0.0000
 14 14    73.6263   0.0000   0.0000   0.0209  -0.2000   0.0000  16.0000   0.3414
           0.4703  -0.2000  15.0000   1.0000  -0.1319   5.9254   0.0000   0.0000
  6 14     0.0000   0.0000   0.0000   1.0000   0.3000   0.0000  26.0000   1.0000
           0.5000  -0.1000  12.0000   1.0000  -0.2000  25.0000   0.0000   0.0000
 13 14     0.0000   0.0000   0.0000   1.0000   0.3000   0.0000  26.0000   1.0000
           0.5000  -0.1000  12.0000   1.0000  -0.2000  10.0000   0.0000   0.0000
  1 13   113.2687   0.0000   0.0000  -1.2036  -0.3000   1.0000  36.0000   0.9310
           0.1703  -0.3500  25.0000   1.0000  -0.0725  15.1736   1.0000   0.0000
  1 12   113.2687   0.0000   0.0000  -1.2036  -0.3000   1.0000  36.0000   0.9310
           0.1703  -0.3500  25.0000   1.0000  -0.0725  15.1736   1.0000   0.0000

 43    ! Nr of off-diagonal terms;   Ediss;Ro;gamma;rsigma;rpi;rpi2
  1  2     0.1239   1.4004   9.8467   1.1210  -1.0000  -1.0000
  2  3     0.0283   1.2885  10.9190   0.9215  -1.0000  -1.0000
  2  4     0.1059   1.8290   9.7818   0.9598  -1.0000  -1.0000
  1  3     0.1156   1.8520   9.8317   1.2854   1.1352   1.0706
  1  4     0.1447   1.8766   9.7990   1.3436   1.1885   1.1363
  3  4     0.1048   2.0003  10.1220   1.3173   1.1096   1.0206
  1  6     0.0541   2.0811  13.5179   1.7778   1.5840  -1.0000
  2  6     0.1659   1.4000  11.7054   1.3437  -1.0000  -1.0000
  3  6     0.1330   2.0545  10.8315   1.7043   1.3773  -1.0000
  4  6     0.1297   1.9384  10.9856   1.6175   1.4045  -1.0000
  1  5     0.1408   1.8161   9.9393   1.7986   1.3021   1.4031
  2  5     0.0895   1.6239  10.0104   1.4640  -1.0000  -1.0000
  1  7     0.1000   1.9000  11.5000  -1.0000  -1.0000  -1.0000
```

```
  2  7   0.0100   1.6000  13.2979  -1.0000  -1.0000  -1.0000
  3  7   0.0955   1.7587  11.9417   1.9052  -1.0000  -1.0000
  5  7   0.1000   1.9000  11.0000  -1.0000  -1.0000  -1.0000
  6  7   0.1000   1.9000  11.0000  -1.0000  -1.0000  -1.0000
  2  8   0.2961   1.7153  13.7662  -1.0000  -1.0000  -1.0000
  3  8   0.1924   1.7793  11.9109   1.9358  -1.0000  -1.0000
  2  9   0.3000   1.5647  13.3924  -1.0000  -1.0000  -1.0000
  3  9   0.1832   1.7503  12.6152   1.6986  -1.0000  -1.0000
  2 10   0.0274   1.6386  13.6906   0.0010  -1.0000  -1.0000
  3 10   0.2033   1.7974  11.2834   1.8164  -1.0000  -1.0000
  5  8   0.2500   1.9000  12.0000  -1.0000  -1.0000  -1.0000
  6  8   0.2500   1.9000  11.0000  -1.0000  -1.0000  -1.0000
  5  9   0.2500   2.1000  10.5000  -1.0000  -1.0000  -1.0000
  6  9   0.2500   2.1000   9.5000  -1.0000  -1.0000  -1.0000
  5 10   0.3000   2.2000  11.5000  -1.0000  -1.0000  -1.0000
  6 10   0.3000   2.2000  10.5000  -1.0000  -1.0000  -1.0000
  3 11   0.0825   1.5904  11.3396   1.5905  -1.0000  -1.0000
  6 11   0.1757   2.0409  13.7267  -1.0000  -1.0000  -1.0000
  2 12   0.0200   1.4000   9.0000   1.8670  -1.0000  -1.0000
  3 12   0.0702   1.7500  12.0414   1.4636  -1.0000  -1.0000
  6 12   0.1000   1.8500  11.0000  -1.0000  -1.0000  -1.0000
  2 13   0.0564   1.4937  12.0744   1.7276  -1.0000  -1.0000
  3 13   0.1960   1.8464  11.1461   1.5646  -1.0000  -1.0000
  6 13   0.0980   1.7870  10.6898  -1.0000  -1.0000  -1.0000
  2 14   0.0300   1.5200  12.5000   0.1000  -1.0000  -1.0000
  3 14   0.0348   1.7637  12.3562   1.7228  -1.0000  -1.0000
 13 14   0.0341   0.7870   9.0714  -1.0000  -1.0000  -1.0000
  6 14   0.0650   1.3563   9.7035  -1.0000  -1.0000  -1.0000
  1 13   0.0056   2.0234  10.5612   1.6080  -1.0000  -1.0000
  1 12   0.0056   2.0234  10.5612   1.6080  -1.0000  -1.0000
135    ! Nr of angles;at1;at2;at3;Thetao,o;ka;kb;pv1;pv2;val(bo)
  1  1  1  59.0573  30.7029   0.7606   0.0000   0.7180   6.2933   1.1244
  1  1  2  65.7758  14.5234   6.2481   0.0000   0.5665   0.0000   1.6255
  2  1  2  70.2607  25.2202   3.7312   0.0000   0.0050   0.0000   2.7500
```

```
1  2  2   0.0000   0.0000   6.0000   0.0000   0.0000   0.0000   1.0400
1  2  1   0.0000   3.4110   7.7350   0.0000   0.0000   0.0000   1.0400
2  2  2   0.0000  27.9213   5.8635   0.0000   0.0000   0.0000   1.0400
1  1  3  49.6811   7.1713   4.3889   0.0000   0.7171  10.2661   1.0463
3  1  3  77.7473  40.1718   2.9802 -25.3063   1.6170 -46.1315   2.2503
1  1  4  66.1305  12.4661   7.0000   0.0000   3.0000  50.0000   1.1880
3  1  4  73.9544  12.4661   7.0000   0.0000   3.0000   0.0000   1.1880
4  1  4  64.1581  12.4661   7.0000   0.0000   3.0000   0.0000   1.1880
2  1  3  65.0000  13.8815   5.0583   0.0000   0.4985   0.0000   1.4900
2  1  4  74.2929  31.0883   2.6184   0.0000   0.0755   0.0000   1.0500
1  2  4   0.0000   0.0019   6.3000   0.0000   0.0000   0.0000   1.0400
1  3  1  73.5312  44.7275   0.7354   0.0000   3.0000   0.0000   1.0684
1  3  3  79.4761  36.3701   1.8943   0.0000   0.7351  67.6777   3.0000
1  3  4  82.4890  31.4554   0.9953   0.0000   1.6310   0.0000   1.0783
3  3  3  80.7324  30.4554   0.9953   0.0000   1.6310  50.0000   1.0783
3  3  4  84.3637  31.4554   0.9953   0.0000   1.6310   0.0000   1.0783
4  3  4  89.7071  31.4554   0.9953   0.0000   1.6310   0.0000   1.1519
1  3  2  70.1880  20.9562   0.3864   0.0000   0.0050   0.0000   1.6924
2  3  3  75.6935  50.0000   2.0000   0.0000   1.0000   0.0000   1.1680
2  3  4  75.6201  18.7919   0.9833   0.0000   0.1218   0.0000   1.0500
2  3  2  85.8000   9.8453   2.2720   0.0000   2.8635   0.0000   1.5800
1  4  1  66.0330  22.0295   1.4442   0.0000   1.6777   0.0000   1.0500
1  4  3 103.3204  33.0381   0.5787   0.0000   1.6777   0.0000   1.0500
1  4  4 104.1335   8.6043   1.6495   0.0000   1.6777   0.0000   1.0500
3  4  3  74.1978  42.1786   1.7845 -18.0069   1.6777   0.0000   1.0500
3  4  4  74.8600  43.7354   1.1572  -0.9193   1.6777   0.0000   1.0500
4  4  4  75.0538  14.8267   5.2794   0.0000   1.6777   0.0000   1.0500
1  4  2  69.1106  25.5067   1.1003   0.0000   0.0222   0.0000   1.0369
2  4  3  81.3686  40.0712   2.2396   0.0000   0.0222   0.0000   1.0369
2  4  4  83.0104  43.4766   1.5328   0.0000   0.0222   0.0000   1.0500
2  4  2  70.8687  12.0168   5.0132   0.0000   0.0222   0.0000   1.1243
1  2  3   0.0000  25.0000   3.0000   0.0000   1.0000   0.0000   1.0400
1  2  4   0.0000   0.0019   6.0000   0.0000   0.0000   0.0000   1.0400
1  2  5   0.0000   0.0019   6.0000   0.0000   0.0000   0.0000   1.0400
```

```
3  2  3   0.0000  15.0000   2.8900   0.0000   0.0000   0.0000   2.8774
3  2  4   0.0000   0.0019   6.0000   0.0000   0.0000   0.0000   1.0400
4  2  4   0.0000   0.0019   6.0000   0.0000   0.0000   0.0000   1.0400
2  2  3   0.0000   8.5744   3.0000   0.0000   0.0000   0.0000   1.0421
2  2  4   0.0000   0.0019   6.0000   0.0000   0.0000   0.0000   1.0400
1  1  5  74.9397  25.0560   1.8787   0.1463   0.0559   0.0000   1.0400
1  5  1  86.9521  36.9951   2.0903   0.1463   0.0559   0.0000   1.0400
2  1  5  74.9397  25.0560   1.8787   0.0000   0.0000   0.0000   1.0400
1  5  2  86.1791  36.9951   2.0903   0.0000   0.0000   0.0000   1.0400
1  5  5  85.3644  36.9951   2.0903   0.1463   0.0559   0.0000   1.0400
2  5  2  93.1959  36.9951   2.0903   0.0000   0.0000   0.0000   1.0400
2  5  5  84.3331  36.9951   2.0903   0.0000   0.0000   0.0000   1.0400
6  6  6  71.0490  32.4076   1.2648   0.0000   0.0133   0.0000   1.2899
2  6  6  77.2616   5.0190   7.8944   0.0000   4.0000   0.0000   1.0400
2  6  2  75.7983  14.4132   2.8640   0.0000   4.0000   0.0000   1.0400
3  6  6  99.8997  26.6610   2.1237   0.0000   0.0100   0.0000   1.4341
2  6  3  73.6998  40.0000   1.8782   0.0000   4.0000   0.0000   1.1290
3  6  3  98.2184  38.9429   0.7727   0.0000   1.1658   0.0000   2.2641
6  3  6  39.2858   1.3068   5.6478   0.0000   3.8972   0.0000   3.0000
2  3  6  79.2126   4.8973   8.0000   0.0000   1.0859   0.0000   2.1209
3  3  6  82.7397  32.1198   1.8862   0.0000   0.1058   0.0000   1.5443
2  2  6   0.0000  47.1300   6.0000   0.0000   1.6371   0.0000   1.0400
6  2  6   0.0000  27.4206   6.0000   0.0000   1.6371   0.0000   1.0400
3  2  6   0.0000   7.0550   3.9236   0.0000   1.6371   0.0000   1.0400
2  2  5   0.0000   0.0019   6.0000   0.0000   0.0000   0.0000   1.0400
1  1  6  72.5239  22.3583   2.0393   0.0000   1.0031   0.0000   1.0400
1  6  1  69.1709  18.9268   2.1226   0.0000   1.0031   0.0000   1.0400
6  1  6  68.6453  18.7377   2.0496   0.0000   1.0031   0.0000   1.0400
1  6  6  68.9902  19.7021   2.0587   0.0000   1.0031   0.0000   1.0400
2  1  6  72.6403  13.6964   2.4702   0.0000   1.0000   0.0000   1.0400
1  6  2  71.8708  14.6864   2.4702   0.0000   1.0000   0.0000   1.0400
4  6  6  60.6199  17.7559   1.0576   0.0000   2.1459   0.0000   1.0400
4  6  4  74.1294  20.6494   2.1244   0.0000   0.7689   0.0000   1.0400
3  6  4  57.0650   9.4985   0.3423   0.0000   0.7689   0.0000   1.0400
```

```
  6  4  6  24.1137   1.7457   0.2198   0.0000   4.1125   0.0000   1.0400
  2  6  4  68.7410  15.5851   1.8545   0.0000   0.8613   0.0000   1.0400
  2  4  6  80.9040   4.0560   1.2284   0.0000   1.6982   0.0000   1.0400
  4  4  6  60.0000  10.0000   0.7500   0.0000   1.0000   0.0000   1.0400
  3  4  6  69.8728  32.7155   1.5875   0.0000   2.2466   0.0000   1.0400
  4  3  6  69.8728  27.1273   1.5875   0.0000   2.2466   0.0000   1.0400
  4  2  6   0.0000  31.0427   4.5625   0.0000   1.6371   0.0000   1.0400
  1  3  6  85.8521  12.6881   1.0112   0.0000   1.0000   0.0000   1.3220
  1  6  3  71.7524  35.8987   1.5000   0.0000   1.0000   0.0000   1.0487
  3  1  6  70.0000   5.0250   1.0000   0.0000   1.0000   0.0000   1.2500
  1  2  6   0.0000   2.5000   1.0000   0.0000   1.0000   0.0000   1.2500
  3  7  3   1.0000   4.9611   2.4541   0.0000   0.5754   0.0000   1.0000
  7  3  7   9.5066   4.2640   3.1438   0.0000   1.9819   0.0000   1.6463
  2  3  7  51.3829   2.5000   0.2500   0.0000   0.0500   0.0000   1.0000
  3  3  7  70.0000  25.0000   1.0000   0.0000   1.0000   0.0000   1.2500
  3  8  3  45.7222   4.2175   3.5761   0.0000   0.6153   0.0000   2.3668
  2  3  8  94.0770   2.0922   6.0000   0.0000   0.7307   0.0000   1.0135
  8  3  8  75.6996   5.2610   3.9306   0.0000   1.9091   0.0000   1.1965
  3  9  3 100.0000   1.2360   6.8249   0.0000   3.2930   0.0000   1.0000
  2  3  9 100.0000   1.0007   9.7740   0.0000   1.4276   0.0000   1.0000
  9  3  9  98.5744   2.1499   1.6268   0.0000   3.7347   0.0000   2.8271
  3 10  3  40.5067   9.9705   4.0000   0.0000   0.0500   0.0000   1.5730
 10  3 10  40.0000   9.5071   4.0000   0.0000   3.7118   0.0000   1.4108
  2  3 10  81.1078   2.0823   5.0000   0.0000   0.7032   0.0000   1.0000
  3  3 10  70.0000  25.0000   1.0000   0.0000   1.0000   0.0000   1.2500
  5  3  7  40.0000   5.0000   2.0000   0.0000   1.0000   0.0000   1.2500
  6  3  7  30.0000  10.0000   2.0000   0.0000   1.0000   0.0000   1.2500
  5  3  8  40.0000  10.0000   2.0000   0.0000   1.0000   0.0000   1.2500
  6  3  8  30.0000  15.0000   2.0000   0.0000   1.0000   0.0000   1.2500
  5  3  9  40.0000   4.0000   2.0000   0.0000   1.0000   0.0000   1.2500
  6  3  9  30.0000   8.0000   2.0000   0.0000   1.0000   0.0000   1.2500
  5  3 10  40.0000  15.0000   2.0000   0.0000   1.0000   0.0000   1.2500
  6  3 10  30.0000  22.5000   2.0000   0.0000   1.0000   0.0000   1.2500
  2 12  2   0.0000  49.8261   0.2093   0.0000   2.0870   0.0000   2.2895
```

```
  2  2 12   0.0000  40.0366   3.1505   0.0000   1.1296   0.0000   1.1110
 12  2 12   0.0000   0.5047   0.8000   0.0000   0.8933   0.0000   4.6650
  2 12 12   0.0000   8.7037   0.0827   0.0000   3.5597   0.0000   1.1198
  3 12  3  16.6660  25.0000   1.4129   0.0000   0.3049   0.0000   1.2391
 12  3 12  58.7093  23.5645   8.1273   0.0000   3.9792   0.0000   1.6907
  2  3 12  47.5370   6.3596   2.6766   0.0000   2.7588   0.0000   2.6720
  2 12  3   0.0000  35.0000   0.3447   0.0000   1.0000   0.0000   1.9494
  3  3 12  70.0000  20.0000   1.0000   0.0000   1.0000   0.0000   1.2500
  6  3 12  30.0000  10.0000   2.0000   0.0000   1.0000   0.0000   1.2500
  3  2 13   0.0000   4.2750   1.0250   0.0000   1.3750   0.0000   1.4750
  2  2 13   0.0000   3.0000   1.0000   0.0000   1.0000   0.0000   1.2500
 13  2 13   0.0000  20.2391   0.1328   0.0000   2.9860   0.0000   1.0870
  2  3 13  88.6163  10.1310   1.6896   0.0000   3.0000   0.0000   1.0000
  3  3 13  34.4326  25.9544   5.1239   0.0000   2.7500   0.0000   1.7141
 13  3 13  13.8580  12.3669   4.4355   0.0000   0.6619   0.0000   1.1908
  2 13  2  67.4229   4.5148   5.9702   0.0000   3.0000   0.0000   2.6879
  2 13  3  41.8108  17.3800   2.6618   0.0000   0.7372   0.0000   1.0100
  3 13  3  55.4358  22.1089   3.7402   0.0000   3.0000   0.0000   2.2064
  3 13 13  32.1032   2.3304   4.5935   0.0000   0.5894   0.0000   1.0140
  2 13 13 180.0000 -26.7860   7.3549   0.0000   1.0000   0.0000   1.0252
  2 13 13  78.2279  37.6504   0.4809   0.0000   1.0000   0.0000   2.9475
  6  3 13   7.1670  11.9291   3.9535   0.0000   1.0000   0.0000   3.4258
  3 14  3  96.2265   4.5610  12.0000   0.0000   0.3211   0.0000   1.5204
  3 14  3   0.0000   9.1552   7.9919   0.0000   0.1660   0.0000   1.5386
 14  3 14 100.0000  10.1065   6.0000   0.0000   1.0000   0.0000   3.6601
  2  3 14  55.0417   3.5032   3.9979   0.0000   1.5171   0.0000   1.0400
  3  3 14  70.0000  30.0000   2.0000   0.0000   1.0000   0.0000   1.2500
  3 14 14  66.7783  14.3146   0.7911   0.0000   1.0000   0.0000   1.2333
 13  3 14  68.0314   6.5925  10.1832   0.0000   3.3231   0.0000   0.8395
  6  3 14 113.9913   7.3197   0.3892   0.0000   3.2258   0.0000   1.1530
 42    ! Nr of torsions;at1;at2;at3;at4;;V1;V2;V3;V2(BO);vconj;n.u;n
  1  1  1  1  -0.2500  34.7453   0.0288  -6.3507  -1.6000   0.0000   0.0000
  1  1  1  2  -0.2500  29.2131   0.2945  -4.9581  -2.1802   0.0000   0.0000
  2  1  1  2  -0.2500  31.2081   0.4539  -4.8923  -2.2677   0.0000   0.0000
```

```
1  1  1  3  -0.3495  22.2142  -0.2959  -2.5000  -1.9066   0.0000   0.0000
2  1  1  3   0.0646  24.3195   0.6259  -3.9603  -1.0000   0.0000   0.0000
3  1  1  3  -0.5456   5.5756   0.8433  -5.1924  -1.0180   0.0000   0.0000
1  1  3  1   1.7555  27.9267   0.0072  -2.6533  -1.0000   0.0000   0.0000
1  1  3  2  -1.4358  36.7830  -1.0000  -8.1821  -1.0000   0.0000   0.0000
2  1  3  1  -1.3959  34.5053   0.7200  -2.5714  -2.1641   0.0000   0.0000
2  1  3  2  -2.5000  70.0597   1.0000  -3.5539  -2.9929   0.0000   0.0000
1  1  3  3   0.6852  11.2819  -0.4784  -2.5000  -2.1085   0.0000   0.0000
2  1  3  3   0.1933  80.0000   1.0000  -4.0590  -3.0000   0.0000   0.0000
3  1  3  1  -1.9889  76.4820  -0.1796  -3.8301  -3.0000   0.0000   0.0000
3  1  3  2   0.2160  72.7707  -0.7087  -4.2100  -3.0000   0.0000   0.0000
3  1  3  3  -2.5000  71.0772   0.2542  -3.1631  -3.0000   0.0000   0.0000
1  3  3  1   2.5000  -0.6002   1.0000  -3.4297  -2.8858   0.0000   0.0000
1  3  3  2  -2.5000  -3.3822   0.7004  -5.4467  -2.9586   0.0000   0.0000
2  3  3  2   2.5000  -4.0000   0.9000  -2.5000  -1.0000   0.0000   0.0000
1  3  3  3   1.2329  -4.0000   1.0000  -2.5000  -1.7479   0.0000   0.0000
2  3  3  3   0.8302  -4.0000  -0.7763  -2.5000  -1.0000   0.0000   0.0000
3  3  3  3  -2.5000  -4.0000   1.0000  -2.5000  -1.0000   0.0000   0.0000
0  1  2  0   0.0000   0.0000   0.0000   0.0000   0.0000   0.0000   0.0000
0  2  2  0   0.0000   0.0000   0.0000   0.0000   0.0000   0.0000   0.0000
0  2  3  0   0.0000   0.1000   0.0200  -2.5415   0.0000   0.0000   0.0000
0  1  1  0   0.0000  50.0000   0.3000  -4.0000  -2.0000   0.0000   0.0000
0  3  3  0   0.5511  25.4150   1.1330  -5.1903  -1.0000   0.0000   0.0000
0  1  4  0  -2.4242 128.1636   0.3739  -6.6098  -2.0000   0.0000   0.0000
0  2  4  0   0.0000   0.1000   0.0200  -2.5415   0.0000   0.0000   0.0000
0  3  4  0   1.4816  55.6641   0.0004  -7.0465  -2.7203   0.0000   0.0000
0  4  4  0  -0.3244  27.7086   0.0039  -2.8272  -2.0000   0.0000   0.0000
4  1  4  4  -5.5181   8.9706   0.0004  -6.1782  -2.0000   0.0000   0.0000
0  1  5  0   3.3423  30.3435   0.0365  -2.7171   0.0000   0.0000   0.0000
0  5  5  0  -0.0555 -42.7738   0.1515  -2.2056   0.0000   0.0000   0.0000
0  2  5  0   0.0000   0.0000   0.0000   0.0000   0.0000   0.0000   0.0000
2  6  6  2   0.0000   0.0000   0.0640  -2.4426   0.0000   0.0000   0.0000
2  6  6  6   0.0000   0.0000   0.1587  -2.4426   0.0000   0.0000   0.0000
0  2  6  0   0.0000   0.0000   0.1200  -2.4847   0.0000   0.0000   0.0000
```

```
0  4  6  0   0.0000   0.0000   0.0000  -2.4426   0.0000   0.0000   0.0000

1  1  3  3  -2.0000  73.0530   1.5000  -9.0000  -2.0000   0.0000   0.0000

1  3  3  1   0.0002  80.0000  -1.5000  -2.5000  -2.0000   0.0000   0.0000

3  1  3  3  -1.8835  20.0000   1.5000  -9.0000  -2.0000   0.0000   0.0000

2  3 14  3  -1.5000   6.8333  -0.1978  -1.4683   0.0000   0.0000   0.0000

1    ! Nr of hydrogen bonds;at1;at2;at3;Rhb;Dehb;vhb1

3  2  3   2.1200  -3.5800   1.4500  19.5000
```

d. FF2 file, generated with the CMA-ES 9 Run 5

```
Reactive MD-force field: C/H/O/N/Al/Mg by Phebe Bonilla July 2018
9.55385547921784E+09 CMA-9-RUN5
 39       ! Number of general parameters
   50.0000 !p_boc1 Eq(4c): Overcoordination parameter
    9.5469 !p_boc2 Eq(4d): Overcoordination parameter
   26.5405 !p_coa2 Eq(15): Valency angle conjugation
    1.7224 !p_trip4 Eq(20): Triple bond stabilisation
    6.8702 !p_trip3 Eq(20): Triple bond stabilisation
   60.4850 !k_c2 Eq(19): C2-correction
    1.0588 !p_ovun6 Eq(12): Undercoordination
    4.6000 !p_trip2 Eq(20): Triple bond stabilisation
   12.1176 !p_ovun7 Eq(12): Undercoordination
   13.3056 !p_ovun8 Eq(12): Undercoordination
  -40.0000 !p_trip1 Eq(20): Triple bond stabilization
    0.0000 !Lower Taper-radius (must be 0)
   10.0000 !R_cut Eq(21): Upper Taper-radius
    2.8793 !p_fe1 Eq(6a): Fe dimer correction
   33.8667 !p_val6 Eq(13c): Valency undercoordination
    6.0891 !p_lp1 Eq(8): Lone pair param
    1.0563 !p_val9 Eq(13f): Valency angle exponent
    2.0384 !p_val10 Eq(13g): Valency angle parameter
    6.1431 !p_fe2 Eq(6a): Fe dimer correction
    6.9290 !p_pen2 Eq(14a): Double bond/angle param
    0.3989 !p_pen3 Eq(14a): Double bond/angle param
    3.9954 !p_pen4 Eq(14a): Double bond/angle param
   -2.4837 !p_fe3 Eq(6a): Fe dimer correction
    5.7796 !p_tor2 Eq(16b): Torsion/BO parameter
   10.0000 !p_tor3 Eq(16c): Torsion overcoordination
    1.9487 !p_tor4 Eq(16c): Torsion overcoordination
   -1.2327 !p_elho Eq(26a): electron-hole interaction
    2.1645 !p_cot2 Eq(17b): Conjugation if tors13=0
    1.5591 !p_vdW1 Eq(23b): vdWaals shielding
    0.1000 !Cutoff for bond order (*100)
```

```
   2.1365 !p_coa4 Eq(15): Valency angle conjugation
   0.6991 !p_ovun4 Eq(11b): Over/Undercoordination
  50.0000 !p_ovun3 Eq(11b): Over/Undercoordination
   1.8512 !p_val8 Eq(13d): Valency/lone pair param
   0.5000 !X_soft Eq(25): ACKS2 softness for X_ij
  20.0000 !d Eq(23d): Scale factor in lg-dispersion
   5.0000 !p_val Eq(27): Gauss exponent for electrons
   0.0000 !1 Eq(13e): disable undecoord in val angle
   2.6962 !p_coa3 Eq(15): Valency angle conjugation
 6    ! Nr of atoms; cov.r; valency;a.m;Rvdw;Evdw;gammaEEM;cov.r2;#
           alfa;gammavdW;valency;Eunder;Eover;chiEEM;etaEEM;n.u.
           cov r3;Elp;Heat inc.;bo131;bo132;bo133;softcut;n.u.
           ov/un;val1;n.u.;val3,vval4
C    1.3825   4.0000  12.0000   1.9133   0.1853   0.9000   1.1359   4.0000
     9.7602   2.1346   4.0000  33.2433  79.5548   5.8678   7.0000   0.0000
     1.2104   0.0000 199.0303   8.6991  34.7289  13.3894   0.8563   0.0000
    -2.8983   2.5000   1.0564   4.0000   2.9663   0.0000   0.0000   0.0000
H    0.8930   1.0000   1.0080   1.3550   0.0930   0.8203  -0.1000   1.0000
     8.2230   5.0518   1.0000   0.0000 121.1250   5.3200   7.4366   1.0000
    -0.1000   0.0000  62.4879   1.9771  62.4879   0.7571   1.0698   0.0000
   -15.7683   2.1488   1.0338   1.0000   2.8793   0.0000   0.0000   0.0000
O    1.2477   2.0000  15.9990   1.9236   0.0904   1.0503   1.0863   6.0000
    10.2127   7.7719   4.0000  36.9573 116.0768   8.5000   8.9989   2.0000
     0.9088   1.0003  60.8726  20.4140   3.3754   0.2702   0.9745   0.0000
    -3.6141   2.7025   1.0493   4.0000   2.9225   0.0000   0.0000   0.0000
N    1.6000   3.0000  14.0000   1.9449   0.1458   0.8596   1.2459   5.0000
     9.7908  26.8500   4.0000  12.5086 100.0000   6.8418   6.3404   2.0000
     1.1098   1.1098 119.9837   1.3701   2.4331   2.4420   0.9745   0.0000
     2.4420   1.5000   1.0183   4.0000   2.8793   0.0000   0.0000   0.0000
Al   2.1967   2.0000  26.9820   2.3738   0.2328   0.4873  -1.6836   3.0000
     9.4002   2.6409   3.0000   0.0076  16.5151  -0.7626   6.4941   0.0000
    -1.0000   0.0000  78.4675  20.0000   0.2500   0.0000   0.8563   0.0000
   -23.1826   1.5000   1.0338   8.0000   2.5791   1.4000   0.2000  13.0000
Mg   1.0224   2.0000  24.3050   2.2464   0.2360   0.6067   1.0000   2.0000
```

```
   8.6050   3.8404   3.0000  38.0000   0.0000  -0.0788   7.0432   0.0000
  -1.3000   0.0000  34.5356  17.8457   2.5273   0.0000   0.0000   0.0000
 -14.7890   2.3663   1.0564   6.0000   2.9663   0.0000   0.0000   0.0000
18    ! Nr of bonds; Edis1;LPpen;n.u.;pbe1;pbo5;13corr;pbo6
                         pbe2;pbo3;pbo4;n.u.;pbo1;pbo2;ovcorr
  1  3 160.4802 105.1700  23.3059  -0.3873  -0.1613   1.0000  10.8900   1.0000
         0.5341  -0.3174   7.0303   1.0000  -0.1463   5.2913   0.0000   0.0000
  1  2 170.2316   0.0000   0.0000  -0.5931   0.0000   1.0000   6.0000   0.7140
         5.2290   1.0000   0.0000   1.0000  -0.0500   6.9136   0.0000   0.0000
  1  1 156.5953 100.0400  80.0000  -0.8157  -0.4591   1.0000  37.7400   0.4235
         0.4527  -0.1000   9.2605   1.0000  -0.0750   6.8316   1.0000   0.0000
  1  5   0.7335   0.0000   0.0000  -1.1952  -0.3000   0.0000  36.0000   0.0519
        10.0126  -0.3500  25.0000   1.0000  -0.0998  10.0122   0.0000   0.0000
  1  6   5.6672  27.6028   1.5259   0.7244   0.2858   0.6690  27.8871   0.3377
         5.3252  -0.4272   8.5966   1.0000  -0.5232  10.4693   0.0000   0.0831
  2  2 153.3934   0.0000   0.0000  -0.4600   0.0000   1.0000   6.0000   0.7300
         6.2500   1.0000   0.0000   1.0000  -0.0790   6.0552   0.0000   0.0000
  2  3 180.4373   0.0000   0.0000  -0.8074   0.0000   1.0000   6.0000   0.5514
         1.2490   1.0000   0.0000   0.0000  -0.0657   5.0451   0.0000   0.0000
  2  4 125.4459   0.0000   0.0000   0.1507   0.0000   1.0000   6.0000   1.0000
        10.2061   1.0000   0.0000   1.0000  -0.0303   7.1619   0.0000   0.0000
  2  5  92.4882   0.0000   0.0000  -0.6483  -0.3000   0.0000  36.0000   0.1537
        10.0375  -0.3500  25.0000   1.0000  -0.0887   7.1999   0.0000   0.0000
  2  6 177.4716  68.7278   1.0130  -0.7224  -0.0302   0.9006  29.5769   0.5377
        22.4801  -0.3883   2.7232   1.0000  -0.4263  10.4470   0.0000  24.1086
  3  3  60.1463 176.6200  51.1430  -0.2802  -0.1244   1.0000  29.6400   0.9114
         0.2441  -0.1239   7.6487   1.0000  -0.1302   6.2919   1.0000   0.0000
  3  4 130.8596 169.4600  40.0000   0.3837  -0.1062   1.0000  35.0000   0.2000
         1.0000  -0.3579   7.0004   1.0000  -0.1193   6.8773   1.0000   0.0000
  3  5 228.1737   0.0000   0.0000  -0.8449  -0.3000   0.0000  36.0000   0.1683
         0.3961  -0.3500  25.0000   1.0000  -0.1956   5.2117   0.0000   0.0000
  3  6  58.7457  98.9765  39.9694   0.8043   0.1690   0.3095  43.6157   0.4375
         2.1271  -0.2483   1.5850   1.0000  -0.0874   6.8620   1.0000  24.4461
  4  4 146.3571  50.0000 193.1610  -1.0000  -0.3096   1.0000  14.4000   1.4628
```

```
        0.8606  -0.2706   9.4303   1.0000  -0.1525   6.3921   1.0000   0.0000
  5  5  34.0777   0.0000   0.0000   0.4832  -0.3000   0.0000  16.0000   0.5154
        6.4631  -0.4197  14.3090   1.0000  -0.1463   6.1608   0.0000   0.0000
  6  5   0.0000   0.0000   0.0000   0.5000  -0.3000   1.0000  16.0000   0.5000
        0.5000  -0.2500  15.0000   1.0000  -0.1000   9.0000   0.0000   0.0000
  6  6  40.5111   0.0000   0.0000   0.2563  -0.2000   0.0000  16.0000   0.2232
        1.5087  -0.2000  10.0000   1.0000  -0.1416   4.4975   0.0000   0.0000
  7    ! Nr of off-diagonal terms; Ediss;Ro;gamma;rsigma;rpi;rpi2
  1  2   0.1239   1.4000   9.8442   1.1203  -1.0000  -1.0000
  1  3   0.1131   1.8523   9.8442   1.2775   1.1342   1.0621
  2  4   0.0287   1.7865   9.8668   1.0284  -1.0000  -1.0000
  2  3   0.0344   1.6800  10.3247   0.9013  -1.0000  -1.0000
  3  4   0.1048   2.0003  10.1220   1.3173   1.1096   1.0206
  3  5   0.1651   1.8998  11.2212   1.5416  -1.0000  -1.0000
  3  6   0.0578   1.9707  11.7836   1.4176  -0.7910  -0.3707
 74    ! Nr of angles;at1;at2;at3;Thetao,o;ka;kb;pv1;pv2
  1  1  1  67.2326  22.0695   1.6286   0.0000   1.7959  15.4141   1.8089
  1  1  2  65.2527  14.3185   6.2977   0.0000   0.5645   0.0000   1.1530
  1  1  3  49.5561   7.3000   4.9568   0.0000   0.7533  15.9906   1.0010
  1  1  4  68.0812  14.0000   5.6000   0.0000   5.0000  50.0000   0.9500
  1  1  5  70.0000  30.0000   2.0000   0.0000   1.0000   0.0000   1.0500
  1  2  1   0.0000   3.4110   7.7350   0.0000   0.0000   0.0000   1.0400
  1  2  2   0.0000   0.0000   6.0000   0.0000   0.0000   0.0000   1.0400
  1  2  3   0.0000  25.0000   3.0000   0.0000   1.0000   0.0000   1.0400
  1  2  4   0.0000   0.0019   6.3000   0.0000   0.0000   0.0000   1.0400
  1  2  4   0.0000   0.0019   6.0000   0.0000   0.0000   0.0000   1.0400
  1  2  5   0.0000   5.0000   1.0000   0.0000   1.0000   0.0000   1.5000
  1  3  1  74.3994  44.7500   0.7982   0.0000   3.0000   0.0000   1.0528
  1  3  2  71.5018  21.7062   0.4735   0.0000   0.5186   0.0000   1.1793
  1  3  3  77.9854  36.6201   2.0201   0.0000   0.7434  67.0264   3.0000
  1  3  4  82.4890  31.4554   0.9953   0.0000   1.6310   0.0000   1.0783
  1  3  5  73.2859  34.0858   1.9937   0.0000   1.0176   0.0000   1.0502
  1  4  1  66.0330  22.0295   1.4442   0.0000   1.6777   0.0000   1.0500
  1  4  2  69.1106  25.5067   1.1003   0.0000   0.0222   0.0000   1.0369
```

```
1   4   3 103.3204  33.0381   0.5787   0.0000   1.6777   0.0000   1.0500
1   4   4 104.1335   8.6043   1.6495   0.0000   1.6777   0.0000   1.0500
1   5   1  85.0000  40.0000   1.1464   0.0000   1.0000   0.0000   2.0191
1   5   2  69.7915  24.1030   0.8107   0.0000   1.0000   0.0000   1.5000
1   5   3  71.0541  29.4591   0.8520   0.0000   1.0000   0.0000   1.1000
1   5   5   0.0000   2.3895   1.0406   0.0000   1.0000   0.0000   1.1505
2   1   2  70.0840  25.3540   3.4508   0.0000   0.0050   0.0000   3.0000
2   1   3  65.0000  14.2057   4.8649   0.0000   0.3504   0.0000   1.7185
2   1   4  74.2929  31.0883   2.6184   0.0000   0.0755   0.0000   1.0500
2   1   5  80.0000  25.0000   2.0000   0.0000   1.0000   0.0000   1.0500
2   2   2   0.0000  27.9213   5.8635   0.0000   0.0000   0.0000   1.0400
2   2   3   0.0000   9.7025   6.0000   0.0000   0.0000   0.0000   1.0400
2   2   4   0.0000   0.0019   6.0000   0.0000   0.0000   0.0000   1.0400
2   2   5   0.0000   3.0000   1.0000   0.0000   1.0000   0.0000   1.2500
2   2   6   0.0000  40.0366   3.1505   0.0000   1.1296   0.0000   1.1110
2   3   2  77.0645  10.4737   1.2895   0.0000   0.9924   0.0000   1.1043
2   3   3  84.9468  23.3540   1.5057   0.0000   2.6374   0.0000   1.3023
2   3   4  75.6201  18.7919   0.9833   0.0000   0.1218   0.0000   1.0500
2   3   5  87.2550  13.1514   1.5130   0.0000   0.3831   0.0000   1.0044
2   3   6 169.2224   7.5994   1.3689  -2.2129  -0.1243  -0.4410   2.9912
2   4   2  70.8687  12.0168   5.0132   0.0000   0.0222   0.0000   1.1243
2   4   3  81.3686  40.0712   2.2396   0.0000   0.0222   0.0000   1.0369
2   4   4  83.0104  43.4766   1.5328   0.0000   0.0222   0.0000   1.0500
2   5   2  67.4229   4.5148   5.9702   0.0000   3.0000   0.0000   2.6879
2   5   3  41.8108  17.3800   2.6618   0.0000   0.7372   0.0000   1.0100
2   5   5 180.0000 -26.7860   7.3549   0.0000   1.0000   0.0000   1.0252
2   5   5  78.2279  37.6504   0.4809   0.0000   1.0000   0.0000   1.0252
2   6   2   0.0000  49.8261   0.2093   0.0000   2.0870   0.0000   2.2895
2   6   3   0.0000  35.0000   0.3447   0.0000   1.0000   0.0000   1.9494
2   6   6   0.0000   8.7037   0.0827   0.0000   3.5597   0.0000   1.1198
3   1   3  77.1171  39.8746   2.5403 -24.3902   1.7740 -42.9758   2.1240
3   1   4  73.9544  12.4661   7.0000   0.0000   3.0000   0.0000   1.1880
3   1   5  70.0000  10.0000   2.0000   0.0000   1.0000   0.0000   1.0500
3   2   3   0.0000   0.0148   6.0000   0.0000   0.0000   0.0000   1.0400
```

```
  3  2  4   0.0000   0.0019   6.0000   0.0000   0.0000   0.0000   1.0400
  3  2  5   0.0000   4.2750   1.0250   0.0000   1.3750   0.0000   1.4750
  3  3  3  80.7324  30.4554   0.9953   0.0000   1.6310  50.0000   1.0783
  3  3  4  84.3637  31.4554   0.9953   0.0000   1.6310   0.0000   1.0783
  3  3  5  34.4326  25.9544   5.1239   0.0000   2.7500   0.0000   1.7140
  3  3  6  70.0000  20.0000   1.0000   0.0000   1.0000   0.0000   1.2500
  3  4  3  74.1978  42.1786   1.7845 -18.0069   1.6777   0.0000   1.0500
  3  4  4  74.8600  43.7354   1.1572  -0.9193   1.6777   0.0000   1.0500
  3  5  3  79.7831  11.9139   2.2055   0.0000   2.9895   0.0000   1.4823
  3  5  5   0.0000   0.0009   0.1000   0.0000   1.0000   0.0000   1.4116
  3  6  3  31.7597 -23.7577  11.4676 -27.8836  -0.3227  25.3454   0.8679
  4  1  4  62.2382  14.0000   8.4000   0.0000   5.0000   0.0000   1.4200
  4  2  4   0.0000   0.0019   6.0000   0.0000   0.0000   0.0000   1.0400
  4  3  4  89.7071  31.4554   0.9953   0.0000   1.6310   0.0000   1.1519
  4  4  4  75.0538  14.8267   5.2794   0.0000   1.6777   0.0000   1.0500
  5  1  5  50.0000  20.0000   1.0000   0.0000   1.0000   0.0000   1.1000
  5  2  5   0.0000  20.2391   0.1328   0.0000   2.9860   0.0000   1.0870
  5  3  5  21.6563  19.3467   4.1473   0.0000   0.6628   0.0000   2.1433
  5  3  6  80.8872  14.2889  14.9126 -21.4842   1.4164   8.4298   5.3675
  5  5  5   0.0000  21.7361   1.4283   0.0000  -0.2101   0.0000   1.3241
  6  2  6   0.0000   0.5047   0.8000   0.0000   0.8933   0.0000   4.6650
  6  3  6  25.5706  12.7838   8.0275   0.0000   1.0124   0.0000   1.7160
 63    ! Nr of torsions;at1;at2;at3;at4;;V1;V2;V3;V2(BO);vconj;n.u;n
  0  1  1  0   0.0000  50.0000   0.3000  -4.0000  -2.0000   0.0000   0.0000
  0  1  2  0   0.0000   0.0000   0.0000   0.0000   0.0000   0.0000   0.0000
  0  2  2  0   0.0000   0.0000   0.0000   0.0000   0.0000   0.0000   0.0000
  0  2  3  0   0.0000   0.1000   0.0200  -2.5415   0.0000   0.0000   0.0000
  0  3  3  0   0.5511  25.4150   1.1330  -5.1903  -1.0000   0.0000   0.0000
  0  1  4  0  -2.4242 128.1640   0.3739  -6.6098  -2.0000   0.0000   0.0000
  0  2  4  0   0.0000   0.1000   0.0200  -2.5415   0.0000   0.0000   0.0000
  0  3  4  0   1.4816  55.6641   0.0004  -7.0465  -2.7831   0.0000   0.0000
  0  4  4  0  -0.3244  27.7086   0.0039  -2.8272  -2.0000   0.0000   0.0000
  1  1  1  1  -0.2500  11.5822   0.1879  -4.7057  -2.2047   0.0000   0.0000
  1  1  3  1   2.0007  25.5641  -0.0608  -2.6456  -1.1766   0.0000   0.0000
```

```
2  1  3  1  -0.9284  34.3952   0.7285  -2.5440  -2.4641   0.0000   0.0000
3  1  3  1  -2.5000  76.0427  -0.0141  -3.7586  -2.9000   0.0000   0.0000
1  3  3  1   2.5000  -0.5332   1.0000  -3.5096  -2.9000   0.0000   0.0000
1  1  1  2  -0.2500  31.2596   0.1709  -4.6391  -1.9002   0.0000   0.0000
2  1  1  2  -0.1770  30.0252   0.4340  -5.0019  -2.0697   0.0000   0.0000
1  1  3  2  -1.1953  42.1545  -1.0000  -8.0821  -1.0000   0.0000   0.0000
2  1  3  2  -2.5000  79.6980   1.0000  -3.5697  -2.7501   0.0000   0.0000
3  1  3  2   0.0345  78.9586  -0.6810  -4.1777  -3.0000   0.0000   0.0000
1  3  3  2  -2.5000   3.3219   0.7180  -5.2021  -2.9330   0.0000   0.0000
2  3  3  2   2.5000  -6.2288   1.0000  -2.6189  -1.0000   0.0000   0.0000
1  1  1  3  -0.7098  22.2951   0.0060  -2.5000  -2.1688   0.0000   0.0000
2  1  1  3  -0.3568  22.6472   0.6045  -4.0088  -1.0000   0.0000   0.0000
3  1  1  3  -0.0528   6.8150   0.7498  -5.0913  -1.0000   0.0000   0.0000
1  1  3  3  -0.0179   5.0603  -0.1894  -2.5000  -2.0399   0.0000   0.0000
2  1  3  3  -0.5583  80.0000   1.0000  -4.4000  -3.0000   0.0000   0.0000
3  1  3  3  -2.5000  66.3525   0.3986  -3.0293  -3.0000   0.0000   0.0000
1  3  3  3   0.0531 -17.3983   1.0000  -2.5000  -2.1584   0.0000   0.0000
2  3  3  3   0.4723 -12.4144  -1.0000  -2.5000  -1.0000   0.0000   0.0000
3  3  3  3  -2.5000 -25.0000   1.0000  -2.5000  -1.0000   0.0000   0.0000
4  1  4  4  -6.6000  10.8000   1.0524  -7.4000  -1.8331   0.0000   0.0000
0  1  3  0   1.7254  86.0769   0.3440  -4.2330  -2.0000   0.0000   0.0000
1  1  4  2  -0.8437  86.3887   0.0320  -7.6835  -1.9825   0.0000   0.0000
1  1  4  3  -2.0000  47.8326  -1.5000  -9.0000  -2.0000   0.0000   0.0000
1  3  4  3   2.0000  96.6281  -1.5000  -3.8076  -2.0000   0.0000   0.0000
2  3  4  3  -0.2997 152.9040  -1.5000  -4.4564  -2.0000   0.0000   0.0000
1  4  4  3   0.1040  70.1152   0.5284  -3.5026  -2.0000   0.0000   0.0000
2  4  4  3   0.1040  70.1152   0.5284  -3.5026  -2.0000   0.0000   0.0000
1  1  3  4   1.2181 119.6186  -1.5000  -7.0635  -2.0000   0.0000   0.0000
2  1  3  4  -2.0000 156.6604   1.1004  -7.3729  -2.0000   0.0000   0.0000
0  1  5  0   0.0000   0.0000   0.0000   0.0000   0.0000   0.0000   0.0000
0  2  5  0   0.0000   0.0000   0.1200  -2.4847   0.0000   0.0000   0.0000
0  3  5  0   0.0000   0.0000   0.1200  -2.4703   0.0000   0.0000   0.0000
0  5  5  0   0.0000   0.0000   0.1200  -2.4426   0.0000   0.0000   0.0000
3  3  5  3   3.5000  20.0000   1.5000  -4.0000   0.0000   0.0000   0.0000
```

```
1  2  3  1   0.0000   1.3164   0.2737  -2.5016   0.0000   0.0000   0.0000
1  1  4  1   1.0000  87.5734   0.6399  -5.9421  -1.6589   0.0000   0.0000
2  1  4  1  -0.0359  88.1512  -0.0959  -7.2511  -1.5996   0.0000   0.0000
2  1  4  1  -0.5092  24.8952   0.4691  -7.6208  -1.8038   0.0000   0.0000
4  1  3  2  -2.4642  11.8541  -1.8692  -3.1855  -0.9000   0.0000   0.0000
2  1  4  2  -0.9868  96.6106   0.7443  -7.5073  -2.1051   0.0000   0.0000
2  1  4  2  -0.5092  24.8952   0.4691  -7.6208  -1.8038   0.0000   0.0000
4  1  4  2   0.5000   2.8273  -0.1650  -7.9605  -2.0202   0.0000   0.0000
3  2  4  2  -1.7508   9.6877  -1.9412  -2.7882  -0.9000   0.0000   0.0000
1  3  2  3  -1.7443  13.8935  -1.3212  -2.5000  -0.9000   0.0000   0.0000
1  4  2  3  -2.5000  10.8893  -0.7189  -2.7243  -0.9000   0.0000   0.0000
2  1  1  4   1.0000  98.8297  -0.2745  -4.9954  -1.9000   0.0000   0.0000
3  1  1  4   0.4250  41.9360   0.6083  -3.8680  -0.9511   0.0000   0.0000
4  1  1  4  -1.0000  21.8427   1.0000  -4.0686  -1.7241   0.0000   0.0000
1  3  2  4  -0.2868  15.6462  -1.0200  -2.6045  -0.9000   0.0000   0.0000
0  2  6  0   0.0000   0.0000   0.1200  -2.4847   0.0000   0.0000   0.0000
0  3  6  0   0.0000   0.0000   0.1200  -2.4703   0.0000   0.0000   0.0000
0  6  6  0   0.0000   0.0000   0.1200  -2.4426   0.0000   0.0000   0.0000
6    ! Nr of hydrogen bonds;at1;at2;at3;Rhb;Dehb;vhb1
3  2  3   1.9682  -4.4628   1.7976   3.0000
3  2  4   2.0000  -6.0000   1.7976   3.0000
4  2  3   1.2000  -2.0000   1.7976   3.0000
4  2  4   1.2979  -6.0000   1.7976   3.0000
1  2  3   2.1397  -4.7669   1.4500  19.5000
1  2  4   2.2924  -2.5509   1.4500  19.5000
```